SLICE PROFILE EFFECTS IN MR PERFUSION IMAGING USING PULSED ARTERIAL SPIN LABELLING

Karam Sidaros

IMM-PHD-2002-93

IMM

ISSN 0909-3192

Preface

This thesis was submitted to the Technical University of Denmark in partial fulfillment of the requirements for obtaining the degree of Ph.D. The studies founding this thesis were commenced in February 1999 and were concluded in January 2002. The work presented in this thesis was performed at three institutions: the department of Informatics and Mathematical Modelling (IMM) at the Technical University of Denmark (DTU), Copenhagen, Denmark, the Danish Research Centre for Magnetic Resonance (DRCMR) at Hvidovre Hospital, Copenhagen, Denmark, and the Department of Radiology at the University of California, San Diego (UCSD), San Diego, USA.

The study was supported financially by a grant from the Technical University of Denmark.

This project was supervised by Professor Lars Kai Hansen, Ph.D. (IMM, DTU), Henrik B.W. Larsson, M.D., Ph.D. (DRCMR) and, during a six-month visit to UCSD, by Professor Richard B. Buxton, Ph.D.

September 2002

Karam Sidaros

Acknowledgements

First of all, I would like to thank my supervisors Lars Kai Hansen and Henrik B.W. Larsson without whom this project would not have been possible. I would like to thank Henrik B.W. Larsson for getting me started in the field of arterial spin labelling and for reading and commenting upon large parts of this manuscript.

I am grateful to the perfusion imaging group at DRCMR for many constructive discussions and would like to thank the staff at both IMM and DRCMR for their warm support and encouragement.

Special thanks go to Thomas T. Liu, Eric C. Wong, Lawrence R. Frank and Richard B. Buxton for welcoming me at UCSD, for being a source of inspiration during my work in San Diego and for the fruitful discussions on the application of offset correction in functional imaging.

I would also like to thank Lars G. Hanson at DRCMR for his advice and comments especially on implementing MR pulse sequences on the scanner and Torben E. Lund at DRCMR for his advice on post-processing algorithms for fMRI. Special thanks also go to Irene K. Andersen at DRCMR, for numerous invaluable discussions on ASL in general, and for reading and commenting upon large portions of this thesis.

Finally, I would like to thank my family and friends for their support, patience and understanding.

Background

The work in this thesis is a continuation of the work in my Master's thesis entitled *MR Perfusion Imaging by Spin Labelling*, which I submitted jointly with Irene K. Andersen in 1998 also to IMM at DTU. During the course of that project we stumbled upon some of the consequences of imperfect slice profiles in FAIR imaging in the form of the signal offset. However, we didn't then understand the underlying mechanisms that caused that offset. A major part of this thesis has therefore been to uncover the sources of the observed offset, and to propose a method of overcoming its effects on perfusion quantification.

Although the reader is not required to have any prior knowledge about MR perfusion measurements in general, or arterial spin labelling in particular, familiarity with the basic principles of nuclear magnetic resonance and magnetic resonance imaging (MRI) is assumed. More specifically, it is assumed that the reader is familiar with the concepts of nuclear spin, spin excitation, relaxation, basic magnetic resonance imaging methods, k-space and echo-planar imaging. These topics are therefore not covered in this thesis. For an introduction to these topics, the reader is referred elsewhere [1–4].

Publications

A number of publications have resulted from the work carried out during the course of this project. These are listed here and are included in appendix C.

- K. Sidaros, I. K. Andersen, H. Gesmar, E. Rostrup and H. B. W. Larsson, *Improved Perfusion Quantification in FAIR Imaging by Offset Correction*, Magn Reson Med 46(1), p.193-197, 2001.
- I. K. Andersen, K. Sidaros, H. B. W. Larsson, E. Rostrup and H. Gesmar, *A Model System for Perfusion Quantification using FAIR*, Magn Reson Imag, 18(5), p. 565-74, 2000.
- I. Andersen, K. Sidaros, H. Gesmar, H. Larsson, E. Rostrup, *The Influence of a Signal Offset on Perfusion Quantification using FAIR*, Proceedings of the 5th Int. Conference on the Mapping of the Human Brain, NeuroImage 9(6), p. S150, 1999.
- K. Sidaros, I. Andersen, H. Larsson, H. Gesmar, E. Rostrup, *Zero Perfusion Calibration of FAIR Imaging with Arbitrary Inversion Slice Profiles*, Proceedings of the 16th Annual Meeting of the European Society for Magnetic Resonance in Medicine and Biology, Magma, 8, suppl. 1, p. 165, 1999.
- K. Sidaros, I. Andersen, H. Larsson, H. Gesmar, E. Rostrup, *Offset Correction in FAIR Imaging*, Proceedings of the 8th Annual Meeting of the International Society of Magnetic Resonance in Medicine, Denver, p. 712, 2000.
- K. Sidaros, I. Andersen, H. Larsson, H. Gesmar, E. Rostrup, *Effect of Slice Profiles on the Accuracy of Fast T_1 Measurements*, Proceedings of the 8th Annual Meeting of the International Society of Magnetic Resonance in Medicine, Denver, p. 429, 2000.
- K. Sidaros, T. T. Liu, E. C. Wong and R. B. Buxton, *Offset Correction in PICORE QUIPSS II Imaging*, Proceedings of the 10th Annual Meeting of the International Society of Magnetic Resonance in Medicine, Honolulu, p. 1063, 2002.
- K. Sidaros, T. T. Liu, T. E. Lund, E. C. Wong and R. B. Buxton, *Improved SNR in Perfusion fMRI by Offset Correction*, Proceedings of the 10th Annual Meeting of the International Society of Magnetic Resonance in Medicine, Honolulu, p. 624, 2002.

Summary

Arterial spin labelling (ASL) is becoming an established method for non-invasive measurements of perfusion using MRI. Although there exists a variety of different ASL methods, they are based on the same principle. Two images are acquired, one in which the arterial blood that perfuses the tissue has been magnetically labelled or tagged and one in which it hasn't. The difference between the two images can be used to determine perfusion.

A general problem in perfusion quantification using ASL is ensuring that the signal from static tissue subtracts out completely in the difference images. In a category of ASL sequences known as pulsed ASL sequences, this is related to the slice profiles of the RF pulses used in the sequence. The common approach of ensuring complete static tissue subtraction involves the introduction of a finite gap between the region in which arterial blood is labelled and the region that is imaged. Unfortunately, this introduces transit delays for the tagged blood to reach the imaging region which in turn affect the quantification of perfusion.

The mechanisms by which the slice profiles affect the degree of static tissue subtraction are investigated in this study. It is shown how imperfect slice profiles may create an offset or bias in the magnetization difference signals. Using simulations and measurements, the dependence of this offset on the gap between the tagging and imaging regions is mapped for various pulsed ASL sequences. It is also demonstrated how the offset is affected by various factors such as B_1 inhomogeneity and the use of presaturation pulses.

Although the offset can be calculated from the theoretical slice profiles of the RF pulses used, an entirely experimental method of estimating the offset on a pixel-by-pixel basis is introduced. The method uses the same ASL sequence used for perfusion measurements to measure the T_1 relaxation curves of both the tag and control experiments. Based on non-linear fitting of a model for the magnetization to the measured curves, a number of parameters can be estimated which enable the calculation of the actual offset.

The proposed method for offset estimation is validated experimentally in both phantoms and *in vivo* studies. It is shown that by subtracting the estimated offset from the magnetization difference images, perfusion can be quantified correctly without the need of ensuring complete static tissue subtraction. The gap between the tagging and imaging regions and hence the transit delays can therefore be reduced while maintaining the correctness of perfusion quantification.

Finally, the proposed method of offset correction is applied in perfusion measurements during functional activation, where it is shown that using offset correction, perfusion changes can be quantified correctly even when static tissue subtraction is incomplete. Furthermore, it is shown that the inversion time in the ASL measurements can be reduced due to the reduced transit delay, thus increasing the activation detectability without sacrificing the quantitative nature of the perfusion measurements.

Dansk Resumé

Effekterne af Skiveprofiler på MR-baseret Perfusionsmålinger ved Hjælp af Pulserende Arteriel Spinmærkning

Arteriel spinmærkning (ASL) er en forholdsvis etableret metode til ikke-invasive perfusionsmålinger vha. magnetisk resonans billeddannelse. Der findes en del forskellige ASL teknikker, der dog er baseret på det samme grundprincip. Der optages to billeder, et hvor det blod, der løber ind i vævet, er magnetisk mærket, og et, hvor det ikke er. Perfusionen kan så beregnes ud fra forskellen mellem de to billeder.

Et generelt problem med perfusionsmåling vha. ASL er at sikre at signalet fra det statiske væv ophæves i differensbilledet. For en bestemt type af ASL sekvenser, kaldet pulserende ASL sekvenser, er dette relateret til skiveprofilerne af de RF pulse, der bruges i sekvenserne. Den generelle måde at sikre at signalet fra det statiske væv ophæves fuldstændigt i differensbilledet er ved at øge afstanden mellem det område, hvor blodet mærkes, og det område, hvor billederne optages. Dette har dog den uheldige konsekvens at transittiden øges for det mærkede blod at nå frem til det område, hvor billederne måles. Denne forsinkelse påvirker udregningen af perfusionen.

Mekanismerne, hvormed skiveprofilerne påvirker graden af ophævelsen af signalet fra det statiske væv, undersøges i denne afhandling. Det vises, hvorledes realistiske skiveprofiler forårsager et såkaldt offset eller bias i differensbillederne. Det kortlægges med simuleringer og målinger, hvorledes dette offset afhænger af afstanden mellem det område, hvor blodet mærkes, og det område, hvor der måles. Dette gentages for forskellige ASL sekvenser. Det påvises også, hvorledes offsettet påvirkes af flere faktorer såsom B_1 inhomogeniteter og brugen af præsaturationspulse.

På trods af at offsettet kan beregnes ud fra de teoretiske skiveprofiler af de anvendte RF pulse, introducerer vi en ren eksperimentel metode til estimering af

det faktiske offset. Metoden er baseret på måling af T_1-relaksationskurver med den samme ASL sekvens som bruges til perfusionsmålingen. Vha. ulineær fitting af en model til de målte relaksationskurver, kan en række parametre estimeres, der tillader beregning af det faktiske offset.

Den foreslåede metode til estimering af offsettet valideres eksperimentelt på fantomer samt *in vivo*. Det vises, at man ved at korrigere de målte signalforskelle for det estimerede offset kan beregne perfusionen korrekt uden at sikre at signalet fra det statiske væv ophæves fuldstændigt i differensbillederne. Afstanden mellem mærkningsområdet og målingsområdet, og derved transittiderne, kan derfor nedsættes uden at påvirke kvantificeringen af perfusionen.

Til sidst anvendes offsetkorrektionen til måling af perfusionsændringer forårsaget af funktionel aktivering af hjernen. Det vises, at perfusionsændringerne måles korrekt på trods af, at signalet fra det statiske væv ikke ophæves fuldstændigt i differensbillederne. Vi viser også at inversionstiden i ASL målingerne kan nedsættes grundet faldet i transittiderne. Dette forøger følsomheden i detektionen af aktiveringen uden at give afkald på kvantificeringen af perfusionen.

Contents

1 Introduction **1**
- 1.1 Objectives . . . 2
- 1.2 Overview . . . 3

2 Perfusion Sensitive Imaging **5**
- 2.1 Definitions . . . 5
- 2.2 Contrast Enhanced Techniques . . . 7
- 2.3 Intravoxel Incoherent Motion . . . 8
- 2.4 Arterial Spin Labelling . . . 9
  - 2.4.1 Continuous ASL . . . 9
  - 2.4.2 Pulsed ASL . . . 11
- 2.5 BOLD Imaging . . . 13

3 Pulsed ASL **15**
- 3.1 Pulsed ASL Sequences . . . 15
  - 3.1.1 EPISTAR-like Sequences . . . 16
  - 3.1.2 FAIR-like Sequences . . . 18
  - 3.1.3 Single-Shot Sequences . . . 21
- 3.2 Quantification Issues . . . 22
  - 3.2.1 T_1 Model . . . 22
  - 3.2.2 ΔM Method . . . 23
  - 3.2.3 Blood T_1 . . . 24
  - 3.2.4 Transit delays . . . 25
  - 3.2.5 General Kinetic Model . . . 26
  - 3.2.6 Transit Delay Insensitivity . . . 28
  - 3.2.7 Intravascular Magnetization . . . 32
  - 3.2.8 Presaturation . . . 33
  - 3.2.9 Choice of Sequence . . . 34
- 3.3 Applications . . . 36

4 RF Pulse Design **39**
4.1 Equations of Motion . . . 39
4.1.1 Hard Pulses . . . 41
4.1.2 Soft Pulses . . . 42
4.1.3 Small Flip Angle Approximation . . . 46
4.2 RF Pulse Properties . . . 46
4.3 Sinc Pulses . . . 48
4.3.1 Refocusing . . . 49
4.3.2 Pulse Duration and Bandwidth . . . 50
4.3.3 Filtering . . . 51
4.4 Adiabatic Pulses . . . 51
4.4.1 Adiabatic Full Passage . . . 53
4.4.2 Hyperbolic Secant Pulses . . . 54
4.4.3 FOCI Modifications . . . 56
4.5 Shinnar-Le Roux Pulses . . . 56
4.5.1 Spin Domain Representation . . . 58
4.5.2 The Forward SLR Transform . . . 59
4.5.3 The Inverse SLR Transform . . . 60
4.5.4 FIR Filter Design . . . 61
4.6 Examples . . . 61
4.6.1 Inversion . . . 61
4.6.2 Excitation . . . 63
4.6.3 Saturation . . . 65
4.7 Discussion . . . 68

5 Slice Profile Effects **69**
5.1 Methods . . . 69
5.1.1 Full Bloch Simulation . . . 70
5.1.2 Slice Profile Functions . . . 70
5.1.3 Integration . . . 71
5.2 Implications for ASL . . . 72
5.3 Magnetization Offset . . . 74
5.3.1 Offset Origin . . . 74
5.3.2 Offset Equations . . . 76
5.3.3 Presaturation . . . 78
5.3.4 QUIPSS Saturation . . . 81
5.3.5 Relaxation Effects . . . 83
5.4 Discussion . . . 83

6 Offset Correction in ASL **89**
6.1 Standard ASL Sequences . . . 90
6.1.1 FAIR . . . 90
6.1.2 PICORE . . . 94
6.2 QUIPSS Sequences . . . 95
6.3 Examples . . . 99

6.4 Implications for Transit Delays 104
6.4.1 Variable Gap 104
6.4.2 Variable Inversion Time 105
6.5 Discussion 107

7 T_1 Measurements 111
7.1 Inversion Recovery 111
7.1.1 Sequence Timing Parameters 112
7.1.2 Polarity Correction 113
7.2 Fast T_1 Measurements 115
7.3 T_1 Measurements in ASL 117
7.4 Effective Relaxation Rates 118
7.4.1 FAIR 118
7.4.2 PICORE 123
7.4.3 PICORE QUIPSS II 125
7.5 Discussion 126

8 ASL in Functional MRI 129
8.1 Functional MRI 129
8.2 ASL in fMRI 130
8.2.1 Perfusion fMRI 131
8.2.2 Simultaneous Perfusion and BOLD fMRI 133
8.2.3 Example 134
8.3 Offset Correction in ASL fMRI 137
8.4 Discussion 145

9 Conclusions 149
9.1 Overall Conclusions 149
9.2 Outlook 151

A Scanner Implementation 153
A.1 DRCMR 153
A.2 UCSD 154

Appendix 153

B Cayley-Klein Parameters 155

C Publications 159

References 183

Chapter 1

Introduction

Magnetic Resonance Imaging (MRI) is a non-invasive imaging technique based on the concept of Nuclear Magnetic Resonance (NMR). MRI is predominantly used in medical contexts and can be used to acquire cross-sectional images of any orientation or true three-dimensional images of tissue and organs with high spatial and temporal resolution.

MRI was initially used as a tool for providing morphological images of various tissues enabling the identification of pathological structures. In recent years, MRI has evolved and various types of physiological information can now be measured using MRI including regional diffusion, perfusion, angiography and functional activation.

Regional perfusion was initially measured with radioactive tracers using various radiographic techniques. With the development of imaging modalities such as single photon emission computed tomography (SPECT) and positron emission tomography (PET), images of regional perfusion could be acquired.

The first attempts to measure perfusion using MRI involved the injection of tracers labelled with fluorine ^{19}F or deuterium ^{2}H, using an approach similar to that of perfusion measurements with radioactive tracers. However, imaging the distribution of the tracers was difficult due to their low concentration. Currently, most MR perfusion measurements are based on proton ^{1}H MRI, which has much higher sensitivity due to the abundance of water in the body. Perfusion can be measured using either exogenous or endogenous tracers as will be described in chapter 2.

There are several reasons to measure perfusion. First of all, perfusion measurements may be used for diagnosis and assessing pathologies with focally de-

creased perfusion, such as ischaemic stroke. Tissue ischaemia due to vascular diseases in the brain or heart is an increasing cause of death and there is therefore a high demand for tools that can assess perfusion. In fact, perfusion measurements can generally be used as a diagnostic tool in pathologies with disturbances of the tissue microvasculature. In research, perfusion measurements provide a powerful tool for investigating the kinetics of blood flow. Perfusion measurements, for example, play a crucial role in the development of models for oxygen consumption during functional activation.

Although this thesis focuses on perfusion measurements in the human brain, the developed methods are applicable to other species and organs as well.

1.1 Objectives

Measurement of perfusion using Arterial Spin Labelling (ASL) is based on the subtraction of two images, one with perfusion weighting and one without. Since the difference between the two images that is related to perfusion is on the order of 1% of the signal in the individual images, it is crucial that the signal that is not related to perfusion cancels completely in the subtraction process.

It is well-known that incomplete static tissue subtraction in pulsed ASL is related to imperfect slice profiles. The common approach, to ensure complete static tissue subtraction, involves the introduction of a finite gap between the tagging and imaging regions. This gap, however, has the unfortunate consequence of introducing a transit delay for tagged blood to reach the imaging region. This transit delay may have a large impact on the quantification of perfusion.

One of the main objectives of this study was therefore to determine how the degree of static tissue subtraction in different ASL sequences is affected by various factors such as the choice of RF pulses, the gap between the tagging and imaging regions and the use of tissue presaturation.

A more thorough understanding of these factors could be used to evaluate how susceptible different ASL sequences are to incomplete static tissue subtraction and how the gap between the tagging and imaging regions can be reduced to minimize the effects of transit delays.

Another objective of this study was to propose an alternative method of overcoming the effects of imperfect slice profiles that does not increase the transit delays. At the same time this method should not decrease the signal-to-noise ratio (SNR) of the measurements.

The method should then be validated both on phantoms and *in vivo* and its performance in quantitative as well as non-quantitative ASL sequences should be investigated. The accuracy of the measured perfusion using the new method should be compared to that using the established method of compensating for imperfect slice profiles.

Finally, another objective was to determine the performance of the proposed method in applications of perfusion measurements, such as functional imaging.

1.2 Overview

Chapter 1 is a general introduction and lists the objectives of the work in this study.

In **chapter 2**, the concept of perfusion is introduced, along with other physiological parameters that influence the kinetics of blood flow. Several MRI techniques used to measure perfusion are described briefly. **Chapter 3** reviews the development and current status of pulsed arterial spin labelling. A variety of spin labelling schemes are presented and issues related to the quantification of absolute perfusion are discussed.

In **chapter 4**, the principles of spin excitation by radiofrequency (RF) pulses are presented with emphasis on the calculation of the slice profiles produced by slice-selective spin excitation. Various types of RF pulses are described and their properties are compared. The methods presented in this chapter serve as a set of tools, which are used in **chapter 5** to examine the effects of imperfect slice profiles in ASL techniques. A novel method of simulating the interaction between the slice profiles of the different RF pulses in ASL sequences is introduced. Using simulations, it is demonstrated how imperfect slice profiles may cause incomplete static tissue subtraction in ASL difference images giving an offset or bias in the magnetization difference signals.

In **chapter 6**, a new method of correcting measured ASL signals for incomplete static tissue subtraction is introduced. It is demonstrated how a T_1 measurement can be used to identify the degree of static tissue subtraction. The method is tested and validated on phantoms and *in vivo*, where it is shown that offset correction of ASL data is feasible without prior knowledge of the actual slice profiles.

In **chapter 7**, the basis of the T_1 measurements used for offset correction is explored in more detail. After a brief introduction to T_1 measurements in general, a key assumption about the T_1 measurements used for offset correction is discussed in detail and its validity is tested using simulations.

Chapter 8 begins with a brief introduction to functional MRI (fMRI) in general and to fMRI using ASL sequences in particular. It is demonstrated *in vivo* how offset correction can be used in ASL fMRI to increase the detectability of activation without compromising the accuracy of perfusion quantification.

Finally, **chapter 9** lists some of the overall conclusions and comments on future directions for perfusion measurements using ASL.

Chapter 2

Perfusion Sensitive Imaging

In this chapter, the concept of perfusion is introduced and various physiological parameters related to the kinetics of blood flow are defined. A brief introduction is thereafter given to various methods of measuring perfusion using MRI. The main principles of dynamic susceptibility contrast imaging, intravoxel incoherent motion imaging, arterial spin labelling and blood oxygenation contrast imaging are described. Note, however, that this chapter is not meant to be a complete review of perfusion measurement techniques in MRI.

2.1 Definitions

The delivery of oxygen and nutrients to tissue cells and the removal of waste products is assured by blood circulation. Oxygenated, arterial blood is delivered to the tissue through the capillary network where oxygen and nutrients are transported, actively or passively, over the capillary membrane into the tissue cells while waste products from metabolism are transported into the capillaries to be removed through the venous system. These processes depend on many parameters such as perfusion, blood pressure, nutrient and oxygen extraction rates, capillary network density and the capillary wall permeability [5, 6]. A number of these quantities will be defined in the following.

Perfusion

The term perfusion is attributed to the blood flow through the capillary network of a unit mass of tissue. The normalization of blood flow by the mass of tissue originates from the conventional perfusion measurements of the uptake

or washout of radionuclide tracers. Perfusion, f, is thus measured in units of volume of blood/mass of tissue/time., typically ml/100g/min or ml/g/s.

In an imaging context, perfusion is thus measured as the blood flow through the capillary network within a voxel divided by the mass of that voxel [7, 8]. Perfusion in the brain is often referred to as cerebral blood flow or CBF.

Blood Volume

Blood volume can be defined either as the total blood volume within a voxel divided by the mass of the voxel or as the fractional volume of the voxel occupied by blood. Blood volume can therefore either be measured in units of volume blood/mass tissue, typically ml/100g, or as a dimensionless quantity.

The blood volume is often divided into arterial, capillary and venous blood volumes. Most of the blood within a voxel is venous or venular [8]. Blood volume in the brain is normally referred to as cerebral blood volume or CBV.

Perfusion and blood volume are two distinct quantities and in principle, there need not be any consistent relation between them. However, they are in practice found to correlate in normal tissue [7].

Tissue-Blood Partition Coefficient

The tissue-blood partition coefficient, λ, of an agent describes the equilibrium distribution of the agent between blood and tissue. In equilibrium the tissue concentration of the agent, C_t, will be given by the arterial concentration of an agent, C_a, and the tissue-blood partition coefficient, such that $C_t = \lambda C_a$ [9]. Due to the history of radionuclide tracer kinetics, λ is typically given in units of ml/g due to the different units of the arterial and tissue concentrations.

For a substance that diffuses freely out of the blood and into the tissue, such as water, λ is approximately 1 ml/g. For an agent that remains in the blood, such as Gd-DTPA in the brain, λ is equal to the blood volume.

Mean Transit Time

The mean transit time (MTT) of an agent is the average amount of time it takes a molecule of the agent to pass through the vasculature of the tissue. For an agent that remains in the blood, such as Gd-DTPA in the brain, MTT is only a few seconds, while for freely diffusible agents, such as water, MTT is much longer.

Extraction Fraction

Perfusion describes the rate at which blood and thus nutrients are delivered to the capillary network supplying the tissue. However, not the entire amount of an agent that is in the blood is extracted into the tissue. The extraction fraction, E, is the fraction of the agent in the blood that is extracted and transported into the tissue. The extraction fraction can under certain conditions be expressed as

$(C_a - C_v)/C_a$, where C_a and C_v are the arterial and venous concentrations of the agent, respectively.

For example, only about 30–50% of the oxygen in the arterial blood is extracted [7], while the rest is removed through the venous system. The cerebral metabolic rate of oxygen, $\mathrm{CMRO_2}$ is thus $E\,f\,C_a^{O_2}$, where $C_a^{O_2}$ is the arterial concentration of O_2.

2.2 Contrast Enhanced Techniques

Exogenous MR contrast agents can be used to measure perfusion, CBV and MTT using a technique commonly referred to as dynamic susceptibility contrast (DSC) MRI. This technique involves the injection of a bolus of contrast agent and repeated rapid measurement of the MRI signal of the tissue of interest. Thus, the effect of the contrast agent on the MRI signal is sampled during the passage of the contrast agent through the tissue.

The most commonly used MR contrast agent for DSC studies is Gadolinium diethylene-triamine-pentaacetic acid (Gd-DTPA), which is paramagnetic. Gd-DTPA does not cross the intact blood-brain barrier and is therefore an intravascular contrast agent in the healthy brain. Being paramagnetic, Gd-DTPA increases the susceptibility of blood plasma by an amount that is proportional to the concentration of the contrast agent. This, in turn, changes the relaxation rates of blood.

Even though Gd-DTPA is an intravascular contrast agent, the change of relaxation rates is not limited to blood. T_1 of tissue is also affected due to water exchange across the blood-brain barrier. Furthermore, the difference in magnetic susceptibility between intravascular and extravascular spins creates magnetic field distortions in the vicinity of blood vessels, which cause additional dephasing of transverse magnetization and hence a reduction in tissue T_2 and T_2^* [8].

In DSC-MRI, the bolus of contrast agent changes the local tissue relaxation rates as it passes through the capillary network of the tissue. A linear relationship is generally assumed between the concentration of the Gd-DTPA and the changes in the transverse relaxation rates. If the MRI signal is repeatedly sampled using a fast imaging technique, such as echo-planar imaging (EPI) [10], the time course of tissue concentration, $C_t(t)$, can be determined from the time course of the measured magnetizations.

If the MRI signal is sampled in an artery, the arterial input function, $C_a(t)$, of contrast agent can be determined as well. The blood volume, CBV, is then given by the integral of $C_t(t)$ normalized by the integral of $C_a(t)$. Determination of CBF, requires furthermore knowledge of the tissue residue impulse response function, $R(t)$, which is the fraction of tracer still present in the tissue at time t after an ideal bolus injection. The tissue concentration is then given by $C_t(t) =$

$f \cdot C_a(t) \otimes R(t)$, where $\otimes$ denotes convolution. Estimating perfusion therefore involves the delicate process of deconvolution of $C_t(t)$ [11, 12]. Once perfusion has been determined, MTT can be calculated using the central volume theory, where MTT = CBV/f [9].

An advantage of the DSC technique is that large signal changes are induced due to changes in the relaxation rates. However absolute quantification of perfusion is somewhat problematic for several reasons. Deconvolution of $C_t(t)$ is not simple, and is very sensitive to noise. Furthermore, it requires correct measurement of $C_a(t)$, which is often underestimated due to partial volume. Another potential source of error is the assumption that the input function in a tissue voxel is identical to that in the large artery used to sample $C_a(t)$, which need not be the case. Another problem, is that the concentration of the tracer isn't measured directly, but is based on an assumed model relating it to the change in relaxation rates.

A general problem with exogenous tracers is the potential toxicity and invasive nature of administration. Furthermore, repeated experiments are problematic using Gd-DTPA due to the low excretion rate from the body.

2.3 Intravoxel Incoherent Motion

In the presence of magnetic field gradients, random or incoherent movement of water molecules causes random phase shifts that destructively interfere with each other. In a spin-echo experiment, this would result in incomplete refocusing of the echo and thus an attenuation of measured signal. The signal is attenuated by a factor $\exp(-bD)$, where b depends on the applied gradient and D is the diffusion coefficient of water [3].

Due to the tortuosity of the capillary network, the flow of blood through capillaries can be regarded as incoherent motion when regarded at the voxel level. This motion causes signal attenuation just as diffusion does, and a pseudo-diffusion coefficient, D^*, is associated with this motion. The signal attenuation due to IntraVoxel Incoherent Motion (IVIM) is $v\exp(-bD^*)$, where v is the fractional voxel volume occupied by flowing blood. D^* is approximately 10 times larger than D, while v is very small, typically a few percent [13, 14].

By measuring the signal attenuation at various b-values, it is possible to estimate D, D^* and v by fitting the attenuation curves to a bi-exponential function. However, the method suffers from low signal-to-noise ratio (SNR), and the bi-exponential behaviour is therefore not always detectable [15–17].

There remains some controversy as to what is actually measured by IVIM imaging. There are different views as to whether the method is sensitive to actual perfusion or to blood volume flow [6, 18].

2.4 Arterial Spin Labelling

Arterial spin labelling (ASL) is a class of MR techniques in which arterial water is used as an endogenous tracer for perfusion measurement. The arterial water is magnetically labelled such that the magnetizations of blood and tissue are in different states. Arterial water flowing in to the imaging slices exchanges with tissue water and changes the magnetization of the latter.

ASL measurements generally conform to the following pattern [19].

- The magnetization of arterial water is inverted or saturated upstream to the imaging slice. This constitutes the labelling or tagging of the blood.
- A delay is allowed for the tagged blood to reach the imaging slice and exchange with tissue water. The arterial magnetization relaxes due to T_1 relaxation during this period.
- The magnetization is measured in the imaging slice(s). This magnetization is a mixture of the tissue magnetization and the change in the magnetization due to inflow of tagged blood.
- A control image is acquired in the same manner as above, except that the arterial water isn't labelled.
- The difference between the two images is dependent only on the amount of tagged blood that entered the imaging slice and exchanged with tissue water. Since the magnetization of the tagged blood is less in the tag image than in the control image, the tag image is subtracted from the control image.
- The difference between the two images is only on the order of 1% of the static tissue magnetization. The perfusion-weighted difference images therefore suffer from inherently low SNR. Repetition of the measurements and averaging is therefore required. Imaging is usually done with alternating tag and control images.

A variety of different ASL sequences have been developed since Detre *et al.* [20] and Williams *et al.* [21] first introduced perfusion imaging using ASL in 1992. ASL sequences generally fall into one of two categories depending on how the tag is applied. These categories are continuous ASL and pulsed ASL, which will be described in the following.

2.4.1 Continuous ASL

The first spin labelling method was proposed by Detre *et al.* [20], who suggested the use of a train of saturation pulses applied repeatedly to saturate blood in the neck. Assuming that saturated arterial water would travel to the brain and exchange with tissue water, the magnetization in the brain would reach a steady state that was lower than when arterial blood was not saturated. Williams *et*

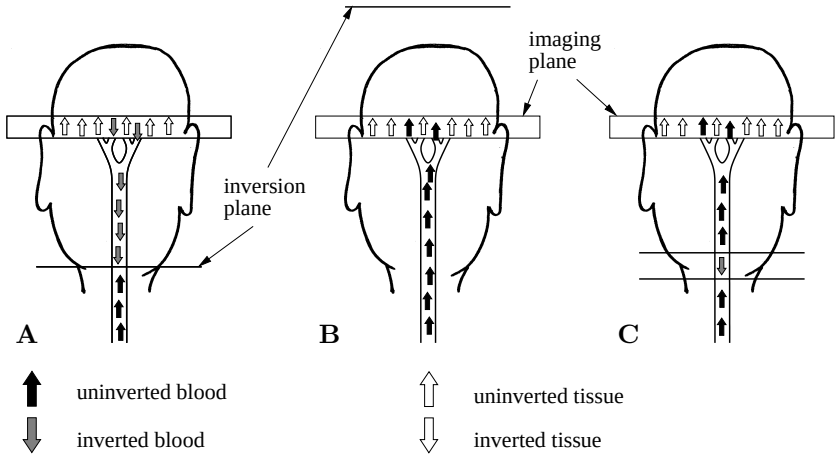

Figure 2.1: Tagging and control techniques in continuous ASL. (A) Tag experiment with inversion plane proximal to the imaging plane. (B) Control experiment, with the inversion plane symmetrically distal to the imaging plane. (C) Control experiment with amplitude modulation RF irradiation giving double inversion.

al. [21] suggested the use of inversion pulses instead of saturation pulses thus doubling the effect of the tagged blood on tissue magnetization. Arterial blood was inverted in a plane proximal to the imaging slice using the principle of adiabatic fast passage. RF irradiation was applied continuously in the presence of a gradient along the flow direction of blood, hence the name *continuous* ASL (CASL). The resonant frequency of the blood would then be spatially dependent such that arterial magnetization would experience a frequency sweep as it passed through the inversion plane. Under certain conditions, such a frequency sweep would invert the arterial magnetization [22]. Figure 2.1A sketches this experiment.

It soon became apparent, though, that the control experiment of not inverting the blood in the inversion plane was not adequate. Although inversion of arterial blood in the tag experiment was far from the imaging slice, the in-slice tissue magnetization was still affected by the prolonged RF irradiation due to magnetization transfer (MT) effects [23]. An alternate control experiment was proposed to overcome MT effects, in which the same RF irradiation was applied as in the tag experiment, but where the inversion plane was moved symmetrically to the opposite side of the imaging plane, typically outside the head, see figure 2.1B. Assuming that the MT effects are symmetrical, the magnetization in the imaging plane is affected equally by the tag and control inversion. This is, however, only completely true exactly halfway between the inversion planes. This type of CASL measurements is therefore only amenable to single-slice imaging where the imaged slice is parallel to the inversion plane.

Zhang *et al.* [24] and Silva *et al.* [25] showed that MT effects can be avoided

altogether by using two RF coils. A small coil is placed next to the carotid arteries and used for spin inversion, while another larger coil is used for imaging. This method allows multislice imaging with any orientation, but requires specialized hardware, which is not readily available.

Another solution was presented by Alsop and Detre [26], where amplitude modulated RF irradiation was applied in the control experiment effectively giving two parallel inversion planes, such that arterial spins are first inverted then reinverted giving no net perturbation, see figure 2.1C. This method also allows multislice imaging at arbitrary orientations, but doesn't require specialized hardware. The disadvantage of this method is, however, that the double inversion isn't perfect, which reduces the labelling efficiency.

Two major problems remained in quantification of perfusion, namely the effects of intravascular signal and long transit delays. The signal from intravascular spins destined for more distal slices may largely overestimate perfusion. Applying bipolar flow-crushing gradients before imaging can alleviate this problem by suppressing signal from moving spins [27].

The transit delay is the time it takes blood to travel from the inversion plane to the imaging slice. Especially in humans, the transit delays are not short compared to the T_1 of blood, and furthermore there is a large variation in transit delays among voxels even within the same imaging slice, which gives rise to a variable degree of attenuation of the ASL signal [28, 29]. This can be overcome by positioning the inversion plane as close as possible to the imaging slice without introducing MT effects, and introducing a delay between tagging and imaging that is long enough to allow all tagged spins to reach the imaging slice and exchange with tissue water before image acquisition. Another advantage of such a delay, is that it allows time for blood flowing through the imaging slice to do so, thus reducing the amount of intravascular spins contributing to the measured signal [27, 28, 30]. The disadvantage of the delay is that it causes signal attenuation and is therefore limited by T_1 of blood and SNR.

Recently, Barbier *et al.* [31, 32] introduced a new type of ASL experiment named Dynamic ASL (DASL). It is related to CASL in that it uses a labelling plane for inverting arterial spins, but instead of alternating tag and control experiments, images are acquired dynamically during the application of the tag after which they are acquired dynamically when the tag is switched off. There is in this case no subtraction of control and tag images, but the measured tissue response is fitted by an appropriate model giving estimates of transit delays, tissue T_1 and perfusion simultaneously.

2.4.2 Pulsed ASL

The other category of ASL sequences is *pulsed* ASL (PASL). The principle difference between CASL and PASL sequences is in the tagging technique. In CASL, arterial spins are inverted using continuous RF irradiation as they pass through

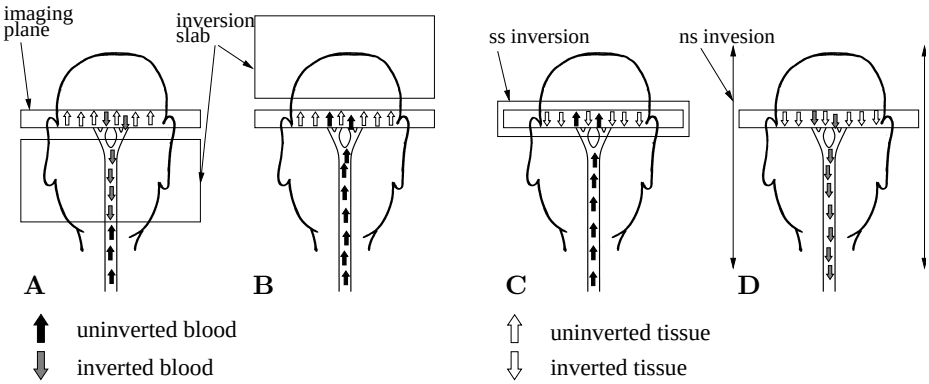

Figure 2.2: Tagging and control techniques in two pulsed ASL sequences, namely EPISTAR and FAIR (without presaturation). (A) Tag experiment in EPISTAR with inversion slab proximal to the imaging plane. Blood entering the imaging slice is inverted. (B) Control experiment in EPISTAR with inversion slab distal to the imaging plane. Blood entering the imaging slice is not inverted. (C) Slice selective inversion experiment in FAIR imaging. (D) Non-selective inversion experiment in FAIR imaging.

an inversion plane. In PASL, the spin inversion is achieved using short inversion pulses, typically 10–15 ms long, which invert spins in a specific region, known as the inversion slab.

In 1994, Edelman *et al.* [33] proposed inverting the magnetization in a thick slab proximal to the imaging slice then imaging the magnetization using EPI after a delay to allow the inverted magnetization to reach the imaging slice. The control experiment utilised inversion in a slab symmetrically distal to the imaging slice thus having the same MT effects. This method is conceptually similar to CASL, and is sketched in figure 2.2A&B. The method was named Echo Planar Imaging and Signal Targeting with Alternating Radiofrequency with the acronym EPISTAR.

Kwong *et al.*, Kim, and Schwarzbauer *et al.* [34–36] proposed a different method consisting of two inversion recovery (IR) measurements, one with slice-selective (ss) inversion and another with non-selective (ns) inversion, see figure 2.2C&D. The method was named Flow sensitive Alternating Inversion Recovery or FAIR. The relaxation of the tissue magnetization after ss inversion is affected by the inflow of uninverted blood, and thus the relaxation rate appears to be increased. In the ns inversion experiment, the relaxation of the tissue magnetization will be unaffected by inflowing blood, assuming that T_1 of blood is equal to that of tissue. The difference between the images acquired in the two cases is therefore perfusion-weighted.

A variety of PASL sequences have since emerged, most of which are alterations of the above sequences in one form or another. Wong *et al.* [29] used the same tag experiment as in EPISTAR, and a control experiment without a

slice-selection gradient in a technique named Proximal Inversion with a Control for Off-Resonance Effects (PICORE). Helpern *et al.* [37] added an inversion pulse in both the tag and control experiments in FAIR such that the in-slice magnetization remained positive in UNinverted Flow-sensitive Alternating Inversion Recovery (UNFAIR). Other modifications were introduced in sequences such as BASE [38], STAR-HASTE [39], TILT [40] and SMART [41]. A conflict of acronyms was nearly inevitable. Two techniques were for example independently named FAIRER by Zhou *et al.* [42] and by Mai *et al.* [43], while EST [44], is the same as UNFAIR.

Unlike CASL, MT effects do not have a large effect on PASL measurements. However, slice selectivity plays an important role. In EPISTAR, the inversion slabs would ideally be adjacent to the imaged slice and in FAIR, the ss inversion slab would ideally be superposed on the imaging slice. However, the inversion and imaging profiles are not perfectly rectangular in shape, and a gap between their edges is therefore needed to avoid incomplete subtraction of the signal from static tissue. For example, Kim [35] proposed a minimum ratio of 3:1 between the thickness of the ss inversion slab and the imaging slice.

Hyperbolic secant adiabatic inversion pulses [45] are known for their sharp inversion profile, and these pulses are therefore usually used for spin inversion in PASL experiments. Although, several attempts have been made to improve the inversion profiles [46, 47], a finite gap is still needed to ensure complete subtraction of the static tissue signal. This gap gives rise to transit delays of the inflowing blood. Although the delays are generally not as large as in CASL, they can be quite substantial in human studies, especially in multislice imaging.

The transit delays can be measured using multiple inversion times, but this is a very time consuming process and is limited by SNR. Alternately, the sensitivity towards transit delays can be overcome by applying a saturation pulse in both the tag and control experiments. In QUantitative Imaging of Perfusion using a Single Subtraction (QUIPSS) version I and II, the saturation pulse is applied in the imaging slice and in the inversion slab respectively [48]. If certain requirements for the sequence delays are met, perfusion can be quantified correctly using QUIPSS imaging without measuring the transit delays.

This thesis focuses on pulsed ASL, and chapter 3 is a review of the main PASL sequences and perfusion quantification issues using these sequences.

2.5 BOLD Imaging

It was mentioned in section 2.1 that the oxygen extraction fraction in the normal brain is in the range of 30–50%. However, the extraction fraction depends on perfusion, and has been found to drop when perfusion increases [7]. An increase in perfusion is therefore accompanied by an increase in the degree of oxygenation of venous blood since less oxygen is extracted from the blood.

T_2^*-weighted MR images, such as those acquired with gradient echo EPI, are sensitive to changes in blood oxygenation. While oxygenated haemoglobin is diamagnetic, de-oxyhaemoglobin is paramagnetic. As with Gd-DTPA, the paramagnetic de-oxyhaemoglobin increases the susceptibility of blood, affecting the relaxation times of blood as well as tissue in the vicinity of blood vessels.

An increase in perfusion is accompanied by a decrease in de-oxyhaemoglobin in venules and veins, which in turn decreases the susceptibility of blood. The end result is therefore a signal increase in T_2^*-weighted images due to the decreased transverse relaxation rates [49, 50]. If MR images are acquired repeatedly in a subject who is exposed to some sort of stimulus that induces a local or global change in perfusion, the affected areas can be identified by the changes in MR signal intensity. This is known as blood oxygenation level dependent (BOLD) contrast.

Although BOLD contrast cannot be used to measure absolute perfusion, it is an indirect measure of perfusion changes and there are several models that relate perfusion changes with the BOLD signal and $CMRO_2$ changes [51, 52]. BOLD imaging is widely used in functional MRI, where localized perfusion changes are expected during functional activation.

Chapter 3

Pulsed ASL

This chapter is a review of current techniques in pulsed arterial spin labelling (PASL) and is meant to provide an overview of different approaches to perfusion quantification using PASL sequences. First, the basic structure of a variety of commonly used PASL sequences is described followed by a more detailed discussion of the related perfusion quantification issues. This includes a comparison of different models for perfusion quantification and the effects of blood T_1 and transit delays. Finally, a number of applications of PASL in research and in clinical settings are mentioned.

The main part of the chapter is therefore a review of publications by other research groups. A couple of examples are, however, included to illustrate certain points. The images in these examples were generated at DRCMR using a local implementation of the PICORE sequence.

3.1 Pulsed ASL Sequences

A vast number of PASL sequences has been developed since Kwong *et al.* [50] first used slice-selective inversion recovery in 1992 to measure perfusion changes during photic stimulation [8, 22]. The basic principles of a number of these sequences are presented in this section.

As mentioned in chapter 2, ASL sequences are composed of two measurements, one in which arterial blood is magnetically labelled, typically by spin inversion, and one in which it is not. In general, the experiment in which the arterial magnetization is inverted is called the *tag* experiment while the experiment in which the arterial magnetization is not inverted is called the *control* experiment. In this manner, the perfusion-weighted magnetization difference is

always calculated as the magnetization in the control experiment, M^{con}, minus the magnetization in the tag experiment, M^{tag},

$$\Delta M = M^{\text{con}} - M^{\text{tag}}\,. \tag{3.1}$$

EPISTAR and FAIR imaging were the first types of PASL sequences to be developed, and most other PASL sequences are conceptually similar to one of these two sequences. Although the remainder of this thesis is focused on FAIR and PICORE imaging, a short description of the tag and control experiments is given in the following for a variety of PASL sequences.

3.1.1 EPISTAR-like Sequences

EPISTAR

In Echo-Planar Imaging and Signal Targeting with Alternating Radiofrequency (EPISTAR) [33], the arterial magnetization is inverted in a slab proximal to the imaging slice. In the control experiment, the magnetization is inverted in a slab distal to the imaging slice, in order to compensate for magnetization transfer (MT) effects [23]. The magnetization in the imaging plane is saturated immediately before the application of the inversion pulses. See figure 3.1. This labelling scheme is combined with echo-planar imaging (EPI) to give fast perfusion weighted images. The delay between the inversion pulses and the imaging pulse is called the inversion time, *TI*, and is on the order of 1 s.

The compensation for MT effects is only complete exactly halfway between the two inversion slabs. This form of EPISTAR is therefore only suited for single-slice imaging. A later improvement was suggested by Edelman *et al.* [53], in which the inversion pulse in the tag experiment is replaced by a 360° pulse. However, since an adiabatic pulse is used, the magnetization is still inverted. In the control experiment, the tag pulse is then substituted by two inversion pulses having the same total RF power as the 360° tag pulse. The MT effects are therefore identical in the tag and control experiments and this sequence is amenable to multislice imaging.

STAR-HASTE

The EPI acquisition in EPISTAR is replaced with HAlf-fourier Single-shot Turbo spin-Echo (HASTE) in a sequence named STAR-HASTE [39], while the labelling scheme is identical to that in EPISTAR. The advantage of using HASTE imaging is a reduction in the sensitivity to susceptibility effects.

PICORE

In Proximal Inversion with a Control for Off-Resonance Effects (PICORE) [29], the tag experiment is identical to that in EPISTAR. The control experiment is an off-resonance non-selective inversion pulse such that the frequency offset is

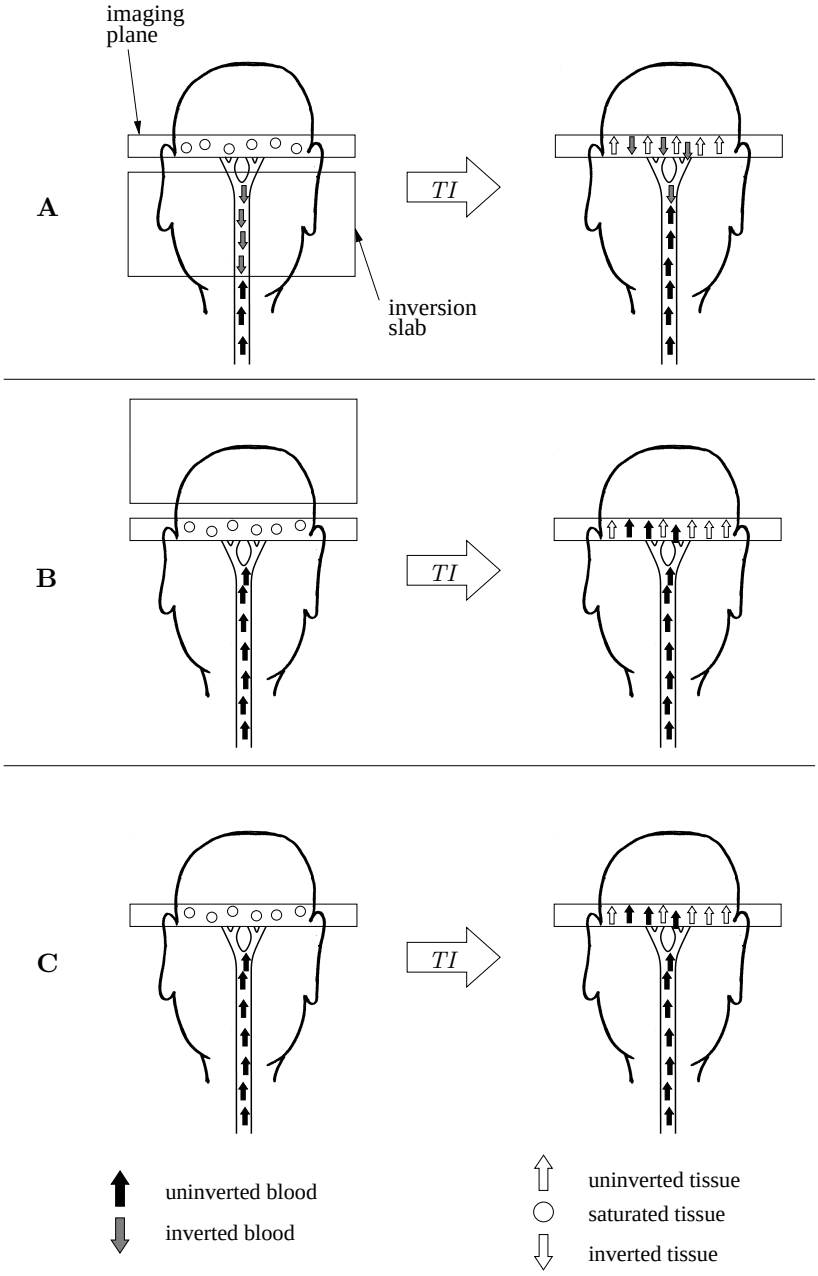

Figure 3.1: The tagging principle in EPISTAR and PICORE sequences. The left column sketches the magnetization immediately after the inversion pulse, while the right column sketches the magnetization just before the imaging pulse. (A) Tag experiment in either EPISTAR or PICORE. (B) Control experiment in EPISTAR. (C) Control experiment in PICORE where the inversion pulse is off resonance and therefore doesn't perturb the spins.

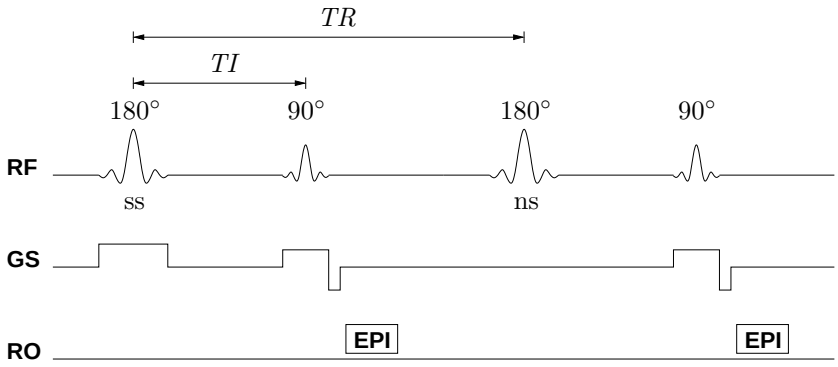

Figure 3.2: The sequence used for FAIR imaging. Alternatingly slice-selective (ss) and non-selective (ns) inversion pulses are followed after a delay *TI* by an imaging pulse. The labels RF, GS and RO refer to the RF irradiation, slice-selection gradients, and readout respectively. The specific RO gradients are not shown, but the timing of the EPI readout is indicated.

identical in the tag and control pulses. The control pulse thus compensates for MT effects without inverting the magnetization anywhere. See figure 3.1.

TILT

In Transfer Insensitive Labelling Technique (TILT) [40], the inversion pulse in the EPISTAR tag experiment is replaced by two consecutive 90° pulses. In the control experiment, two 90° pulses are also given in the same position as in the tag experiment, but with opposite phases, so that they have no net effect.

3.1.2 FAIR-like Sequences

FAIR

Already in 1992, Kwong *et al.* [50] measured perfusion changes due to photic stimulation using slice-selective (ss) inversion recovery (IR). It was, however, not possible to measure the resting state perfusion using this sequence. The idea was, however, developed further, and it was found that by alternating between ss and non-selective (ns) inversion, it was possible to measure the resting state perfusion [34–36]. The method was named Flow-sensitive Alternating Inversion Recovery or FAIR. See figures 3.2 and 3.3.

Although it is the image in the ss IR experiment that is perfusion weighted, it is considered the *control* experiment while the ns IR experiment that does not produce perfusion-weighted images, is considered the *tag* experiment. This is because the arterial magnetization is inverted in the ns experiment. The magnetization measured in the ss and the ns experiments will later in this thesis be referred to as M^{ss} and M^{ns} respectively. However, if the reference appears

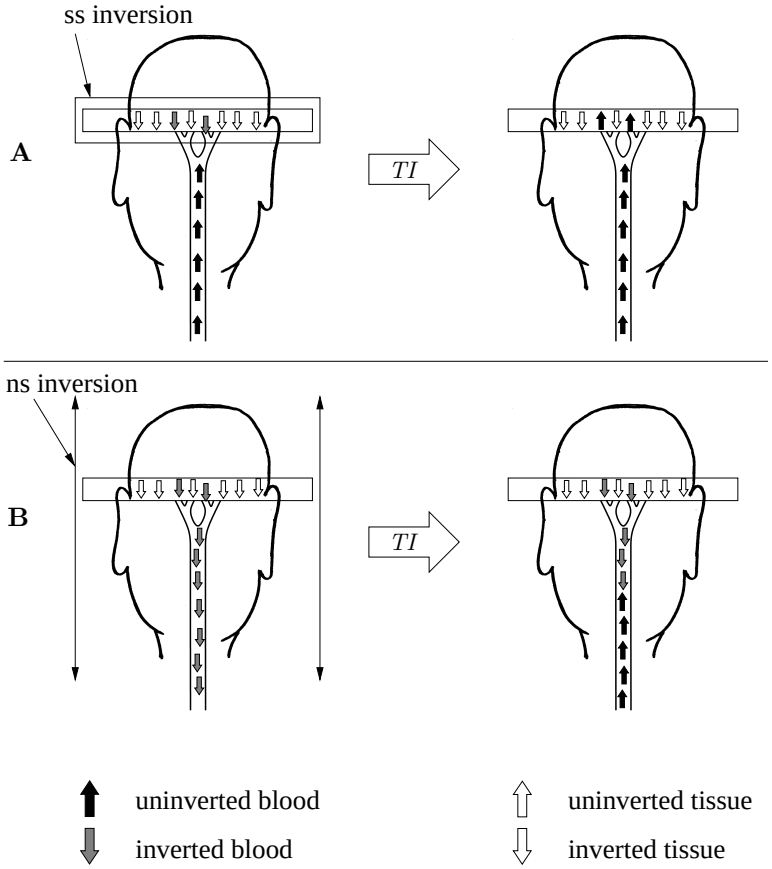

Figure 3.3: Tagging scheme in FAIR imaging. The left column sketches the magnetization immediately after the inversion pulse, while the right column sketches the magnetization just before the imaging pulse. (A) Slice-selective (ss) inversion. (B) Non-selective (ns) inversion.

in a context that is not specific to FAIR, they may be referred to as M^{con} and M^{tag}.

UNFAIR or EST

In UNinverted FAIR (UNFAIR) [37, 54], the tagging scheme is as in FAIR, except that the in-slice magnetization is not inverted. This is done by applying a ns inversion pulse immediately followed by a ss one in the tag experiment. In the control experiment, it is in principle not necessary to apply any inversion pulses, but applying two consecutive ns inversion pulses makes the sequence more symmetric. See figure 3.4. The same sequence was later referred to as Extra-slice Spin Tagging (EST) [44].

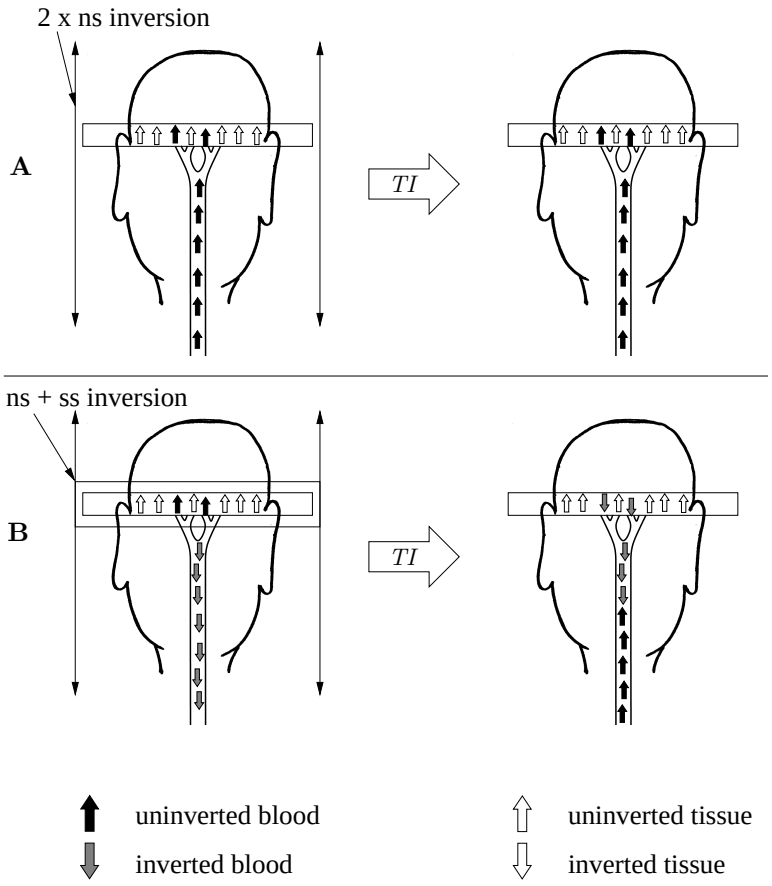

Figure 3.4: Tagging scheme in UNFAIR imaging. The left column sketches the magnetization immediately after the inversion pulses, while the right column sketches the magnetization just before the imaging pulse. (A) Two successive non-selective (ns) inversion pulses. (B) A ns inversion pulse followed by a slice-selective (ss) inversion pulse.

FAIRER

Zhou *et al.* [42] introduced very weak magnetic field gradients during the inversion recovery, spin-echo and predelay periods of a FAIR sequence to overcome the effects of radiation damping [55, 56]. Radiation damping provides an additional pathway for the spin system to relax, thus decreasing the apparent T_1. It can thus affect T_1 measurements using the FAIR sequence, especially in phantoms. They named the sequence FAIR Excluding Radiation damping (FAIRER).

FAIRER

Mai *et al.* [43, 57] used the acronym FAIRER for FAIR with an Extra Radiofrequency pulse, in which the in-slice magnetization is saturated immediately before or after the ss and ns inversion pulses. Using this scheme, the ss magnetization is always larger than the ns magnetization in the measured magnitude images, regardless of the inversion time. This is not the case with FAIR, where M^{ns} is larger than M^{ss} in magnitude images for short inversion times, i.e. before the zero crossing in the relaxation curves.

DEFAIR

Thomas *et al.* [58] introduced Double-Echo FAIR (DEFAIR) where two echoes are measured enabling the quantification of T_2. This in turn enables quantification of CBV as well as perfusion.

BASE

Schwarzbauer and Heincke [38] developed the idea of Kwong *et al.* [50] to use ss IR experiments for measuring perfusion changes. By alternating between an unprepared basis (BA) image and a selective (SE) inversion prepared image, it is possible to measure absolute perfusion changes. The sequence, which was named BASE, cannot be used to measure resting state perfusion. However, since no ns inversion is applied, the sequence can be used with small coils.

ASSIST

Attenuating the Static Signal In arterial Spin Tagging (ASSIST) [59] is similar to FAIR with an extra radiofrequency pulse in that the in-slice tissue magnetization is suppressed. In ASSIST this is done using two additional ns inversion pulses during the preparation phase. By suppressing the static tissue signal, the noise is reduced.

3.1.3 Single-Shot Sequences

A couple of sequences have been developed that do not follow the typical pattern of acquiring a control and a tag image, but acquire the perfusion-weighted image directly. This is done by suppressing the static tissue signal.

SEEPAGE

In Spin Echo Entrapped Perfusion imAGE (SEEPAGE) [60], the in-slice magnetization is first saturated and then prevented from recovering by a train of ns inversion pulses. Only spins entering the imaging slice after the initial presaturation will contribute to the acquired image.

SSPL

Another approach by Duyn *et al.* is a mixture between the original ss IR experiments by Kwong *et al.* and the ASSIST technique for static tissue signal suppression described above. In Single-Shot Perfusion Labelling (SSPL) [61] only the ss inversion experiment is done, but an additional inversion pulse is introduced approximately 250–300 ms before image acquisition. This suppresses the static tissue signal, giving images that are almost only perfusion-weighted. The method is, however, mostly suited to functional imaging, unless a control experiment is added to remove the remaining static tissue signal.

3.2 Quantification Issues

As mentioned earlier, the difference between the control and tag images acquired in an ASL sequence is perfusion-weighted. However, absolute quantification of perfusion requires a mathematical model that relates the measured magnetization difference to perfusion. Various such models are presented in this section, and various factors affecting perfusion quantification using PASL sequences are discussed.

3.2.1 T_1 Model

In the presence of perfusion, the evolution of the tissue magnetization can be described by the modified Bloch equation [20]

$$\frac{\mathrm{d}M^t(t)}{\mathrm{d}t} = \frac{M_0^t - M^t(t)}{T_1^t} + f\left[M^a(t) - M^v(t)\right], \tag{3.2}$$

where M^t is the tissue magnetization per unit mass, M^a and M^v are the magnetizations of arterial water and venous water per unit volume, respectively, M_0^t is the equilibrium value of the tissue magnetization, T_1^t is T_1 of tissue and f is perfusion in volume of blood/mass of tissue/time.

Assuming that there is fast exchange between blood and tissue water, the venous magnetization becomes

$$M^v(t) = \frac{M^t(t)}{\lambda}, \tag{3.3}$$

where λ is the brain-blood partition coefficient of water in ml/g. Inserting equation (3.3) into equation (3.2) and rearranging the terms gives

$$\begin{aligned}\frac{\mathrm{d}M^t(t)}{\mathrm{d}t} &= \left(\frac{1}{T_1^t} + \frac{f}{\lambda}\right) \cdot \left(\frac{\frac{M_0^t}{T_1^t} + fM^a(t)}{\frac{1}{T_1^t} + \frac{f}{\lambda}} - M^t(t)\right) \\ &= \frac{M_0^{\mathrm{app}} - M^t(t)}{T_1^{\mathrm{app}}},\end{aligned} \tag{3.4}$$

where

$$M_0^{\text{app}} = \frac{\dfrac{M_0^t}{T_1^t} + fM^a(t)}{\dfrac{1}{T_1^t} + \dfrac{f}{\lambda}} \,, \tag{3.5}$$

and

$$\frac{1}{T_1^{\text{app}}} = \frac{1}{T_1^t} + \frac{f}{\lambda} \,. \tag{3.6}$$

The above equations show that when the arterial magnetization is different from the tissue magnetization, the apparent relaxation time of tissue, T_1^{app}, will be shorter than the true relaxation time of tissue, T_1^t. Depending on the value of $M^a(t)$, the apparent equilibrium magnetization, M_0^{app}, may also differ from the true one.

FAIR

The tissue magnetization in a FAIR experiment is inverted in both the ss and ns experiments and will thus recover according to equation (3.2). In the ss experiment, the arterial magnetization is not inverted, and if transit delays are ignored for now, the arterial magnetization will be in equilibrium, $M^a(t) = M_0^t/\lambda$. Inserting this into equation (3.5) gives $M_0^{\text{app}} = M_0^t$. The tissue magnetization in the ss experiment will therefore recover with $T_1^{\text{ss}} = T_1^{\text{app}}$ towards the equilibrium value of M_0^t.

In the ns experiment, the arterial magnetization is inverted just as the tissue magnetization. Assuming for now that blood T_1 is equal to tissue T_1, the arterial magnetization becomes $M^a(t) = M^t(t)/\lambda$. Inserting this along with equation (3.3) into equation (3.2), the perfusion effects in the latter cancel out. The tissue magnetization in the ns experiment will therefore recover with $T_1^{\text{ns}} = T_1^t$ towards M_0^t.

If T_1 is measured in both a ss IR experiment and a ns IR experiment, perfusion can be calculated from the difference in T_1

$$\frac{f}{\lambda} = \frac{1}{T_1^{\text{ss}}} - \frac{1}{T_1^{\text{ns}}} \qquad \text{or} \qquad \frac{f}{\lambda} = R_1^{\text{ss}} - R_1^{\text{ns}} \,, \tag{3.7}$$

where $R_1^{\text{ss}} = 1/T_1^{\text{ss}}$ and $R_1^{\text{ns}} = 1/T_1^{\text{ns}}$. This is known as perfusion estimation using the T_1-method.

3.2.2 ΔM Method

The solution to the Bloch equation in the FAIR experiment is

$$M^{\text{ss}}(TI) = M_0^t - 2\alpha M_0^t \mathrm{e}^{-TI/T_1^{\text{app}}} \,, \tag{3.8}$$

$$M^{\text{ns}}(TI) = M_0^t - 2\alpha M_0^t \mathrm{e}^{-TI/T_1^t} \,, \tag{3.9}$$

where α represents the degree of inversion such that $\alpha = 1$ for complete inversion, $\alpha = 0.5$ for saturation, and $\alpha = 0$ for no perturbation. The difference magnetization is then

$$\Delta M(TI) = M^{\mathrm{ss}}(TI) - M^{\mathrm{ns}}(TI) \tag{3.10}$$

$$= 2\alpha M_0^t \left[\mathrm{e}^{-TI/T_1^{\mathrm{app}}} - \mathrm{e}^{-TI/T_1^t} \right] . \tag{3.11}$$

Inserting equation (3.6) into (3.11) gives

$$\Delta M(TI) = 2\alpha M_0^t \mathrm{e}^{-TI/T_1^t} \left[1 - \mathrm{e}^{-\frac{f}{\lambda} TI} \right] . \tag{3.12}$$

Since f is on the order of 0.01 ml/g/s, λ is about 1 ml/g and TI is around 1 s, $\frac{f}{\lambda} TI \ll 1$ and equation (3.12) can be approximated with

$$\Delta M(TI) = 2\alpha M_0^t \frac{f}{\lambda} TI \cdot \mathrm{e}^{-TI/T_1^t} , \tag{3.13}$$

which is the basic equation used for perfusion quantification using the FAIR sequence [34, 35].

3.2.3 Blood T_1

The relaxation equations presented above, all assume that T_1 of blood, which is on the order of 1.2–1.4 s, equals that of tissue. Although this may not be too bad an approximation for grey matter (GM), which has a T_1 of approximately 0.9–1.0 s, it is certainly not valid for white matter (WM), which has a T_1 on the order of 0.6–0.7 s [62]. For FAIR imaging, the ss magnetization will not depend on T_1 of blood, T_1^{b}, since the arterial magnetization is not inverted. The ns magnetization, on the other hand will experience bi-exponential relaxation and the resulting magnetization difference becomes [34, 63]

$$\Delta M(TI) = 2\alpha M_0^t \frac{f}{\lambda} \left[\frac{\mathrm{e}^{-TI/T_1^{\mathrm{app}}} - \mathrm{e}^{-TI/T_1^{\mathrm{b}}}}{\frac{1}{T_1^{\mathrm{b}}} - \frac{1}{T_1^{\mathrm{app}}}} \right] . \tag{3.14}$$

If it is ignored that $T_1^{\mathrm{b}} \neq T_1^t$, perfusion will be overestimated for both GM and WM, but mostly for WM. The fractional perfusion error increases with TI, but is essentially independent of the size of any reasonable blood volume fraction [34].

Although the control and tag magnetizations in an EPISTAR measurement are very different from the ss and ns magnetizations in a FAIR sequence, the difference magnetization, $\Delta M(TI)$, is identical. This is because the blood is in principle tagged equally in the two ASL schemes while only the tissue magnetization is different. Equation (3.14) is therefore also valid for EPISTAR [22, 63].

3.2.4 Transit delays

It was mentioned briefly in chapter 2, that the slice profiles of the inversion and imaging pulses used in PASL sequences are not perfectly rectangular. In FAIR imaging, the ss inversion slab is therefore thicker than the imaging slice. For single-slice FAIR a ratio of 3:1 is typically used [35]. If the ss inversion slab only just covers the imaging slice, the static tissue signal will not completely cancel in the magnetization difference images. For the same reason, the inversion slabs in EPISTAR are not completely adjacent to the imaging slice, but a gap is left between them.

Due to this gap between the edge of the inversion slab and the edge of the imaging slice, there will be a delay before tagged blood in EPISTAR or untagged blood in FAIR reaches the tissue in the imaging slice. This delay is referred to as the *transit delay*, δt.

The transit delays in small animals such as rats are quite small, and the errors introduced in perfusion quantification by neglecting them are small [64]. In humans, however, transit delays are quite large and vary across voxels in the imaged slice. It has been found that transit delays are typically around 700 ms in GM for a 1 cm gap, but can vary between 400 and 1200 ms for commonly used gaps [27, 48].

Since the inversion slab in the tag experiment in EPISTAR-like sequences has a finite thickness, only a finite bolus of inverted blood will enter the imaging slice. Let the *tag width* measured in time be τ. The time at which this bolus ends, and uninverted blood starts to enter the imaging slice is therefore $\tau_e = \delta t + \tau$ and is called the *trailing time*. In FAIR imaging a trailing time is relevant in the ns experiment if the ns inversion isn't truly global. The magnetization is only inverted within the range of the coil, so unless a body coil is used for inversion, the inverted magnetization will also constitute a bolus.

The tag width has in humans been found to be about 700–900 ms for a 10 cm inversion slab [30, 48] while the trailing time in ns FAIR experiments has been found to be around 2 s [65].

The magnetization equations presented previously are only valid in the limit of $\delta t = 0$ and $\tau > TI$. Since this is generally not the case, the equations must be modified in order to quantify perfusion correctly.

Assuming again for a moment, that $T_1^{\mathrm{b}} = T_1^t$ in a FAIR experiment, it can be shown that M^{ss} is given by [66]

$$M^{\mathrm{ss}}(TI) = \begin{cases} M_0 - 2\alpha M_0 \mathrm{e}^{-TI/T_1} , & TI \leq \delta t \\ M_0 - 2\alpha M_0 \mathrm{e}^{-TI/T_1 - (TI-\delta t)f/\lambda} , & TI > \delta t , \end{cases} \tag{3.15}$$

where the label "t" has been dropped from T_1^t and M_0^t. M^{ns} is similarly given by

$$M^{\mathrm{ns}}(TI) = \begin{cases} M_0 - 2\alpha M_0 \mathrm{e}^{-TI/T_1} , & TI \leq \tau_e \\ M_0 - 2\alpha M_0 \mathrm{e}^{-TI/T_1 - (TI-\tau_e)f/\lambda} , & TI > \tau_e . \end{cases} \tag{3.16}$$

The difference magnetization is then given by

$$\Delta M(TI) = \begin{cases} 0 , & TI \leq \delta t \\ 2\alpha M_0 (TI - \delta t) \frac{f}{\lambda} \mathrm{e}^{-TI/T_1} , & \delta t < TI \leq \tau_e \\ 2\alpha M_0 (\tau_e - \delta t) \frac{f}{\lambda} \mathrm{e}^{-TI/T_1} , & TI > \tau_e . \end{cases} \tag{3.17}$$

In the limit of $\delta t = 0$ and $\tau_e > TI$, equations (3.15)–(3.17) simplify to equations (3.8), (3.9) and (3.13), respectively. However, for realistic values of δt and τ_e in humans, using equation (3.13) to model the magnetization difference, generally underestimates perfusion. Correct perfusion estimation requires measurements with at least two values of TI that satisfy $\delta t < TI \leq \tau_e$. This would enable the estimation of both perfusion and the transit delay.

Estimating perfusion using the T_1-method as described in section 3.2.1 without taking the transit delays into consideration can lead to either overestimation or underestimation of perfusion depending on the value of δt [67].

3.2.5 General Kinetic Model

Buxton *et al.* developed a general kinetic model [62] for the difference magnetization in ASL experiments, where the parameters of the model can easily be adjusted for both CASL and PASL experiments.

The model is based on the definition of the following quantities

- The delivery function $c(t)$, which is the normalized arterial concentration of magnetization arriving in the voxel at time t.
- The residue function $r(t - t')$, which is the fraction of the tagged water arriving in the voxel at time t' that is still in the voxel at time t.
- The relaxation function $m(t - t')$, which is the fraction of the original longitudinal magnetization tag carried by the water that arrived at time t' and that remains at time t.

The magnetization difference at time t is then

$$\Delta M(t) = 2M_0^{\mathrm{b}} f \int_0^t c(t') r(t - t') m(t - t') \mathrm{d}t' , \tag{3.18}$$

where M_0^{b} is the equilibrium magnetization of blood. Equation (3.18) is a general model that can be used to calculate $\Delta M(t)$ under various assumptions. The set of assumptions comprising the standard model for PASL used in the previous sections is

$$c(t) = \begin{cases} 0\,, & 0 < t \leq \delta t \\ \alpha \mathrm{e}^{-t/T_1^{\mathrm{b}}}\,, & \delta t < t \leq \delta t + \tau \\ 0\,, & \delta t + \tau < t\,, \end{cases} \tag{3.19}$$

$$r(t) = \mathrm{e}^{-ft/\lambda}\,, \tag{3.20}$$

$$m(t) = \mathrm{e}^{-t/T_1}\,. \tag{3.21}$$

Equation (3.19) states that tagged blood only enters the imaging slice for $\delta t < t \leq \delta t + \tau$. Equation (3.20) assumes that the ratio of the total tissue water concentration to the venous water concentration is a constant equal λ. This is the limit of fast exchange. Equation (3.21) assumes that labeled water relaxes with T_1 of tissue after it reaches the tissue voxel.

Inserting equations (3.19)–(3.21) into (3.18) gives[1]

$$\Delta M(t) = \begin{cases} 0\,, & t \leq \delta t \\ 2\alpha M_0^{\mathrm{b}}(t - \delta t) f \mathrm{e}^{-t/T_1^{\mathrm{b}}} \cdot q(t)\,, & \delta t < t \leq \delta t + \tau \\ 2\alpha M_0^{\mathrm{b}} \tau f \mathrm{e}^{-t/T_1^{\mathrm{b}}} \cdot q(t)\,, & \delta t + \tau < t\,, \end{cases} \tag{3.22}$$

where

$$q(t) = \begin{cases} \dfrac{\mathrm{e}^{kt}\left(\mathrm{e}^{-k\delta t} - \mathrm{e}^{-kt}\right)}{k(t - \delta t)}\,, & \delta t < t \leq \delta t + \tau \\ \dfrac{\mathrm{e}^{kt}\left(\mathrm{e}^{-k\delta t} - \mathrm{e}^{-k(\delta t + \tau)}\right)}{k\tau}\,, & \delta t + \tau < t\,, \end{cases} \tag{3.23}$$

and

$$k = \frac{1}{T_1^{\mathrm{b}}} - \frac{1}{T_1^{\mathrm{app}}}\,. \tag{3.24}$$

The quantity $q(t)$ contains the factors related to the difference in relaxation times between tissue and blood, and the effects of venous clearance of the tag. $q(t)$ is dimensionless and close to unity.

[1] Note that Buxton *et al.* define perfusion in units of volume of blood/volume of tissue/time instead of volume of blood/mass of tissue/time as used elsewhere in this chapter. To switch between the two units, multiplication with the density of the tissue is needed [62].

Note that ΔM in equation (3.22) is expressed in terms of M_0^b rather than M_0 of tissue. This is equivalent to the results in the previous section when λ is defined as M_0/M_0^b. However, the scaling of ΔM with M_0^b is a global scaling and not a local, tissue-dependent scaling. Both M_0 and λ are tissue dependent, and using M_0/λ for scaling gives the impression that the scale is tissue dependent. Typically, when M_0/λ is used for scaling, M_0 and T_1 are measured while an average value is assumed for λ. When M_0^b is used for scaling, optimally both M_0^b and T_1^b should be measured, but typically M_0^b is measured (directly or indirectly) while a value is assumed for T_1^b. The advantage of the latter approach is that T_1^b is a global parameter, and it is therefore more reasonable to assume a value for it than for λ.

Equation (3.22) is valid for all PASL sequences that rely on the subtraction of a tag and a control image, as long as there is complete subtraction of the static tissue signal. As in section 3.2.4, quantification of perfusion requires at least two measurements of ΔM at different inversion times, such that δt also can be estimated.

3.2.6 Transit Delay Insensitivity

Wong *et al.* proposed two techniques to render the magnetization difference in PASL sequences less sensitive to transit delays, such that correct quantification of perfusion can be done with measurements at a single inversion time [48, 68, 69]. The techniques were named QUantitative Imaging of Perfusion using a Single Subtraction (QUIPSS) versions I and II.

The techniques are based on using an additional saturation pulse to control the tag width of the bolus of inverted blood that gives rise to ΔM in a conventional PASL sequence such as FAIR, EPISTAR or PICORE. The saturation pulse is applied a time TI_1 after the inversion pulse in both the tag and control experiments. Imaging is then applied at a time TI_2 after the inversion pulse. QUIPSS I and II differ in where the saturation pulse is applied. See figures 3.5 and 3.6.

QUIPSS I

In QUIPSS I, the saturation pulse is applied in the imaging slice at TI_1 after inversion. Since the saturation pulse is applied in both the tag and control experiments, it removes the contribution to the magnetization difference of any blood that arrives in the imaging slice before TI_1. Only blood that arrives between TI_1 and TI_2 will contribute to ΔM.

If the conditions

$$TI_1 > \delta t \tag{3.25}$$

$$TI_2 < \delta t + \tau \tag{3.26}$$

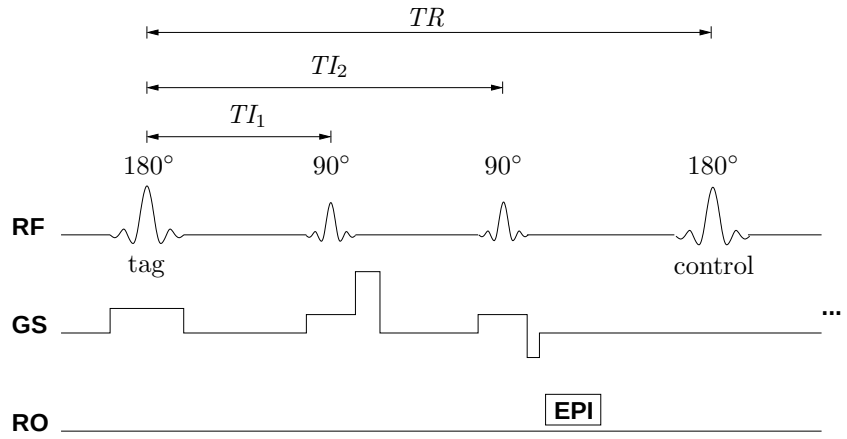

Figure 3.5: The sequence used for QUIPSS I and QUIPSS II imaging. A saturation pulse is applied at TI_1 while the imaging pulse is applied at TI_2.

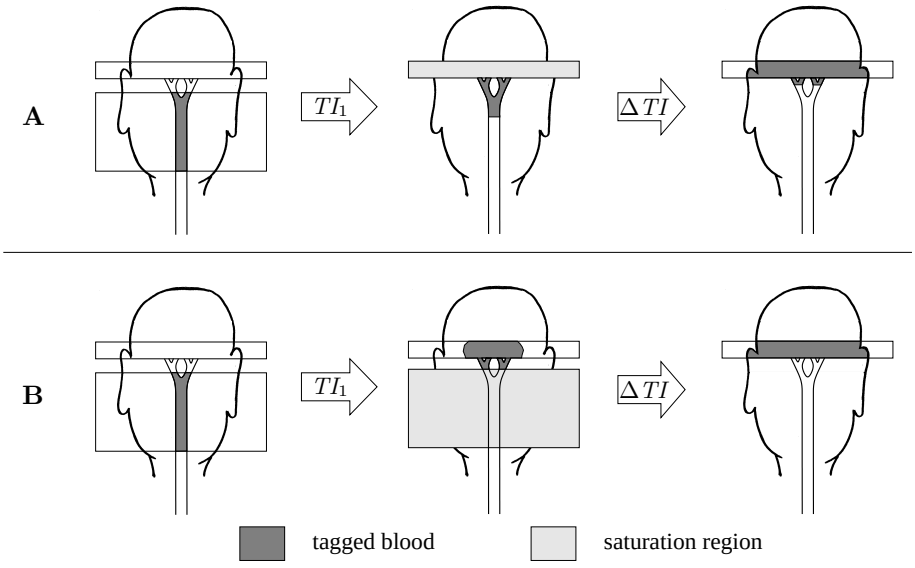

Figure 3.6: The principle of (A) QUIPSS I and (B) QUIPSS II imaging. The saturation pulse is applied at TI_1 while the imaging pulse is applied at TI_2. QUIPSS I removes the contribution of the leading edge of the tag, while QUIPSS II removes the contribution of the trailing edge of the tag. $\Delta TI = TI_2 - TI_1$.

are fulfilled, tagged blood will enter the imaging slice for the all the duration of $\Delta TI = TI_2 - TI_1$ and using equation (3.22), the magnetization difference will be given by [48]

$$\Delta M(TI_2) = 2\alpha M_0^{\mathrm{b}}\, \Delta TI\, f\, \mathrm{e}^{-TI_2/T_1^{\mathrm{b}}} \cdot q\ . \tag{3.27}$$

The terms δt and τ do no appear in the equation since they have been replaced by TI_1 and ΔTI, which are known from the sequence and are global throughout the imaged slice. Quantification of perfusion using equation (3.27) can therefore be done with measurements at a single value of TI_2.

QUIPSS II

In QUIPSS II, the saturation pulse is applied in the tagging region instead of the imaging slice. This has the effect that only blood that has left the tagging region within TI_1 will contribute to the magnetization difference.

If the conditions

$$TI_1 < \tau \tag{3.28}$$

$$TI_2 > TI_1 + \delta t \tag{3.29}$$

are fulfilled, all tagged blood that has left the tagging region within TI_1 will have entered the imaging slice before TI_2. Thus the tag width in this case becomes TI_1, and the magnetization difference will be given by [48]

$$\Delta M(TI_2) = 2\alpha M_0^{\mathrm{b}}\, TI_1\, f\, \mathrm{e}^{-TI_2/T_1^{\mathrm{b}}} \cdot q\ . \tag{3.30}$$

Again the terms δt and τ do no appear in the equation, and quantification of perfusion can be done with a single value of TI_2.

Figure 3.7 shows the effect of QUIPSS II saturation on the magnetization difference images in PICORE measurements. The measurements were performed at DRCMR. See appendix A for notes on the sequence implementation on the scanner. Imaging parameters are 10 cm inversion slab, 1 cm gap, $TR = 2.14$ s, 8 mm slice thickness and 70 acquisitions. $TI = 1.4$ s for the experiment without QUIPSS II while $TI_1 = 700$ ms and $TI_2 = 1400$ ms for the experiment with QUIPSS II. The magnetization difference level in GM is much more uniform when QUIPSS II saturation is applied. This is because ΔM reflects regional differences in perfusion as well as transit delays when QUIPSS II saturation is not applied.

Comparison

It is generally desirable to choose sequence parameters that maximize the magnetization difference in order to get the optimal SNR. In QUIPSS I imaging, this is done by maximizing ΔTI while not violating equations (3.25) and (3.26).

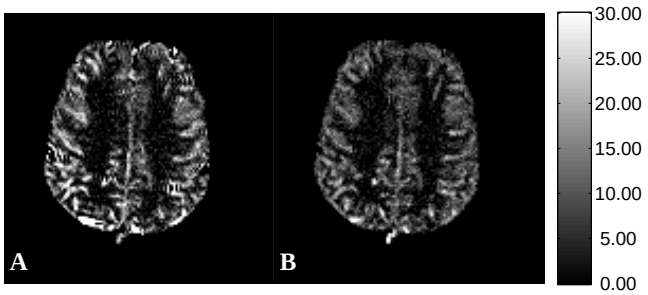

Figure 3.7: Magnetization difference images [a.u.] in single-slice PICORE measurements (A) without and (B) with QUIPSS II saturation. See text for imaging parameters.

Typical values for human subjects, using a PICORE or EPISTAR sequence with a 1 cm gap and 10 cm inversion slab are $TI_1 = 600$ ms and $TI_2 = 1200$ ms.

In QUIPSS II imaging, ΔM is maximized by maximizing TI_1 and minimizing TI_2 while not violating equations (3.28) and (3.29). Typical values for a PICORE or EPISTAR sequence with a 1 cm gap and 10 cm inversion slab are $TI_1 = 700$ ms and $TI_2 = 1400$ ms [48].

Since the in-slice magnetization is saturated in QUIPSS I imaging, it is only amenable to single-slice imaging. This is a large drawback compared to QUIPSS II, which can be used for multislice imaging.

Although QUIPSS I and II facilitate perfusion quantification, the saturation pulse used decreases SNR of the magnetization difference. Due to the conditions on TI_1 and TI_2, the saturation pulse removes part of the tag that could have contributed to ΔM. This should be kept in mind in the choice of sequence for a given objective.

Non-selective Inversion

As mentioned in section 3.2.4, it is generally assumed in the non-selective part of FAIR imaging that all incoming blood has been inverted by the inversion pulse. However, this only holds within the range of the RF coil being used, and since a head coil is the most commonly used coil for CBF measurements, blood that is in the neck region or below during the inversion pulse is not inverted. This becomes a problem when using large inversion times, since this allows uninverted spins to reach the imaging region in the ns experiment as well as in the ss experiment leading to underestimation of perfusion [70]. The problem can be solved in one of two ways

- Increasing the range of the coil by using a head and neck coil or a body coil will delay the arrival of uninverted blood. However, the head coil is usually preferred due to its higher SNR.

- Creating a bolus of known length of uninverted spins by using QUIPSS II will overcome the problem giving accurate quantitative results. The drawback is again a loss in SNR.

3.2.7 Intravascular Magnetization

Another source of error in perfusion quantification is the contribution of intravascular spins to the magnetization difference. Tagged blood in arteries and arterioles in the imaging slice may give a very large contribution to ΔM compared to tissue. This can typically be seen as bright spots in ΔM images.

One method of suppressing the intravascular signal is by applying bipolar gradients between the imaging pulse and the readout [3]. In a FAIR experiment, Ye *et al.* [27] found that applying bipolar gradients with a b-value[2] of 4.5 s/mm^2 attenuates ΔM in a GM region of interest (ROI) by almost 50%, while the attenuation in M^{ss} only is 3%.

It is important to distinguish between two groups of intravascular spins. The first group consists of arterial spins that are destined for tissue distal of the imaging slice. These spins are merely flowing through the imaging plane, and should not contribute to ΔM since they are not related to perfusion in the imaging slice. Their signal can, however, be suppressed using small bipolar gradients since the flow velocity in them is relatively large.

The second group consists of spins in arterioles that ultimately perfuse tissue in the imaging plane. There is some debate whether these spins should be included in ΔM for perfusion estimation. Suppression of the signal from these spins, however, may have a large effect on the transit delays. If arteriolar spins are suppressed, the tagged blood will not contribute to ΔM till it reaches the capillaries. Excessive spoiling of intravascular spins therefore increases the transit delays, but doesn't improve the accuracy of perfusion estimation [62].

Extraction Fraction

In the original T_1 model, it was assumed that water is freely diffusible and that labelled water is completely extracted into the tissue. There is, however, evidence that this assumption does not hold, at least not at high perfusion levels [71], where the extraction of water becomes limited by diffusion.

The tissue contribution to ΔM in that case is $E \cdot f$ where E is the extraction fraction. Note, however, that the extraction fraction is itself a function of perfusion, where E typically decreases for increasing perfusion. The measured perfusion would then be $E \cdot f$, which is lower than the true perfusion. However, it has been found that the capillary (and to some extent venous) contribution to the MR signal is significant and actually counterbalances the effect of restricted

[2]For bipolar gradients of duration δ, spacing Δ and amplitude G, $b = \gamma^2 G^2 \delta^2 (\Delta - \delta/3)$. The attenuation of the measured signal with bipolar gradients is $\exp(-bD)$, where D is the diffusion coefficient [3].

water exchange between blood and tissue [62, 72]. This should not discourage the use of crusher gradients to spoil the arterial contribution since the signal from very small vessels is typically not affected [8].

T_2 Effects

Blood water that contributes to the ASL signal raises a secondary complication. T_2 of blood is approximately three times longer than T_2 of tissue (240 ms compared to 80 ms) [22]. If EPI is used for imaging, the signal will be weighted towards the intravascular compartment due to the finite *TE*. For T_1 measurements with multiple inversion times, the signal shifts from the intravascular compartment to the tissue compartment as a function of *TI*. T_2 effects will affect this shift in signal and could affect the estimated values of perfusion.

3.2.8 Presaturation

As with FAIRER [43] and EPISTAR [33], in-slice presaturation is commonly used in ASL sequences to minimize the signal from static tissue. Presaturation is usually applied in the imaging plane or slab immediately before or after the tag and control pulses and may be given as one or two 90° pulses separated by a large crusher gradient. The presaturation pulse(s) and the tag/control pulse are also separated by a crusher gradient.

In principle, the static tissue signal cancels out in the magnetization difference images, but presaturation may improve the magnetization difference image quality due to one or more of the following reasons

- Incomplete cancelling of the static tissue signal due to image artefacts.
- Incomplete cancelling of the static tissue signal due to slight motion between the measurements.
- Better use of the available dynamic range since the difference signal becomes relatively larger compared to the measured signals.

Although, the dynamics of the static tissue change dramatically due to presaturation, the perfusion signal is not affected. In the FAIR sequence, for example, applying presaturation (to give FAIRER) changes the static tissue dynamics from inversion recovery to saturation recovery.

The contrast in the tag and control images is therefore strongly dependent on presaturation. Figure 3.8A shows the control images in a PICORE QUIPSS II experiment with and without presaturation. The measurements were performed at DRCMR (see appendix A). The imaging parameters were identical to those listed on page 30 for figure 3.7. It is clear from the figure, that although image contrast is dramatically changed in the control image by presaturation, the magnetization difference images (figure 3.8B) are not affected. Figure 3.8C shows the standard deviation images of the magnetization difference (over time). The noise level in the ΔM images is lower when presaturation is applied because the

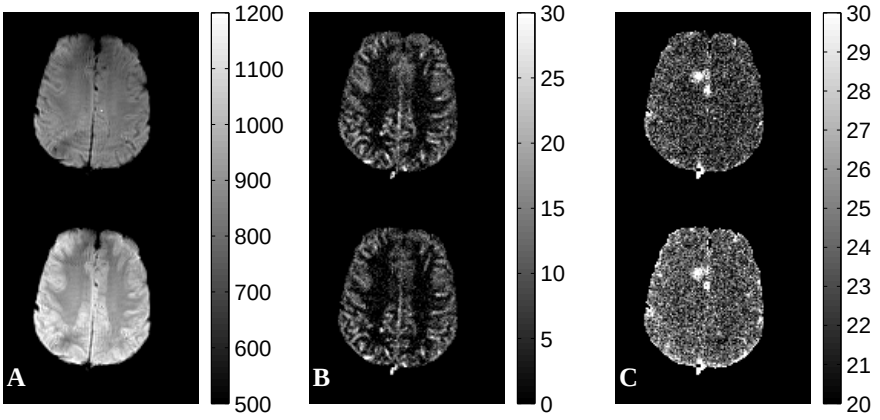

Figure 3.8: Effect of presaturation in a PICORE QUIPSS II sequence. Top row is with presaturation while bottom row is without. (A) Mean of the measured magnetization in the control experiment [a.u.]. (B) Mean of the magnetization difference. (C) Standard deviation of the magnetization difference.

noise in the tag and control images scales with the signal itself, as we have found previously [73]. Presaturation can therefore improve SNR in ASL images.

3.2.9 Choice of Sequence

As seen in this chapter, there is a vast number of pulsed ASL sequences, and a large number of features that can be added, such as presaturation, QUIPSS I or QUIPSS II saturation and bipolar gradients. The choice of sequence for a given purpose is therefore not obvious. A few considerations will be discussed in this section, that may assist in the choice of sequence.

Basic Sequence

There is a basic difference in the areas in which blood is tagged in, for example, FAIR, EPISTAR and PICORE. In FAIR imaging, the tag pulse is the ns inversion pulse, and blood on both sides of the imaging slice is inverted. Blood entering the imaging slice will therefore contribute equally to ΔM regardless of the direction from which it entered the slice. In PICORE, the tag is only applied proximal to the imaging slice, and any blood entering the imaging slice from the distal side will not contribute to ΔM. In EPISTAR, the tag is only applied proximal to the imaging slice as well, but the control pulse is applied distal to the imaging slice. Any blood that enters the imaging slice from the distal side will therefore contribute negatively to ΔM [29].

In axial brain imaging, it is reasonable to assume that arterial blood enters the imaging slice from the proximal side, while any blood that enters from the distal side is most likely to be venous blood. This means that veins are likely

to appear as bright spots in FAIR ΔM images, as dark spots in EPISTAR ΔM images and not at all in PICORE ΔM images [29]. PICORE imaging may therefore be preferable when arterial blood predominantly enters the imaging slice from one side.

If the images are coronal or sagittal on the other hand, arterial blood may enter the imaging slice from either or both sides. In this case, PICORE would underestimate perfusion while FAIR would include the tag entering the imaging slice from either side. However, coronal and sagittal ASL imaging are not commonly used in brain perfusion measurements, since there is a risk that the arteries supplying part of the tissue will be in the imaging slice. In such a situation, the blood would not be tagged, leading to severe underestimation of perfusion.

Quantitative vs. Non-Quantitative

Absolute perfusion quantification is not always needed, and the choice of quantitative measures such as QUIPSS saturation and bipolar gradients, should therefore be considered for each study.

If an ASL sequence, for example, is used to detect areas in the brain, where there are perfusion changes due to functional activation, it may be best not to use QUIPSS saturation. Although the sequence becomes non-quantitative, the detection power increases. However, if the aim of the study is to quantify perfusion, a quantitative sequence must be used, e.g. by using QUIPSS I or II saturation or by measuring at multiple inversion times.

The use of bipolar gradients depends on the sequence being used and is not always needed. For example, QUIPSS I imaging is more sensitive to intravascular effects than QUIPSS II imaging, since the latter allows more time for intravascular spins to reach the capillary net before imaging. Since bipolar gradients are applied between the imaging pulse and the readout, TE is inevitably increased, which may be a disadvantage that outweighs the benefit of crushing the intravascular signal.

Timing Parameters

A final issue in the choice of sequence concerns the timing parameters of the sequence, i.e. TR, TE and TI or TI_1 and TI_2. Since ASL generally suffers from low SNR, it is important to adjust the sequence timing, so that maximum perfusion signal is achieved.

For non-quantitative sequences, the optimal TI depends on T_1 of both tissue and blood, δt and τ. For the ideal case where $\delta t = 0$ and $\tau > TI$, the optimal TI lies somewhere between T_1 and T_1^{b}. For realistic values of δt and τ, the optimal TI is the minimum of $\delta t + \tau$ and $\delta t+$ a value between T_1 and T_1^{b}. These are only rough guidelines, however. Simulations of the sequence with expected δt and τ values should be done to find the exact optimum.

For quantitative sequences using QUIPSS I saturation the shortest TI_1 and longest TI_2 satisfying equations (3.25) and (3.26) give the maximum ΔM. For QUIPSS II saturation, the longest TI_1 and shortest TI_2 satisfying equations (3.28) and (3.29) give the maximum ΔM.

It is generally assumed that the arterial magnetization is fully relaxed before the application of the tag inversion pulse or that it has been fully replaced by fresh arterial spins before the following repetition of the sequence. If TR becomes very short, in for example FAIR imaging, the blood inverted in the ns experiment may still flow into the imaging slice in the ss experiment. This would decrease the labelling efficiency of the ASL measurement and could underestimate perfusion.

However, as long as TR is long enough for arterial spins in one acquisition to be fully replaced before the following inversion pulse, the magnetization difference is independent of TR [74]. The contrast in the tag and control images, on the other hand, generally depends on TR, but using in-slice presaturation immediately before inversion can render the tag and control magnetizations independent of TR as well. It has, however, been shown that perfusion estimation using the T_1-method in FAIR without presaturation is sensitive to short values of TR [74].

The majority of ASL sequences are implemented using EPI for image acquisition. The measured signals are therefore T_2^*-weighted to some degree. Generally, shorter TE values give higher ASL signal and therefore higher SNR. For this reason, ASL is usually implemented with the shortest TE that the scanner is capable of. Spiral [75] EPI, where available, is therefore preferable from an ASL point of view due to the very short echo-times.

As shall be seen in chapter 8, there is one application of ASL, where very short TE is not desirable, and that is for combined perfusion and BOLD imaging using ASL sequences. Here the T_2^*-weighting is needed to extract information about blood oxygenation from ASL images.

3.3 Applications

Although ASL has predominantly been used for perfusion measurements in the brain, it is not specific to this one organ. In fact, ASL has been used to measure pulmonary perfusion [76, 77], renal perfusion [78, 79] and muscular perfusion [80] as well.

The most common application of ASL is probably in functional MRI (fMRI) in the brain, where perfusion changes due to functional activation are detected [29]. Using ASL, it has been found that not only does perfusion increase with activation, but transit delays drop in activated areas as well [81].

Perfusion imaging using ASL has also been used to test models of the relations between changes in perfusion, blood volume, oxygen consumption ($CMRO_2$) and blood oxygenation [51, 52, 82]. The general idea is to calibrate relative changes in

perfusion and oxygenation during functional activation with the relative changes during graded hypercapnia.

ASL has also been used in pharmacological studies on rats to measure the effects of various substances on perfusion such as amphetamine and different anaesthetics [25, 83].

Finally, ASL has also been used for perfusion measurements in various pathologies such as temporal lobe epilepsy [84], traumatic brain injury [85], stroke [86, 87] and brain tumours [88]. However, there is one limitation to the use of perfusion measurement with ASL in stroke patients. Due to perfusion of ischaemic tissue through secondary pathways, the transit delays may become substantially longer than T_1^{b}. In such cases, ASL measurements could severely underestimate perfusion.

Chapter 4

RF Pulse Design

As mentioned in the previous chapter, imperfect slice profiles may cause incomplete static tissue subtraction in ASL imaging. Designing RF pulses with good slice profiles is therefore an important tool in optimising ASL pulse sequences.

In this chapter, the principles of spin excitation are discussed with emphasis on RF pulse design and optimization. The main focus is on selective spin excitation or soft pulses. Hard pulses are not used in this thesis, and are therefore only mentioned briefly. The RF pulses used for inversion, excitation and saturation in this thesis are presented and discussed.

The principles that are presented in this chapter are meant as a set of tools for evaluating and minimizing slice profile effects in ASL sequences.

4.1 Equations of Motion

In this section, the equations of motion of a spin ensemble under RF irradiation are presented. Equations for the calculation of the magnetization profiles of both hard and soft RF pulses are deduced. Finally various approximations that facilitate numerical implementation are introduced and discussed.

The Bloch equation in the laboratory frame of reference is

$$\frac{\mathrm{d}\mathbf{M}^{\mathrm{lab}}}{\mathrm{d}t} = \gamma\mathbf{M}^{\mathrm{lab}} \times \mathbf{B} - \frac{\mathbf{i}M_x^{\mathrm{lab}} + \mathbf{j}M_y^{\mathrm{lab}}}{T_2} + \mathbf{k}\frac{(M_0 - M_z^{\mathrm{lab}})}{T_1}, \tag{4.1}$$

where M_0 is the equilibrium magnetization, $\mathbf{M}^{\mathrm{lab}} = (M_x^{\mathrm{lab}}, M_y^{\mathrm{lab}}, M_z^{\mathrm{lab}})^T$ is the magnetization in the laboratory frame of reference and

$$\mathbf{B}(\mathbf{r}, t) = \mathbf{k}(B_0 + \mathbf{G}(t) \cdot \mathbf{r}) + \mathbf{B}_1(t), \tag{4.2}$$

is the magnetic field at position $\mathbf{r}$ at time t, and $\mathbf{G}(t)$ is the applied gradient, B_0 is the static magnetic field, and $\mathbf{B}_1(t)$ is the applied RF field. It is here assumed that $\mathbf{B}_1$ is independent of $\mathbf{r}$. $\mathbf{B}_1(t)$ rotates with an angular frequency, ω, and has the form

$$\mathbf{B}_1(t) = \mathbf{i}B_1(t)\cos(\omega t + \phi(t)) - \mathbf{j}B_1(t)\sin(\omega t + \phi(t)), \tag{4.3}$$

where $B_1(t)$ and $\phi(t)$ are the amplitude and the phase of the applied RF field respectively. This corresponds to left handed precession about the z-axis, which is the same direction as that for spin precession in the absence of RF irradiation.

The Bloch equation can also be written in matrix form as [2]

$$\frac{\mathrm{d}\mathbf{M}^{\mathrm{lab}}}{\mathrm{d}t} = \mathbf{Q}^{\mathrm{lab}}\mathbf{M}^{\mathrm{lab}} + \mathbf{k}\frac{M_0}{T_1}, \tag{4.4}$$

where

$$\mathbf{Q}^{\mathrm{lab}} = \begin{pmatrix} -1/T_2 & \gamma(B_0 + \mathbf{G}(t)\cdot\mathbf{r}) & \gamma B_1(t)\sin(\omega t + \phi(t)) \\ -\gamma(B_0 + \mathbf{G}(t)\cdot\mathbf{r}) & -1/T_2 & \gamma B_1(t)\cos(\omega t + \phi(t)) \\ -\gamma B_1(t)\sin(\omega t + \phi(t)) & -\gamma B_1(t)\cos(\omega t + \phi(t)) & -1/T_1 \end{pmatrix} \tag{4.5}$$

Introducing a rotating coordinate frame through the anti-clockwise linear transformation matrix $\mathbf{U}^{-1}$, given by

$$\mathbf{U}^{-1} = \begin{pmatrix} \cos\omega t & -\sin\omega t & 0 \\ \sin\omega t & \cos\omega t & 0 \\ 0 & 0 & 1 \end{pmatrix}, \tag{4.6}$$

the representation of the magnetization in the rotating frame becomes

$$\mathbf{M} = \mathbf{U}^{-1}\mathbf{M}^{\mathrm{lab}}. \tag{4.7}$$

Applying the transformation to equation (4.4) gives

$$\frac{\mathrm{d}\mathbf{M}}{\mathrm{d}t} = \mathbf{Q}\mathbf{M} + \mathbf{k}\frac{M_0}{T_1}, \tag{4.8}$$

where

$$\mathbf{Q} = \mathbf{U}^{-1}\mathbf{Q}^{\mathrm{lab}}\mathbf{U} + \frac{\partial\mathbf{U}^{-1}}{\partial t}\mathbf{U}. \tag{4.9}$$

Inserting equations (4.5) and (4.6) into equation (4.9) gives

$$\mathbf{Q} = \begin{pmatrix} -1/T_2 & \Delta\omega(\mathbf{r},t) & \omega_1(t)\sin\phi(t) \\ -\Delta\omega(\mathbf{r},t) & -1/T_2 & \omega_1(t)\cos\phi(t) \\ -\omega_1(t)\sin\phi(t) & -\omega_1(t)\cos\phi(t) & -1/T_1 \end{pmatrix}, \tag{4.10}$$

where $\omega_1(t) = \gamma B_1(t)$ and $\Delta\omega(\mathbf{r}, t) = \gamma(B_0 + \mathbf{G}(t) \cdot \mathbf{r}) - \omega$. This corresponds to an effective magnetic field in the rotating frame of reference,

$$\begin{aligned}\mathbf{B}_{\text{eff}}(\mathbf{r}, t) &= \mathbf{i}B_1(t)\cos\phi(t) - \mathbf{j}B_1(t)\sin\phi(t) + \mathbf{k}\left(B_0 + \mathbf{G}(t)\cdot\mathbf{r} - \frac{\omega}{\gamma}\right) \\ &= \frac{1}{\gamma}\left(\mathbf{i}\omega_1(t)\cos\phi(t) - \mathbf{j}\omega_1(t)\sin\phi(t) + \mathbf{k}\Delta\omega(\mathbf{r}, t)\right)\end{aligned} \tag{4.11}$$

It is convenient in the following to split $\mathbf{Q}$ into two parts

$$\mathbf{Q} = \mathbf{A} + \mathbf{T}, \tag{4.12}$$

where

$$\mathbf{A} = \begin{pmatrix} 0 & \Delta\omega(\mathbf{r}, t) & \omega_1(t)\sin\phi(t) \\ -\Delta\omega(\mathbf{r}, t) & 0 & \omega_1(t)\cos\phi(t) \\ -\omega_1(t)\sin\phi(t) & -\omega_1(t)\cos\phi(t) & 0 \end{pmatrix} \tag{4.13}$$

contains no relaxation terms, and

$$\mathbf{T} = \begin{pmatrix} -1/T_2 & 0 & 0 \\ 0 & -1/T_2 & 0 \\ 0 & 0 & -1/T_1 \end{pmatrix}, \tag{4.14}$$

contains only the relaxation terms.

4.1.1 Hard Pulses

Hard pulses are normally short intense broadband RF pulses designed to interact equally with the spin population throughout the extent of the transmitter coil. In this case, the applied field, $B_1(t)$, is time independent which gives the following solution [2] to equation (4.8)

$$\mathbf{M}(t) = \mathrm{e}^{\mathbf{Q}t}\mathbf{M}(0) + \mathbf{k}M_0\left(1 - \mathrm{e}^{-t/T_1}\right). \tag{4.15}$$

Hard pulses are characterized by being very short. In order to achieve useful flip angles, they are therefore correspondingly intense, which corresponds to $\omega_1 \gg \Delta\omega$. The hard pulse approximation then lies in neglecting both the $\Delta\omega$ terms and the relaxation terms in $\mathbf{Q}$. Assuming for a moment that $\phi(t) = 0$, the propagator matrix in equation (4.15) then simplifies to [2]

$$\mathrm{e}^{\mathbf{Q}t} = \begin{pmatrix} 1 & 0 & 0 \\ 0 & \cos\omega_1 t & \sin\omega_1 t \\ 0 & -\sin\omega_1 t & \cos\omega_1 t \end{pmatrix}, \tag{4.16}$$

which corresponds to a rotation about the x-axis, where the rotation angle is given by $\Phi = \omega_1 t = \gamma B_1 t$. In general, rotation matrices for positive rotations by an angle β about the x, y and z axes are given respectively by

$$\mathbf{R}_x(\beta) = \begin{pmatrix} 1 & 0 & 0 \\ 0 & \cos\beta & \sin\beta \\ 0 & -\sin\beta & \cos\beta \end{pmatrix}, \tag{4.17}$$

$$\mathbf{R}_y(\beta) = \begin{pmatrix} \cos\beta & 0 & \sin\beta \\ 0 & 1 & 0 \\ -\sin\beta & 0 & \cos\beta \end{pmatrix}, \tag{4.18}$$

and

$$\mathbf{R}_z(\beta) = \begin{pmatrix} \cos\beta & -\sin\beta & 0 \\ \sin\beta & \cos\beta & 0 \\ 0 & 0 & 1 \end{pmatrix}. \tag{4.19}$$

Thus, in the case of $\phi(t) = 0$, $\mathrm{e}^{\mathbf{Q}t} = \mathbf{R}_x(\gamma B_1 t)$. Similarly, for $\phi(t) = \frac{\pi}{2}$, $\mathrm{e}^{\mathbf{Q}t} = \mathbf{R}_y(\gamma B_1 t)$. A 90°_x RF pulse which rotates the magnetization by 90° about the x-axis is therefore obtained by having $\phi(t) = 0$ and setting the pulse amplitude, B_1, such that $\gamma B_1 T = \frac{\pi}{2}$, where T is the pulse duration.

4.1.2 Soft Pulses

All the pulses used in the ASL sequences presented in this thesis, are soft pulses, which generally have a narrower frequency bandwidth than the irradiated spin population. This is achieved by applying linear magnetic field gradients and using RF pulses that are long compared to hard pulses. The amplitude of the pulse is generally modulated and sometimes the phase is as well. One advantage of this approach is the ability to selectively excite spins based on their position.

One disadvantage of soft pulses, is that the Bloch equation cannot generally be solved analytically for a pulse shape given by equation (4.3). The evolution of the magnetization must therefore be calculated by numerical integration of equation (4.8). Earlier approaches to solving the Bloch equation before numerical computations were feasible include the use of perturbation theory [89]. Although current methods are based on numerical integration, they are numerically quite demanding, and there are therefore several numerical approximations to the solution to the Bloch equation that vary in their assumptions and accuracy.

The general approach is based on dividing the applied RF pulse into a number of small time-steps of length Δt, within which $B_1(t)$ and $\phi(t)$ are assumed constant, i.e. assuming that $\mathbf{B}_1(t)$ is piece-wise constant. This is a good approximation of the way RF pulses in general are implemented on commercial MR scanners. Equation (4.8) is then solved for each segment of the pulse. As long

as the time steps used are small, the approximation is accurate. Three degrees of approximation are discussed in the following.

Approximation 1

Neglecting relaxation terms, equation (4.8) reduces to

$$\frac{\mathrm{d}\mathbf{M}}{\mathrm{d}t} = \mathbf{Q}\mathbf{M} \;=\; \mathbf{A}\mathbf{M}, \tag{4.20}$$

which for constant $\mathbf{Q}$ has the solution

$$\mathbf{M}(t) = \mathrm{e}^{\mathbf{Q}t}\mathbf{M}(0) \;=\; \mathrm{e}^{\mathbf{A}t}\mathbf{M}(0). \tag{4.21}$$

Let the RF pulse be divided into n segments, where $B_1(t)$ and $\phi(t)$ are constant within each segment (see figure 4.1). However, it is not assumed that $\omega_1 \gg \Delta\omega$ as with the hard pulses. Let $B_1(t) = B_{1,j}$ and $\phi(t) = \phi_j$ during segment j, i.e for $(j-1)\Delta t < t < j\Delta t$, $j = 1, \ldots, n$. The magnetization after the j'th segment of the RF pulse is therefore given by

$$\mathbf{M}_j = e^{\mathbf{A}_j \Delta t}\mathbf{M}_{j-1} \;\;=\;\; \mathbf{R}_j\mathbf{M}_{j-1}, \quad j = 1, \ldots, n \;\;, \tag{4.22}$$

where $\mathbf{R}_j$ is a simple rotation matrix about the effective magnetic field during segment j, $\mathbf{B}_{\mathrm{eff},j}(\mathbf{r})$, by an angle $\Phi_j(\mathbf{r}) = \gamma|\mathbf{B}_{\mathrm{eff},j}(\mathbf{r})|\Delta t$. Writing out the recursion in equation (4.22) gives the magnetization after n steps

$$\mathbf{M}_n = \mathbf{R}_n\mathbf{R}_{n-1}\cdots\mathbf{R}_1\mathbf{M}(0). \tag{4.23}$$

In order to find the rotation matrix, $\mathbf{R}_j$, we need to express the rotation of the magnetization about $\mathbf{B}_{\mathrm{eff},j}$ by angle Φ_j in terms of the angles Φ_j, ϕ_j and θ_j shown in figure 4.2, where $\theta_j(\mathbf{r}) = \tan^{-1}\left[\omega_{1,j}/\Delta\omega_j(\mathbf{r})\right]$. Let us define a new coordinate system in which the z-axis points along $\mathbf{B}_{\mathrm{eff},j}$. Such a coordinate system is achieved by rotating our coordinate system through an angle ϕ_j about the z-axis then through an angle $-\theta_j$ about the y-axis. In this new coordinate system, $\mathbf{R}_j = \mathbf{R}_z(-\Phi_j)$, where $\mathbf{R}_z$ is given by equation (4.19). We then need to transform the result back to our original coordinate system. The propagation matrix can therefore be expressed as

$$\mathrm{e}^{\mathbf{A_j}\Delta t} = \mathbf{R}_j = \mathbf{R}_z(-\phi_j) * \mathbf{R}_y(\theta_j) * \mathbf{R}_z(-\Phi_j) * \mathbf{R}_y(-\theta_j) * \mathbf{R}_z(\phi_j), \tag{4.24}$$

Inserting equations (4.18) and (4.19) into equation (4.24) gives an overall rotation matrix of [90]

$$\mathbf{R}_j(\mathbf{r}) = \mathrm{e}^{\mathbf{A}_j\Delta t} = \begin{pmatrix} e_0^2+e_1^2-e_2^2-e_3^2 & 2(e_1e_2+e_0e_3) & 2(e_1e_3-e_0e_2) \\ 2(e_1e_2-e_0e_3) & e_0^2-e_1^2+e_2^2-e_3^2 & 2(e_2e_3+e_0e_1) \\ 2(e_1e_3+e_0e_2) & 2(e_2e_3-e_0e_1) & e_0^2-e_1^2-e_2^2+e_3^2 \end{pmatrix}, \tag{4.25}$$

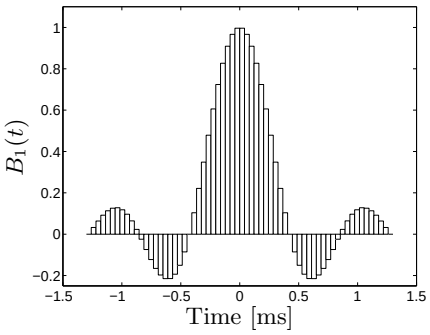

Figure 4.1: An RF pulse consisting of $n = 64$ segments, where $B_1(t)$ is constant within each segment.

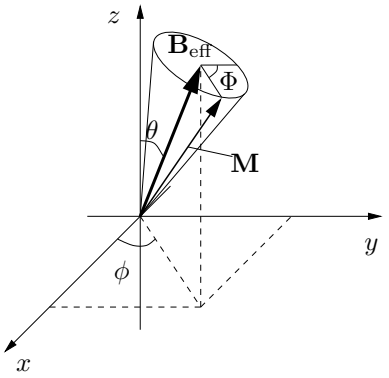

Figure 4.2: Rotation of the magnetization $\mathbf{M}$ around the effective magnetic field in the rotating frame of reference, $\mathbf{B}_{\text{eff}}$, by an angle Φ.

where

$$\begin{aligned} e_0 &= \cos\frac{\Phi}{2}\,, & e_1 &= \cos\phi\sin\theta\sin\frac{\Phi}{2}\,, \\ e_2 &= -\sin\phi\sin\theta\sin\frac{\Phi}{2}\,, & e_3 &= \cos\theta\sin\frac{\Phi}{2}\,, \end{aligned} \tag{4.26}$$

and the index j is implicit in e_0–e_3 and the angles ϕ, θ and Φ.

Approximation 2

The propagation matrix, $\mathbf{R}_j$, in equation (4.25) is computationally demanding since it is a function of both $\mathbf{r}$ and j. If the rotation angle Φ_j about $\mathbf{B}_{\text{eff},j}$ is small, it can be approximated by rotations about the longitudinal and transverse components of $\mathbf{B}_{\text{eff},j}$ separately. In other words, the approximation is based on rotating the magnetization about $\mathbf{B}_{1,j}$ in the xy-plane followed by free precession about z due to the longitudinal component of $\mathbf{B}_{\text{eff},j}$.

In mathematical terms, $\mathbf{R}_j$ is approximated as

$$\mathbf{R}_j \approx \tilde{\mathbf{R}}_{z,j}\tilde{\mathbf{R}}_{xy,j}, \tag{4.27}$$

where

$$\tilde{\mathbf{R}}_{z,j}(\mathbf{r}) = \mathbf{R}_z(\Delta\omega_j(\mathbf{r})\Delta t) = \begin{pmatrix} \cos(\Delta\omega_j\Delta t) & \sin(\Delta\omega_j\Delta t) & 0 \\ -\sin(\Delta\omega_j\Delta t) & \cos(\Delta\omega_j\Delta t) & 0 \\ 0 & 0 & 1 \end{pmatrix}, \tag{4.28}$$

$$\begin{aligned} \tilde{\mathbf{R}}_{xy,j} &= \mathbf{R}_z(-\phi_j) * \mathbf{R}_y(\frac{\pi}{2}) * \mathbf{R}_z(-\tilde{\Phi}_j) * \mathbf{R}_y(-\frac{\pi}{2}) * \mathbf{R}_z(\phi_j) \\ &= \begin{pmatrix} \cos\tilde{\Phi}_j \sin^2\phi_j + \cos^2\phi_j & (\cos\tilde{\Phi}_j - 1)\sin\phi_j\cos\phi_j & \sin\phi_j\sin\tilde{\Phi}_j \\ (\cos\tilde{\Phi}_j - 1)\sin\phi_j\cos\phi_j & \cos\tilde{\Phi}_j\cos^2\phi_j + \sin^2\phi_j & \cos\phi_j\sin\tilde{\Phi}_j \\ -\sin\phi_j\sin\tilde{\Phi}_j & -\cos\phi_j\sin\tilde{\Phi}_j & \cos\tilde{\Phi}_j \end{pmatrix}, \end{aligned} \tag{4.29}$$

and $\tilde{\Phi}_j = \gamma B_{1,j}\Delta t$. The advantage of this approximation is that $\tilde{\mathbf{R}}_{xy,j}$ is only a function of j. Although $\tilde{\mathbf{R}}_{z,j}$ depends on both $\mathbf{r}$ and j, it is faster to compute than $\mathbf{R}_j$ in equation (4.25) and equation (4.27) is therefore computationally simpler than equation 4.25.

The validity of this approximation depends on the size of Φ_j which has to be small. For typical RF pulses, the number of segments used in equation (4.23) is 512, which gives, on average, very small rotation angles for each segment.

Approximation 3

Assuming that Δt is sufficiently small, so that the rotations in each time-step are infinitesimal, equations (4.28) and (4.29) can be simplified further. More specifically, as $\Delta t \to 0$, $\sin(\Delta\omega_j\Delta t) \to \Delta\omega_j\Delta t$ and $\cos(\Delta\omega_j\Delta t) \to 1$. Similarly, $\sin\tilde{\Phi}_j \to \gamma B_{1,j}\Delta t$ and $\cos\tilde{\Phi}_j \to 1$. Inserting these limits in equations (4.28) and (4.29) gives

$$\tilde{\mathbf{R}}_{z,j}(\mathbf{r}) \approx \begin{pmatrix} 1 & \Delta\omega_j(\mathbf{r})\Delta t & 0 \\ -\Delta\omega_j(\mathbf{r})\Delta t & 1 & 0 \\ 0 & 0 & 1 \end{pmatrix}, \tag{4.30}$$

$$\tilde{\mathbf{R}}_{xy,j} \approx \begin{pmatrix} 1 & 0 & \gamma B_{1,j}\Delta t\sin\phi_j \\ 0 & 1 & \gamma B_{1,j}\Delta t\cos\phi_j \\ -\gamma B_{1,j}\Delta t\sin\phi_j & -\gamma B_{1,j}\Delta t\cos\phi_j & 1 \end{pmatrix} \tag{4.31}$$

The accuracy of equations (4.30) and (4.31) depends on the size of Δt. Since the maximum B_1 typically is on the order of 0.1–0.2 Gauss, Δt values on the order of 10 μs are usually acceptable. This corresponds to rotations less then 0.5° per time-step.

Relaxation

So far, relaxation terms have been ignored in the presented solutions. When the relaxation matrix, $\mathbf{T}$ in equation (4.12) cannot be ignored, the propagation matrix in equation (4.24) becomes $\mathrm{e}^{(\mathbf{A_j}+\mathbf{T})\Delta t}$. And since $\mathbf{A_j}$ and $\mathbf{T}$ do not generally commute, $\mathrm{e}^{\mathbf{A_j}+\mathbf{T}} \neq \mathrm{e}^{\mathbf{A_j}}\mathrm{e}^{\mathbf{T}}$, and the propagation matrix no longer becomes a simple product of rotation matrices.

However, if one assumes that $\mathrm{e}^{\mathbf{A_j}+\mathbf{T}} \approx \mathrm{e}^{\mathbf{A_j}}\mathrm{e}^{\mathbf{T}}$ thus neglecting the interaction between relaxation and rotation, equation (4.24) becomes

$$\mathrm{e}^{\mathbf{Q_j}\Delta t} = \mathrm{e}^{(\mathbf{A_j}+\mathbf{T})\Delta t} \approx \mathrm{e}^{\mathbf{A_j}\Delta t}\mathrm{e}^{\mathbf{T}\Delta t} = \mathbf{R}_j\mathrm{e}^{\mathbf{T}\Delta t}. \tag{4.32}$$

Equation (4.22) must therefore be modified to

$$\mathbf{M}_j = \mathbf{R}_j\mathbf{M}_{j-1}\,\mathrm{e}^{\mathbf{T}\Delta t} + \mathbf{k}M_0\left(1-\mathrm{e}^{-\frac{\Delta t}{T_1}}\right), \quad j = 1,\ldots,n. \tag{4.33}$$

4.1.3 Small Flip Angle Approximation

If the total angle of rotation is small and the initial magnetization is in equilibrium, one can approximate the longitudinal magnetization to be constant, such that $M_z(t) \approx M_0$ and $dM_z/dt \approx 0$. Inserting this in equation (4.10) and ignoring relaxation terms gives

$$\frac{\mathrm{d}}{\mathrm{d}t}\begin{pmatrix}M_x\\M_y\\M_z\end{pmatrix} = \begin{pmatrix}0 & \Delta\omega(\mathbf{r},t) & \omega_1(t)\sin\phi(t)\\ -\Delta\omega(\mathbf{r},t) & 0 & \omega_1(t)\cos\phi(t)\\ 0 & 0 & 0\end{pmatrix}\begin{pmatrix}M_x\\M_y\\M_z\end{pmatrix}. \tag{4.34}$$

Let $M_{xy} = M_x + iM_y$. Furthermore, if $\Delta\omega$ is time independent, equation (4.34) can be written as

$$\frac{\mathrm{d}M_{xy}}{\mathrm{d}t} = -i\Delta\omega(\mathbf{r})M_{xy} + i\omega_1(t)\mathrm{e}^{-i\phi(t)}M_0. \tag{4.35}$$

If the pulse duration is T, the solution to equation (4.35) is [91]

$$M_{xy}(\mathbf{r}) = i\gamma M_0\mathrm{e}^{-i\Delta\omega(\mathbf{r})\frac{T}{2}}\mathcal{F}^{-1}\left\{B_1(t)\mathrm{e}^{-i\phi(t)}\right\}_{f=\frac{\Delta\omega}{2\pi}}, \tag{4.36}$$

where $\mathcal{F}^{-1}\left\{B_1(t)\mathrm{e}^{-i\phi(t)}\right\}$ is the inverse Fourier transform of the applied RF pulse, $B_1(t)\mathrm{e}^{-i\phi(t)}$. This directly relates the transverse magnetization profile, $M_{xy}(\mathbf{r})$ to the applied RF pulse. However, as we shall see in section 4.3, this only holds for small flip angles.

4.2 RF Pulse Properties

RF pulses have several properties that affect the degree to which they can fulfill their role in a pulse sequence. These properties include slice profile, flip angle, pulse duration, B_1 sensitivity, RF power and amplitude, and bandwidth. The definition and importance of these properties is given in the following.

Slice Profile

The slice profile of an RF pulse is given by the profile across frequency of the magnetization after the pulse is applied. If a slice selection gradient is applied during the RF irradiation, the frequency axis can be translated into a position axis, normally chosen to be z. For single band pulses, the slice profile is composed of a pass band, two stop bands and two transition bands as defined in reference [92].

The slice width is defined as the FWHM and the width of the transition band compared to the slice width is a measure of how good the pulse is. In most cases, it is desirable to have as narrow transition bands as possible. The ripples in the pass and stop bands are also a measure of goodness. The acceptable ripple amplitudes depend on the role an RF pulse plays in the sequence where it is used. The slice profile of an RF pulse can be calculated by solving the Bloch equation as described in section 4.1.

Flip Angle

The magnetization in the irradiated body is flipped with an angle that depends on the frequency difference between the applied pulse and the spins at any position as given by the slice profile. However, the term flip angle is used to denote the angle with which magnetization is flipped for spins with zero frequency offset.

Pulse Duration

The pulse duration is the time during which RF irradiation is applied. The pulse duration affects the pulse bandwidth and has a large effect on the slice profile. Short pulses tend to have wider transition bands than comparable long pulses. The pulse duration of selective RF pulses is usually on the order of 1–20 ms.

B_1 Sensitivity

Due to the non-ideal characteristics of transmitter and receiver coils, the applied RF field is not homogeneous throughout the irradiated volume. And since the solution of the Bloch equation depends on B_1, the slice profile of an applied RF pulse will not be constant throughout the imaged volume.
Some RF pulses, such as adiabatic pulses, are more robust towards B_1 inhomogeneities than others.

RF Power and Amplitude

As seen in section 4.1, the angle of rotation for hard pulses is $\gamma B_1 T$ where T is the duration of the pulse. The same rotation can therefore be achieved for a short pulse as for a long pulse by adjusting the RF amplitude, B_1. Similar properties are valid for many soft pulses. There are, however limitations to the amplitude of RF pulses. First, there are hardware limits to the voltage that can be applied to the RF coil. Secondly, RF irradiation induces heating of the

irradiated objects, and there are therefore limits to the amount of RF power that can be applied per unit time without heating up the subjects.

The international standard defined by the International Electrotechnical Commission (IEC) setting the limits for the RF irradiation is based on allowing core heating of the body of no more than 1°C, or localized heating to 38°C in the head, 39°C in the trunk and 40°C in the extremities [93]. The standard, IEC 60601-2-33, defines different operating modes that depend on the specific absorption rates (SAR) that are associated with RF irradiation. The limits for normal operating mode comprise values of whole body SAR less than 1.5 W/kg for 15 min, head SAR less than 3 W/kg for 10 min, local tissue SAR less than 8 W/kg for 5 min in the head or torso, and local tissue SAR less than 12 W/kg for 5 min in the extremities [93].

Bandwidth

The bandwidth of a pulse is the frequency range within which a pulse affects the magnetization. For slice selective pulses, the bandwidth, BW, defines the amplitude of the gradient needed for a given slice width through the relation $BW = \gamma G_z \Delta$, where G_z is the slice selection gradient, and Δ is the slice width, FWHM.

4.3 Sinc Pulses

Sinc pulses are probably the most widely used RF pulses in MRI. In this section, the characteristics of sinc pulses will be presented, and this class of pulses will be used to demonstrate the principles of refocusing, bandwidth and filtering.

In section 4.1.3 we saw that the amplitude of the transverse magnetization for small flip angles is proportional to the inverse Fourier transform of the applied RF pulse. In order to achieve a rectangular slice profile, which is the ideal case, an infinite sinc pulse would be needed, where $B(t) = \mathrm{sinc}(\pi t) = \frac{\sin \pi t}{\pi t}$. However, infinite pulses are not possible in real life, and we therefore need to consider finite pulses, but we will start out with sinc pulses nonetheless.

Let an RF pulse be given by

$$B_1(t) = A\,\mathrm{sinc}(\frac{2m\pi t}{T}), \qquad -\frac{T}{2} \leq t \leq \frac{T}{2}, \tag{4.37}$$

where m is the number of zero crossings on each side of the pulse centre. The number of lobes in the sinc pulse thus is $2m - 1$ including the central lobe. Figure 4.3A shows such a pulse for $m = 3$. Figure 4.3B shows the imaginary part of equation (4.36) which corresponds to M_y. It is clear that the Fourier transform is not a perfect rectangle since the pulse is finite.

Figure 4.3C shows the magnetization after the pulse calculated using equations (4.27)–(4.29), where the pulse amplitude was scaled to give a 30° flip angle

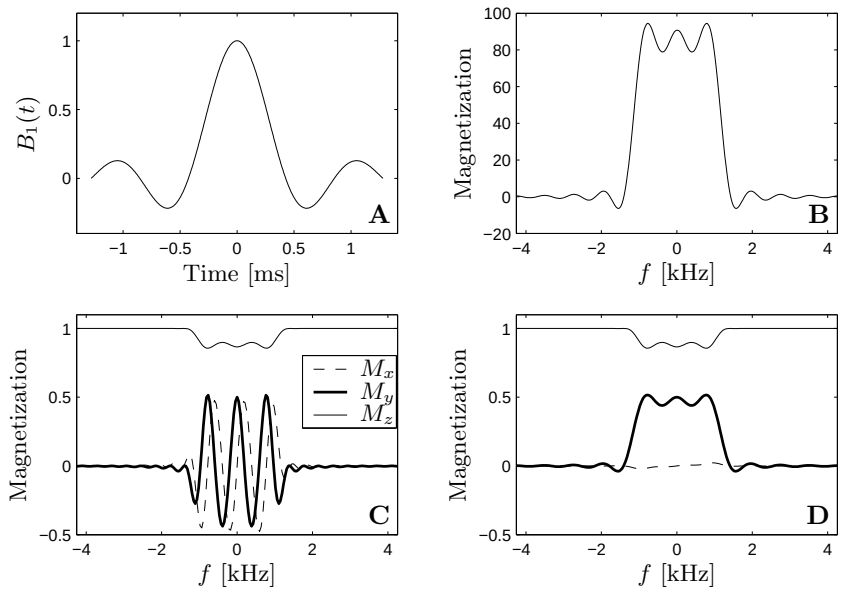

Figure 4.3: The slice profile of a 2.56 ms 30° 5-lobe sinc pulse. (A) The RF amplitude, $B_1(t)$, normalized to a maximum of 1. (B) The small flip angle approximation to the slice profile which is the inverse Fourier transform [arbitrary units]. (C) The x, y and z magnetization as a function of frequency offset, calculated by solving the Bloch equation before refocusing. (D) Same as (C) after refocusing the transverse magnetization.

at $f = 0$. Since the pulse is real ($\phi(t) = 0$), this scaling is straightforward, where the flip angle is given by

$$\Phi = 2\pi\gamma \int_{-\frac{T}{2}}^{\frac{T}{2}} B_1(t)\mathrm{d}t \; . \tag{4.38}$$

4.3.1 Refocusing

It is clear from figure 4.3C that the phase of the M_x and M_y magnetizations isn't constant across the slice. This phase twist is not present in figure 4.3B since it was removed by the $\mathrm{e}^{-i\Delta\omega T/2}$ term in equation (4.36). The signal that is measured on the scanner is the integral of the M_x and M_y curves[1] in figure 4.3C, which is almost zero just after the RF pulse. However, if the gradient during the pulse, $\mathbf{G}$, is constant, the phase twist can be corrected by applying a gradient, $-\mathbf{G}$, for half the duration of the pulse, i.e. $\frac{T}{2}$, which corresponds to the $\mathrm{e}^{-i\Delta\omega T/2}$ term in equation (4.36). This process is known as refocusing, and is needed for all RF pulses that produce transverse magnetization with a linear phase.

[1] Both M_x and M_y are only measured for coils having quadrature detection. For other coils only M_x, M_y or a linear combination of the two is measured.

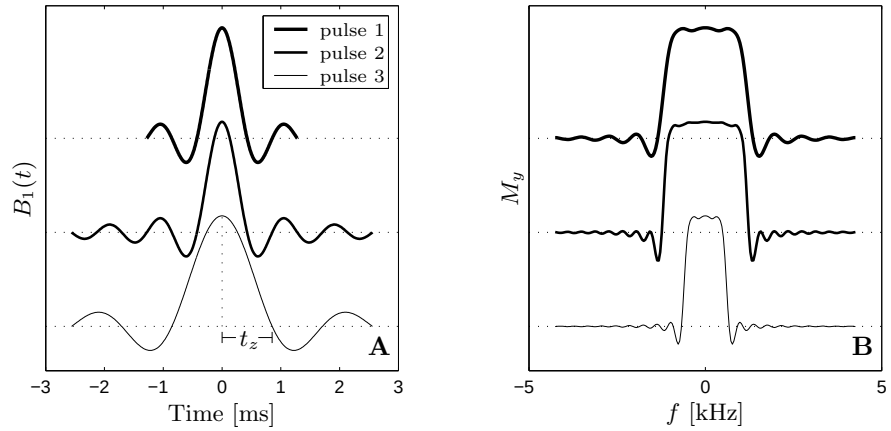

Figure 4.4: Effect of pulse duration and number of lobes on the magnetization profile. (A) and (B) show three 90° sinc pulses and their corresponding M_y profiles. Pulse 1 is a 5-lobe ($m = 3$) pulse with pulse duration $T = 2.56$ ms, pulse 2 is an 11-lobe ($m = 6$) pulse with duration $2T$, and pulse 3 is a 5-lobe ($m = 3$) pulse with pulse duration $2T$.

The need for refocusing the magnetization arises from the fact that most of the magnetization is flipped during the central part of the symmetric RF pulse, where $B_1(t)$ has the largest amplitude. If one imagines that all the magnetization is flipped at the centre of the pulse, the transverse magnetization will undergo dephasing due the gradient during the second half of the pulse. The magnetization then needs to be refocused with a negative refocusing gradient before the signal is acquired. The integral of the refocusing gradient is normally about half the integral of the slice selection gradient. The exact ratio may, however, deviate slightly from 0.5 depending on the pulse used (see figure 4.13).

Figure 4.3D shows the magnetization after refocusing. The M_y profile is very similar to that predicted by the inverse Fourier transform in equation (4.36) shown in figure 4.3B. This demonstrates the accuracy of the small flip angle approximation. The amplitude of M_y at the pulse centre ($f = 0$) is $\sin\Phi = 0.5$ while the amplitude of M_z at $f = 0$ is $\cos\Phi = 0.866$).

4.3.2 Pulse Duration and Bandwidth

Figure 4.4 shows three 90° sinc pulses and their corresponding M_y profiles. Pulses 2 and 3 are twice as long as pulse 1, but the extra time is used differently in the two pulses. Pulse 3 is identical in shape to pulse 1 where the only difference is in the time scale. Both pulses have 5 lobes ($m = 3$). Their magnetization profiles are therefore identical in shape, but with a difference in the frequency scale corresponding to difference in the time scale. In other words the two pulses have the same profile but the bandwidth of pulse 1 is double that of pulse 3.

Pulse 2 has the same time scale as pulse 1, and the extra time is used to include more lobes in the RF pulse. The two pulses have the same bandwidth,

but pulse 2 has a sharper profile, i.e. closer to the ideal rectangular shape. Note that although the two pulses have the same bandwidth, the ripples in pulse 2 have a higher frequency than those in pulse 1. This is because the frequency of the ripples is proportional to the pulse duration, while the bandwidth is inversely proportional to t_z, where t_z is defined in figure 4.4A. For sinc pulses the relation becomes

$$BW = \frac{2\pi}{t_z}\,. \tag{4.39}$$

4.3.3 Filtering

The ripples in the slice profiles demonstrated in figures 4.3 and 4.4 may have undesired effects, since the magnetization in quite a large region outside the slice will be affected by the RF pulse. The ripples are mainly due to the truncation of the sinc pulse and figure 4.4 demonstrates that increasing the number of lobes in the pulse is not enough to avoid the ripples.

Figure 4.5 shows the effect of filtering the RF pulse, where the amplitude of the pulse, $B_1(t)$, is multiplied by a Hamming filter, $H(t)$, where

$$H(t) = 0.54 - 0.46\cos\left(\pi\frac{2t+T}{T}\right)\,, \qquad -\frac{T}{2} \le t \le \frac{T}{2}\,. \tag{4.40}$$

$H(t)$ is depicted in figure 4.5C and the filtered RF pulse, $B_1(t)\cdot H(t)$ is shown in figure 4.5D. Comparing the slice profiles of the unfiltered and the filtered pulse (figures 4.5B, E and F), it is clear the filtering of the pulse smoothes the slice profile, so that the ripples are suppressed at the price of widening the transition bands.

An alternative to the Hamming filter is the Hanning filter which is very similar in shape and effect. The filter is given by

$$H_n(t) = 0.5\left(1 - \cos\left(\pi\frac{2t+T}{T}\right)\right)\,, \qquad -\frac{T}{2} \le t \le \frac{T}{2}\,. \tag{4.41}$$

The only difference in the two filters, is that the Hanning filter suppresses the RF pulse to zero at the edges, while the Hamming filter only suppresses the RF pulse by 92%.

4.4 Adiabatic Pulses

In this section, the reader is presented with the principle of adiabacity and its application in B_1-insensitive RF pulses. More specifically, the principle of adiabatic full passage is explained, and exemplified with hyperbolic secant pulses and FOCI pulses.

The flip angle for a sinc pulse, given by equation (4.38), is clearly sensitive to changes in the applied RF field, $B_1(t)$. Due to RF coil properties, $B_1(t)$ is not

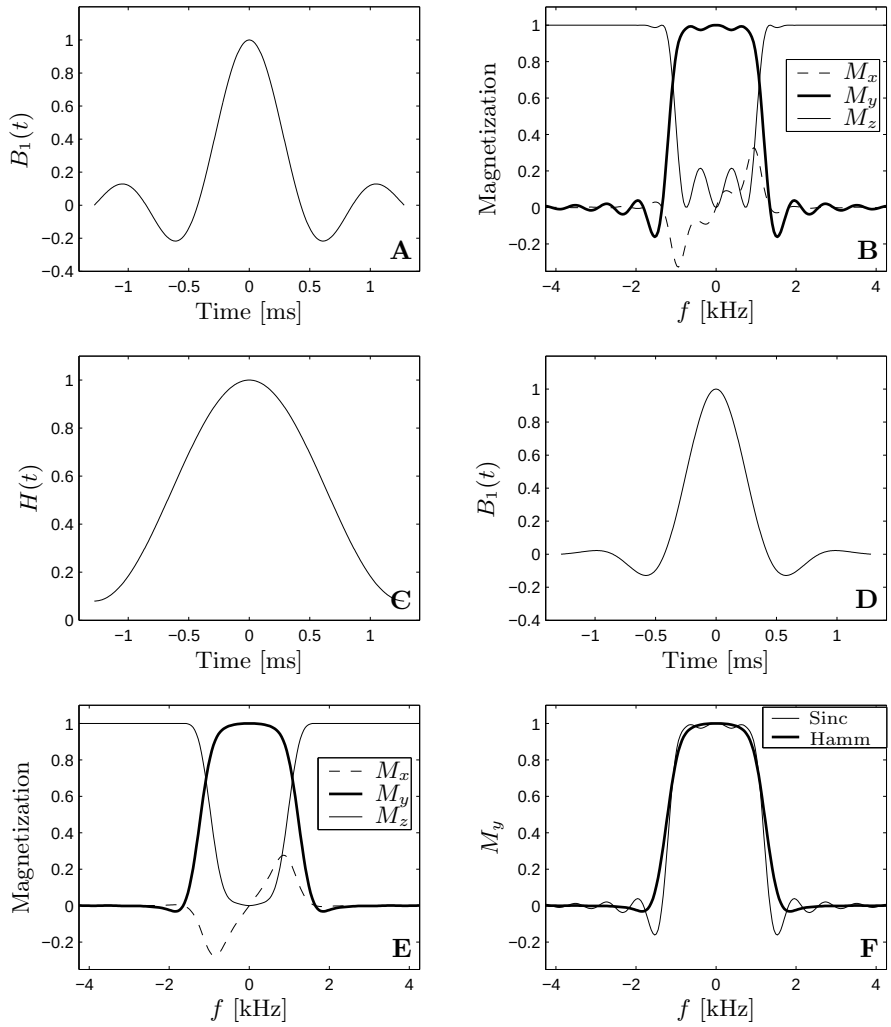

Figure 4.5: Effect of applying a Hamming filter to a 90° sinc pulse on the magnetization profiles. (A) Unfiltered RF pulse. (B) Slice profiles of the unfiltered pulse, where there are significant ripples. (C) The Hamming filter which is applied. (D) The filtered RF pulse. (E) The slice profiles of the filtered pulse. The ripples are markedly suppressed. (F) Broadening of the transition bands in M_y due to filtering.

uniform throughout the volume of the imaged object. Adjusting the amplitude of $B_1(t)$ to flip the magnetization by say, 90°, will only on average flip the magnetization by 90°. The actual flip angle may vary, for example, between 70° and 110° depending on the position within the coil. This may have very unfortunate effects in some sequences. Adiabatic RF pulses are a type of RF pulses that are insensitive towards B_1 inhomogeneities, and thus overcome the

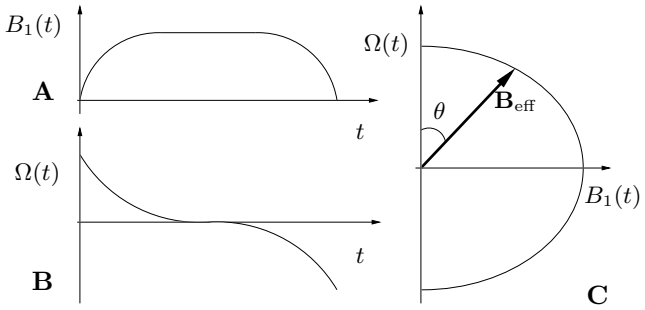

Figure 4.6: Principle of adiabatic full passage RF pulses. The amplitude of the pulse, $B_1(t)$, and the offset frequency of the pulse, $\Omega(t)$, are modulated in a manner similar that shown in (A) and (B), where $\Omega(t) = \omega_0 - \omega(t)$. (C) $\mathbf{B}_{\text{eff}}$ will initially point along $+z$ and gradually rotate in the xz plane in the rotating frame of reference, point along x when $\Omega(t) = 0$ then continue rotating to end along $-z$.

above-mentioned problem [94].

Sinc pulses and other conventional pulses are usually applied at a constant frequency, ω, while the amplitude, $B_1(t)$, and possibly the phase, $\phi(t)$, of the pulse are modulated. In adiabatic pulses, the frequency is also modulated[2], such that the instantaneous frequency is $\omega(t) = \omega_0 - \Omega(t)$. Only one of the most commonly used classes of adiabatic pulses, namely Adiabatic Full Passage (AFP) will be described here. For a description of other classes of adiabatic pulses such as adiabatic half passage (AHP) and B_1 insensitive rotation (BIR), the reader is referred elsewhere [94–103].

4.4.1 Adiabatic Full Passage

For adiabatic full passage (AFP) pulses, the frequency modulation takes the form of a frequency sweep, where the RF frequency begins far from resonance, is swept through resonance and ends far from resonance on the other side of the resonant frequency as illustrated in figure 4.6B. Meanwhile the amplitude of the pulse, $B_1(t)$, is modulated in some manner, such that the amplitude is small in the beginning and the end of the pulse and large at the centre of the pulse (figure 4.6A).

Assuming for simplicity that the phase of the RF pulse is zero, the effective magnetic field for spins at $\mathbf{r} = 0$ is

$$\mathbf{B}_{\text{eff}}(t) = \mathbf{i}B_1(t) + \mathbf{k}\frac{\Omega(t)}{\gamma}\,, \tag{4.42}$$

[2]Although the frequency modulation can be translated into phase modulation, as described by equation (4.46), the description of adiabatic pulses is most easily done when regarding the frequency modulation.

where $\Omega(t) = \omega_0 - \omega(t)$. Initially, $B_1(t)$ is small and $\Omega(t)$ is large, and $\mathbf{B}_{\text{eff}}$ points along $+z$ in the rotating frame of reference, see figure 4.6C. As $B_1(t)$ increases and $\Omega(t)$ decreases, $\mathbf{B}_{\text{eff}}$ rotates in the xz-plane and points along the x-axis when $\Omega = 0$. As $\Omega(t)$ becomes negative and $B_1(t)$ decreases again, $\mathbf{B}_{\text{eff}}$ rotates towards and ends along $-z$.

It can be shown, that if the rate of change of the angle θ is small compared to $\gamma|\mathbf{B}_{\text{eff}}|$, i.e.

$$\left|\frac{\mathrm{d}\theta}{\mathrm{d}t}\right| \ll \gamma\,|\mathbf{B}_{\text{eff}}|\,, \tag{4.43}$$

and the initial angle between the magnetization and $\mathbf{B}_{\text{eff}}$ is small, the magnetization will follow $\mathbf{B}_{\text{eff}}$ through its trajectory from $+z$ to $-z$. This gives an inversion of the magnetization that is independent of B_1 since changing the amplitude of B_1 doesn't change the starting and end direction of $\mathbf{B}_{\text{eff}}$, only the trajectory. For this same reason, conventional adiabatic pulses of this type can only be used for 90° and 180° pulses.

For spins, that are not on resonance, e.g. due to an applied gradient, the frequency offset will be $\Omega(t) + \Delta\omega(\mathbf{r})$, where $\Delta\omega(\mathbf{r}) = \mathbf{G}\cdot\mathbf{r}$ in the case of a gradient. At the end of the pulse, $\mathbf{B}_{\text{eff}}(\frac{T}{2}) = \frac{1}{\gamma}(\Omega(\frac{T}{2}) + \Delta\omega(\mathbf{r}))$. If $|\Delta\omega(\mathbf{r})| > |\Omega(\frac{T}{2})|$, $\mathbf{B}_{\text{eff}}$ will point in the same direction at the beginning and the end of the pulse, which means that the magnetization will not be flipped. The bandwidth of AFP pulses is therefore equal to the range of the frequency sweep, $\Omega(t)$.

4.4.2 Hyperbolic Secant Pulses

There is a wide variety of choices for the amplitude and frequency modulation functions, $B_1(t)$ and $\Omega(t)$ [94, 103]. One choice which is widely used is the hyperbolic secant (HS) pulse [45, 104], where

$$B_1(t) = A_0 \operatorname{sech}\beta t\,, \tag{4.44}$$

$$\Omega(t) = -\mu\beta\,\tanh\beta t\,, \qquad -\frac{T}{2} \le t \le \frac{T}{2}\,, \tag{4.45}$$

which has the bandwidth, $BW = 2\mu\beta$. Figure 4.7 shows the amplitude and frequency modulations, $B_1(t)$ and $\Omega(t)$ as well as the inversion profile corresponding to an HS pulse with $\mu = 10$, $\beta = 800$ Hz and pulse duration, $T = 15$ ms. For comparison, the inversion profile of a 41-lobe Hamming filtered sinc pulse with the same bandwidth and a pulse duration of 16.5 ms. It is clear that the HS pulse offers a much sharper inversion profile than the corresponding sinc pulse.

Furthermore, the HS pulse is robust towards changes in the B_1 amplitude, A_0 in equation (4.44). Figure 4.8A shows the inversion profile at the amplitudes $A_0 = 0.18$ G, $10A_0$ and $30A_0$. There is almost no difference between the inversion profiles at A_0 and $10A_0$. Even at an amplitude of $30A_0$, the inversion profile is still quite good, although the transition bands starts to widen slightly. The deterioration of the pulse is, however, not related to the adiabacity of the pulse,

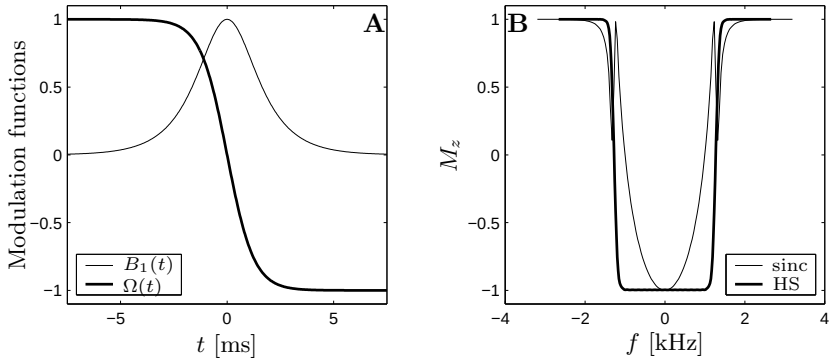

Figure 4.7: Hyperbolic secant (HS) pulse with $\mu = 10$, $\beta = 800$ Hz and $T = 15$ ms. (A) Amplitude and frequency modulation functions, $B_1(t)$ and $\Omega(t)$, where $\Omega(t)$ is normalized by the factor $\mu\beta$. (B) Inversion profile of the HS pulse compared to that of a 41-lobe sinc pulse with a pulse duration of 16.5 ms and the same bandwidth as the HS pulse.

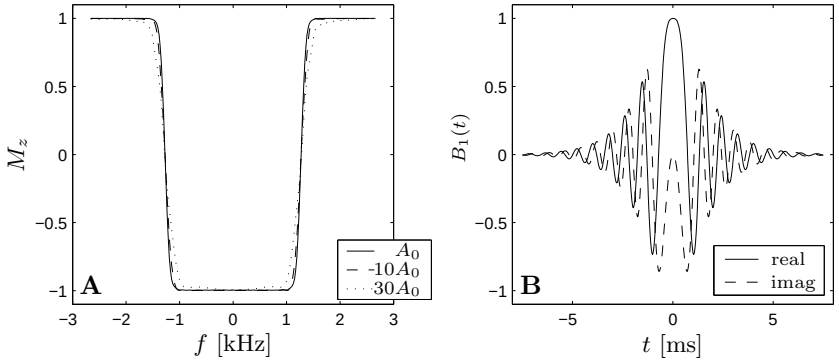

Figure 4.8: Hyperbolic secant (HS) pulse with $\mu = 10$, $\beta = 800$ Hz and $T = 15$ ms. (A) Robustness of inversion profile towards B_1 inhomogeneities. The profile is shown for magnitudes A_0, $10A_0$ and $30A_0$. (B) Real and Imaginary parts of $\mathbf{B}_1(t)$ given by equation (4.47), where the frequency modulation is translated into phase modulation.

but rather to the truncation of the pulse. When the maximum amplitude of the pulse is $30A_0$, the amplitude at $t = \pm T/2$ is no longer negligible.

The form of the HS RF pulse given in equations (4.44) and (4.45) cannot be implemented directly on most commercial scanners since frequency modulation is usually not supported. However, the frequency modulation of the pulse can be translated into a phase modulation through the equation

$$\mathrm{e}^{i\phi(t)} = \exp\left[\int_{-\frac{T}{2}}^{t} i\Omega(t')\mathrm{d}t' + i\phi\left(-\tfrac{T}{2}\right)\right], \tag{4.46}$$

where $\phi(t)$ is the phase of the RF pulse. The RF pulse can then be written as

$B_1(t)e^{i\phi(t)}$. For the HS pulse inserting equation (4.45) into (4.46) gives

$$\mathbf{B}_1(t) = A_0(\text{sech}\beta t)^{1+i\mu}. \tag{4.47}$$

Figure 4.8B shows the real and imaginary parts of $\mathbf{B}_1(t)$ which constitute the same RF pulse as shown in figure 4.7A.

4.4.3 FOCI Modifications

Another choice of the amplitude and frequency modulation functions $B_1(t)$ and $\Omega(t)$ is that given by the Frequency Offset Corrected Inversion (FOCI) pulse [105]. $B_1(t)$ and $\Omega(t)$ for the FOCI pulse can be derived from the corresponding functions of the HS pulse. The pulse amplitude, the frequency offset and the slice selection gradient of the HS pulse are multiplied by a modulation function, $A(t)$, where

$$A(t) = \begin{cases} \cosh(\beta t), & \cosh(\beta t) < p \\ p, & \text{otherwise} \end{cases}. \tag{4.48}$$

The factor p is defined as the ratio between the maximum available gradient on the scanner, and the one used in the slice-selective HS inversion. The basic idea of the FOCI pulse is to have a prolonged period with maximum RF power compared to the HS pulse. The resulting error in the inversion profile is then corrected by adjusting the frequency offset and the gradient.

Figure 4.9 shows the RF amplitudes, frequency offsets and slice-selection gradients used for both an HS and a FOCI pulse giving a 1 cm inversion slab thickness. The parameters for both pulses are $T = 10.24$ ms, $\mu = 2.72$ and $\beta = 1214$ Hz, and the FOCI pulse has $p = 10$.

Figure 4.10 compares the calculated inversion profiles, M_z, for the HS and FOCI pulses shown in figure 4.9. The inversion profile of the FOCI pulse is clearly much sharper than that of the HS pulse. The disadvantage of the FOCI pulse is the high RF power deposition.

4.5 Shinnar-Le Roux Pulses

Design of sinc pulses and adiabatic pulses presented in sections 4.3 and 4.4 is based on defining the pulse parameters, and then calculating the resulting slice profiles by solving the equations of motion. It is generally not possible to do the inverse, where one defines the desired slice profile and then calculates a sinc pulse or an adiabatic pulse that gives rise to such a profile.

However, there exists a method to design an RF pulse, that is neither a sinc pulse nor an adiabatic pulse, based on specifications of the desired slice profile. The method was developed simultaneously and independently by Shinnar *et al.* [106–110] and Le Roux [111, 112] and is named the Shinnar-Le Roux (SLR) algorithm. An overview of the algorithm is given in [113].

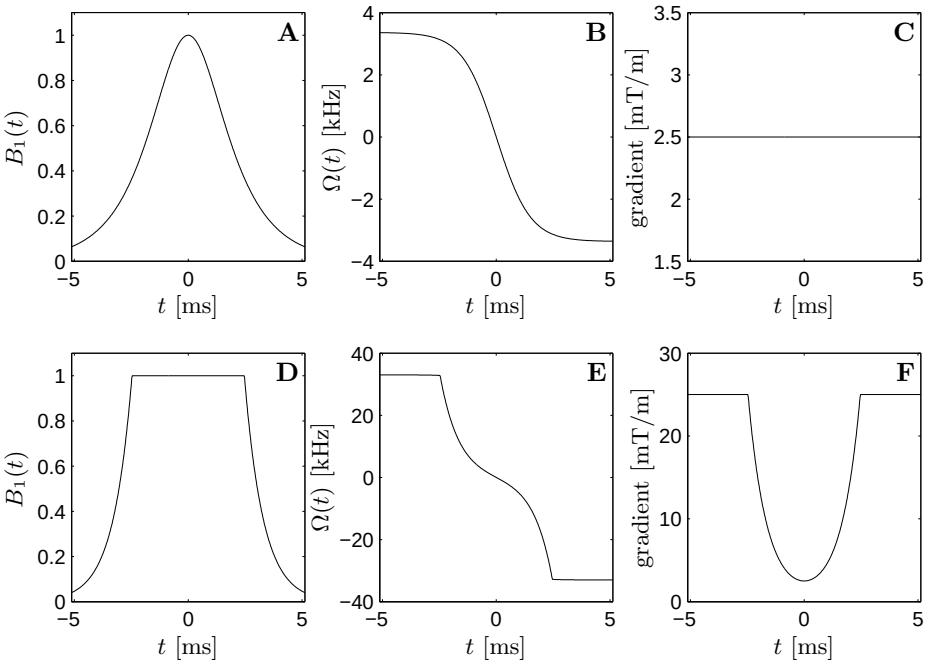

Figure 4.9: The RF amplitudes $B_1(t)$, the frequency offsets $\Omega(t)$ and slice selection gradients for a 1 cm inversion slab. Pulse parameters are $T = 10.24$ ms, $\mu = 2.72$ and $\beta = 1214$ Hz. (A–C) HS pulse. (D–F) FOCI pulses based on the HS pulse with $p = 10$.

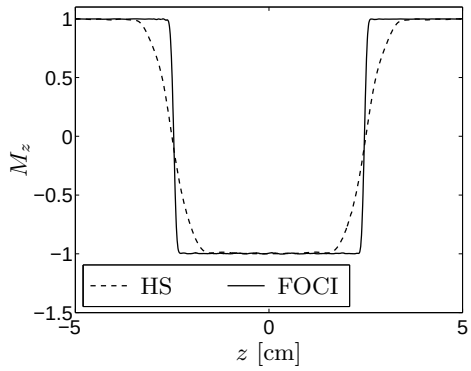

Figure 4.10: The inversion profiles of an HS and a FOCI pulse for a 5 cm inversion slab. Pulse parameters are $T = 10.24$ ms, $\mu = 2.72$ and $\beta = 1214$ Hz for both pulses and $p = 10$ for the FOCI pulse.

In short, the algorithm is based on an invertible transformation between the spin domain representation of an RF pulse and two complex polynomials that correspond to finite impulse response (FIR) filters. The design of RF pulses is done by designing FIR filters that represent the desired slice profile followed by calculation of the RF pulse that corresponds to the designed filters.

4.5.1 Spin Domain Representation

As seen in section 4.1, the solution to the Bloch equation neglecting relaxation involves the rotation of the magnetization about $\mathbf{B}_{\text{eff}}$ by an angle Φ. This is represented by a 3×3 rotation matrix given by equation (4.25). In the spin domain representation, rotation matrices are given by 2×2 complex unitary matrices containing the Cayley-Klein parameters, α and β, such that

$$\mathbf{Q} = \begin{pmatrix} \alpha & -\beta^* \\ \beta & \alpha^* \end{pmatrix}, \tag{4.49}$$

where $\alpha\alpha^* + \beta\beta^* = 1$. This matrix corresponds fully to the 3×3 rotation matrices dealt with in section 4.1. See Appendix B for details on the transformation between the two representations.

The complex Cayley-Klein parameters are given by

$$\alpha = e_0 + ie_3 \ , \qquad\qquad \beta = -e_2 + ie_1 \ , \tag{4.50}$$

where e_0–e_3 are defined in equation (4.26).

As described in equation (4.23), the overall rotation of the magnetization due to an RF pulse is given by the product of the rotation matrices corresponding to each RF segment, where the $\mathbf{B}_1$ field is assumed constant. That is, $\mathbf{Q} = \mathbf{Q}_n\mathbf{Q}_{n-1}\ldots\mathbf{Q}_1$, where $\mathbf{Q}_j$ is the j'th rotation matrix corresponding to segment j of the RF pulse. $\mathbf{Q}_j$ is given by

$$\mathbf{Q}_j = \begin{pmatrix} a_j & -b_j^* \\ b_j & a_j^* \end{pmatrix}, \tag{4.51}$$

where a_j and b_j correspond to α and β in equation (4.50) with substitution of the j'th angles, ϕ_j, θ_j and Φ_j into equation (4.26)

The matrix product $\mathbf{Q}_n\mathbf{Q}_{n-1}\ldots\mathbf{Q}_1$ giving the product of rotations up to n can be written out as

$$\begin{pmatrix} \alpha_n & -\beta_n^* \\ \beta_n & \alpha_n^* \end{pmatrix} = \begin{pmatrix} a_n & -b_n^* \\ b_n & a_n^* \end{pmatrix} \ldots \underbrace{\begin{pmatrix} a_j & -b_j^* \\ b_j & a_j^* \end{pmatrix} \ldots \begin{pmatrix} a_0 & -b_0^* \\ b_0 & a_0^* \end{pmatrix}}_{\begin{pmatrix} \alpha_j & -\beta_j^* \\ \beta_j & \alpha_j^* \end{pmatrix}} \tag{4.52}$$

It is clear that there is a redundancy of information in the matrix $\begin{pmatrix} \alpha_j & -\beta_j^* \\ \beta_j & \alpha_j^* \end{pmatrix}$ since either column contains all the information needed to define the product of rotations up to j. The state of rotation after the j'th segment can therefore be

represented by a vector $(\alpha_j, \beta_j)^T$ and the effect of the pulse may be calculated by propagating this vector

$$\begin{pmatrix} \alpha_j \\ \beta_j \end{pmatrix} = \begin{pmatrix} a_j & -b_j^* \\ b_j & a_j^* \end{pmatrix} \begin{pmatrix} \alpha_{j-1} \\ \beta_{j-1} \end{pmatrix}, \tag{4.53}$$

where the starting condition is no rotation, hence $\Phi_0 = 0$ and

$$\begin{pmatrix} \alpha_0 \\ \beta_0 \end{pmatrix} = \begin{pmatrix} 1 \\ 0 \end{pmatrix}. \tag{4.54}$$

Equation (4.53) is termed the state-space description of the spin domain rotations.

It can be shown (see appendix B), that if the initial magnetization is in equilibrium, the excitation slice profile of an RF pulse is given by $M_{xy} = M_x + iM_y = 2\alpha_n^*\beta_n M_0$ and the inversion slice profile is $M_z = (\alpha_n\alpha_n^* - \beta_n\beta_n^*)M_0$.

4.5.2 The Forward SLR Transform

The key step in the SLR algorithm is using an approximation to the rotation matrices. Using this approximation, the state-space equation, (4.53), can be transformed into two complex polynomials. The mapping of the RF pulse into two complex polynomials is called the forward SLR transform [113].

The approximation used, which is called the hard pulse approximation is based on assuming that the rotation of the magnetization about $\mathbf{B}_{\text{eff}}$ can be divided into a free precession about the longitudinal component of $\mathbf{B}_{\text{eff}}$ by an angle of $\Delta\omega\Delta t$, where $\Delta\omega = \gamma(\mathbf{B}_0 + \gamma\mathbf{G}\cdot\mathbf{r}) - \omega$, followed by a rotation about $\mathbf{B}_1$, which is in the xy-plane by an angle of $\Phi_j = \gamma B_{1,j}\Delta t$.[3] Using this approximation, the rotation matrix, (4.51) becomes

$$\mathbf{Q}_j = \begin{pmatrix} C_j & -S_j^* \\ S_j & C_j \end{pmatrix} \begin{pmatrix} p^{\frac{1}{2}} & 0 \\ 0 & p^{-\frac{1}{2}} \end{pmatrix}, \tag{4.55}$$

where

$$C_j = \cos\frac{\Phi_j}{2}, \qquad S_j = ie^{i\phi_j}\sin\frac{\Phi_j}{2}, \qquad p = e^{i\Delta\omega\,\Delta t}. \tag{4.56}$$

Note that it is here implicitly assumed that the gradient, $\mathbf{G}$, is constant. Inserting equation (4.55) into equation (4.53) gives

$$\begin{pmatrix} \alpha_j \\ \beta_j \end{pmatrix} = p^{\frac{1}{2}} \begin{pmatrix} C_j & -S_j^* \\ S_j & C_j \end{pmatrix} \begin{pmatrix} 1 & 0 \\ 0 & p^{-1} \end{pmatrix} \begin{pmatrix} \alpha_{j-1} \\ \beta_{j-1} \end{pmatrix}. \tag{4.57}$$

[3] This approximation is very similar to Approximation 2 in section 4.1.2. The difference between the two is the order of the longitudinal and transverse rotations. Here the free precession is done before the rotation about $\mathbf{B}_1$ where the opposite order was used in section 4.1.2.

Inserting

$$A_j = p^{-\frac{j}{2}}\alpha_j \ , \qquad\qquad B_j = p^{-\frac{j}{2}}\beta_j \tag{4.58}$$

into equation (4.57) gives

$$\begin{pmatrix} A_j \\ B_j \end{pmatrix} = \begin{pmatrix} C_j & -S_j^* p^{-1} \\ S_j & C_j p^{-1} \end{pmatrix} \begin{pmatrix} A_{j-1} \\ B_{j-1} \end{pmatrix} \ , \quad \text{where} \quad \begin{pmatrix} A_0 \\ B_0 \end{pmatrix} = \begin{pmatrix} 1 \\ 0 \end{pmatrix} . \tag{4.59}$$

Multiplying out equation (4.59) to the n'th step gives

$$A_n(p^{-1}) = \sum_{j=0}^{n-1} a_j p^{-j} \ , \qquad\qquad B_n(p^{-1}) = \sum_{j=0}^{n-1} b_j p^{-j} \tag{4.60}$$

which are two $n-1$ order polynomials in $p^{-1} = \mathrm{e}^{-i\Delta\omega\Delta t}$. The representation of the effect of an RF pulse is thereby reduced from a 3×3 matrix to two polynomials. Since the polynomials $A_n(p^{-1})$ and $B_n(p^{-1})$ are the elements of a unitary rotation matrix, they satisfy the condition

$$|A_n(p^{-1})|^2 + |B_n(p^{-1})|^2 = 1. \tag{4.61}$$

The polynomials, A_n and B_n can be regarded as finite impulse response (FIR) filters [111, 113] and the problem of designing RF pulses is therefore transformed to a problem of designing FIR filters.

4.5.3 The Inverse SLR Transform

The problem of obtaining the RF pulse corresponding to a set of polynomials, A_n and B_n, is easily solved by inverting equation (4.59).

$$\begin{pmatrix} A_{j-1} \\ B_{j-1} \end{pmatrix} = \begin{pmatrix} C_j & S_j^* \\ -S_j p & C_j p \end{pmatrix} \begin{pmatrix} A_j \\ B_j \end{pmatrix} \ = \ \begin{pmatrix} C_j A_j + S_j^* B_j \\ p(-S_j A_j + C_j B_j) \end{pmatrix} \tag{4.62}$$

Since $A_j(p^{-1})$ and $B_j(p^{-1})$ are $j-1$ order polynomials in p^{-1} while $A_{j-1}(p^{-1})$ and $B_{j-1}(p^{-1})$ are $j-2$ order polynomials, both the $p^{-(j-1)}$ terms and the p^{+1} terms on the right hand side of equation (4.62) must cancel out. The latter of these conditions gives $-S_j A_{j,0} + C_j B_{j,0} = 0$, where $A_{j,0}$ and $B_{j,0}$ are the p^{-0} terms in $A_j(p^{-1})$ and $B_j(p^{-1})$ respectively. This gives

$$\frac{B_{j,0}}{A_{j,0}} = \frac{S_j}{C_j} = \frac{i\mathrm{e}^{i\phi_j} \sin\frac{\Phi_j}{2}}{\cos\frac{\Phi_j}{2}}, \tag{4.63}$$

where Φ_j is the rotation angle produced by the j'th segment of the pulse and ϕ_j is the phase of that segment. Solving for Φ_j and ϕ_j gives

$$\Phi_j = 2\tan^{-1}\left|\frac{B_{j,0}}{A_{j,0}}\right| \ , \qquad\qquad \phi_j = \angle\left(-i\frac{B_{j,0}}{A_{j,0}}\right) \ , \tag{4.64}$$

and the j'th segment of the RF pulse is then given in complex notation by

$$\mathbf{B}_{1,j} = \frac{\Phi_j}{\gamma \Delta t} \mathrm{e}^{i\phi_j}. \tag{4.65}$$

Using equations (4.62) and (4.64) it is therefore possible to calculate the RF pulse corresponding to the two polynomials $A_n(p^{-1})$ and $B_n(p^{-1})$. This is known as the inverse SLR transform.

4.5.4 FIR Filter Design

We have seen in the previous sections how there exists an invertible transformation between an RF pulse, $\mathbf{B}_1(t)$, and two complex polynomials $A_n(p^{-1})$ and $B_n(p^{-1})$. The remaining step in designing RF pulses with a specific slice profile is therefore the design of the two polynomials. This is a FIR filter design problem and will only be sketched here. A more detailed description is given in [113].

By introducing the position dependence in p (through the $\mathbf{G} \cdot \mathbf{r}$ term in $\Delta\omega$), the ideal FIR filter $B_{\text{ideal}}(p^{-1})$ is identical to the desired slice profile. The trick is then to find the polynomial $B_n(p^{-1})$ that optimally approximates $B_{\text{ideal}}(p^{-1})$. One way to do that is using the Parks-McClellan (PM) algorithm for the design of linear-phase FIR digital filters. The algorithm requires the specification of the edges of the in-slice and out-of-slice regions as well as the relative ripples in each. Once $B_n(p^{-1})$ has been determined, $A_n(p^{-1})$ can be calculated to be consistent with equation (4.61) subject to the additional condition that the resulting RF pulse have minimum energy. When both $A_n(p^{-1})$ and $B_n(p^{-1})$ are determined, the RF pulse is calculated using the inverse SLR transform.

The Shinnar-Le Roux algorithm is a very powerful tool in RF pulse design and can be used to design RF pulses with highly improved slice profiles compared to conventional sinc pulses. An implementation of the SLR algorithm can be found in the Matlab® program `matpulse` written by Gerald Matson [92], which has been used in this thesis. Examples of RF pulses generated using the SLR algorithm are presented in section 4.6.

4.6 Examples

In this section various examples of the RF pulses used in this thesis are presented. The pulses are divided into three categories, inversion, excitation and saturation.

4.6.1 Inversion

Selective spin inversion is the backbone of roughly all ASL techniques. It is therefore very important to have inversion pulses with good slice profiles. As seen in figure 4.7, sinc pulses give very poor inversion profiles. Using the SLR

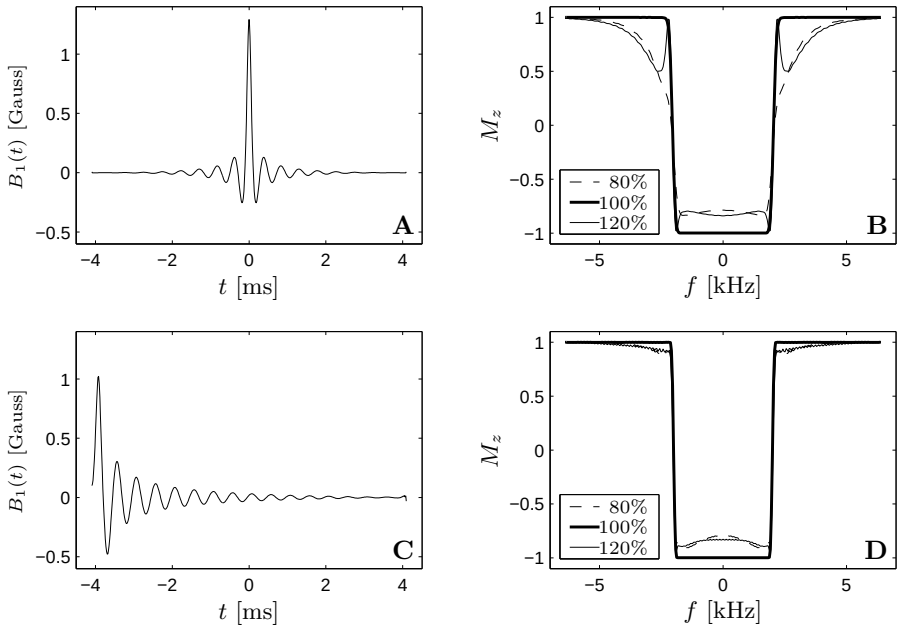

Figure 4.11: Two examples of inversion pulses designed using the SLR algorithm. Both pulses have a duration of 8.192 ms, bandwidth 4 kHz, passband ripple 0.1% and reject-band ripple 0.4%. (A) A Hamming filtered refocused pulse with maximum B_1 of 1.29 Gauss. (B) The inversion profiles of the pulse in (A) given at 80%, 100% and 120% of the amplitude required for a 180° flip angle. (C) A maximum phase pulse with maximum B_1 of 1.02 Gauss. (D) The inversion profiles of the pulse in (C) given at 80%, 100% and 120% of the amplitude required for a 180° flip angle.

algorithm good inversion profiles can be achieved with real pulses. Figure 4.11 shows two such examples.

Figures 4.11A and B show the RF waveform and inversion profiles of a Hamming filtered refocused SLR pulse[4] with pulse duration 8.192 ms, bandwidth 4 kHz, passband ripple 0.1% and reject-band ripple 0.4%. The B_1 amplitude required to give a 180° flip angle is 1.29 Gauss. The inversion profile is shown for three levels of B_1, where the 100% level is 1.29 Gauss. It is clear, that the pulse has an excellent inversion profile when B_1 is correct. However, if B_1 deviates from the nominal value, the profile deteriorates significantly. This is inevitable in real life due to B_1 inhomogeneities. Figures 4.11C and D show the RF waveform and inversion profiles of a maximum phase SLR pulse with the same parameters

[4]It may seem strange to filter an optimized pulse that is designed to meet certain specifications. The aim of the filtering, however, is to reduce the reject-band ripples in the magnetization profiles. Although the amplitude of the ripples is specified in the design of the SLR pulse, the ripples are not damped far from the pass band. Filtering the pulse damps the oscillations, but widens the transition bands.

as the previous pulse, except that the pulse is not Hamming filtered[5]. Although the inversion profile of the maximum phase pulse at the nominal B_1 amplitude is comparable to that of the refocused pulse, the first clearly outmatches the latter when B_1 deviates from the nominal value. Furthermore, the maximum B_1 amplitude required for 180° flip angle is 21% less for the maximum phase pulse than for the refocused pulse.

The relatively poor performance of the refocused SLR pulse is due to the restriction in its design, that the transverse magnetization have a linear phase, which can be refocused using a gradient. However, the transverse magnetization is generally of no interest in inversion pulses[6] and the maximum phase pulse is therefore preferable for inversion. However, neither of the pulses in figure 4.11 match the B_1 insensitivity of the adiabatic HS pulse illustrated in figure 4.8. Adiabatic inversion pulses are generally superior to other types of inversion pulses in that respect.

Figure 4.12 shows the effect of varying the pulse parameters of HS pulses on the inversion profiles. Figure 4.12A shows that for a given bandwidth and fixed pulse duration, higher μ and lower β gives a sharper inversion profile. This is only true to a certain limit though, since lowering β too much will violate the adiabatic condition, equation (4.43), which shows as ripples in the inversion profile of the $(\mu, \beta) = (10, 1000)$ pulse.

Figure 4.12B shows the effect of varying the pulse duration for a given set of (μ, β). If the pulse duration is too short, the adiabatic condition is violated, and the inversion profile breaks down, as can be seen for the 5 ms pulse. However, if the adiabatic condition is fulfilled, increasing the pulse duration does not affect the inversion profile, as can be seen from the 10 and 15 ms pulses.

4.6.2 Excitation

Excitation pulses are required for all measurements of magnetization. In 3D imaging, non-selective spin excitation may be used, and the use of hard pulses is justified. However, the most common acquisition mode in MRI is multislice 2D imaging, where it is important to use excitation pulses with good slice profiles for multiple reasons. One reason is to avoid having the magnetization in one slice affect the signal measured in adjacent slices, while another reason, applicable especially to ASL, is to avoid complex interactions with the slice profiles of inversion pulses in the sequence.

Figures 4.4 and 4.5 show examples of the excitation profiles of both filtered and non-filtered sinc pulses. Figure 4.13 shows the pulse shape and excitation profile of a 5.12 ms 90° excitation pulse designed using the SLR algorithm with a bandwidth of 2 kHz, pass-band ripple of 0.04% and reject-band ripple of 0.1%.

[5]Hamming filtering is only valid for symmetric pulses, and the maximum phase SLR pulse is clearly not symmetric.

[6]Here inversion implies the inversion of longitudinal magnetization. For spin-echo pulses, the transverse magnetization is of course of major importance. The transverse magnetization may also be important in inversion of longitudinal magnetization if there is a danger of inducing unwanted stimulated echoes with the use of multiple pulses

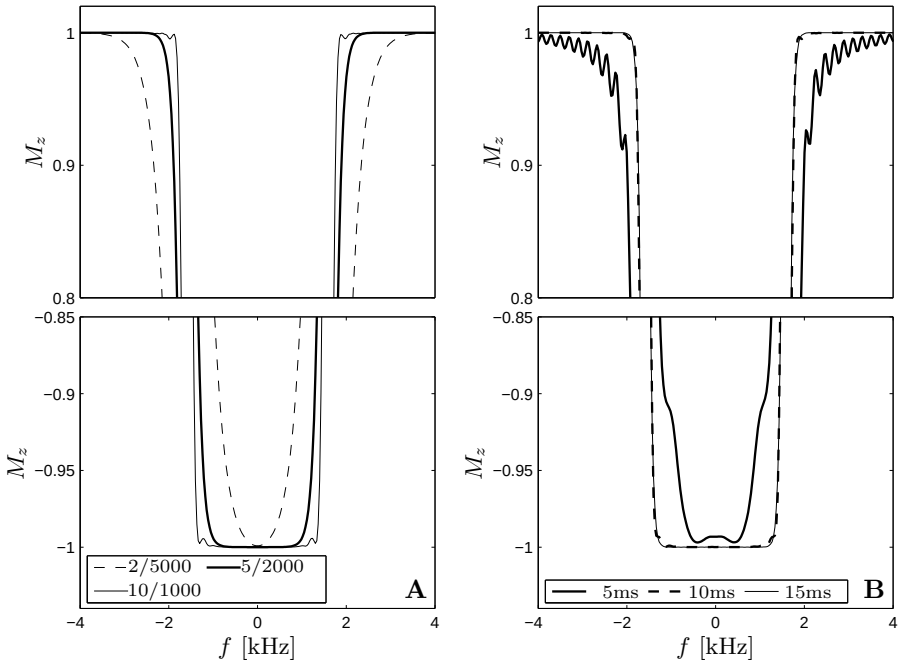

Figure 4.12: The effect of pulse parameters on the inversion profiles of HS pulses. The plot is zoomed in on the bottom and top parts of the inversion profiles for clarity. The transition bands are close to linear in the parts not shown in the figure. (A) Effect of changing μ and β for a constant pulse duration of 10 ms. The parameter pairs are $(\mu, \beta) = (2, 5000)$, $(5, 2000)$ and $(10, 1000)$, where the bandwidth is kept constant.(B) Effect of changing the pulse duration for fixed $(\mu, \beta) = (10, 1000)$.

Figure 4.13B shows M_x and M_y when the magnetization is refocused using a gradient that has an area equal to 0.5 of the slice selection gradient and opposite sign, i.e. a refocusing factor of 0.5. It is clear that M_x is not negligible, although it is asymmetric and integrates to zero. This is not desirable since the magnetization that is directed along x will in this case not be detected. If the refocusing factor is increased to 0.5123, as shown in figure 4.13C, the amplitude of M_x decreases significantly, and the profile of M_y is markedly improved.

Figure 4.14 compares the SLR pulse in figure 4.13 with a corresponding Hamming-filtered 9-lobe sinc pulse with the same duration and bandwidth. Note that the SLR pulse is not Hamming-filtered. Figure 4.14A shows that the SLR pulse has slightly larger RF amplitude, but otherwise is very similar to the sinc pulse. However, the SLR pulse offers highly suppressed side bands compared to the sinc pulse without sacrificing the profile in the pass band or the transition band as seen in figure 4.14B. On the contrary, the transition band is slightly narrower for the SLR pulse.

Figure 4.14C shows the effect of incorrect B_1 amplitude on the excitation

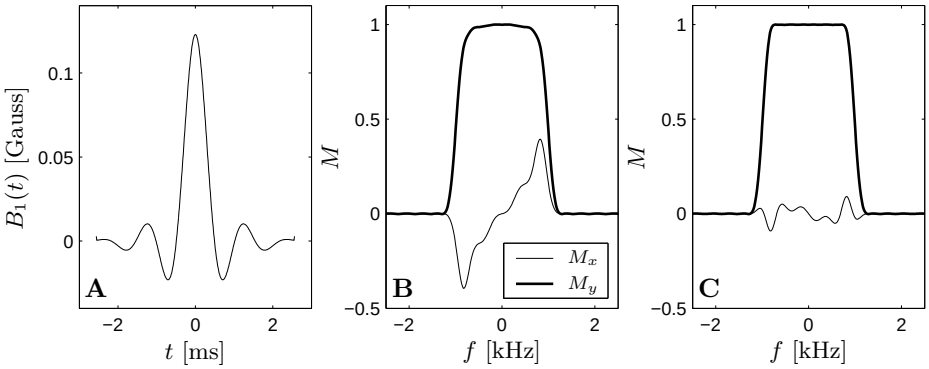

Figure 4.13: A 5.12 ms 90° excitation pulse designed using the SLR algorithm with a bandwidth of 2 kHz. (A) Pulse shape and amplitude. (B) The excitation profile (M_x and M_y) with refocusing factor of 0.5. (C) The excitation profile with the optimal refocusing factor of 0.5123.

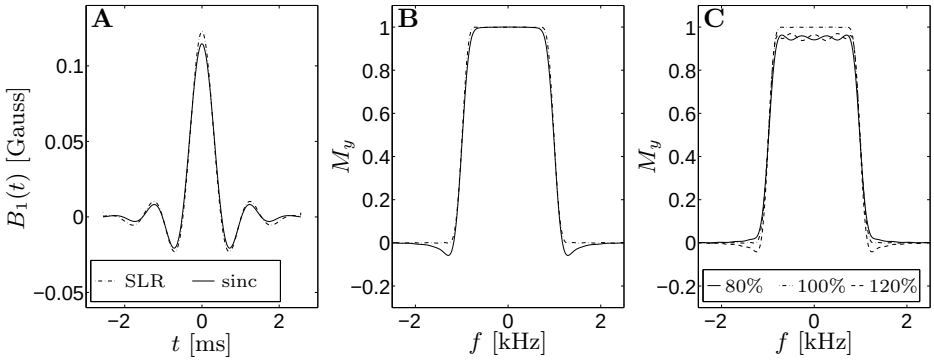

Figure 4.14: Comparison between SLR pulse and corresponding Hamming-filtered sinc pulse. (A) The SLR pulse has slightly higher RF amplitude. (B) The excitation profiles, M_y, of the pulses in (A) at the optimal refocusing factors, 0.5123 for the SLR pulse and 0.5135 for the sinc pulse. (C) Effect of incorrect B_1 amplitude on the excitation profile of the SLR pulse. Amplitudes of 80%, 100% and 120% of the nominal amplitude required for a 90° flip angle are used.

profile of the SLR pulse. Although there is some deterioration in the profile for too high or too low B_1, the effect isn't as strong as for the SLR inversion pulse shown in figure 4.11B.

4.6.3 Saturation

Saturation pulses are in principle the same as excitation pulses, except that the profile of interest is M_z instead of M_x and M_y. The transverse magnetization is usually dephased using crusher gradients after the 90° pulse. It is therefore not necessary and perhaps not even desirable to use refocused pulses. As was

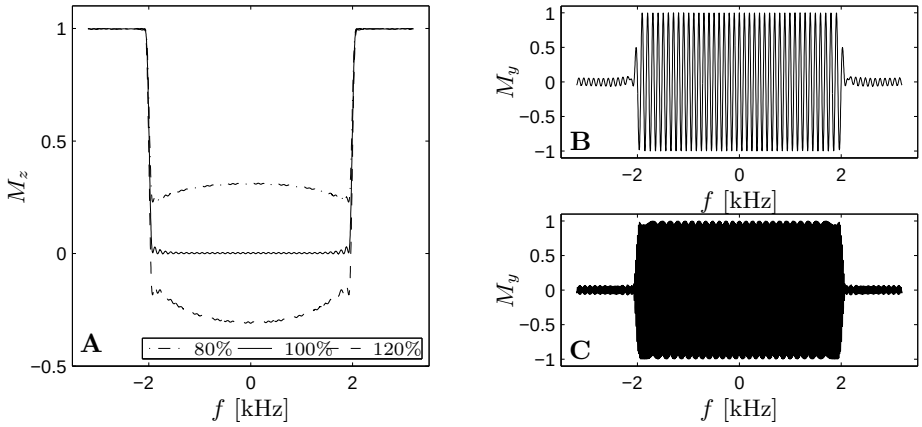

Figure 4.15: Slice profiles of a 10.24 ms maximum phase SLR pulse. (A) Saturation profile, M_z at 80%, 100% and 120% of the nominal B_1 amplitude for a 90° flip angle. (B) The M_y profile with no gradient following the pulse. The M_x profile is similar, where the only difference is 90° phase shift. (C) the M_y profile after a crusher gradient with an area equal to six times that of the slice selection gradient.

seen with inversion pulses, maximum phase pulses are more robust towards B_1 inhomogeneities than refocused pulses and actually give slightly sharper profiles.

Figure 4.15A shows the saturation profile of a 10.24 ms maximum phase SLR pulse with 0.5% passband ripple and 0.5% reject-band ripple. The figure shows the profile at B_1 amplitudes of 80%, 100% and 120% of the nominal B_1 value for a 90° flip angle. Figure 4.15B shows the M_y profile created by the same saturation pulse. Due to the magnetization oscillations, no signal would actually be measured, since the integral of the M_y profile is very small. The profile of M_x is approximately the same as that of M_y phase shifted by 90°. Figure 4.15C shows the M_y profile after further dephasing using a crusher gradient with an area equal to six times that of the slice selection gradient. It is clear that the frequency of the oscillations in the magnetization profile increases due to the gradient and signal nulling becomes more efficient.

Since the degree of saturation is strongly dependent on the B_1 amplitude, one way of overcoming the effect of B_1 inhomogeneities is using more than one saturation pulse. Although a better saturation profile may be acquired with multiple pulses, the mechanism of saturation is different from that of one pulse. Figure 4.16 shows the saturation profile after two saturation pulses separated by a crusher gradient with the same pulse and gradient parameters as in figure 4.15. The strong oscillations in the M_y profile in figure 4.15C are flipped into the z direction by the second pulse and the saturation profile after the second pulse becomes very different from that in figure 4.15A. However, even though M_z is not zero in the passband of the pulse, the frequency of the oscillations is high, and a following excitation pulse would give no signal due to signal nulling within

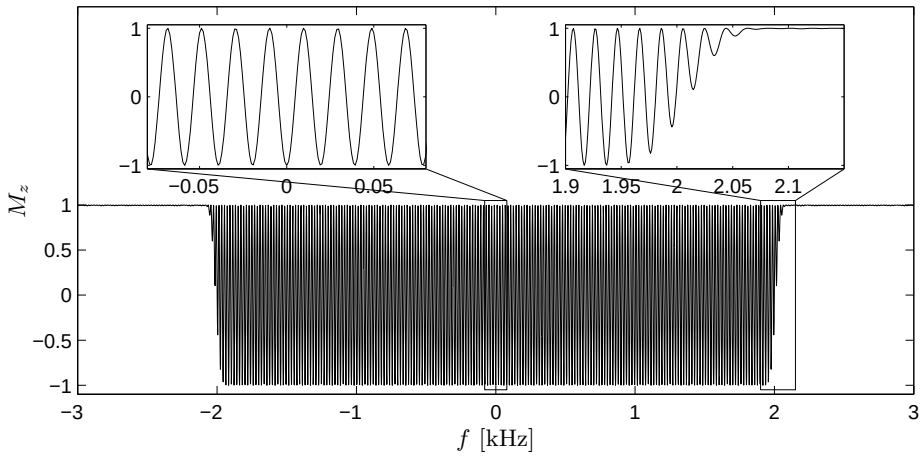

Figure 4.16: Saturation profile of two saturation pulses separated by a crusher gradient. The upper boxes zoom in on the indicated boxes to illustrate the oscillating nature of the profile.

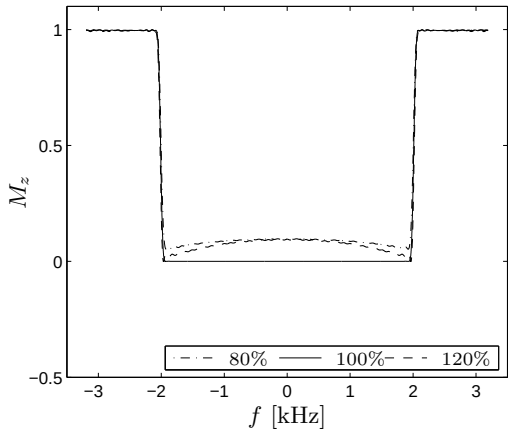

Figure 4.17: The approximate effective saturation profile of two saturation pulses, where it is assumed that the crusher gradients after the first pulse, completely null the transverse magnetization before the second pulse. Amplitudes of 80%, 100% and 120% of the nominal amplitude for a 90° flip angle are used.

the excited volume. The effective saturation profile of two saturation pulses can therefore approximately be calculated by assuming that the crusher gradients after the first pulse completely null the transverse magnetization before the second pulse is given. This gives the saturation profiles shown in figure 4.17, which are clearly more robust towards towards B_1 inhomogeneities than the case in figure 4.15A.

Note that this approximation is only valid for two saturation pulses. If more than two pulses are used, the spin profiles become somewhat more complex, and the approximation no longer gives an accurate description of the effective profile in the general case.

4.7 Discussion

We have in this chapter seen how the Bloch equations can be solved either through direct numerical integration or various numerical approximations to give the magnetization profiles induced by an applied RF pulse.

Three types of pulses, namely sinc pulses, adiabatic pulses and SLR pulses were presented, and the main properties of these pulses were illustrated through examples. Sinc pulses were used to demonstrate the concepts of bandwidth and pulse filtering. Adiabatic pulses were shown to be B_1 insensitive, while SLR pulses offered the possibility of actually designing RF pulses that give rise to magnetization profiles with specified characteristics.

Finally, examples were shown of inversion, excitation and saturation pulses, which are the types of pulses used in this thesis. As was seen in these examples the magnetization profiles may depend immensely on the choice of RF pulse. If anything, these examples demonstrate that there is always room for improvement of the magnetization profiles by designing better or more robust RF pulses. This is almost a separate branch of NMR/MRI where there is still lots of ongoing research[7], and it is beyond the scope of this thesis to work on actual development of new RF pulses.

However, magnetization profiles play a very important role in the main topic of the thesis, and it was therefore necessary to have a good understanding of the mechanisms of the RF pulse design and the principles of magnetization profile optimization.

The actual choice of RF pulses for a given sequence is not straightforward. It is not given that replacing an RF pulse with another that has sharper magnetization profiles will improve image quality. This replacement may for example introduce large sensitivity towards B_1 inhomogeneities which could degrade image quality. It is therefore important to judge the role of each RF pulse in a sequence and its interaction with other pulses in order to choose the optimal pulse.

Furthermore, the actual implementation of pulse sequences is largely based on modifying existing sequences which can save a lot of time. One disadvantage is that one tends to reuse the same RF pulses as in the original sequence, unless there is a large difference in the role of the pulses. Unfortunately, most of the pulses used in the original sequences on the scanner are not optimal and there is therefore need for improvement.

As we shall see in chapter 5, not all the ASL measurements in this thesis are performed with RF pulses providing good magnetization profiles. Although this may seem unfortunate, it has actually proven to be a major part of the thesis, i.e. how to improve the sensitivity of ASL even if the RF pulses provide poor magnetization profiles.

[7]For example, at the latest meeting of the International Society of Magnetic Resonance in Medicine, held in Glasgow in April, 2001, there were more than 20 abstracts about either the development of new RF pulses or their application to new branches of NMR/MRI.

Chapter 5

Slice Profile Effects

The effect of slice profiles on ASL perfusion measurements is discussed in this chapter. A new method is introduced for simulating the effect of multiple RF pulses. Along with the established method, this new method is used to calculate the degree of static tissue nulling in ASL experiments. The effects of various factors such as presaturation and the choice of RF pulses on the degree of static tissue subtraction are mapped as functions of the gap between the inversion and imaging regions. The implications of slice profile effects in ASL are discussed and exemplified through a comparison of different ASL sequences.

5.1 Methods

In chapter 4, we saw how the Bloch equations could be solved numerically in order to give the magnetization profiles resulting from a given RF pulse. The magnetization profiles, which were functions of frequency offset can directly be translated to a slice profile when a gradient is applied. The frequency dependence becomes a spatial dependence through the Larmor equation. If the gradient is applied in the z-direction, the relation becomes

$$f = \frac{1}{2\pi}\gamma\, G\, z. \tag{5.1}$$

In the calculation of most of the slice profiles illustrated in chapter 4, it was assumed that the magnetization before the application of the RF pulses was in the equilibrium state. When more than one pulse is applied in succession or the repetition time of the sequence isn't very long, this will not be the case. The magnetization profiles after each pulse will then depend on both the RF pulse and the profile before the application of the pulse.

In order to calculate the magnetization profiles at various times during a sequence, it is in general necessary to do a full simulation of the Bloch equations for all the RF pulses in the sequence. There is, however, a certain type of sequences, where a simpler approximation can be used with very good accuracy. This is described in the remainder of this section.

5.1.1 Full Bloch Simulation

In section 4.1, it was shown how the magnetization profiles due to a given RF pulse can be calculated. The initial magnetization before the pulse, $\mathbf{M}(0)$ in equation (4.23), was in almost all chapter 4 assumed to be $\mathbf{M}_0$. The equations that were deduced, however, do not depend on this, and $\mathbf{M}(0)$ can therefore assume any value.

Let the magnetization profile at the beginning of the sequence be $\mathbf{M}(0, \mathbf{r})$, where the spatial dependence is expressed explicitly through $\mathbf{r}$. If RF pulses are applied at $t = t_1$ and $t = t_2$, the magnetization will relax during the period from $t = 0$ to $t = t_1$ with the time constants T_1 and T_2. Any gradients will dephase or refocus the transverse magnetization by the factor $\exp\left(-i\gamma \int_0^{t_1} \mathbf{G}(t) \cdot \mathbf{r}\, \mathrm{d}t\right)$. The magnetization at $t = t_1$, $\mathbf{M}(t_1, \mathbf{r})$, will then play the role of $\mathbf{M}(0)$ in equation (4.23) and the magnetization after the RF pulse can be calculated as described in section 4.1. The magnetization then relaxes between t_1 and t_2 with dephasing/refocusing due to gradients and $\mathbf{M}(t_2, \mathbf{r})$ is then manipulated by the RF pulse at time t_2.

This method was used for calculating the profiles in figures 4.15 and 4.16 where two saturation pulses were applied in succession. The transverse magnetization produced by the first RF pulse interacted with the second pulse giving an entirely different final profile than that after just one pulse.

Depending on the length of the RF pulses compared to T_1 and T_2, relaxation effects can be included in the calculation of the effect of the RF pulses (equation (4.33)) or one can assume that the pulses are infinitely short and ignore relaxation during RF irradiation.

5.1.2 Slice Profile Functions

In some cases, an approximation can be used to calculate the magnetization profiles after multiple pulses. We introduce a new method that is computationally faster and much simpler than simulating the Bloch equations for each pulse. If the following conditions are satisfied, it yields as accurate results as the full Bloch simulation:

1. The delays between RF pulses in the sequence are large enough for the transverse magnetization created by one pulse to completely relax (not just dephase) before the following RF pulse.

2. The duration of the RF pulses is much shorter than T_1 so that T_1 relaxation during the RF irradiation can be ignored.

For a given RF pulse, let the function $g_z(z)$ be the profile of the longitudinal magnetization, M_z, calculated using the simulation of the Bloch equations where the initial magnetization is assumed to be in equilibrium. Similarly, let $g_x(z)$ and $g_y(z)$ be the profiles of M_x and M_y. The functions $g_x(z)$, $g_y(z)$ and $g_z(z)$, which will be referred to as *slice profile functions*, are unique for a given RF pulse and do not depend on the sequence in which the pulse is used, as we have previously shown [114–116]. Therefore they only need be computed once.

In a given sequence, where such an RF pulse is applied at time t_0, let the magnetization just before the pulse be purely longitudinal with the profile $M_z(t_0^-, z)$. The magnetization immediately after pulse is then given by

$$\begin{aligned} M_x(t_0^+, z) &= g_x(z) \cdot M_z(t_0^-, z) \,, \\ M_y(t_0^+, z) &= g_y(z) \cdot M_z(t_0^-, z) \,, \\ M_z(t_0^+, z) &= g_z(z) \cdot M_z(t_0^-, z) \,. \end{aligned} \tag{5.2}$$

If the RF pulse is an imaging pulse, $M_x(t_0^+, z)$ and $M_y(t_0^+, z)$ can be used to calculate the profiles of the magnetization that is actually measured, while only $M_z(t_0^+, z)$ need be used for further calculation of the effect of subsequent RF pulses.

5.1.3 Integration

Regardless of whether the magnetization profiles are simulated using full Bloch simulation or using the slice profile functions, the simulations are often used to predict and compare the role of various RF pulses on the measured signals in a sequence. The aim of this could for example be to find an RF pulse that maximizes the measured signal in the case of excitation, or minimizes the signal in the case of saturation.

The theoretical signal is obtained by integrating the transverse magnetization profiles after the imaging pulse over the slice direction. If quadrature detection is available, both M_x and M_y would be measured. Since most imagers produce magnitude images, the theoretical signals correspond to the amplitude of the integral of $M_x + iM_y$, or

$$M^{\text{signal}}(t) = \left| \int_{-\infty}^{\infty} \Big(M_x(t, z) + iM_y(t, z) \Big) \, \mathrm{d}z \right| . \tag{5.3}$$

The quantities $M_x(t, z)$ and $M_y(t, z)$ naturally depend on transverse relaxation and dephasing or refocusing due to gradients that are applied after the imaging RF pulse. It is of course also possible to do a full simulation of the imaging process knowing the imaging gradients and hence the k-space trajectories. This is, however, not necessary for the simulations presented in this thesis.

5.2 Implications for ASL

Slice profiles play a very important role in ASL. Since ASL is based on the subtraction of one image from another, it is crucial that the signal that is unrelated to perfusion be identical in the two images. ASL measurements on a phantom for example, should therefore give identical tag and control images since there is no perfusion.

Figure 5.1A sketches the slice profile problem for a FAIR sequence. The figure shows the inversion profiles generated by the slice selective (ss) and the non-selective (ns) inversion pulses along with the location of five imaging slices. The M_z^{ss} and M_z^{ns} profiles are identical at the central part of the ss inversion profile, but differ significantly at the edge of the ss inversion profile due to the non-ideal shape of the inversion profile. The magnetization being imaged in the outer slices will therefore be slightly different in the ss and ns cases unrelated to perfusion. Figure 5.1B sketches the problem for a PICORE sequence, where the problem exists for the slice(s) that is closest to the inversion slab [29, 46].

The non-ideal shape of the inversion profile is affected further by relaxation during the inversion pulse. Figure 5.2 shows the inversion profile of a 15 ms HS inversion pulse with $\mu = 10$, $\beta = 800$ Hz (see section 4.4) with and without relaxation effects. The case of $T_1 = \infty$, $T_2 = \infty$ is the ideal case without relaxation. The other case has T_1 and T_2 values that are artificially short (approximately half the physiological values) to better illustrate the effect.

The transverse relaxation rounds the corners of the inversion profile on both sides of the transition bands, while longitudinal relaxation gives an asymmetric inversion band due to the inversion of one side of the inversion band before the other. Furthermore, both transverse and longitudinal relaxation decrease

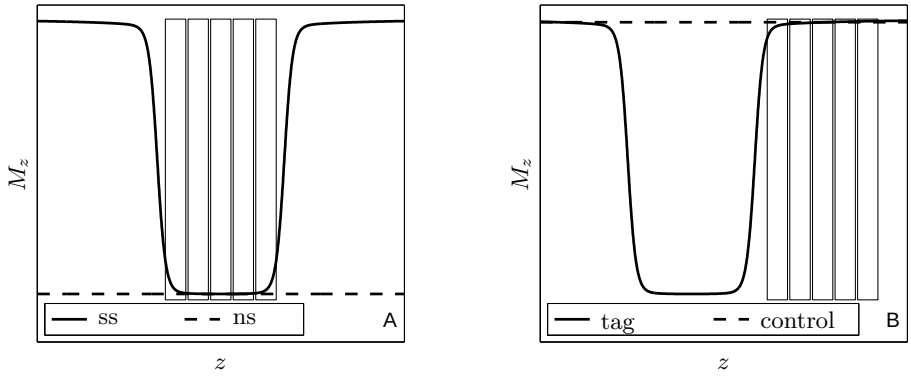

Figure 5.1: (A) Sketch of the slice profile problem for a FAIR sequence. Curves are the inversion profiles, M_z, for the slice selective (ss) and the non-selective (ns) inversion pulses, while the boxes indicate the imaging slice positions in a five-slice measurement. (B) The corresponding sketch for a PICORE sequence. Curves are tag and control inversion profiles.

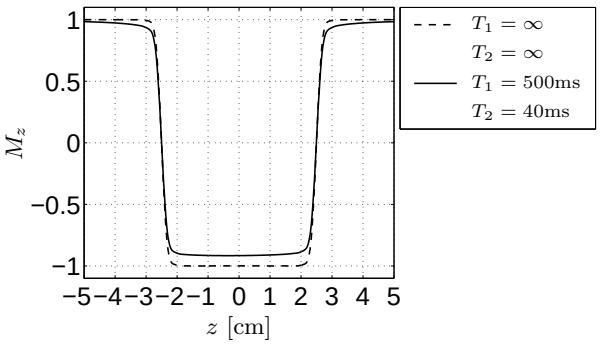

Figure 5.2: Effect of relaxation on the inversion profile of a 15 ms HS inversion pulse with $\mu = 10$, $\beta = 800$ Hz and an inversion band of 5 cm.

the size of the magnetization in the pass band of the profile [46]. Longitudinal relaxation will therefore not affect a PICORE or EPISTAR measurement, but may give slice to slice variations in the intensity in a ss FAIR measurement. Transverse relaxation, on the other hand will affect mainly the outer slices in FAIR and EPISTAR, and mainly the proximal slices in PICORE.

Although adiabatic pulses are generally used for inversion in ASL, a lot of effort has gone into improving the inversion profile of the inversion pulses in order to reduce the effect of imperfect slice profiles. Reducing the length of the RF pulse, for example, reduces relaxation effects in general and thus gives sharper profiles, while reducing the RF power gives less T_2 relaxation since the magnetization spends less time in the transverse plane [46]. Another approach is to use modified adiabatic pulses such as FOCI pulses [47, 105, 117, 118] or VERSE pulses [119] that produce highly improved inversion profiles compared to HS pulses. A third approach is based on using adiabatic excitation and refocusing pulses to achieve good excitation profiles [120].

However, even when the inversion pulse is optimized as much as possible, the inversion profile is still not ideal. And since the inversion slabs used in PICORE or multislice FAIR are quite large, a difference in the tag and control magnetizations that is unrelated to perfusion may arise in at least one of the slices, which would give erroneous results for the measured perfusion [116, 121, 122]. This magnetization difference, which is due to incomplete static tissue subtraction is referred to as an *offset* in the remainder of this thesis [115, 116, 121, 123, 124].

The common approach to solve this problem is to introduce a gap between the edge of the inversion slab and the edge of the imaging region [34–36, 38, 42, 48, 54, 62, 65, 66, 74, 125–128]. The minimum required gap depends on the slice profiles of both the inversion pulse and the imaging pulse [116]. A gap of approximately 10–15 mm is not uncommon for HS pulses, although with optimization of the slice profiles, smaller gaps can be used without subtraction errors.

Introducing a gap between the edge of the inversion slab and the imaging region has an unfortunate consequence, though. The tagged blood moves with a finite velocity, and there is therefore a delay, δt, before the leading edge of the tagged blood reaches the imaging region. This delay is called the transit

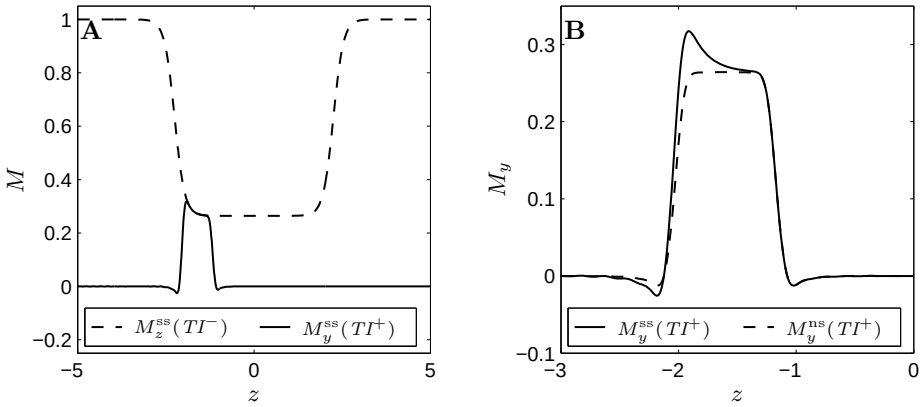

Figure 5.3: Origin of offset in a FAIR measurement. (A) The longitudinal magnetization profile in the slice selective experiment immediately before the imaging pulse, $M_z^{ss}(TI^-)$ and the transverse magnetization profile immediately after the imaging pulse, $M_y^{ss}(TI^+)$. (B) Comparison of $M_y(TI^+)$ profiles for slice selective and non-selective experiments.

delay [29, 48, 62]. The transit delay reduces the amount of tagged blood that reaches the tissue within a specified inversion time, which in turn affects perfusion quantification. Since the transit delay increases with the gap, it is desirable to minimize the gap thus minimizing the transit delay effects.

However, when the gap becomes narrower than that required for complete static tissue nulling, the offset described above will affect perfusion quantification. If one can estimate the gap that minimizes the transit delays without introducing subtraction errors, it would be possible to overcome the effects of both the offset and the transit delays. This is the motivation for studying the offset.

The following section inspects in detail the origin of the signal offset and its dependence on different sequence parameters.

5.3 Magnetization Offset

5.3.1 Offset Origin

FAIR

Figure 5.3A shows the magnetization profile in a slice selective FAIR experiment immediately before the imaging pulse, namely $M_z^{ss}(TI^-)$, where $TI = T_1 = 1$ s. This magnetization is then flipped into the transverse plane by the narrower imaging pulse to give $M_y^{ss}(TI^+)$ which is the transverse magnetization that is actually measured. In this case, there is no gap between the edge of the inversion slab and the edge of the imaging region. Only the magnetization profile of one imaging slice is shown corresponding to the outer slice in figure 5.1A.

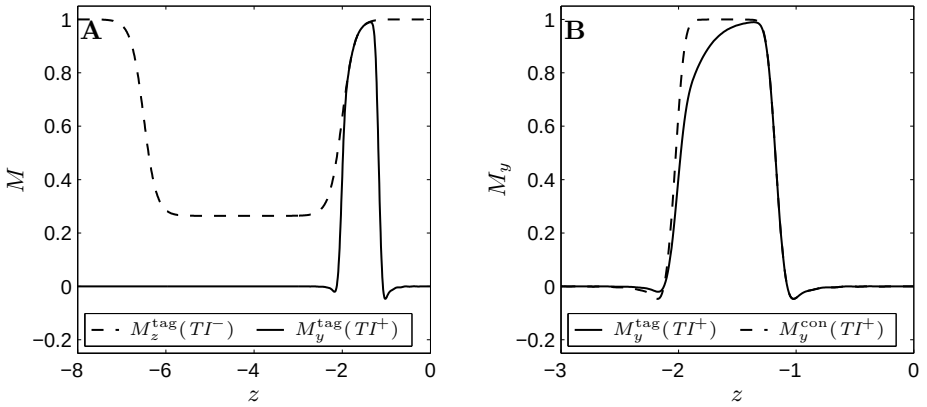

Figure 5.4: Origin of offset in a PICORE measurement. (A) The longitudinal magnetization profile in the tag experiment immediately before the imaging pulse, $M_z^{\text{tag}}(TI^-)$ and the transverse magnetization profile immediately after the imaging pulse, $M_y^{\text{tag}}(TI^+)$. (B) Comparison of $M_y(TI^+)$ profiles for tag and control experiments.

Figure 5.3B compares the M_y profiles immediately after the imaging pulse in the ss and the ns experiments. It is clear that there is a difference that originates from the slice profiles of the inversion and imaging pulses. The measured signals are the integrals of the profiles in figure 5.3B and are therefore not equal. This difference in static tissue signal, which is unrelated to perfusion, is an *offset* in the magnetization difference since it is added to the magnetization difference that is due to perfusion.

The offset in FAIR imaging is symmetric about the center of the imaging region, since the ss inversion slab and the imaging region have the same center. This means that the proximal and distal slices (in the case of axial slices) have in principle equal offsets. This will only apply in principle though, since there will inevitably be a difference in inversion times between different slices and hence the signal intensities.

PICORE

Figure 5.4 shows magnetization curves corresponding to those in figure 5.3, but for a PICORE measurement. Here, the imaging pulse is affected by the outer part of the edge of the inversion pulse. The difference in magnetization profiles between the tag and control experiments, shown in figure 5.4B, gives rise to different measured signals unrelated to perfusion.

The offset in PICORE imaging is largest in the proximal side of the imaging slab (for axial imaging), and decreases with distance from the edge of the imaging slab.

The mechanism of the offset is the same for EPISTAR as for PICORE. The only difference is that, in principle, the offset is symmetric about the center of

the imaging region as with FAIR imaging.

5.3.2 Offset Equations

As mentioned above, the measured signal is the integral of the transverse magnetization profiles given by equation (5.3). The transverse magnetization produced by the imaging pulse is usually refocused along the y-axis, with only a very small portion remaining along the x-axis. Furthermore, M_x is usually asymmetric and therefore integrates to zero. Without loss of generality, we can therefore drop the M_x term from equation (5.3). For a simple FAIR sequence without presaturation or QUIPSS saturation using the notation of slice profile functions gives the following expression for the measured signal in the ss experiment

$$M^{\mathrm{ss}}(TI) = \int_{-\infty}^{\infty} M_y^{\mathrm{ss}}(TI^+, z)\,\mathrm{d}z \tag{5.4}$$

$$= \int_{-\infty}^{\infty} M_0 \left[\left(g_z^{\mathrm{ss}}(z) - 1\right) \mathrm{e}^{-R_1 TI} + 1\right] \cdot g_y^{90}(z)\,\mathrm{d}z, \tag{5.5}$$

where g^{ss} and g^{90} are the slice profile functions of the ss inversion pulse and the imaging pulse respectively (see section 5.1.2). Similarly, the measured ns signal becomes

$$M^{\mathrm{ns}}(TI) = \int_{-\infty}^{\infty} M_y^{\mathrm{ns}}(TI^+, z)\,\mathrm{d}z \tag{5.6}$$

$$= \int_{-\infty}^{\infty} M_0 \left[\left(g_z^{\mathrm{ns}}(z) - 1\right) \mathrm{e}^{-R_1 TI} + 1\right] \cdot g_y^{90}(z)\,\mathrm{d}z, \tag{5.7}$$

where $g^{\mathrm{ns}}(z)$ is the slice profile function of the ns inversion pulse. The offset, which is the magnetization difference in the absence of perfusion becomes

$$\begin{aligned} M^{\mathrm{off}}(TI) &= M^{\mathrm{ss}}(TI) - M^{\mathrm{ns}}(TI) \\ &= \int_{-\infty}^{\infty} M_0 \left[g_z^{\mathrm{ss}}(z) - g_z^{\mathrm{ns}}(z)\right] \mathrm{e}^{-R_1 TI} \cdot g_y^{90}(z)\,\mathrm{d}z \end{aligned} \tag{5.8}$$

Figure 5.5 shows the dependence of the offset at $TI = 0$ as a function of the thickness of the ss inversion slab for three different imaging pulses: a Hamming filtered 3-lobe sinc ($T = 2560\,\mu$s, BW = 1 kHz), a Hamming filtered 5-lobe sinc ($T = 5120\,\mu$s, BW = 4 kHz) and an optimized SLR pulse ($T = 5120\,\mu$s, BW = 2 kHz, 0.01% pass band ripple, 0.4% reject band ripple). The inversion pulse in all three cases was an adiabatic HS pulse ($\mu = 5$, $\beta = 675$ Hz, $T = 10240\,\mu$s). The figure shows the simulated offset using equation (5.8) for a single slice experiment with slice thickness 10 mm. Also shown is the offset[1] found experimentally for the 3-lobe sinc imaging pulse (the imaging parameters

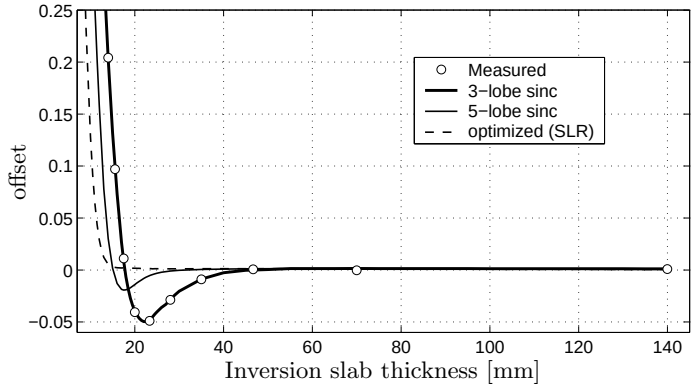

Figure 5.5: The theoretical offset (curves) calculated using equation (5.8) for three excitation pulses: a 3-lobe sinc (used experimentally), a 5-lobe sinc and an optimized SLR pulse. An adiabatic HS pulse was used for inversion in all three cases. The imaging slice had a constant thickness of 10 mm. Also shown is the offset, $M^{\text{off}}(0)$, found experimentally in phantom measurements (points), relative to M_0, as a function of the slice thickness of the inversion slab (FWHM).

are described in section 6.3). There is clearly excellent agreement between the simulations and the experimental data.

As the figure indicates, there is a large difference in both the shape and amplitude of the offset as a function of the inversion slab thickness. There is a range of inversion slab thicknesses that results in a negative offset for both sinc pulses, while the offset is always positive for the SLR pulse. This is due to the negative side lobes of the M_y profile of the sinc pulses. The side lobes of the SLR pulse are much smaller and do not cause a negative offset. As argued previously, the offset vanishes when the inversion slab is much wider than the imaging region. This applies to all imaging pulses.

Keeping in mind that the magnetization difference due to perfusion is on the order of 1% of M_0, the minimum slab thickness required to have a negligible offset ($\ll$1%) in the three examples in figure 5.5 varies from about 20 mm to 45 mm corresponding to gaps of 5 to 18 mm between the edges of the inversion and imaging slabs. Taking into consideration that the minimum gap and slab thickness scale with the thickness of the imaging region, this could give very large gaps for multislice imaging that in turn would give very large transit delays. This shows the importance of choosing RF pulses with good slice profiles for ASL measurements.

The offset equations for PICORE can be deduced in the same manner as

[1]The measurements were not done at $TI = 0$, but are estimated from T_1 measurements as described in section 6.1.1.

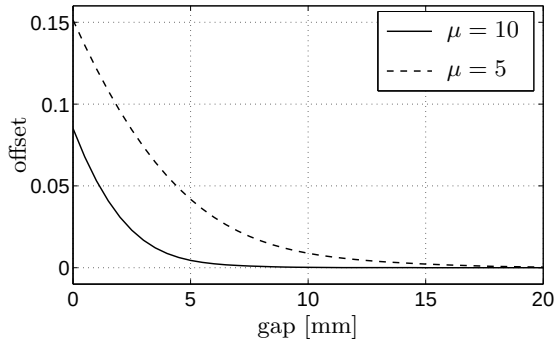

Figure 5.6: The theoretical offset relative to M_0 in a PICORE sequence as a function of the gap between the inversion slab and the closest imaging slice. Examples of two HS inversion pulses are shown. In both cases, $\beta = 800$ Hz, $T = 15$ ms. The imaging pulse is a 3.2 ms Hamming filtered 7-lobe sinc pulse with 8 mm slice thickness.

done above for FAIR. The offset at $t = TI$ becomes

$$\begin{aligned} M^{\text{off}}(TI) &= M^{\text{con}}(TI) - M^{\text{tag}}(TI) \\ &= \int_{-\infty}^{\infty} M_0 \left[g_z^{\text{con}}(z) - g_z^{\text{tag}}(z) \right] \mathrm{e}^{-R_1 TI} \cdot g_y^{90}(z)\, \mathrm{d}z\,, \end{aligned} \tag{5.9}$$

where M^{con} and M^{tag} are the measured control and tag magnetizations, and $g^{\text{con}}(z)$ and $g^{\text{tag}}(z)$ are slice profile functions of the control and tag inversion pulses respectively. Figure 5.6 shows the theoretical offset in a PICORE sequence as a function of the gap between the inversion slab and the closest imaging slice. The offset in the most proximal slice is plotted for two adiabatic HS pulses with markedly different performance. The minimum gap required for the pulse with $\mu = 10$ is approximately 10 mm, while that for the pulse with $\mu = 5$ is 20 mm.

5.3.3 Presaturation

Presaturation plays an important and sometimes surprising role in determining the offset in an ASL experiment. The effect of presaturation is furthermore dependent on the type of ASL sequence used as will be demonstrated in this section.

Presaturation is usually applied in a slab covering all imaging slices. The slab is normally extended to halfway between the edges of the imaging region and the inversion slab, i.e. halfway in the gap.

For PICORE, one would intuitively expect that presaturation decreases the offset since it decreases the static tissue signals in both the tag and control images. This is, however, only true to a certain degree.

Since presaturation usually is applied immediately before the tag and control inversion pulses, the transverse magnetization created by the presaturation (psat) pulse cannot be ignored when calculating the effect of the inversion pulses. Furthermore, presaturation is often achieved using multiple psat pulses to improve the saturation profiles (see section 4.6.3). The slice profile functions can therefore not be used directly in the offset equations, but full Bloch simulations

should be used. Alternatively, one can regard the psat pulse(s), crusher gradient and inversion pulse as one long complex pulse with a single slice profile function. In the latter case, equations (5.8) and (5.9) can still be used.

Figure 5.7A shows the theoretical signals, M^{con} and M^{tag} calculated using full simulation of the Bloch equations for a PICORE sequence with $TI = 1$ s, five 8 mm slices, $TR = \infty$, $T_1 = 1$ s. Inversion is achieved with a 15 ms adiabatic HS pulse with $\mu = 10$ and $\beta = 800$ Hz, while the psat pulses are 12.8 ms Hamming filtered sinc pulses. Imaging is done with a 3.2 s Hamming filtered sinc pulse. The figure shows the signal when 0–3 psat pulses are applied immediately before the inversion pulse. The psat pulses are separated by a crusher gradient with an area equal to 6.6 times that of the slice selection gradient. The choice of these parameters is based on the actual implementation of PICORE at UCSD (see appendix A).

It is clear that the signal with one psat pulse ($npsat = 1$) is markedly lower than that with $npsat = 0$ as would be expected. Increasing $npsat$ to 2 decreases the signal further, but introduces oscillation in M^{tag}. When $npsat = 3$, the signal increases again and the oscillations in M^{tag} are amplified. The oscillation in M^{tag} is due to the transverse magnetization being flipped into the z-direction by the second and third psat pulses as shown in figure 4.16. This magnetization then interacts with the edge of the inversion pulse to give the illustrated result.

Figure 5.7B shows the offset, $M^{\text{con}} - M^{\text{tag}}$, as a function of the gap, and is largely dependent on the number of psat pulses, $npsat$. The offset is clearly smallest when $npsat = 1$. Figure 5.8 shows the result of swapping the order of the inversion and psat pulses, so that the inversion pulse precedes the psat pulse(s). All other parameters are kept the same as above. Comparing the offset with that in figure 5.7B, the order of the pulses apparently influences the offset

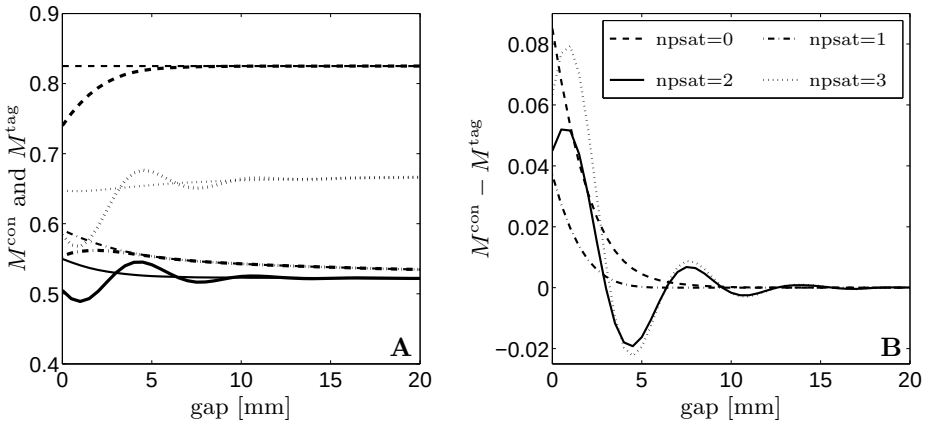

Figure 5.7: Effect of the number of presaturation pulses on the offset in a PICORE experiment. (A) Simulated M^{con} (thin curves) and M^{tag} (thick curves) as a function of the gap between the imaging slab and the tagging slab. Only the signal in the most proximal slice is shown. (B) The offset, $M^{\text{con}} - M^{\text{tag}}$.

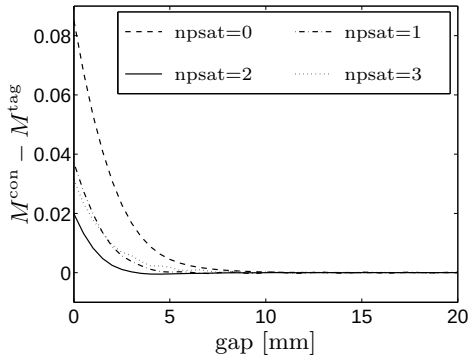

Figure 5.8: The effect of swapping the order of the inversion pulse and the psat pulses on the offset, $M^{con} - M^{tag}$ in a PICORE experiment. Offset as a function of the gap when the inversion pulse precedes the psat pulses.

when more than one psat pulse is applied. When the inversion pulse precedes the psat pulses, there are no oscillations in the offset curve and the minimum offset is achieved with $npsat = 2$.

The optimal choice of the number of psat pulses in a PICORE sequence therefore depends both on the gap used and the order in which the inversion and psat pulses are applied. If a large gap is used, so that there is no offset, two pulses give the best static signal suppression. However, if a small gap is used so that a significant offset will be present and presaturation precedes inversion, using one psat pulse will minimize that offset. The exact limiting gap separating the "small" gap region from the "large" gap region (decision boundary) depends on the specific RF pulses used, the width of the tagging slab and the imaging region and the area of the crusher gradients. Further simulations showed, however, that the strongest factor is the shape of the inversion slice profile (data not shown).

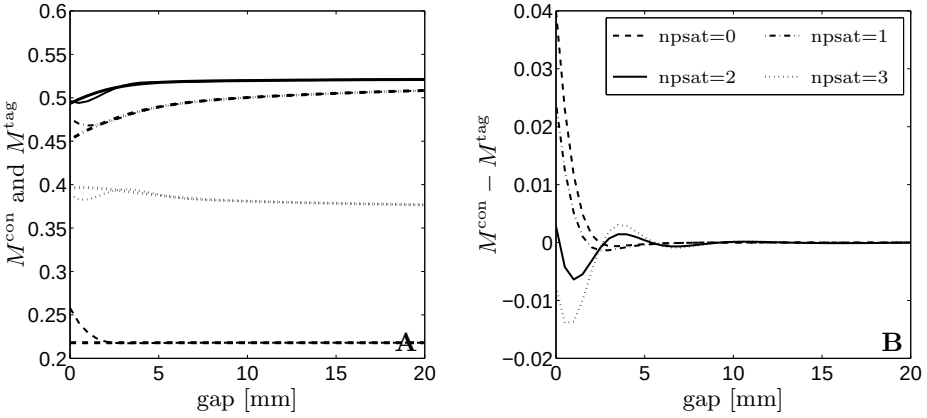

Figure 5.9: Effect of the number of presaturation pulses on the offset in a FAIR experiment. (A) Simulated M^{con} (thin curves) and M^{tag} (thick curves) as a function of the gap between the imaging slab and the tagging slab. Only the signal in the most proximal slice is shown. (B) The offset, $M^{con} - M^{tag}$.

In FAIR imaging, the in-slice magnetization is inverted in both the tag or ns and control or ss experiments. Normally, the inversion time is about 1 s, which is long enough for the magnetization to become positive before the imaging pulse (at least for grey matter and white matter). The static tissue magnetization will therefore have a larger value if presaturation is applied than if it is omitted.

Figure 5.9A shows the tag (ns) and control (ss) magnetizations in a simulation of a FAIR experiment with $npsat = 0$–3, as a function of the gap between the edge of the ss inversion slab and the imaging region. The pulse parameters are the same as those used above for the PICORE sequences with presaturation applied before inversion. Again, only the most proximal slice is shown. As expected, the signal values are clearly higher when presaturation is applied. It is interesting to note, though, that the signal with 3 psat pulses is actually lower than that with 2 psat pulses. This is due to the limited efficiency of presaturation when $npsat > 2$ (same as in figure 5.7A).

Figure 5.9B shows the offset as a function of the gap. The offset decreases slightly when going from $npsat = 0$ to $npsat = 1$, but changes form completely for $npsat \geq 2$. This is due to the effects of the transverse magnetization being flipped along the z-axis and then back into the xy-plane again.

As with the PICORE sequence, the order of presaturation and inversion has a significant effect on the offset. Figure 5.10A shows the effect of applying inversion before presaturation on the offset. All other parameters are as in figure 5.9B. The figure shows that the offset changes form for $npsat \geq 3$ instead of $npsat \geq 2$ as was the case in figure 5.9B.

It was mentioned above, that the offset curve in PICORE imaging was sensitive to the shape of the inversion profile. This is even more so for FAIR as illustrated in figures 5.10B&C. The figures show the offset curves corresponding to those in figure 5.9B and 5.10A respectively when the B_1 amplitude of the HS inversion pulse is reduced from 0.2936 G to 0.1468 G, but with the same pulse shape and duration. This corresponds to decreasing the degree of inversion from 0.99998 to 0.982.

The RF power reduction has no significant effect on the offset for $npsat \leq 1$ when presaturation precedes inversion, but things change drastically for $npsat \geq 2$, where the offset is large even for a gap of 20 mm. This is due to the specific shape of the oscillations in $M(z)$ and is not limited to the outer slice, but is present in all slices. The exact shape may, however, differ from slice to slice.
When inversion precedes presaturation, the offset again dramatically changes shape as seen in figure 5.10C. Here the largest offset is found with $npsat = 1$ and 3.

5.3.4 QUIPSS Saturation

One might expect that the QUIPSS saturation (qsat) pulses have as large an effect on the signal offset as the psat pulses do. However, this is not the case since the qsat pulses are not followed by an inversion pulse, and generally the time between the inversion and qsat pulses, TI_1, is long compared to T_2, so that

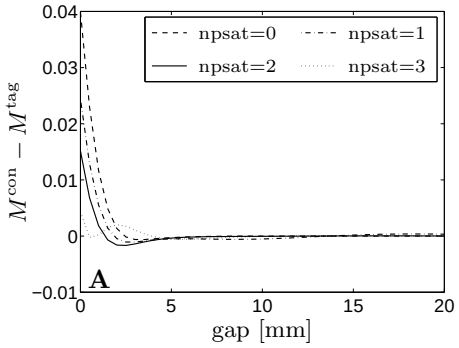

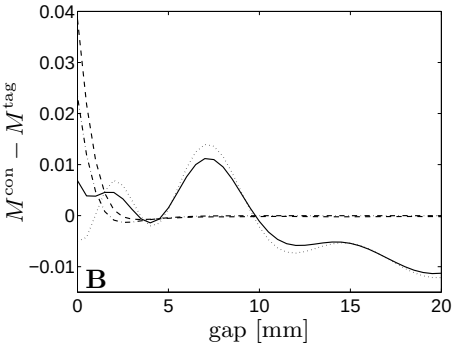

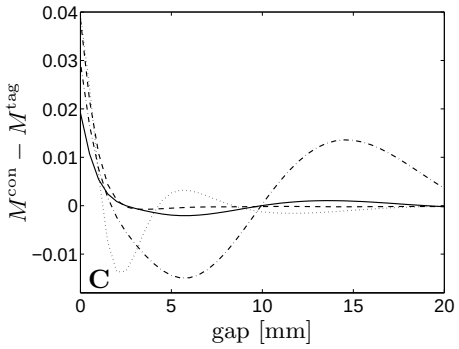

Figure 5.10: (A) The offset, $M^{\text{con}} - M^{\text{tag}}$, in a FAIR experiment as a function of the gap when the inversion pulse precedes the psat pulses. Compare with figure 5.9B. (B) and (C) Effect of using insufficient B_1 giving incomplete inversion. (B) Presaturation precedes inversion and (C) inversion precedes presaturation.

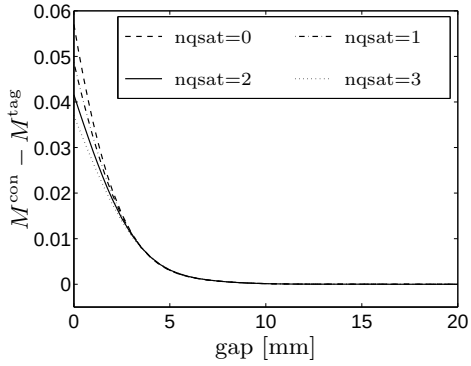

Figure 5.11: The effect of varying the number of qsat pulses on the offset in a PICORE QUIPSS II experiment without presaturation.

no remaining transverse magnetization is present when the qsat pulse(s) are applied. Furthermore, the qsat pulses are applied outside the imaging region, and it is therefore only the outer edge of the pulse that may affect the imaged magnetization when the gap is small. Even then, the effect on the offset is limited since the qsat pulses are identical in the tag and control images.

Figure 5.11 shows the simulated offset as a function of the gap for a PICORE QUIPSS II sequence with different numbers of qsat pulses (*nqsat*) and no presaturation. The qsat pulses are 12.8 ms Hamming filtered sinc pulses. The sequence parameters are equal to those used in figure 5.7 except that

$TI_1/TI_2 = 700/1400$ ms. It is clear that *nqsat* only affects the offset to a small degree compared to *npsat* and has no significant effect on the offset for gaps larger than 3 mm.

5.3.5 Relaxation Effects

In the previous simulations, it was assumed that there was no relaxation during RF irradiation although T_1 was set to 1 s for relaxation between RF pulses. However, longitudinal and transverse relaxation during RF irradiation affect the slice profiles of RF pulses as illustrated in figure 5.2. Since the magnetization offset is strongly dependent on the slice profiles, it is bound to be affected by relaxation. As mentioned earlier, longitudinal relaxation mainly affects the pass band of the inversion band for HS inversion pulses while transverse relaxation rounds the edges of the profile.

The offset in PICORE measurements is therefore not expected to be sensitive to changes in T_1, but only to changes in T_2, and the strongest dependence on T_2 would be for the most proximal slice with small gaps. In FAIR imaging, the sensitivity would also depend on the slice position. For the central slices, it would be expected that the offset is sensitive to T_1 while for the outer slices, the offset would be most sensitive towards changes in T_2. However, the offset in the outer slices becomes sensitive to T_1 when the gap becomes large, since no slices will interact with the edge of the inversion profile.

These expectations are confirmed by simulations as illustrated in figure 5.12. The offset in the PICORE sequence was not affected significantly by changes in T_1 (not shown), but was affected by T_2 for small gaps. In the FAIR sequence, the simulations showed that the offset in the outer slice was only sensitive to T_1 for large gaps, but sensitive to both T_1 and T_2 for small gaps. In the latter case, the dependence on T_2 was stronger than T_1.

5.4 Discussion

We have in this chapter seen how the effects of slice profiles in multiple-pulse sequences can be calculated using either full simulation of the Bloch equations or the numerically simpler slice profile functions. Such calculations are a powerful tool in assessing the implications of the slice profiles on the measured signals in ASL sequences.

It was demonstrated that the gap between the edge of the tagging and imaging regions has a profound effect on the degree of static tissue nulling in ASL difference images. A finite gap can compensate for imperfections in the slice profiles of RF pulses used. This, however, results in a transit delay of the incoming blood. If the gap is too small, incomplete static tissue subtraction gives an offset or bias in the difference signal. The behaviour of this offset as a function of the gap depends on the type of ASL sequence used, the specific RF pulses, the

number of presaturation and/or QUIPSS saturation pulses that are applied, the order of presaturation and inversion and the area of crusher gradients. Furthermore, the slice profiles of the RF pulses used also depend on the width of the tagging, presaturation, QUIPSS saturation and imaging regions as well as the number of slices, slice thickness and the tissue relaxation rates.

Due to this large number of factors affecting the offset behaviour, it is not realistic to seek a global optimum minimizing the offset for a given gap. Instead, the aim has been to understand the mechanisms affecting the offset and to provide a set of tools for predicting the offset for a given set of parameters.

It was found that the offset can be either positive or negative and sometimes exhibits oscillatory behaviour. One common feature that was found for ASL sequences without presaturation, was that the offset becomes positive at very small gaps. Negative lobes as in figure 5.5 were found to be caused by the side lobes of the imaging pulse, while oscillatory behaviour as in figure 5.7B was found to originate from the transverse magnetization created when using multiple psat pulses.

One major difference between the offset in FAIR and PICORE sequences is the role of the inversion pulse. In FAIR, the central flat part of the inversion profile is what interacts with the imaging pulses. The edge of the inversion profile may also affect the offset in the outer slices if the gap is small. However, in PICORE, it is only the edge of the inversion profile that affects the offset, and

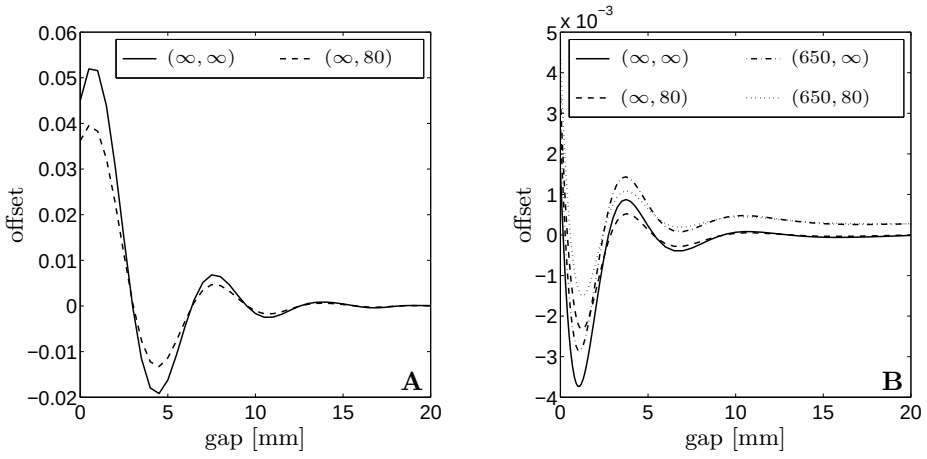

Figure 5.12: Effect of relaxation during RF irradiation on the offset. The legends show (T_1, T_2) [ms] used during RF irradiation. (A) Offset in the proximal slice of a PICORE sequence with $npsat = 2$. $T_1 = 1$ s (GM) is assumed for relaxation between RF pulses. Using physiological value of T_2 reduces the offset oscillation amplitude. (B) Offset in the outer slice of a FAIR sequence with $npsat = 2$. $T_1 = 650$ ms (WM) is assumed for relaxation between RF pulses. The offset is affected by changes in both T_1 and T_2.

the offset must therefore vanish for large gaps. The type of behaviour found in figure 5.10B for FAIR does therefore not occur for PICORE.

The behaviour of the offset found for a given setup is in general not invariant to scaling. Without presaturation, however, there are a few exceptions. Multiplying the slice thickness and ss inversion slab thickness in a FAIR experiment by the same factor does not affect the offset behaviour. Similarly, multiplying the slice thickness, gap and inversion slab thickness by the same factor in a PICORE experiment will also not affect the offset. Although a presaturation pulse could be scaled in the same manner, the crusher gradient would have to be scaled inversely to the width of the presaturation slab for the offset to remain constant.

The order in which presaturation and inversion are applied was shown to have a surprisingly large effect on the offset behaviour. The oscillations found in PICORE with $npsat \geq 2$ when presaturation preceded inversion vanished when the opposite order was used. For FAIR, the oscillatory behaviour stopped for $npsat = 2$ and was reduced for $npsat = 3$. However, when B_1 was reduced in the FAIR experiment, switching the order of presaturation and inversion changed the offset behaviour in an entirely different manner. This illustrates why it is necessary to perform the simulations with exactly the set of parameters that is to be used experimentally.

The effect of lowering the RF amplitude, illustrated in figure 5.10B&C shows that the offset behaviour is strongly dependent on the degree of inversion of the inversion pulse. Due to B_1 inhomogeneities, the RF amplitude is bound to be lower than the nominal value in some parts of the image. Although adiabatic pulses are insensitive towards B_1 inhomogeneities as long as B_1 is above a certain threshold (see section 4.4), low B_1 can still be a problem. The RF amplitude is commonly chosen just above the threshold needed for inversion in order to reduce SAR effects. In most types of sequences, this is not a problem since the degree of inversion will be quite high throughout the image. For the pulse used in figures 5.9 and 5.10, reducing B_1 by 50% only reduces the degree of inversion from 0.99998 to 0.982. The latter is still a very high degree of inversion and is quite adequate for labelling blood, but gives a huge effect on the interaction of the presaturation and inversion pulses resulting in a very large offset. This implies two things. Firstly, the offset is bound to vary throughout the image due to B_1 inhomogeneities. Figure 5.13 shows the difference image in a phantom measured with a FAIR sequence and is therefore a direct image of the offset. The signal varies both in amplitude and sign where the slow variations in the signal across the phantom are likely to be due to B_1 inhomogeneities. Secondly, B_1 inhomogeneities can easily result in discrepancies between simulations and measurements simply because the experimental conditions are slightly different from what is expected. It is therefore not always possible to get a perfect match between the measured offset and the simulations. The simulations do, however, still give a very good picture of the mechanisms that affect the offset and pro-

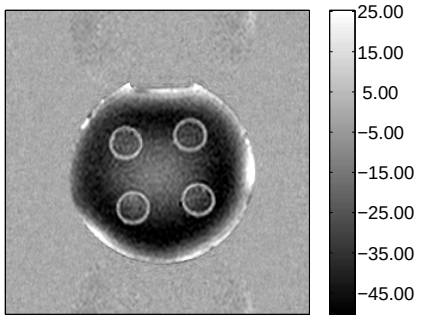

Figure 5.13: Difference signal (offset) in a phantom. The slow variations in the signal across the phantom are likely to be due to B_1 inhomogeneities.

vide a set of tools for predicting at least the qualitative and often quantitative behaviour of the offset.

As seen in section 5.3.5, the effect of tissue T_1 and T_2 during RF irradiation on the slice profiles is propagated to the offset. Furthermore, the offset is also affected by the tissue T_1 due to relaxation between the RF pulses. The $npsat = 2$ curve in figure 5.9B assumes $T_1 = 1000$ ms between RF pulses corresponding to GM, while the (∞, ∞) curve in figure 5.12 assumes $T_1 = 650$ ms between RF pulses corresponding to WM. Both curves disregard relaxation during RF irradiation and all other parameters are identical. While the two offset curves have the same shape, the short T_1 curve is damped by approximately 40% compared to the high T_1 curve.

It is very interesting to note that increased relaxation, whether during or in between RF pulses, decreases the amplitude of the offset. This is not surprising, since the more the magnetization relaxes towards equilibrium, the smaller the difference between the tag and control experiments there is. The offset in WM can therefore generally be expected to be less than that in GM.

It was shown that the effect of QUIPSS saturation on the offset is much smaller than that of presaturation. However, given the fact that qsat pulses are given in a fairly large slab (about 10 cm), their saturation profiles are not very sharp. Furthermore the pulses are more susceptible towards B_1 inhomogeneities than narrow pulses. Luh et al. proposed a method to overcome this effect. The method is named Q2TIPS (QUIPSS II with thin-slice TI_1 periodic saturation) and is based on using a train of narrow saturation pulses instead of one wide qsat pulse [129]. The narrow saturation pulses have much sharper profiles and thus give better saturation of the spins which in turn gives more accurate perfusion estimates.

Transit Delays

The focus of this chapter has been on determining the offset as a function of the gap between the imaging and tagging regions. The aim of this was to find

the minimum gap that does not give any significant offset so as to minimize the transit delay of incoming blood. However, the transit delay does not only depend on the gap, but also depends on vessel size and geometry and on slice orientation. Wong et al. found that the transit delay across a 10 mm gap may vary from 400 ms to over 1200 ms [48] depending on position. The transit delay in the occipital lobe for example was found to be much larger than in the parietal lobes even though perfusion values were comparable [29]. They also found that the transit delay increases by approximately 150 ms for each additional gap of 10 mm.

It is therefore impossible to predict the exact reduction in transit delay that results from a reduction of the gap. However, it is reasonable to assume, that as blood approaches the tissue that it is perfusing, the blood vessels become narrower albeit more plentiful resulting in a decreased flow velocity. Reducing the gap from 10 to 5 mm should therefore give a larger reduction in the transit delay than reducing the gap from 20 to 15 mm. Results in chapter 6 support this hypothesis since it is found that the reduction of the gap from 10 to 5 mm in a PICORE QUIPSS II sequence reduces the transit delay in GM by 300 ms. This reduction is clearly higher than that mentioned above, found by Wong et al. for gaps larger than 10 mm.

Chapter 6

Offset Correction in ASL

In the previous chapter, it was shown how the gap between the edges of the inversion and imaging regions in ASL affects the static tissue subtraction. It was found that small gaps may lead to incomplete subtraction giving an offset in the magnetization difference images. In this chapter, a new method is introduced by which the actual offset can be determined experimentally. Once it has been determined, the offset can be subtracted from the magnetization difference, enabling correct quantification of perfusion despite incomplete static tissue subtraction. This enables the use of small gaps, which reduces the transit delays of incoming blood, and actually improves the quantification of perfusion in some cases.

The principle of offset correction is based on modelling the measured signals in an ASL sequence as functions of the inversion time. If ASL images are acquired at different inversion times, this model can be fit to the images leading to an estimate of the offset along with the other model parameters.

The model has basically the same structure for different ASL sequences, but depends on the number of groups of RF pulses in the sequence. Here, a group of RF pulses refers to successive RF pulses with an overall duration that is short compared to T_1. The pulses may be separated by crusher gradients. The presaturation and inversion pulses in a PICORE sequence, for example, would comprise one such group.

Standard ASL sequences such as FAIR and PICORE, with or without presaturation consist of two groups of RF pulses: (presaturation)/inversion and imaging. QUIPSS saturation pulses comprise a third group and hence need separate consideration. In the following, the models describing the dependence of the measured signals on the inversion time will be presented for both standard

ASL sequences and QUIPSS sequences.

6.1 Standard ASL Sequences

First we look at ASL sequences without QUIPSS saturation. Although the models that will be deduced for FAIR and PICORE are very similar, they will be considered individually.

Two measurements will be considered in the following. One will be referred to as the ASL measurement, while the other will be referred to as the T_1 measurement. The ASL measurement is the normal measurement using an ASL sequence with a single inversion time and multiple acquisitions for averaging. The T_1 measurement uses the same sequence as the ASL measurement, but with multiple inversion times and fewer acquisitions.

6.1.1 FAIR

Offset Estimation

The measured signals in a FAIR sequence are given by the integral of the transverse magnetization over the slice direction immediately after the imaging pulse as expressed by equations (5.4)–(5.7). Multiplying out equation (5.5) for the slice selective signal gives

$$\begin{aligned} M^{\text{ss}}(TI) &= \int \tilde{M}_0 \left[\left(g_z^{\text{ss}}(z) - 1 \right) \mathrm{e}^{-R_1^{\text{ss}} TI} + 1 \right] \cdot g_y^{90}(z)\,\mathrm{d}z, \\ &= \tilde{M}_0 \mathrm{e}^{-R_1^{\text{ss}} TI} \int g_z^{\text{ss}}(z) \cdot g_y^{90}(z)\,\mathrm{d}z \;+\; \tilde{M}_0 \left(1 - \mathrm{e}^{-R_1^{\text{ss}} TI} \right) \int g_y^{90}(z)\,\mathrm{d}z \\ &= \tilde{p}^{\text{ss}} \tilde{M}_0 \mathrm{e}^{-R_1^{\text{ss}} TI} \;+\; p_0 \tilde{M}_0 \left(1 - \mathrm{e}^{-R_1^{\text{ss}} TI} \right) , \end{aligned} \tag{6.1}$$

where $\tilde{M}_0$ is the equilibrium magnetization per unit length, R_1^{ss} is the effective longitudinal relaxation rate in the ss experiment, and

$$\tilde{p}^{\text{ss}} = \int g_z^{\text{ss}}(z) \cdot g_y^{90}(z)\,\mathrm{d}z \,, \qquad\qquad p_0 = \int g_y^{90}(z)\,\mathrm{d}z \,. \tag{6.2}$$

The integrals in equations (6.1) and (6.2) and in the remaining of this chapter are implicitly assumed to be over $]-\infty;\infty[$. The scalar parameters $\tilde{p}^{\text{ss}}$ and p_0 only depend on the slice profiles of the inversion and imaging pulses.

It is assumed in equation (6.1) that the relaxation of the magnetization can be described by an effective relaxation rate, R_1^{ss}. Due to the transit delays of incoming blood, this is only an approximation, albeit a good one. The validity of this assumption is tested and discussed in chapter 7.

Given equation (6.1), the boundary conditions for zero and infinite inversion times, are

$$M^{\text{ss}}(0) = \tilde{p}^{\text{ss}} \tilde{M}_0 \,, \qquad\qquad M^{\text{ss}}(\infty) = p_0 \tilde{M}_0 \,. \tag{6.3}$$

Let the observed magnetization at infinite inversion time be $M_0 \equiv p_0 \tilde{M}_0$ and let

$$p^{\mathrm{ss}} \;=\; \frac{\tilde{p}^{\mathrm{ss}}}{p_0} \;=\; \frac{\int g_z^{\mathrm{ss}}(z) \cdot g_y^{90}(z)\,\mathrm{d}z}{\int g_y^{90}(z)\,\mathrm{d}z}\,. \tag{6.4}$$

Inserting these relations in equations (6.1) and (6.3) gives

$$M^{\mathrm{ss}}(\,TI\,) = M_0 \left(p^{\mathrm{ss}} - 1\right) \mathrm{e}^{-R_1^{\mathrm{ss}}\,TI} \;+\; M_0\,, \tag{6.5}$$

with the boundary conditions

$$M^{\mathrm{ss}}(0) = p^{\mathrm{ss}} M_0\,, \qquad\qquad M^{\mathrm{ss}}(\infty) = M_0\,. \tag{6.6}$$

The magnetizations $M^{\mathrm{ss}}(\,TI\,)$ and M_0 are the measured magnetizations while p^{ss} is a dimensionless scalar that reflects the degree of inversion. $p^{\mathrm{ss}} \in [-1;1]$, where $p^{\mathrm{ss}} = -1$ corresponds to perfect inversion for all z that are relevant for the imaging pulse profile, while $p^{\mathrm{ss}} = 1$ corresponds to no spin perturbation for all relevant z.

The dependence of the measured magnetization on the slice profiles of the inversion and imaging pulses is thus reduced to one scalar parameter, p^{ss}, which for a FAIR experiment without presaturation is numerically close to -1 since the magnetization is inverted within the imaging region.

Similarly, the signal equation for the non-selective experiment is

$$M^{\mathrm{ns}}(\,TI\,) = M_0 \left(p^{\mathrm{ns}} - 1\right) \mathrm{e}^{-R_1^{\mathrm{ns}}\,TI} \;+\; M_0\,, \tag{6.7}$$

where R_1^{ns} is the effective longitudinal relaxation rate during the ns experiment and

$$p^{\mathrm{ns}} \;=\; \frac{\int g_z^{\mathrm{ns}}(z) \cdot g_y^{90}(z)\,\mathrm{d}z}{\int g_y^{90}(z)\,\mathrm{d}z}\,. \tag{6.8}$$

If the magnetizations M^{ss} and M^{ns} are measured at multiple inversion times, equations (6.5) and (6.7) can be fit to the measured magnetizations using non-linear fitting giving estimates of the parameters M_0, p^{ss}, p^{ns}, R_1^{ss} and R_1^{ns}. This type of measurement will be referred to as a T_1 measurement.

The relaxation rates, R_1^{ss} and R_1^{ns} will only differ in the case of non-zero perfusion, and in the absence of transit delays the difference between them is in principle equal to perfusion (see section 3.2.1). Quantification of perfusion using the difference in R_1 is, however, not very robust due to transit delays [67] and the uncertainties in the estimation of R_1^{ss} and R_1^{ns}. The difference between R_1^{ss} and R_1^{ns} for grey matter is on the order of 0.01 s^{-1}, while R_1^{ss} and R_1^{ns} are about 1 s^{-1}. Quantification of perfusion using the T_1 method therefore requires

an accuracy of the curve fitting that is significantly better than 1%, which in most cases is not realistically achievable.

Since the parameters p^{ss} and p^{ns} reflect the magnetizations at $TI = 0$, they are not dependent on perfusion. If $p^{\mathrm{ss}} \neq p^{\mathrm{ns}}$, then $M^{\mathrm{ss}}(0) \neq M^{\mathrm{ns}}(0)$ which means that the static tissue signal will not subtract out in the magnetization difference images. The magnetization difference at $TI = 0$,

$$\Delta M(0) = M^{\mathrm{ss}}(0) - M^{\mathrm{ns}}(0) = (p^{\mathrm{ss}} - p^{\mathrm{ns}})\, M_0\,, \tag{6.9}$$

is therefore an offset or bias in ΔM. This is the offset discussed in chapter 5. The offset decreases as a function of TI due to longitudinal relaxation such that

$$M^{\mathrm{off}}(TI) = M^{\mathrm{off}}(0) \cdot \mathrm{e}^{-R_1 TI} = (p^{\mathrm{ss}} - p^{\mathrm{ns}})\, M_0\, \mathrm{e}^{-R_1 TI}, \tag{6.10}$$

where R_1 is the relaxation rate of the tissue in the absence of perfusion. R_1^{ns} is numerically very close to R_1 and can in practice be substituted for R_1 without any loss of accuracy.

Short Repetition Time

In equation (6.1), it is assumed that TR is long enough for the magnetization to reach equilibrium between measurements. This is generally not the case since the time efficiency of the sequence would be very small [74, 127]. If a short TR is taken into consideration, where it is still assumed that $TR - TI \gg T_2$, so that the transverse magnetization created by the imaging pulse dies out before the following psat or inversion pulse, equation (6.5) becomes

$$M^{\mathrm{ss}}(TI) = M_0 \left(p^{\mathrm{ss}} \cdot \left[1 - \mathrm{e}^{-R_1^{\mathrm{ss}}(TR-TI)} \right] - 1 \right) \mathrm{e}^{-R_1^{\mathrm{ss}} TI} \;+\; M_0\,. \tag{6.11}$$

The corresponding equation for the ns experiment is

$$M^{\mathrm{ns}}(TI) = M_0 \left(p^{\mathrm{ns}} \cdot \left[1 - \mathrm{e}^{-R_1^{\mathrm{ns}}(TR-TI)} \right] - 1 \right) \mathrm{e}^{-R_1^{\mathrm{ns}} TI} \;+\; M_0\,. \tag{6.12}$$

Equations (6.11) and (6.12) should be used for fitting the parameters M_0, p^{ss}, p^{ns}, R_1^{ss} and R_1^{ns} to the data from the T_1 measurement in a FAIR sequence with short TR.

If TR is varied during the T_1 measurement such that $TR - TI$ is constant, the term $\left[1 - \mathrm{e}^{-R_1^{\mathrm{ss}}(TR-TI)}\right]$ in equation (6.11) becomes constant. Inserting

$$p_\dagger^{\mathrm{ss}} = p^{\mathrm{ss}} \cdot \left[1 - \mathrm{e}^{-R_1^{\mathrm{ss}}(TR-TI)} \right], \qquad p_\dagger^{\mathrm{ns}} = p^{\mathrm{ns}} \cdot \left[1 - \mathrm{e}^{-R_1^{\mathrm{ns}}(TR-TI)} \right] \tag{6.13}$$

into equations (6.11) and (6.12) gives

$$M^{\mathrm{ss}}(TI) = M_0 \left(p_\dagger^{\mathrm{ss}} - 1 \right) \mathrm{e}^{-R_1^{\mathrm{ss}} TI} \;+\; M_0\,, \tag{6.14}$$

$$M^{\mathrm{ns}}(TI) = M_0 \left(p_\dagger^{\mathrm{ns}} - 1 \right) \mathrm{e}^{-R_1^{\mathrm{ns}} TI} \;+\; M_0\,, \tag{6.15}$$

that are identical in form to equations (6.5) and (6.7). Therefore, if equations (6.5) and (6.7) are fit to data from a T_1 measurement with a short TR, the fit will be identical to that using of equations (6.11) and (6.12). The only difference will be in the value and interpretation of the fitted parameters p^{ss} and p^{ns}.

If $TR - TI$ in the ASL measurement is the same as that in the T_1 measurement, the offset in the ASL measurement becomes

$$M^{\mathrm{off}}(TI) = \left(p_{\dagger}^{\mathrm{ss}} - p_{\dagger}^{\mathrm{ns}}\right) M_0 \, \mathrm{e}^{-R_1 \, TI}, \tag{6.16}$$

which has the same form as equation (6.10).

In summary, if TR is long, or if TR is short and $TR - TI$ is constant, equations (6.5) and (6.7) should be fit to the data from the T_1 measurement and the offset is given by equation (6.10). In the latter case, equations (6.4) and (6.8) are not valid though. If TR is short and $TR - TI$ is not constant, equations (6.11) and (6.12) should be fit to the data from the T_1 measurement and the offset can be calculated from equations (6.11) and (6.12).

Presaturation

If presaturation is applied, the slice profile functions, $g_z^{\mathrm{ss}}(z)$ and $g_z^{\mathrm{ns}}(z)$ used in equations (6.4) and (6.8) will not only reflect the effect of the inversion pulse, but rather the effect of the psat pulse or pulses, crusher gradients and the inversion pulse regarded as one entity. Due to the presaturation, the functions $g_z^{\mathrm{ss}}(z)$ and $g_z^{\mathrm{ns}}(z)$ will be close to zero within the imaging region, and hence the parameters p^{ss} and p^{ns} will also be close to zero.

Although presaturation essentially halves the dynamic range of the relaxation curves measured with varying "inversion time", parameter estimation using equations (6.5) and (6.7) is still feasible.

Offset Correction

Once the model parameters are fit to the relaxation curves from the T_1 measurement and the offset is estimated using equation (6.10), it can be subtracted from the magnetization difference images in subsequent ASL measurements. This requires that the same sequence parameters (except for inversion time) are used in the T_1 measurement and all other ASL measurements.

The perfusion related magnetization difference, ΔM^{perf}, can be recovered from the measured magnetization difference, which is the sum of ΔM^{perf} and the offset. This is done by subtracting the estimated offset from the magnetization difference,

$$\Delta M^{\mathrm{perf}} = \Delta M^{\mathrm{meas}} - M^{\mathrm{off}}(TI), \tag{6.17}$$

where ΔM^{meas} is the measured magnetization difference and $M^{\mathrm{off}}(TI)$ is given by equation (6.10). ΔM^{perf} is then the corrected magnetization difference which

corresponds to the magnetization difference one would expect in the absence of an offset.

The offset can still be calculated even if $TR - TI$ is different in the ASL measurement and the T_1 measurement. In this case the offset has to be scaled by a factor than can be calculated using equations (6.11) and (6.12). In the remainder of the thesis, however, it is assumed that TR is either long, or that $TR - TI$ is constant such that equations (6.5) and (6.7) are valid.

Using the method presented here, it is thus possible to perform ASL measurements with either slice profiles or sequence parameters that give rise to a significant offset without compromising the correctness of the perfusion estimates.

6.1.2 PICORE

Offset Estimation

Analogous to the deduction of the measured signal equations for FAIR, the measured signals in a PICORE experiment are

$$M^{\text{tag}}(TI) = M_0 \left(p^{\text{tag}} - 1\right) \mathrm{e}^{-R_1^{\text{tag}}\, TI} \; + \; M_0 \tag{6.18}$$

$$M^{\text{con}}(TI) = M_0 \left(p^{\text{con}} - 1\right) \mathrm{e}^{-R_1^{\text{con}}\, TI} \; + \; M_0 \; , \tag{6.19}$$

where $p^{\text{tag}}$and $p^{\text{con}}$are given by

$$p^{\text{tag}} = \frac{\int g_z^{\text{tag}}(z) \cdot g_y^{90}(z)\, \mathrm{d}z}{\int g_y^{90}(z)\, \mathrm{d}z} \; , \qquad p^{\text{con}} = \frac{\int g_z^{\text{con}}(z) \cdot g_y^{90}(z)\, \mathrm{d}z}{\int g_y^{90}(z)\, \mathrm{d}z} \; , \tag{6.20}$$

and R_1^{tag} and R_1^{con} are the effective relaxation rates in the tag and control experiments, respectively. Analogous to equation (6.10), the offset in a PICORE experiment is

$$M^{\text{off}}(TI) = \left(p^{\text{con}} - p^{\text{tag}}\right) M_0\, \mathrm{e}^{-R_1\, TI}. \tag{6.21}$$

The parameters p^{tag} and p^{con} are close to unity when no presaturation is applied. Especially p^{con} is very close to 1 since $g_z^{\text{con}}(z)$ is approximately one for all relevant z. p^{tag} will depend on the gap between the inversion and imaging slabs but will generally be close to 1. This means that M^{tag} and especially M^{con} are rather insensitive towards changes in TI. Fitting equations (6.18) and (6.19) to the measured signal at varying TI is therefore poorly conditioned and cannot give good estimates of the parameters p^{tag}, p^{con}, $R_1^{\text{tag}}$and R_1^{con}. It is therefore not possible to measure the offset in a PICORE experiment using a T_1 measurement when presaturation is not applied.

Just as with FAIR imaging, equations (6.18), (6.19) and (6.21) can still be used when TR is short as long as $TR - TI$ is kept constant during the T_1 measurement. Equation (6.20) is not valid, though, for short TR.

Presaturation

As with FAIR, when presaturation is applied in a PICORE sequence, the parameters p^{tag} and p^{con} become approximately zero. In this case, the relaxation equations (6.18) and (6.19) become sensitive towards changes in TI and a T_1 measurement can be used for fitting the parameters M_0, p^{tag}, p^{con}, R_1^{tag} and R_1^{con}. Inserting the fitted parameters in equation (6.21) gives an estimate of the offset.

Offset Correction

Once the offset is estimated, it can be subtracted from the measured magnetization difference in subsequent ASL measurements in exactly the same manner as for FAIR measurements using equation (6.17). The offset corrected magnetization difference is then only the perfusion weighted part of the measured magnetization difference.

6.2 QUIPSS Sequences

For both FAIR and PICORE sequences, introducing a qsat pulse affects the magnetization relaxation between the inversion and imaging pulses. The signal equations deduced in the previous section are therefore inadequate to model the relaxation process in the presence of qsat pulses.

If multiple qsat pulses are used for saturation at TI_1, they can be regarded as one entity with one slice profile function, $g^{\mathrm{q}}(z)$. The measured magnetization in the tag[1] experiment will in the case of long TR be

$$M^{\mathrm{tag}}(TI_1, TI_2) = \int \tilde{M}_0 \left\{ 1 + \left[g_z^{\mathrm{q}}(z) \left(\left[g_z^{\mathrm{tag}}(z) - 1 \right] \mathrm{e}^{-R_1^{\mathrm{tag}} TI_1} + 1 \right) - 1 \right] \mathrm{e}^{-R_1^{\mathrm{tag}} \Delta TI} \right\} g_y^{90}(z) \mathrm{d}z, \tag{6.22}$$

where $\Delta TI = TI_2 - TI_1$ and $\tilde{M}_0$ is the equilibrium magnetization per unit length.

[1] The equations are valid for both PICORE and FAIR measurements with QUIPSS saturation. For FAIR, the tag experiment is the ns experiment.

Multiplying out equation (6.22) gives

$$\begin{aligned} M^{\mathrm{tag}}(TI_1, TI_2) = &\ \tilde{M}_0 \left(1 - \mathrm{e}^{-R_1^{\mathrm{tag}} \Delta TI}\right) \int g_y^{90}(z)\, \mathrm{d}z \\ + &\ \tilde{M}_0 \left(\mathrm{e}^{-R_1^{\mathrm{tag}} \Delta TI} - \mathrm{e}^{-R_1^{\mathrm{tag}} TI_2}\right) \int g_z^{\mathrm{q}}(z) \cdot g_y^{90}(z)\, \mathrm{d}z \\ + &\ \tilde{M}_0 \mathrm{e}^{-R_1^{\mathrm{tag}} TI_2} \int g_z^{\mathrm{tag}}(z) \cdot g_z^{\mathrm{q}}(z) \cdot g_y^{90}(z)\, \mathrm{d}z\ . \end{aligned} \tag{6.23}$$

Inserting

$$p_0 = \int g_y^{90}(z)\, \mathrm{d}z\ , \tag{6.24}$$

$$p_1 = \int g_z^{\mathrm{q}}(z) \cdot g_y^{90}(z)\, \mathrm{d}z\ , \tag{6.25}$$

$$p_2 = \int g_z^{\mathrm{tag}}(z) \cdot g_z^{\mathrm{q}}(z) \cdot g_y^{90}(z)\, \mathrm{d}z\ , \tag{6.26}$$

into equation (6.23) and rearranging the terms gives

$$M^{\mathrm{tag}}(TI_1, TI_2) = \tilde{M}_0 \left(p_0 + \left[(p_2 - p_1)\, \mathrm{e}^{-R_1^{\mathrm{tag}} TI_1} + p_1 - p_0\right] \mathrm{e}^{-R_1^{\mathrm{tag}} \Delta TI}\right). \tag{6.27}$$

Assuming that $p_0 \neq 0$ and $p_1 \neq 0$, equation (6.27) can be rewritten as

$$M^{\mathrm{tag}}(TI_1, TI_2) = p_0 \tilde{M}_0 \left(1 + \left[\frac{p_1}{p_0} \left\{\left(\frac{p_2}{p_1} - 1\right) \mathrm{e}^{-R_1^{\mathrm{tag}} TI_1} + 1\right\} - 1\right] \mathrm{e}^{-R_1^{\mathrm{tag}} \Delta TI}\right). \tag{6.28}$$

Inserting the measured magnetization at infinite inversion times, $M_0 \equiv p_0 \tilde{M}_0$ and defining

$$p^{\mathrm{q}} = \frac{p_1}{p_0}, \qquad\qquad p^{\mathrm{tag}} = \frac{p_2}{p_1}, \tag{6.29}$$

gives

$$M^{\mathrm{tag}}(TI_1, TI_2) = M_0 \left(1 + \left[p^{\mathrm{q}} \left\{\left(p^{\mathrm{tag}} - 1\right) \mathrm{e}^{-R_1^{\mathrm{tag}} TI_1} + 1\right\} - 1\right] \mathrm{e}^{-R_1^{\mathrm{tag}} \Delta TI}\right). \tag{6.30}$$

Similarly, the measured magnetization in the control experiment is

$$M^{\mathrm{con}}(TI_1, TI_2) = M_0 \left(1 + \left[p^{\mathrm{q}} \left\{\left(p^{\mathrm{con}} - 1\right) \mathrm{e}^{-R_1^{\mathrm{con}} TI_1} + 1\right\} - 1\right] \mathrm{e}^{-R_1^{\mathrm{con}} \Delta TI}\right), \tag{6.31}$$

where $p^{\mathrm{con}} = p_3/p_1$ and $p_3 = \int g_z^{\mathrm{con}}(z) \cdot g_z^{\mathrm{q}}(z) \cdot g_y^{90}(z)\, \mathrm{d}z$. Note that the definitions of p^{tag} and p^{con} are different here than in equation (6.20) for ASL without QUIPSS saturation.

If the tag and control signals are measured for a series of TI_1 and ΔTI values, it is possible to fit equations (6.30) and (6.31) to the measured data giving estimates of the six parameters M_0, p^{tag}, p^{con}, p^{q}, R_1^{tag} and R_1^{con}.

The parameters p^{tag} and p^{con} assume values similar to those in section 6.1, i.e. they are close to -1 for FAIR without presaturation, close to 1 for PICORE without presaturation and close to zero for both FAIR and PICORE with presaturation. The parameter p^{q} reflects the effect of the qsat pulse(s) on the imaging region, and it therefore depends on whether QUIPSS I or QUIPSS II [48] is used. For QUIPSS I, where saturation is applied in the imaging region, p^{q} will be close to zero, while for QUIPSS II, where saturation is applied in the tagging region, p^{q} will generally be close to 1.

As in section 6.1, equations (6.30) and (6.31) become ill-conditioned for fitting p^{tag} and p^{con} for a PICORE sequence without presaturation. Furthermore, the parameters cannot be estimated robustly when p^{q} is close to zero, i.e. for neither FAIR QUIPSS I nor PICORE QUIPSS I. This means that parameter estimation using equations (6.30) and (6.31) is only possible for QUIPSS II saturation.

As can be seen from the above, the effect of QUIPSS saturation is the introduction of a sixth parameter, p^{q}, and the fact that both TI_1 and TI_2, or rather TI_1 and ΔTI, must be varied in the T_1 measurement. Apart from that, the method of determining the offset is the same as without QUIPSS saturation.

In the absence of perfusion, the relaxation rates R_1^{tag} and R_1^{con} must both be equal to R_1 of tissue. The offset can therefore be determined by inserting $R_1^{\mathrm{tag}} = R_1$ and $R_1^{\mathrm{con}} = R_1$ into equations (6.30) and (6.31) and subtracting M^{tag} from M^{con}.

$$M^{\mathrm{off}}(TI_1, TI_2) = M^{\mathrm{con}}\Big|_{R_1^{\mathrm{con}}=R_1} - M^{\mathrm{tag}}\Big|_{R_1^{\mathrm{tag}}=R_1} . \tag{6.32}$$

The dependence on TI_1 cancels out giving

$$M^{\mathrm{off}}(TI_2) = M_0\, p^{\mathrm{q}} \left(p^{\mathrm{con}} - p^{\mathrm{tag}}\right) \mathrm{e}^{-R_1\, TI_2} . \tag{6.33}$$

In principle, the value of $R_1 = R_1^{\mathrm{con}}$ should be used in PICORE while $R_1 = R_1^{\mathrm{tag}}$ should be used in FAIR, since these are the relaxation rates least affected by perfusion. However, in practice, it makes no difference whether R_1^{tag}, R_1^{con}, or their average is used.

As for FAIR and PICORE without QUIPSS saturation, equations (6.30), (6.31) and (6.33) are still valid for short TR as long as $TR - TI_2$ is constant during the T_1 measurement, even though their deduction assumed that TR is long. The parameters p^{tag} and p^{con} will, however, not be given by p_2/p_1 and p_3/p_1 for short TR. p^{q} on the other hand will still be equal to p_1/p_0.

QUIPSS I

As mentioned above, equations (6.30) and (6.31) cannot be used to estimate the parameters in a QUIPSS I sequence. For QUIPSS I imaging, p_1, p_2 and p_3 may be zero, or very close to zero and p^{tag} and p^{con} become undefined (equation (6.29)). Instead of rewriting equation (6.27) into (6.28), it can be rewritten as

$$M^{\text{tag}}(TI_1, TI_2) = M_0 \left(1 + \left[p_*^{\text{tag}} \mathrm{e}^{-R_1^{\text{tag}} TI_1} + (p^{\text{q}} - 1)\right] \mathrm{e}^{-R_1^{\text{tag}} \Delta TI}\right) . \quad (6.34)$$

Similarly,

$$M^{\text{con}}(TI_1, TI_2) = M_0 \left(1 + \left[p_*^{\text{con}} \mathrm{e}^{-R_1^{\text{con}} TI_1} + (p^{\text{q}} - 1)\right] \mathrm{e}^{-R_1^{\text{con}} \Delta TI}\right) , \quad (6.35)$$

where the parameters

$$p_*^{\text{tag}} = \frac{p_2}{p_0} - \frac{p_1}{p_0} , \qquad p_*^{\text{con}} = \frac{p_3}{p_0} - \frac{p_1}{p_0} , \quad (6.36)$$

are close to or equal to zero. Equations (6.34) and (6.35) are more robust for fitting the magnetization in a QUIPSS I experiment. The offset is then given by

$$M^{\text{off}}(TI) = M_0 \left(p_*^{\text{con}} - p_*^{\text{tag}}\right) \mathrm{e}^{-R_1 TI_2} . \quad (6.37)$$

Although equations (6.34) and (6.35) also can be used in a QUIPSS II experiment, the parameters p^{tag} and p^{con} are preferable over p_*^{tag} and p_*^{con} since their values are easier to interpret as the effect of the tag and control pulses on the in-slice magnetization.

Since QUIPSS I has the disadvantage of being amenable only to single slice imaging and being more sensitive to intra-vascular spins than QUIPSS II, the remainder of this chapter will focus on offset estimation and correction in QUIPSS II imaging.

Common Parameters

By inspecting the relaxation equations for the tag and control magnetizations, given by equations (6.5) and (6.7) or (6.18) and (6.19), it is clear that there is one common parameter, namely M_0. For equations (6.30) and (6.31), the parameter p^{q} is also common.

Instead of fitting the tag and control relaxation curves individually, they can be fit simultaneously thus reducing the total number of parameters that are estimated. This slightly increases the precision of the non-linear fits due to the increased degrees of freedom. This approach has been used throughout this thesis.

Offset Correction

Once the offset has been estimated using a T_1 measurement and non-linear fitting, it can be subtracted from the measured magnetization difference in subsequent ASL measurements, using equation 6.17 in the same manner as described in section 6.1.

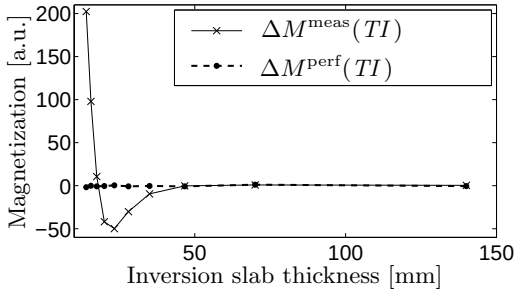

Figure 6.1: The measured magnetization difference, $\Delta M^{\mathrm{meas}}(TI)$, and the offset-corrected magnetization difference, $\Delta M^{\mathrm{perf}}(TI)$ as functions of the inversion slab thickness in a single-slice FAIR experiment.

6.3 Examples

Phantom Studies

A single-slice FAIR experiment was carried out at DRCMR (see appendix A), where a homogeneous gel phantom doped with Gd-DTPA, giving it a T_1 of approximately 1.1 s was imaged. The imaging parameters were $TI/TR = 1/10$ s, 230 mm FOV and 64 acquisitions. The imaging slice thickness was 10 mm while the inversion slab thickness was varied from 14 to 140 mm. For each inversion slab thickness, a T_1 measurement was also performed with 17 TI values in the range of 50–5000 ms, $TR = 10$ s and 4 acquisitions. The data were imaged over a small ROI (37 pixels). See reference [116].

Figure 5.5 compared the estimated offset, $M^{\mathrm{ss}}(0) - M^{\mathrm{ns}}(0)$, calculated using equation (6.9), with the theoretical offset calculated using the slice profile functions (equation (5.8)). The parameters M_0, p^{ss}, p^{ns}, R_1^{ss} and R_1^{ns} were estimated from the T_1 measurement by fitting equations (6.5) and (6.7) to the measured relaxation curves. The figure shows, that there is excellent agreement between the theoretical offset and that calculated using the fitted values of M_0, p^{ss}, p^{ns}, R_1^{ss} and R_1^{ns}.

Figure 6.1 shows the measured magnetization difference before and after offset correction in the experiment. It is clear that there is a large offset before offset correction when the inversion slab thickness is small. After offset correction, however, there is no residual magnetization difference corresponding to the absence of perfusion in the phantom.

Figure 6.2 shows the magnetization difference before and after offset correction as a function of the gap between the inversion and imaging regions in a 5-slice PICORE QUIPSS II experiment with presaturation. The experiment was carried out at UCSD on a gel phantom with $T_1/T_2 \sim 1200/110$ ms. The sequence parameters are $TI_1/TI_2/TR = 0.7/1.4/6$ s, $TE = 40$ ms, slice thickness 8 mm, 20 acquisitions (10 tag and 10 control). The T_1 measurements were done with $TI_1 = 50/150/350/700$ ms, and four TI_2 for each TI_1 value logarithmically spaced between $TI_1 + 50$ ms and 5 s. Both presaturation and QUIPSS saturation consisted of two 12.8 ms Hamming filtered sinc pulses. As in the previous

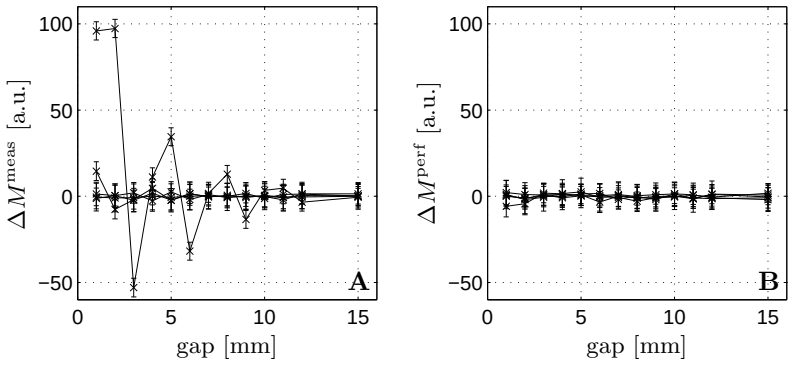

Figure 6.2: Dependence of the difference magnetization on the gap between the imaging and tagging slabs in a 5-slice PICORE QUIPSS II experiment with presaturation. Each curve is for one slice. Values are mean of ROI ± std. (A) The measured signal before offset correction. For comparison, $M_0 \sim 4000$ on the same scale. The most proximal slice has large oscillations for small gaps. (B) The difference magnetization after offset correction using equation (6.17).

example, there is no perfusion in the phantom, and any significant difference magnetization is therefore an offset due to slice profile effects. Before offset correction, the measured offset exhibits oscillatory behaviour as a function of the gap, similar to that predicted by simulations in figure 5.7B.

The offset corrected magnetization difference, ΔM^{perf}, shown in figure 6.2B is not significantly different from zero ($p > 0.39$) for any of the slices, proving that offset correction using equation (6.17) indeed works.

Human Studies

Figure 6.3 shows mean magnetization difference images in three slices in a PICORE QUIPSS II experiment with presaturation. The measurements were done at UCSD. The imaging parameters were $TI_1/TI_2/TE = 700/1400/40$ ms, TR=2 s, FOV = 240 mm, 135 acqs, *npsat*=*nqsat*=2 and a slice thickness of 8 mm. The images in the top row were acquired with a 10 mm gap between the imaging and tagging regions, while those in the bottom row were acquired with a gap of 5 mm. The 10 mm gap was sufficiently large for avoiding an offset in all slices, while the 5 mm gap gave a significant offset in the most proximal slice.

The offset for the 5 mm gap experiment was determined using three runs of T_1 measurements with 16 TI_1/TI_2 values. TI_1 values used were 50/150/350/700 ms and 4 values of TI_2 were used for each TI_1, logarithmically distributed between $TI_1 + 50$ ms and 5000 ms. $TR - TI_2$ was kept constant at 2900 ms (for the first slice). Two acquisitions were done per TI_1/TI_2 pair.

Figure 6.4 shows the fitted parameters, M_0, p^{con}, p^{tag}, R_1^{con}, $R_1^{\mathrm{tag}}$and p^{q} obtained by fitting equations (6.30) and (6.31) to the data from the T_1 measurements. Only the parameter maps for the most proximal slice of 5 mm gap experiment in figure 6.3 are shown. Figure 6.5 shows the offset for all three slices

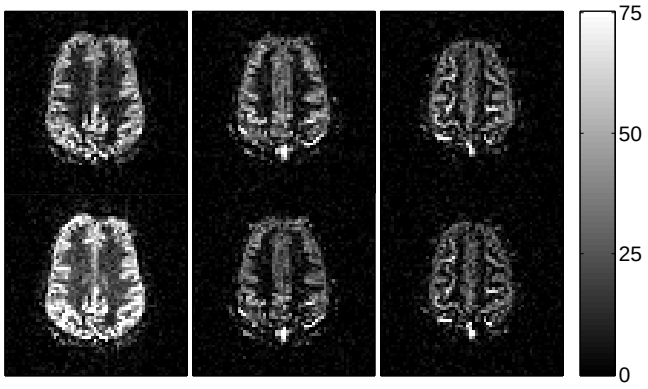

Figure 6.3: Magnetization difference images measured using PICORE QUIPSS II with presaturation before offset correction. $TI_1/TI_2 = 700/1400$ ms. Top row is with 10 mm gap giving no significant offset in any of the three slices while bottom row is with 5 mm gap giving a large offset in the most proximal slice. Left to right is proximal to distal [123].

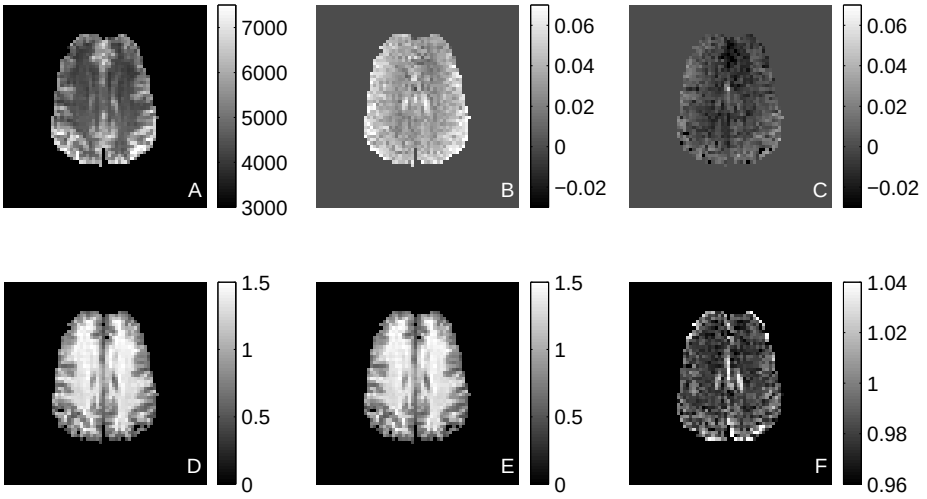

Figure 6.4: The fitted parameters to the data from a T_1 measurement in a PICORE QUIPSS II sequence with presaturation. Only the most proximal slice is shown. The fitted parameter maps are (A) M_0 [a.u.], (B) p^{con}, (C) p^{tag}, (D) R_1^{con} [s^{-1}], (E) R_1^{tag} [s^{-1}], and (F) p^{q}.

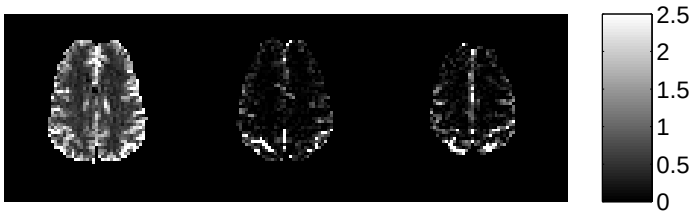

Figure 6.5: The offset in percent of M_0 in a PICORE QUIPSS II sequence with presaturation and 5 mm gap. $TI_1/TI_2 = 700/1400$ ms. The offset is calculated using equation (6.33). Left to right is proximal to distal.

relative to M_0 in the 5 mm gap experiment, calculated using equation (6.33). As predicted in the previous chapter, the offset is smaller in WM than in GM. The perfusion related magnetization difference can be obtained by subtracting the offset (figure 6.5) from the measured magnetization difference (bottom row in figure 6.3).

GM and WM ROIs were thresholded from the R_1^{con} maps, so that $0.95 < T_1 < 1.25$ s for GM and $T_1 < 0.8$ s for WM. The offset averaged over the GM and WM ROIs in the 5 mm gap experiment is listed slice by slice in table 6.1 for three subjects. The images shown in figures 6.3–6.5 correspond to subject number 2 in table 6.1. The offset is clearly only significant in the ROI as a whole in the most proximal slice. This is also evident from figure 6.3, where the magnetization difference is biased high in the proximal slice of the 5 mm gap. Offset correction is therefore only done in the most proximal slice.

It is, however, worth noting that figure 6.5 indicates that there is a significant offset in the other slices in some pixels. This is most likely due to partial volume effects between GM and cerebrospinal fluid (CSF), where relaxation is bi-exponential and equations (6.30) and (6.31) no longer model the relaxation curves to a high enough degree. These pixels, however, are not included in the ROIs due to their high T_1. A smaller ROI from the same study is analysed in chapter 8.

It is very interesting to note that the offset in subject 3 is very small compared to the other two subjects. This may be due to a different loading of the coil, giving different B_1 field patterns which in turn may affect the offset as described in section 5.3.3.

Table 6.2 shows the calculated perfusion using equation (3.30) for the GM and WM ROIs averaged over all three subjects. Here, the perfusion values for the 10 mm gap experiment are regarded as the true values since there is no offset, and they are therefore used to verify the values from the 5 mm gap experiment. The standard deviation in table 6.2 was calculated as the standard error of the mean, averaged over the ROI, but not over acquisitions.

Perfusion was calculated for the proximal slice in the 5 mm gap experiment both before and after offset correction. The perfusion values before offset cor-

ROI	Subject	Slice 1	Slice 2	Slice 3
GM	1	64±5	2±8	7±10
	2	76±5	-2±6	1±8
	3	7±3	0±3	-3±6
WM	1	123±7	-5±8	25±33
	2	187±7	4±7	-5±4
	3	45±9	-3±13	6±18

Table 6.1: The offset in percent of the magnetization difference for GM and WM ROIs in three subjects (mean±std). Results are from a PICORE QUIPSS II experiment with a 5 mm gap. Slice 1 is the most proximal slice. Only slice 1 exhibits a significant offset.

ROI	Gap [mm]	Slice 1	Slice 2	Slice 3
GM	10	65±6	62±6	54±7
	5	93±6*	57±6	52±7
		65±6†		
WM	10	13±5	11±6	9±7
	5	31±5*	9±6	13±7
		14±5†		

Table 6.2: GM and WM perfusion values [ml/100g/min] averaged over three subjects (mean±std). Slice 1 is the most proximal slice. Perfusion values for slice 1 marked with a * are before offset correction, while values marked with a † are after offset correction. For all other values, there was no significant offset. [123]

rection are clearly significantly higher than the true values, whereas the values after offset correction are in excellent agreement with those from the 10 mm gap experiment. The standard deviation of the perfusion estimates does not increase significantly with offset correction since the variation of ΔM over acquisitions is much greater than the error of offset estimation.

There seems to be a trend for perfusion values to drop for increasing slice number. This is unrelated to the offset and is observed in both the 10 mm gap and 5 mm gap experiments. The trend is more significant in GM than in WM and is most likely due to increased partial volume problems in the more distal slices.

6.4 Implications for Transit Delays

The motivation for developing the technique of offset correction was to be able to reduce the gap between the imaging and tagging regions in ASL measurements hence reducing the transit delays of incoming blood.

Two examples are presented here that illustrate the effect that reducing the gap has on the transit delays. The first is a FAIR measurement at variable gaps, but with fixed inversion time, while the second is a PICORE QUIPSS II measurement with presaturation at a reduced gap and variable inversion time.

6.4.1 Variable Gap

In this study, four subjects (25–27 years) were imaged at DRCMR using a single slice FAIR sequence without presaturation. Imaging parameters were $TI/TR = 1/3$ s, 60 acquisitions (30 ss and 30 ns), 10 mm slice thickness, FOV=230 mm, 64×64 matrix. T_1 measurements were done using the sequence repeated with 11 different inversion times within the range of 50–5000 ms and 10 acquisitions. Each set of FAIR and T_1 measurements was repeated for each subject at a number (4–6) of inversion slab thicknesses ranging from 18–54 mm corresponding to 4–22 mm gaps between the edges of the inversion slab and imaging slice.

Equations (6.5) and (6.7) were fitted to the T_1 relaxation curves giving estimates of the parameters M_0, p^{ss}, p^{ns}, R_1^{ss} and R_1^{ns}. Perfusion was calculated using the following equation, which does not take transit delays into account.

$$\frac{f}{\lambda} = \frac{\Delta M^{\mathrm{meas}}(TI) - M^{\mathrm{off}}(TI)}{(M_0 - M^{\mathrm{ss}}(0))\, e^{-R_1^{\mathrm{ns}} TI} \cdot TI}, \tag{6.38}$$

where $M^{\mathrm{off}}(TI)$ was calculated using equation (6.10). The results from these measurements have been published in [116].

Figure 6.6A shows the calculated perfusion for all subjects in a GM ROI normalised to the perfusion value at the minimum inversion slab thickness. Figure 6.6B shows the perfusion values for the same ROIs if no offset correction is done, i.e. constraining the non-linear fit of equations (6.5) and (6.7) to $p^{\mathrm{ss}} = p^{\mathrm{ns}}$. There is clearly a large variation in the calculated perfusion values when offset correction is omitted.

As the inversion slab thickness increases, a decreasing trend in the offset corrected perfusion values is found. This agrees well with the fact that transit delays increase with the width of the gap. This illustrates that perfusion is underestimated at large gaps if transit delays are not taken into account.

Figure 6.7 shows the dependence of R_1^{ss} and R_1^{ns} on the inversion slab thickness. An approximately linear relation is found. However, only R_1^{ss} has a significant slope ($p < 0.005$). The slope of R_1^{ns} was not significantly different from zero ($p > 0.38$). This illustrates how the increasing transit delay affects the measured magnetization. As the gap increases, R_1^{ss}, which is the effective relaxation rate during the ss experiment, decreases due to the increased delay of arrival of incoming uninverted blood. R_1^{ns}, on the other hand is not affected by the

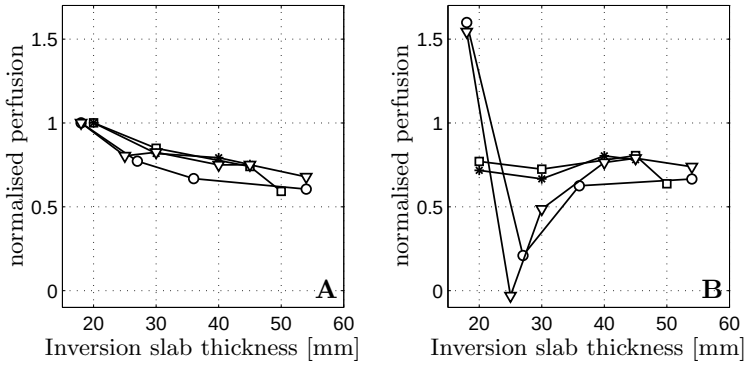

Figure 6.6: Normalised perfusion values in GM ROIs in four subjects as a function of the inversion slab thickness. (A) Results after offset correction. (B) Results without offset correction. Each marker type is for one subject.

transit delay, and therefore exhibits no significant dependence on the inversion slab thickness.

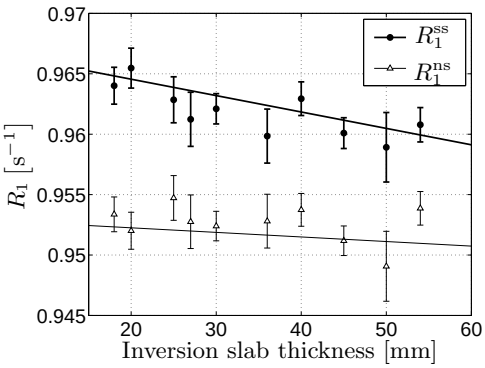

Figure 6.7: Fitted values of R_1^{ss} and R_1^{ns} as a function of the inversion slab thickness. Only R_1^{ss} has a significantly negative slope. The data points shown are mean values ± standard error while the lines are found using linear regression.

6.4.2 Variable Inversion Time

In this study, perfusion was measured in three subjects at UCSD using a PICORE QUIPSS II sequence with presaturation (see appendix A). The inversion slab thickness was 10 cm in all the measurements, $TI_1 = 700$ ms, 64×64 matrix, FOV=240 mm, $TR = 2$ s, 135 acquisitions. The gap between the edges of the most proximal imaging slice and the inversion slab was either 5 or 10 mm. For the 10 mm gap experiment, TI_2 was 1400 ms, while for the 5 mm gap experiment, TI_2 was 1100/1200/1300/1400 ms. For each TI_2/gap combination, two runs were measured. The perfusion values from the 1400 ms/10 mm experiments are regarded as the correct values in this experiment since there is no offset, and

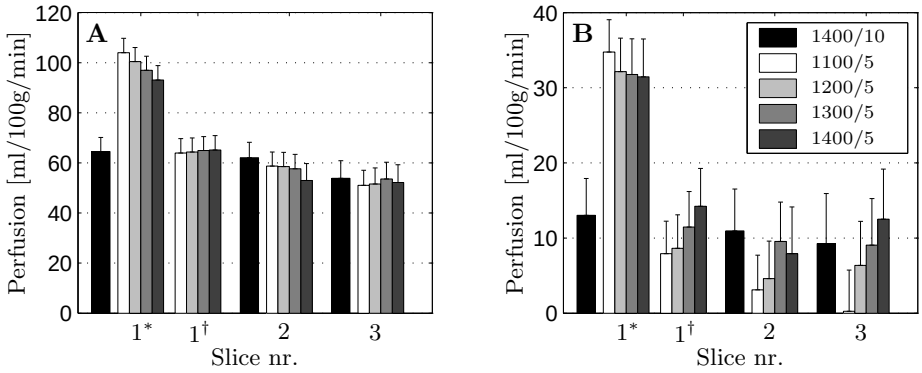

Figure 6.8: (A) GM and (B) WM perfusion values acquired in a three-slice PICORE QUIPSS II measurement averaged over three subjects. Five different values of TI_2 [ms] and gap [mm] are shown (see legend). Values for slice 1 which is the most proximal slice are shown with* and without† offset correction. All values are mean±SEM of ROI.

TI_2 satisfies the condition needed for correct quantification of perfusion, equation (3.29). [48]

Three runs of T_1 measurements were done for the 5 mm gap experiments with 16 TI_1/TI_2 values. TI_1 values used were 50/150/350/700 ms and 4 values of TI_2 were used for each TI_1, logarithmically distributed between $TI_1 + 50$ ms and 5000 ms. $TR - TI_2$ was kept constant at 2900 ms (for the first slice). Two acquisitions were done per TI_1/TI_2 pair.

Equations (6.30) and (6.31) were fit to the data from the T_1 measurements and the fitted parameters were used to calculate the offset using equation (6.33). Only the most proximal slice (slice 1) had a significant offset. Perfusion was calculated using equation (3.30). T_1^{b} was assumed to be 1.5 s, M_0^{b} was assumed to be equal to that of GM and q was assumed to be 1. Perfusion in slice 1 was calculated both with and without offset correction using equation (6.17). GM and WM ROIs were selected as described earlier.

Figure 6.8 shows the mean absolute perfusion calculated in GM and WM for each slice. For slice 1 the values are shown both before and after correction, while the values were not offset corrected for the other slices. The standard error was calculated as in section 6.3. Before offset correction, all the 5 mm gap experiments clearly overestimate perfusion in the first slice due to the large offset. In GM, all the 5 mm gap experiments give the same value of perfusion after offset correction as the TI_2/gap=1400/10 experiments for all values of TI_2. This indicates that even $TI_2 = 1100$ ms satisfies equation (3.29). On the other hand, the situation is quite different for WM where perfusion is underestimated in the 1100/5 and 1200/5 experiments after offset correction. The perfusion values of the 1300/5 and 1400/5 experiments are in much better agreement with the 1400/10 experiments. This indicates that $TI_2 < 1300$ ms does not satisfy

equation (3.29), which means that the transit delay, δt is longer for WM than for GM. This effect is amplified in the distal slices. These results have been published in [123].

Comparing the WM perfusion values in the three slices indicates that the TI_2/gap value of 1400/10 in the standard experiment does not satisfy equation (3.29) for the distal slices. This explains the decreasing trend for WM perfusion in the 1400/10 experiment for increasing slice number. For GM on the other hand, this is not the case. The decreasing trend in GM perfusion in the 1400/10 experiment is therefore much more likely to be due to partial volume effects.

6.5 Discussion

We have in this chapter seen how the dependence of the measured signals on the slice profiles could be utilized in estimating the offset in the magnetization difference in various ASL experiments.

Through the use of slice profile functions, it was shown that the effect of each group of RF pulses and crusher gradients on the measured magnetization can be expressed by a single scalar parameter. Although these parameters can be calculated theoretically using the slice profile functions, they can in most cases also be measured experimentally using non-linear fitting of the signal equations to data from a T_1 measurement, where the inversion time is varied.

Once the parameters have been estimated from the T_1 measurement, the actual offset can be calculated on a pixel by pixel basis. Alternately, the data from the T_1 measurement can be averaged over an ROI before non-linear fitting. We have found this to give more robust offset estimates than averaging the pixelwise offset.

Although the parameters p^{ss} and p^{ns}, or p^{tag} and p^{con}, express the effect of the slice profiles, no direct knowledge of the slice profile functions is required. This is a huge advantage since the slice profile functions are affected by B_1 inhomogeneities and susceptibility artefacts. These effects would be very difficult to include in the calculation of the slice profile functions.

It is interesting to note that the magnetization equations for the measured magnetizations, are identical to those deduced if the effects of imperfect slice profiles only were included as average effects. For example, let the longitudinal magnetization immediately after inversion in a FAIR experiment be $M^{\mathrm{ss}}(0)$ and $M^{\mathrm{ns}}(0)$ for the ss and ns experiments, respectively, where there is no z-dependence in the quantities M^{ss} and M^{ns}. Assuming that the measured signal is equal to the longitudinal magnetization immediately before the imaging pulse, the equations for the measured signals simply become the initial magnetizations,

$M^{\mathrm{ss}}(0)$ and $M^{\mathrm{ns}}(0)$, affected by longitudinal relaxation,

$$M^{\mathrm{ss}}(TI) = (M^{\mathrm{ss}}(0) - M_0)\,\mathrm{e}^{-R_1^{\mathrm{ss}}\,TI} + M_0 \tag{6.39}$$

$$M^{\mathrm{ns}}(TI) = (M^{\mathrm{ns}}(0) - M_0)\,\mathrm{e}^{-R_1^{\mathrm{ns}}\,TI} + M_0\,, \tag{6.40}$$

which are identical to equations (6.5) and (6.7) when $M^{\mathrm{ss}}(0) = p^{\mathrm{ss}}M_0$ and $M^{\mathrm{ns}}(0) = p^{\mathrm{ns}}M_0$. These conditions are indeed fulfilled, as given by equation (6.6).
Similar arguments are valid for equations (6.18), (6.19), (6.30) and (6.31).

Another interesting result, is that the offset in QUIPSS imaging is independent of TI_1 (equations (6.33) and (6.37)). This is because the offset is created by the difference between the slice profiles of the tag and control pulses. Although, the qsat pulses affect the offset, the time at which they are applied is not important as long as both TI_1 and $\Delta TI \gg T_2$ so that the transverse magnetization dies out between the RF pulse groups.

Although the offset is independent of TI_1 in QUIPSS imaging, it is generally not possible to estimate the offset by fitting $M^{\mathrm{con}} - M^{\mathrm{tag}}$ defined by equations (6.30) and (6.31) to the measured magnetization difference in a T_1 measurement where only TI_2 is varied. The perfusion weighted part of ΔM^{meas} is proportional to TI_1, and therefore, equation (6.33) can only be directly fit to give the offset when there is no perfusion, i.e. in a phantom. In that case, $M_0 p^{\mathrm{q}}\,(p^{\mathrm{con}} - p^{\mathrm{tag}})$ would form a single parameter in the fit, which would be a simple exponential decay.

Multislice versus 3D Imaging

The magnetization equations presented in this chapter are based on single slice or multislice imaging. The slice profile function $g_y^{90}(z)$ in for example equations (6.24)–(6.26) can be applied for each slice individually. The parameters p^{tag}, p^{con} and p^{q} are therefore slice dependent. However, the method for determining these parameters experimentally using the T_1 measurements is identical for all slices.

In true 3D imaging, the imaging pulse will either be non-selective, or slice selective but encompassing all slices. The magnetization equations must in that case be modified to include the point spread function in the slice direction, which makes the theoretical calculation of the parameters more complicated. The experimental procedure for offset estimation and correction, however, remains unchanged.

Parameter Values

It is assumed in equations (6.28) and (6.29) that the parameter p_0 defined by equations (6.24) is not equal to zero. This assumption is reasonable since if $g_y^{90}(z)$ integrated to zero, no signal would be detected. However, it should be noted that M_x has been neglected since section 5.3.2 (see equations (5.3) and (5.4)).

The parameter p_0 should in principle consist of contributions from both M_x and M_y, and if $g_x^{90}(z)$ doesn't integrate to zero, e.g. due to relaxation effects during the imaging pulse, p_0 should be substituted by $p_0 = \sqrt{p_{0,x}^2 + p_{0,y}^2}$, where $p_{0,y}$ is given by equation (6.24), and $p_{0,x}$ is given by a similar expression.

Short Inversion Times

The use of slice profile functions in the deduction of the magnetization equations in this chapter assumes that the delays between the groups of RF pulses in the sequence are long enough for the transverse magnetization to fully relax. This requirement is generally fulfilled in normal ASL measurements, where $TI \sim 1$ s when no QUIPSS saturation is applied and $TI_1 \sim 700$ ms and $TI_2 \sim 1.4$ s when QUIPSS II saturation is applied. In the T_1 measurements, however, images are acquired at various inversion times some of which are as short as possible, typically 30–50 ms. At such short inversion times, the transverse magnetization will not have relaxed between the RF pulses, and there is a risk of the transverse magnetization, generated by the inversion or saturation pulses, playing a minor role in the measured magnetization.

It is not likely, however, that this would significantly affect offset estimation using the T_1 measurement for the following reasons. Firstly, there are many points on the T_1 relaxation curves measured in this thesis. Only one or a few of these points would potentially be affected. Secondly, the magnetization equations are fit to the measured M^{tag} and M^{con} signals, not the difference magnetization. SNR is therefore usually quite high, which also strengthens the first reason. Thirdly, if an effect does exist, it is likely to be absorbed by the effective relaxation rates, R_1^{tag} and R_1^{con}. The subject is, however, worth investigating in future work.

Noise Considerations

If the estimated value of the offset from the T_1 measurement is $\hat{M}^{\text{off}}$, the estimated perfusion related magnetization difference becomes

$$\Delta\hat{M}^{\text{perf}} = \Delta M^{\text{meas}} - \hat{M}^{\text{off}}\,. \tag{6.41}$$

Any errors in the estimation of the offset will propagate to $\Delta\hat{M}^{\text{perf}}$ and hence to the perfusion estimate through equation (3.30). The relative contributions of the measurement noise and the offset noise to the noise of $\Delta\hat{M}^{\text{perf}}$ will typically depend on the number of acquisitions in the measurement and on the accuracy of the T_1 fit. The latter depends on the number of acquisitions in the T_1 measurement which is limited by imaging time, on the choice of inversion times in the T_1 measurement, and on the correctness of the model being fitted. Although the models presented here are fairly accurate, they do not take the effects of partial volume into account where the relaxation is not mono-exponential.

Table 6.1 suggests that the uncertainty of $\hat{M}^{\text{off}}$ doesn't necessarily scale with $\hat{M}^{\text{off}}$. For very small offsets, the noise introduced by offset correction will there-

fore outweigh the benefit of the correction. In such cases, one is better off not correcting for the offset as for example in slices 2 and 3 in table 6.2.

Transit Delays

It was shown that the reduction of the gap between the imaging and tagging regions, which is the source of the offset, has the advantage that the transit delays are reduced. The reduced transit delays decrease the extent of underestimation of perfusion using ASL sequences without QUIPSS saturation [121]. Alternately, the reduced transit delays can be used to decrease TI_2 in QUIPSS II imaging without violating the condition for quantification, equation (3.29) [123]. It was shown that reducing the gap from 10 to 5 mm allows the reduction of TI_2 in PICORE QUIPSS II to 1100 ms for GM (in the three slices that were imaged) and 1300 ms for WM (in the two most proximal slices only). The reduction of TI_2 gives a larger ΔM^{meas} signal and hence a larger $\Delta \hat{M}^{\text{perf}}$ due to less longitudinal relaxation. This signal increase can outweigh the noise added by offset correction, giving an overall sensitivity increase [124]. This can be used to increase detectability in perfusion fMRI as will be shown in chapter 8.

Chapter 7

T_1 Measurements

It was seen in the previous chapter that offset estimation is based on fitting relaxation equations to relaxation curves measured in T_1 measurements. In this chapter the principles of T_1 measurements will be explored, and the validity of the assumptions underlying offset estimation using T_1 measurements will be addressed.

There are a variety of methods for measuring T_1. A review of a number of these methods such as progressive saturation, saturation recovery, inversion recovery, two-point methods, variable tip-angle methods, stimulated echo imaging and multiple readout methods is given in [130]. Two of these methods will be discussed in this chapter, namely inversion recovery and fast T_1 imaging using multiple readout methods.

7.1 Inversion Recovery

In inversion recovery (IR) T_1 measurements, the magnetization is inverted using either a slice-selective or a non-selective inversion pulse. After a delay, known as the inversion time, TI, where the magnetization is allowed to partially recover towards equilibrium, an imaging pulse is applied, and the magnetization is measured, e.g. by EPI [131]. After another delay, TD, the experiment is repeated giving a repetition time of $TR = TI + TD$. The experiment is then repeated for a whole range of TI values, thus sampling the recovery of the magnetization. A general expression for the magnetization in an IR experiment is obtained by solving the Bloch equation, giving

$$M(TI) = M_0 + (M(0) - M_0) \cdot \mathrm{e}^{-TI/T_1} \ , \tag{7.1}$$

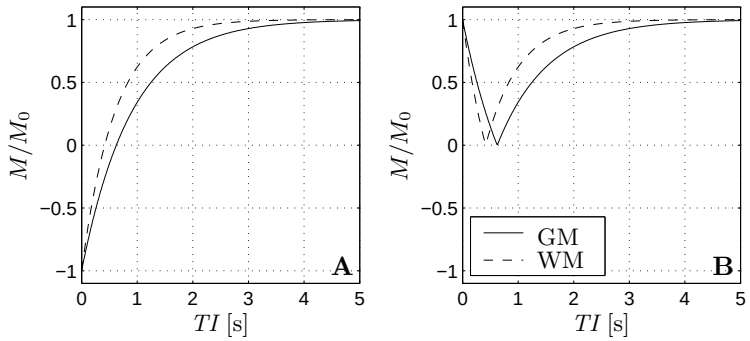

Figure 7.1: Relaxation curves for GM and WM. (A) Relaxation curves given by equation (7.2) with $\alpha = 1$. (B) Measured relaxation curves in magnitude images.

where $M(0)$ is the magnetization just after the inversion pulse. $M(0)$ will depend on how good the inversion pulse is as well as on TD. Alternately, equation (7.1) can be rewritten as

$$M(TI) = M_0 \left[1 - 2\alpha \mathrm{e}^{-TI/T_1}\right] , \tag{7.2}$$

where α is the degree of inversion and is given by

$$\alpha = \frac{1}{2}\left(1 - \frac{M(0)}{M_0}\right) . \tag{7.3}$$

Figure 7.1A shows the relaxation curves for GM and WM given by equation (7.2) with $\alpha = 1$, $T_1 = 0.9$ s for GM and 0.6 s for WM. When the magnetization is measured at multiple values of TI, equation (7.2) can be fit to the measured magnetizations giving estimates of M_0, α, and T_1. This is typically done using non-linear least-squares fitting [132].

7.1.1 Sequence Timing Parameters

Two typical approaches to the timing of the sequence are the use of either constant TR or constant TD for varying TI.

Constant TR

If TR is constant, it must be large enough to allow image acquisition at the longest TI used in the measurements. However, increasing TR beyond that does not give better estimates of T_1 [133]. Equation (7.2) cannot be used directly for fitting relaxation curves measured with a constant TR since $M(0)$ and hence α will also depend on TI. Assuming that the imaging pulse is a 90° pulse, the magnetization just before the following inversion pulse will be

$$M(TR^-) = M_0 \left[1 - \mathrm{e}^{-TD/T_1}\right] , \tag{7.4}$$

where $TD = TR - TI$. It is this magnetization that is inverted by the inversion pulse giving $M(0) = \alpha_0 M(TR^-)$, where $\alpha_0 = -1$ for perfect inversion.

Constant TD

If TR varies between experiments, such that TD is constant, the magnetization recovers by an equal amount between each imaging pulse and the following inversion pulse. $M(0)$ in this case is independent of TI and equation (7.2) can be used directly for fitting the relaxation parameters to the measured data.

7.1.2 Polarity Correction

As indicated in figure 7.1A, the magnetization is negative for short inversion times. This can pose a problem since acquired images generally are presented as magnitude images only. This is normally done since the absolute phase of the acquired signals is of little use due to phase errors caused by pulse sequence timing errors, phase delay of electronic circuits, gradient ramping, eddy currents, static field inhomogeneity and moving spins [130]. The measured relaxation curves will therefore resemble those shown in figure 7.1B. There are several approaches to correcting the signal polarity for short TI values.

In one approach, an additional image is acquired using the same sequence, except that no inversion pulse is applied. The phase in this additional image is then compared to the phase in the images from the T_1 measurement. Assuming that the phase errors are identical or at least very similar in all the measurements, the phase difference will be either approximately 0° or 180°. The polarity of the magnetization for TI values with a phase difference of approximately 180° can be reversed, transforming the relaxation curves back to the form in figure 7.1A [134].

In another approach the k-space data of the image with the longest TI are subtracted from the k-space data of the images at all other inversion times before image reconstruction. This subtraction gives images with identical polarity regardless of TI. The magnetization equations are then modified accordingly [135].

A third approach utilises a two-step fitting technique, where a magnitude relaxation curve is first fit to the magnitude data. The original complex relaxation curves are then phase corrected with the phase of the image with the shortest TI to give real relaxation curves. The estimate of the parameter α in the first fit is then smoothed over the image and used as a fixed constant when fitting equation (7.2) to the real relaxation curves [136].

I have used two different approaches in accounting for the signal polarity during the course of this work. These approaches will be described in the following. For both approaches, non-linear fitting was done using an implementation of the Levenberg Marquardt method [132] in MATLAB.

Approach 1

Keeping in mind that the true magnetization increases monotonically, and assuming that the relaxation curve isn't sampled very closely near the zero crossing, it is straightforward to find the inversion time giving the smallest of the measured (magnitude) magnetizations. Let this inversion time be TI_0. All points on the measured relaxation curve that have $TI < TI_0$ are necessarily negative in the true curve and their polarity is therefore reversed, while all points with $TI > TI_0$ are necessarily positive and their polarity is therefore not changed. The only inversion time that is questionable is TI_0.

Equation (7.2) is then fit to data once where the polarity of $M(TI_0)$ is reversed and once where it is left unchanged. The polarity providing the best fit, i.e. having the least summed square of errors, is assumed to be the correct one. This approach is very simplistic, but is very effective when the number of samples on the relaxation curves isn't very small and SNR is sufficiently high.

The reason this approach works is the following: If $M(TI_0)$ is significantly larger than the noise level, changing its polarity will significantly affect how well equation (7.2) fits the data. The goodness of fit is therefore a good measure of determining the polarity of $M(TI_0)$. The smaller $M(TI_0)$ is, the smaller effect its polarity will have on the goodness of fit, but also the smaller effect its polarity will have on the fit as a whole. One crucial assumption in this approach is that the equation used for fitting actually models the measured magnetization to a high degree.

For the T_1 measurements done in this thesis, the smallest number of TI values used was 11, which proved highly sufficient for this approach.

Approach 2

The second approach used in this thesis was based on adjusting equation (7.2) to magnitude data instead of correcting the polarity of the data. It is thus assumed that $M(TI)$ follows the equation

$$M(TI) = \left| M_0 \left[1 - 2\alpha \mathrm{e}^{-TI/T_1} \right] \right| \tag{7.5}$$

instead of using equation (7.2). The disadvantage of this method, is that the non-linear fitting routines used for fitting the equation to the measured data, generally need to evaluate the fitted function and its derivative at the measured time points. However, the derivative of equation (7.5) is not defined at the zero crossing, which could in principle give numerical problems for the fitting routine[1]. However, this would require that one of the TI values used in the measurement should coincide exactly with the zero crossing, which is very unlikely. Even if one of the measurements is at a TI value close to the zero crossing, reducing the

[1] Although, it is possible to use a different fitting algorithm, such as Powell's method [132], which does not require computation of the derivatives, this did not prove necessary.

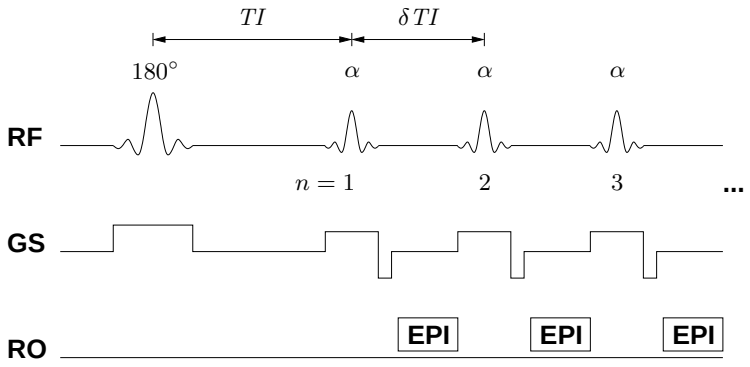

Figure 7.2: Look-Locker EPI sequence which can be used for acquiring T_1 maps in just 3 seconds. An inversion pulse is followed by a series of α-pulses. Each α-pulse is followed by EPI data acquisition.

step-size in the numerical fitting routine, would overcome any problems in the vast majority of all cases.

For the T_1 measurements carried out during the course of this project, no numerical problems were observed when using this method for fitting the relaxation parameters.

One remaining concern when using the magnitude data, is that the noise in the measured magnetization near the zero-crossing is biased positive. This may affect the estimated T_1 value if the number of TI values is small. However, with the relatively large number of TI values used in this thesis, there was no significant difference in the fitted parameters using the two approaches described above. And since the second approach doesn't require any manipulation of the measured data, this approach was used for all the T_1 measurements presented in this thesis.

7.2 Fast T_1 Measurements

One disadvantage of measuring T_1 using IR sequences as described above, is that the sequence contains a lot of delays. Mapping T_1 in multiple slices is therefore a lengthy process. An alternative method providing fast T_1 measurements is that developed by Look and Locker [137] in NMR spectroscopy with later implementations in imaging contexts [138–141].

The sequence, which is outlined in figure 7.2, consists of an inversion pulse followed by a series of α-pulses, where α is a relatively small angle. If the transverse magnetization created by each α-pulse is sampled using an imaging scheme such as EPI, a series of images can be collected after each inversion pulse. The contrast in the images will depend on T_1, the flip angle α and the sequence timing parameters TI and δTI, defined in figure 7.2.

Let M_n be the magnetization measured immediately after the n^{th} α-pulse, where $n = 1, 2, \ldots, N$. Assuming that the transverse magnetization is fully dephased between the α-pulses, and ignoring e^{-TE/T_2^*} in the terms for the measured magnetizations, M_n is given by

$$M_n = \frac{b}{1-a}\left(1 - a^{n-1}\right) M_0 \sin\alpha + a^{n-1} M_1 \ , \tag{7.6}$$

where

$$M_1 = \left[M_0 + (M(0) - M_0)\,\mathrm{e}^{-TI/T_1}\right] \cdot \sin\alpha \ , \tag{7.7}$$

$$a = \cos\alpha \cdot \mathrm{e}^{-\delta TI/T_1} \ , \tag{7.8}$$

$$b = 1 - \mathrm{e}^{-\delta TI/T_1} \ . \tag{7.9}$$

Inserting

$$M_\infty = \lim_{n\to\infty} M_n = \frac{bM_0 \sin\alpha}{1-a} = \frac{\left(1 - \mathrm{e}^{-\delta TI/T_1}\right) M_0 \sin\alpha}{1 - \cos\alpha \cdot \mathrm{e}^{-\delta TI/T_1}} \tag{7.10}$$

into equation (7.6) gives

$$M_n = M_\infty + a^{n-1}\left(M_1 - M_\infty\right) \ . \tag{7.11}$$

Equation (7.11) has the general form of the solution to Bloch equation in an IR experiment with an apparent relaxation time, T_1^*, given by

$$a^{n-1} = \mathrm{e}^{-(n-1)\delta TI/T_1^*} = \left[\cos\alpha \cdot \mathrm{e}^{-\delta TI/T_1}\right]^{n-1} \ . \tag{7.12}$$

Equation (7.11) can therefore be rewritten as

$$M_n = M_\infty + (M_1 - M_\infty)\,\mathrm{e}^{-(n-1)\delta TI/T_1^*} \ . \tag{7.13}$$

Solving equation (7.12) for T_1^* gives

$$\frac{1}{T_1^*} = \frac{1}{T_1} - \frac{\ln(\cos\alpha)}{\delta TI} \ . \tag{7.14}$$

Estimating M_0 and T_1 by fitting equation (7.6) requires knowledge of the angle α. Although estimating M_∞ and T_1^* by fitting equation (7.13) doesn't require prior knowledge of α, calculating M_0 and T_1 from M_∞ and T_1^* does. The angle α must therefore be known in order to estimate M_0 and T_1.

As can be seen from equation (7.14), T_1^* decreases and approaches zero as α increases towards 90°. When T_1^* becomes very small, it is not possible to measure the relaxation curve using this method. The angle α must therefore be relatively small. Freeman *et al.* [142] found that for $N = 24$, the optimal flip angle and image spacing were $\alpha = 24°$ and $\delta TI = 0.1$ s respectively.

One problem with the fast T_1 measurements described here is that the estimated T_1 values are very sensitive to the flip angle α, which inevitably varies across the images due to B_1 inhomogeneities. Correct estimation of T_1 therefore requires mapping of the B_1 field as well [143].

Furthermore, the angle α is a function of the slice direction, such that $\alpha = \alpha(z)$. Knowledge of the slice profile, $\alpha(z)$ is therefore in principle necessary in order to measure T_1 correctly. Equations (7.6) and (7.13) are therefore also functions of z and should be integrated over z in order to give the correct measured magnetizations.

We have, however, previously shown that it is sufficient to use the existing equations with a mean angle $\overline{\alpha}$ that is typically less that the nominal flip angle. See reference [114], which is included in appendix C on page 179, for more details.

7.3 T_1 Measurements in ASL

As was seen in chapter 6, T_1 measurements are an essential part of offset estimation and correction in ASL. This section is a discussion about the choice of T_1 measurement method that is best suited offset correction in ASL.

The largest advantage of the fast T_1 method is naturally its speed. The data for a T_1 map in one slice can be acquired in a single shot in less than 3 seconds. Such a time is just enough to acquire one point on the relaxation curve using the IR method. However, SNR in the fast T_1 method is very low due to the combination of low flip angles ($\sim 25°$) with EPI readout[2]. Averaging is therefore needed in order to increase the SNR of the estimated parameters. This in turn reduces the speed advantage of the fast T_1 measurement.

Regardless of the measurement SNR and the duration of the T_1 measurement, there is one crucial requirement that the fast T_1 method cannot fulfill. The offset in ASL sequences arises from the interaction of the slice profiles of the inversion and the imaging pulses (and other pulses if present). If the T_1 measurements are to be used to model the offset in the ASL measurement, the same interaction between the slice profiles must be present in the T_1 measurements and the ASL measurements. Although the same inversion pulse can be used in the fast T_1 measurements as in the ASL measurements, the same imaging pulse cannot be used. The fast T_1 measurements require a small flip angle while the ASL measurements typically use a 90° imaging pulse.

Equations such as (6.5) and (6.7) can be fit to the measured relaxation curves measured using two IR sequences, one with ss inversion and one with ns inversion. The fitted parameters can then be used to calculate the offset as indicated in chapter 6. When the ASL sequence includes saturation pulses, these pulses

[2]Although it is possible to use other forms of readout than EPI, this will not be considered here, since the imaging in the ASL sequence is done with EPI and it is necessary that the T_1 map have the same spatial distortions as the ASL images.

must also be included in the T_1 measurements. The easiest approach is therefore to use the same sequence for both ASL and T_1 measurements, where the latter is repeated with different inversion times. The tag and the control T_1 measurements are thus acquired in an interleaved manner.

Although fast T_1 measurements cannot be used for offset correction, they do provide a good alternative to IR methods for perfusion measurements using the T_1-method (see section 3.2.1). However, since the T_1-method is not as reliable as the ΔM method [67, 116] and is sensitive towards transit delays, it will not be used in this thesis.

7.4 Effective Relaxation Rates

In the derivation of the relaxation equations in chapter 6, it was assumed that the effect of relaxation could be expressed by a single effective relaxation rate for each of the tag and control experiments, i.e. R_1^{tag} and R_1^{con} or R_1^{ss} and R_1^{ns}. This assumption is generally not strictly valid, since the relaxation rate changes as a function of the instantaneous arterial magnetization that enters the imaging slice. In this section, it is demonstrated that although the relaxation rate varies during the inversion time of the ASL experiments, the relaxation equations developed in chapter 6 model the actual relaxation curves to a very high degree of precision.

This is done using numerical simulations, where the Bloch equation is expressed as a function of the arterial magnetization. It can then be integrated numerically to give the tissue magnetization as a function of time. This is used to artificially generate data from T_1 measurements. The simple relaxation equations from chapter 6 that assume an effective relaxation rate are then fit to the simulated data. The resulting parameters are used to calculate the offset, which is compared with the true offset in the simulations.

The simulations were done for FAIR, PICORE and PICORE QUIPSS II, and are presented in the following.

7.4.1 FAIR

Methods

Figure 7.3 shows a flowchart illustrating the steps of the simulations for a FAIR sequence. The steps are

1. The Bloch equation for the tissue magnetization in the presence of perfusion is given by equation (3.2), which is repeated here for the case of fast exchange

$$\frac{\mathrm{d}M}{\mathrm{d}t} = R_1 \cdot \Big[M_0 - M(t)\Big] + f \cdot \left[M^{\mathrm{b}}(t) - \frac{M(t)}{\lambda}\right] , \qquad (7.15)$$

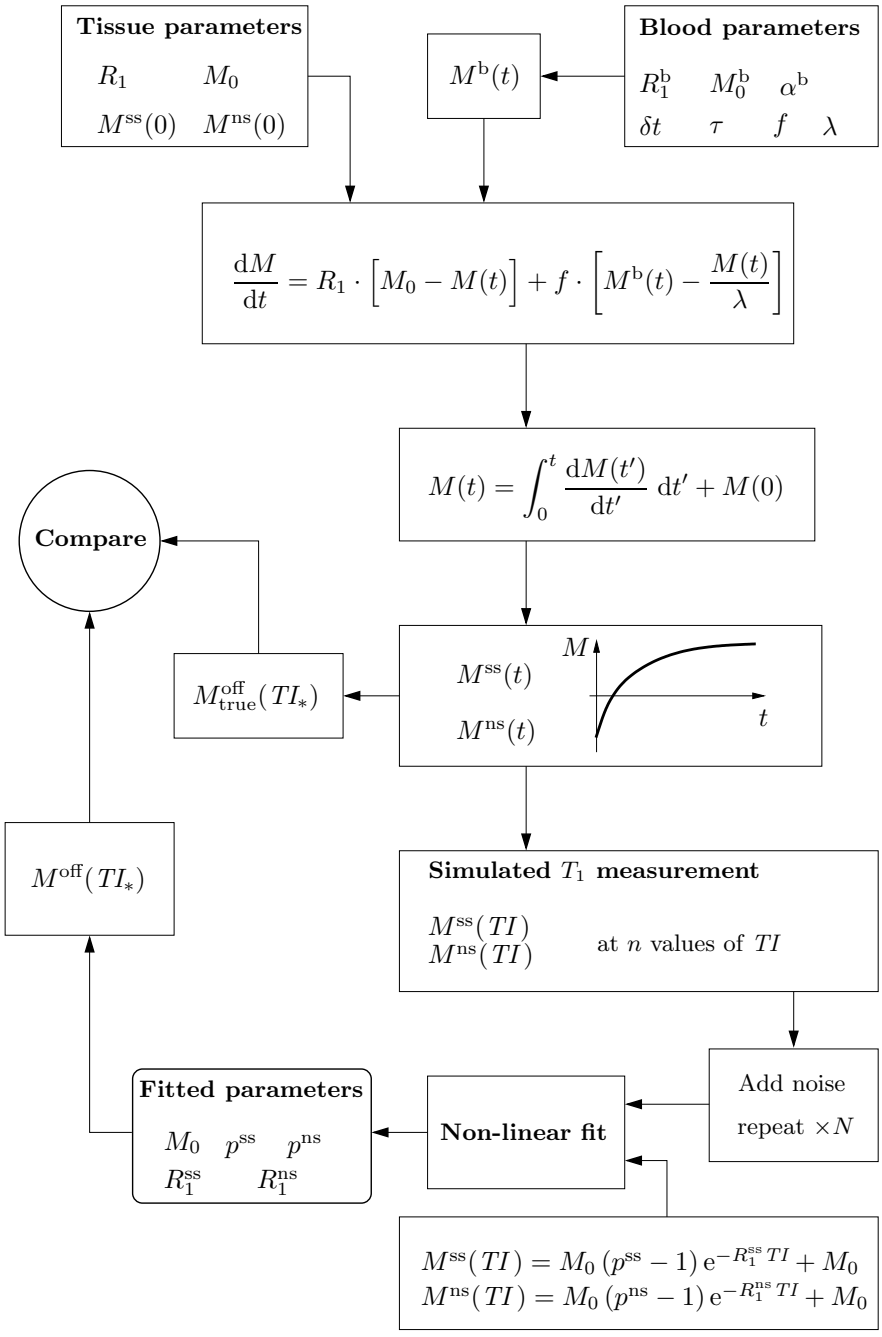

Figure 7.3: Flowchart illustrating the simulations used to check the validity of offset estimation using equation (6.10) for a FAIR sequence. See text for details.

where $M^{\mathrm{b}}(t)$ is the magnetization of arterial blood entering the imaging slice and R_1 is the relaxation rate of tissue.

2. The tissue parameters, M_0, R_1, $M^{\mathrm{ss}}(0)$ and $M^{\mathrm{ns}}(0)$ were given realistic values corresponding to GM. The blood parameters M_0^{b}, R_1^{b}, δt, τ, f, λ and α^{b} were also given realistic values, where α^{b} is the degree of inversion of blood. The values given in the simulations are listed in table 7.1.

3. The function $M^{\mathrm{b}}(t)$, which is different in the ss and the ns experiments is defined by the blood parameters

$$M_{\mathrm{ss}}^{\mathrm{b}}(t) = \begin{cases} M_0^{\mathrm{b}} \left[1 - 2\alpha^{\mathrm{b}} \cdot \mathrm{e}^{-R_1^{\mathrm{b}} t}\right] , & t \leq \delta t \\ M_0^{\mathrm{b}} , & t > \delta t \end{cases} \tag{7.16}$$

$$M_{\mathrm{ns}}^{\mathrm{b}}(t) = \begin{cases} M_0^{\mathrm{b}} \left[1 - 2\alpha^{\mathrm{b}} \cdot \mathrm{e}^{-R_1^{\mathrm{b}} t}\right] , & t \leq \tau \\ M_0^{\mathrm{b}} , & t > \tau . \end{cases} \tag{7.17}$$

4. Equations (7.16) and (7.17) were inserted into equation (7.15), which was integrated to give the functions $M^{\mathrm{ss}}(t)$ and $M^{\mathrm{ns}}(t)$.

5. $M^{\mathrm{ss}}(t)$ and $M^{\mathrm{ns}}(t)$ were calculated at $t = TI_*$, which is the inversion time used in the ASL measurements. The true offset was then $M_{\mathrm{true}}^{\mathrm{off}}(TI_*) = M^{\mathrm{ss}}(TI_*) - M^{\mathrm{ns}}(TI_*)$. The label "true", refers to the fact that it has not been assumed that the relaxation curves can be approximated by an effective relaxation rate.

6. $M^{\mathrm{ss}}(t)$ and $M^{\mathrm{ns}}(t)$ were also calculated at a series of TI values corresponding to those used in a T_1 measurement. Let the number of TI values be n. The n TI values chosen were logarithmically distributed between 50 and 5000 ms.

7. Noise was added to the magnetizations M^{ss} and M^{ns} to represent measured data. The noise was normally distributed, $N(0, \sigma^2)$.

8. Equations (6.5) and (6.7) were fit simultaneously to the noisy data, to give estimates of M_0, p^{ss}, p^{ns}, R_1^{ss} and R_1^{ns}.

9. The estimated offset was calculated using equation (6.10) and the fitted parameters.

10. The estimated offset was compared with the true offset calculated in step 5 above.

11. Steps from number 7 above were repeated N times to find the mean and standard deviation of the estimated offset.

Parameter	Value	Parameter	Value
M_0^{b}/M_0	1.1	f	0.01 s^{-1}
α^{b}	0.95	λ	0.9 ml/g
T_1^{b}	1.3 s	T_1	0.9/0.6 s (GM/WM)
$\Delta M(0)$	$0.15M_0 \rightarrow 0$	$TR - TI$	2 s
TI_*	1 s	$M^{\mathrm{ns}}(0)$	$-0.98M_0\,\mathrm{e}^{-R_1(TR-TI)}$
δt	$0 \rightarrow 700$ ms	τ	2.5 s
TI	$50 \rightarrow 5000$ ms	n	11
N	1000	σ	0.01

Table 7.1: Parameters used in the simulations of offset estimation in the FAIR sequence.

The simulations were repeated for a number of initial parameters representing different gaps between the edges of the imaging slice and the inversion slab resulting in different offsets and transit delays. The simulations were done for 15 values of δt linearly spaced between 0 and 700 ms. The offset was assumed to decrease linearly with increasing δt such that $\Delta M(0)$ was 0 for $\delta t = 700$ ms and $0.15M_0$ for $\delta t = 0$. Finally, all the simulations were repeated with a T_1 value corresponding to WM.

Results

Figure 7.4 shows the estimated offset at time TI_* assuming an effective relaxation rate versus the true offset for both GM and WM. There is an excellent agreement between the estimated and the true offsets within the standard deviation of the estimation. The estimated offset is on average, however, roughly 3% lower than the true offset. The systematic underestimation is well within the estimation error, and will therefore not influence the performance of the offset estimation *in vivo*.

The parameters p^{ss} and p^{ns} estimated from the non-linear fitting should in principle reflect the initial magnetizations $M^{\mathrm{ss}}(0)$ and $M^{\mathrm{ns}}(0)$ normalized by M_0. The estimated values of p^{ss} and p^{ns} were found to be significantly biased compared to the true $M^{\mathrm{ss}}(0)/M_0$ and $M^{\mathrm{ns}}(0)/M_0$. The bias was, however, equal for p^{ss} and p^{ns} such that the offset estimation using equation (6.10) gave the correct result.

Figure 7.5 shows the dependence of the effective relaxation rates, R_1^{ss} and R_1^{ns} on the transit delay δt. Only the results for GM are shown. R_1^{ss} clearly decreases as δt increases while R_1^{ns} is almost independent of δt. This is in excellent agreement with figure 6.7, which depicts the dependence of R_1^{ss} and R_1^{ns} on the

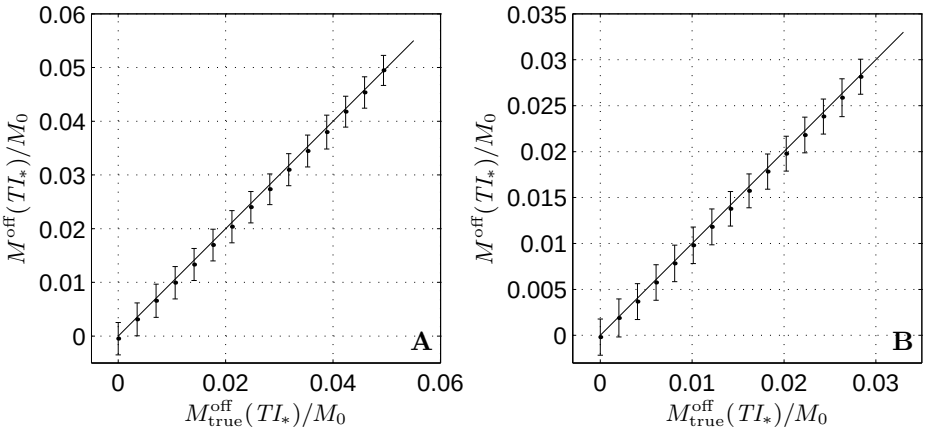

Figure 7.4: The estimated offset versus the true offset for (A) GM and (B) WM in simulations of a FAIR sequence. The offset values are normalized by M_0. Values are mean ± standard deviation. The plotted line is that of identity.

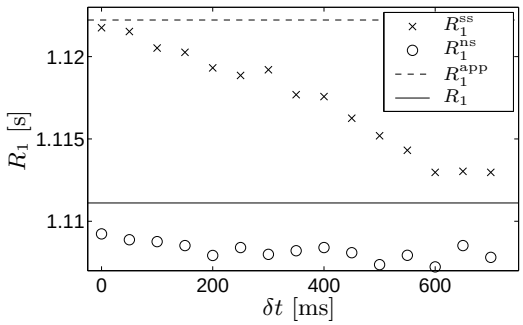

Figure 7.5: Dependence of the fitted effective relaxation rates, R_1^{ss} and R_1^{ns} in a FAIR experiment simulation on the transit delay δt. The parameters used correspond to GM. Compare with experimental data shown in figure 6.7.

inversion slab thickness in experimental *in vivo* data. When $\delta t = 0$, the values of R_1^{ss} and R_1^{ns} correspond roughly to R_1^{app} and R_1 respectively (the constant curves in the figure), where $R_1^{\mathrm{app}} = R_1 + f/\lambda$. The small difference between R_1^{ns} and R_1 is due to the difference between R_1 and R_1^{b}. The standard deviations of the estimated values of R_1^{ss} and R_1^{ns} were on the order of 0.014 s^{-1}.

Further simulations showed that the variation of R_1^{ss} and R_1^{ns} in figure 7.5 is independent of the offset. Changing the value of the tag width τ, however, shifts the points. A smaller value of τ shifts the points upwards and vice versa.

The behaviour of R_1^{ss} and R_1^{ns} for WM was similar to that of GM. The difference between R_1^{ns} and R_1 was, however, larger for WM due to the larger difference between R_1 and R_1^{b}.

7.4.2 PICORE

Methods

The simulations were done in the same manner as for the FAIR sequence, but the simulation parameters were set to correspond to a PICORE sequence with presaturation. The parameters that were changed were τ and $M^{\mathrm{con}}(0)$. The parameters are listed in table 7.2. The time dependence of the blood magnetization was assumed to be

$$M_{\mathrm{tag}}^{\mathrm{b}}(t) = \begin{cases} M_0^{\mathrm{b}} \,, & t \leq \delta t \\ M_0^{\mathrm{b}} \left[1 - 2\alpha^{\mathrm{b}} \cdot \mathrm{e}^{-R_1^{\mathrm{b}} t}\right] \,, & \delta t < t \leq \delta t + \tau \\ M_0^{\mathrm{b}} \,, & t > \delta t + \tau \end{cases} \tag{7.18}$$

$$M_{\mathrm{con}}^{\mathrm{b}}(t) = M_0^{\mathrm{b}} \,, \qquad \forall t \,. \tag{7.19}$$

Equations (6.18) and (6.19) were used for the non-linear fitting of the relaxation curves, and equation (6.21) was used for offset estimation. The parameters R_1^{con}, R_1^{tag}, p^{con} and p^{tag} were thereby used instead of R_1^{ss}, R_1^{ns}, p^{ss} and p^{ns} respectively.

Results

Figure 7.6A shows the estimated offset as a function of the true offset for GM. The same bias was found between the estimated and true values of p^{con} and p^{tag} as with the FAIR sequence. However, the bias was again equal in p^{con} and p^{tag}, thus giving almost the correct offset. The estimated offset was on average roughly 2% lower than the true offset, which is well below the standard deviation of the offset estimate.

Figure 7.6B shows the dependence of the effective relaxation rates R_1^{con} and R_1^{tag} on the transit delays. Unlike the FAIR sequence, it is here R_1^{con} that is

Parameter	Value	Parameter	Value
M_0^{b}/M_0	1.1	f	0.01 s^{-1}
α^{b}	0.95	λ	0.9 ml/g
T_1^{b}	1.3 s	T_1	0.9 s
$\Delta M(0)$	$0.15M_0 \rightarrow 0$	$TR - TI$	2 s
$M^{\mathrm{con}}(0)$	$0.02M_0\,\mathrm{e}^{-R_1(TR-TI)}$	TI_*	1 s
δt	$0 \rightarrow 700$ ms	τ	900 ms
TI	$50 \rightarrow 5000$ ms	n	11
N	1000	σ	0.01

Table 7.2: Parameters used in the simulation of offset estimation in a PICORE sequence with presaturation.

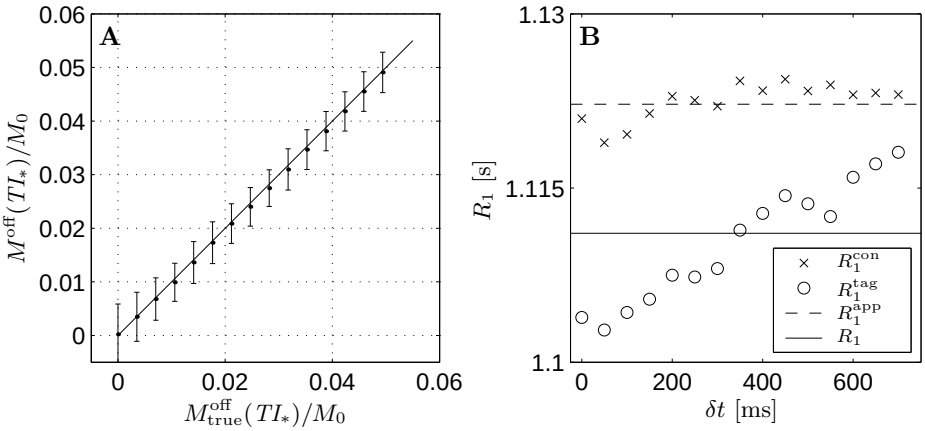

Figure 7.6: Results from simulations of offset estimation in a PICORE sequence with presaturation. (A) Estimated offset (mean±std) versus true offset normalized by M_0. (B) Dependence of the effective relaxation rates R_1^{tag} and R_1^{con} on the transit delays δt.

constant while R_1^{tag} depends on δt. This is not surprising, though, since it the ns experiment in FAIR and the control experiment in PICORE that don't involve finite transit delays. The standard deviations of the estimated R_1^{con} and R_1^{tag} values were on the order of 0.026 s^{-1}.

7.4.3 PICORE QUIPSS II

Methods

The simulations were again done in a manner similar to that of the FAIR sequence and the PICORE sequence, where the parameters were adjusted to a PICORE QUIPSS II sequence. A new parameter, β^{b}, was introduced, which is the degree of saturation of blood due to the qsat pulse, such that $\beta^{\text{b}} = 1$ corresponds to perfect saturation and $\beta^{\text{b}} = 0$ corresponds to no saturation. The parameter p^q, which represents the effect of the qsat pulse on the in-slice magnetization was assumed to vary linearly from 0.9 for $\Delta M(0) = 0.15 M_0$ to 0.99 for $\Delta M = 0$. The simulation parameters are listed in table 7.3.

Assuming that $TI_1 < \tau$, the blood magnetization was set to

$$M_{\text{tag}}^{\text{b}}(t) = \begin{cases} M_0^{\text{b}} \,, & t \leq \delta t \\ M_0^{\text{b}} \left[1 - 2\alpha^{\text{b}} \cdot \text{e}^{-R_1^{\text{b}} t}\right] \,, & \delta t < t \leq \delta t + TI_1 \\ M_0^{\text{b}} \left[1 - \beta^{\text{b}} \cdot \text{e}^{-R_1^{\text{b}}(t - TI_1)}\right] \,, & \delta t + TI_1 < t \leq \delta t + TI_1 + \tau \\ M_0^{\text{b}} \,, & t > \delta t + TI_1 + \tau \,, \end{cases} \tag{7.20}$$

$$M_{\text{con}}^{\text{b}}(t) = \begin{cases} M_0^{\text{b}} \,, & t \leq \delta t + TI_1 \\ M_0^{\text{b}} \left[1 - \beta^{\text{b}} \cdot \text{e}^{-R_1^{\text{b}}(t - TI_1)}\right] \,, & \delta t + TI_1 < t \leq \delta t + TI_1 + \tau \\ M_0^{\text{b}} \,, & t > \delta t + TI_1 + \tau \,. \end{cases} \tag{7.21}$$

The T_1 measurements were simulated with four values of TI_2 for each of four values of TI_1. TI_2 was logarithmically distributed between $TI_1 + 50$ ms and 5000 ms. Equations (6.30) and (6.31) were fit to the relaxation curves and equation (6.33) was used to calculate the estimated offset.

The values of TI_1 and TI_2 used on the ASL experiments, and at which the offset is compared, are denoted TI_{1*} and TI_{2*} corresponding to TI_* in the previous sections.

Results

Figure 7.7A shows the estimated offset versus the true offset. Again, there was an equal bias in the estimated values of p^{con} and p^{tag}, which subtracted out in

Parameter	Value	Parameter	Value
M_0^{b}/M_0	1.1	f	0.01 s^{-1}
α^{b}	0.95	λ	0.9 ml/g
T_1^{b}	1.3 s	T_1	0.9 s
$\Delta M(0)$	$0.15M_0 \rightarrow 0$	$TR - TI_2$	2 s
$M^{\mathrm{con}}(0)$	$0.02M_0\,\mathrm{e}^{-R_1(TR-TI_2)}$	n	4×4
TI_{1*}	0.7 s	TI_{2*}	1.4 s
δt	$0 \rightarrow 700$ ms	τ	900 ms
β^{b}	0.95	p^q	$0.9 \rightarrow 0.99$
TI_1	50/150/350/700 ms	TI_2	$TI_1 + 50 \rightarrow 5000$ ms
N	10000	σ	0.01

Table 7.3: Parameters used for the simulations of offset estimation for the PICORE QUIPSS II sequence.

the calculation of the offset. The estimated offset was overestimated by roughly 3% on average compared to the true offset. This difference was, however, well below the standard deviation of the estimated offset.

Figure 7.7B shows the fitted values of p^q versus the original values of p^q used in the simulations. There is clearly an excellent agreement. The estimated p^q was on average overestimated by 0.1% compared to the true value of p^q, which is much lower than the standard deviation of the estimation.

Figure 7.7C shows the dependence of R_1^{con} and R_1^{tag} on the transit delay. Since both $M_{\mathrm{con}}^{\mathrm{b}}$ and $M_{\mathrm{tag}}^{\mathrm{b}}$ depend on δt, both R_1^{con} and R_1^{tag} vary with δt. All values of R_1^{con} and R_1^{tag}, however, are between R_1 and R_1^{app}, except for one value of R_1^{tag}. The standard deviations of the estimated R_1^{con} and R_1^{tag} values were on the order of 0.026 s^{-1}.

7.5 Discussion

Some considerations on T_1 measurements were presented in this chapter. It was argued, that although fast T_1 measurements using Look-Locker EPI have great advantages over conventional IR measurements with respect to imaging duration, they are not compatible with offset estimation in ASL by T_1 measurements.

It was argued that the simplest and most direct approach for offset estimation is to use the same sequence for T_1 measurements as that used for ASL measurements. This enables robust non-linear fitting of the parameters needed for offset estimation with imaging times that are on the order of a few minutes. The exact number of acquisitions and number of inversion times used to sample

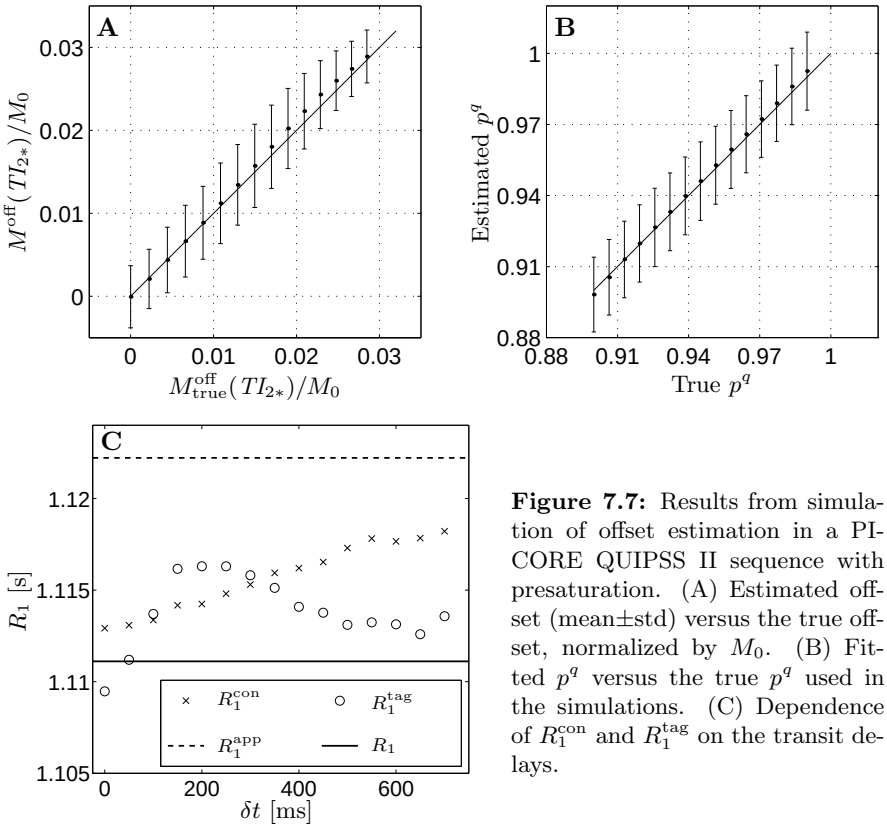

Figure 7.7: Results from simulation of offset estimation in a PICORE QUIPSS II sequence with presaturation. (A) Estimated offset (mean±std) versus the true offset, normalized by M_0. (B) Fitted p^q versus the true p^q used in the simulations. (C) Dependence of R_1^{con} and R_1^{tag} on the transit delays.

the relaxation curves depends on the time available for T_1 measurements.

The principle of assuming an effective relaxation rate for each of the tag and control experiments in offset estimation was validated using simulations. The actual relaxation rate of tissue is not constant from the time of inversion till imaging is carried out. Instead, the instantaneous relaxation rate depends on the magnetization of arterial blood entering the imaging slice at any moment, $M^{\text{b}}(t)$, which depends on the labelling scheme used, and is different for the tag and control experiments.

Due to the functional form of the arterial magnetization, the tissue relaxation curves are neither mono-exponential nor bi-exponential, but experience shifts in the relaxation rates that coincide with the transit delays and trailing times of tagged blood. It should be noted, however, that the effects of the shifts in the relaxation rates are much smaller than the effects of bi-exponential relaxation due to partial volume.

The mono-exponential relaxation equations used in chapter 6 are inadequate to completely model the true relaxation curves due to the shifts in the relaxation

rates. However, the estimated parameters by fitting these mono-exponential relaxation equations to the true relaxation curves can be used to correctly determine the offset. Especially the parameters p^{con} and p^{tag} were significantly biased, but only the difference between them is used for offset estimation, and since the bias was almost equal in the two parameters, the difference could be estimated with a very small error. The effective relaxation rates, R_1^{con} and R_1^{tag}, depended on the transit delays, but were on the order of the true tissue R_1. The equilibrium magnetization, M_0, was determined correctly in all the simulations.

It was thus illustrated that assuming mono-exponential relaxation in ASL T_1 measurements gives an underestimation of the offset by merely 3% in FAIR, 2% in PICORE and an overestimation of the offset by 3% in PICORE QUIPSS II. These errors are much lower than the standard deviation of the estimated offsets, which justifies the use of mono-exponential relaxation equations.

Since the estimated values of R_1^{con} and R_1^{tag} didn't match the values of $R_1^{\text{app}}$and R_1, the simulations confirmed that perfusion quantification using the T_1 method is inaccurate in the presence of finite transit delays.

Chapter 8

ASL in Functional MRI

The application of ASL sequences in functional neuroimaging is discussed in this chapter. The concepts of functional imaging and BOLD contrast are introduced briefly, followed by a description of how ASL sequences can be used to measure changes in both perfusion and blood oxygenation during functional activation. Offset estimation and correction that were developed in chapter 6 are applied to functional imaging as a means of increasing the activation detectability in perfusion-weighted timeseries.

8.1 Functional MRI

It is generally believed that neuronal activation causes local changes in cerebral blood flow (CBF), cerebral blood volume (CBV) and blood oxygenation. By repeated imaging during functional activation using a sequence that is sensitive to CBF, CBV, and/or oxygenation, and inducing a certain pattern of stimulation, it is possible to detect signal changes that correlate with this pattern, localized to the brain tissue that is activated.

The most commonly used contrast mechanism in functional MRI (fMRI) is Blood Oxygenation Level Dependent (BOLD) contrast [49, 50, 144, 145], where changes in the blood oxygenation level are measured. Gradient echo signals are sensitive to changes in blood oxygenation since de-oxygenated haemoglobin is paramagnetic while oxygenated haemoglobin is diamagnetic [49, 146, 147]. Increasing concentrations of de-oxyhaemoglobin therefore decrease T_2^*, which causes the signal in a gradient echo experiment to drop.

Several models have been developed to explain how neuronal activation affects the dynamics of perfusion, blood volume, blood oxygenation and the cerebral metabolic rate of oxygen ($CMRO_2$) [51, 52, 82, 148–158]. There is general

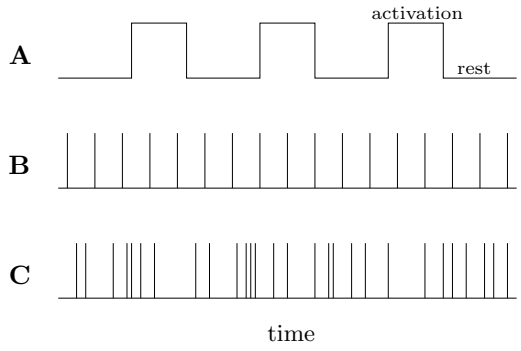

Figure 8.1: Types of activation paradigms. (A) Box-car with alternating periods of activation and rest. (B) Periodic event-related, with the activation taking place in short events that are equally inter-spaced. (C) Random event-related, with the activation taking place in short events randomly inter-spaced.

agreement though, that neuronal activation causes a localized increase in oxygen consumption which is compensated for by an increase in perfusion. However, as perfusion increases, the mean residence time of red blood cells and the oxygen extraction fraction drop, which causes the concentration of de-oxyhaemoglobin to drop. This, in turn, causes T_2^* to increase which gives the signal increase known as the BOLD signal.

During functional measurements, images are acquired continuously in a number of slices as fast as possible. EPI is therefore generally used for imaging. Typical repetition times are between 1 and 4 s depending on the number of slices covered and on the gradient capabilities of the scanner.

During the measurement, the subject is exposed to a certain pattern of activation, known as a paradigm. Some of the first fMRI studies involved activation in the visual cortex during photic stimulation [50, 144], and activation in the motor cortex during finger tapping [145]. The activation paradigms consisted in these experiments of alternating periods of rest and activation. This type of activation is known as a box-car paradigm, see figure 8.1A. Box-car paradigms in various forms are probably the most commonly used type of activation paradigms. Another type of activation is event-related activation [159–162] where the activation takes place as very short events. The events can either occur periodically or randomly as indicated in figure 8.1. Box-car paradigms usually have higher detection power, while event-related paradigms typically are better suited for estimating the haemodynamic response [162], which is the signal response to an infinitesimally short yet infinitely large event. Event-related paradigms are also better suited for some tasks, especially neuropsychological tasks.

8.2 ASL in fMRI

As mentioned above, BOLD contrast is the most commonly used contrast mechanism in functional imaging. Although there are several models that relate the BOLD signal to neural activation, it is generally agreed that perfusion changes are a more direct marker of neural activation than the BOLD signal. Further-

more, BOLD dynamics depend on blood flow dynamics [29, 51] and a measure of perfusion changes during activation is therefore needed to study the dynamics of BOLD.

ASL sequences are very well suited to measure perfusion dynamically, since they can provide either a qualitative or quantitative measure of perfusion at a relatively high sampling rate. In this section, the use of ASL sequences in functional imaging is described and exemplified. Furthermore, extraction of both perfusion and BOLD signal from the measured data is discussed and shown.

8.2.1 Perfusion fMRI

When a series of alternating tag and control images are acquired during a functional study, it is possible to monitor perfusion changes during activation. A perfusion signal timeseries can be generated from the acquired images in two ways.

- Each pair of tag and control images are regarded as one unit and are subtracted from each other giving $N/2$ difference images, where N is the number of acquired images. The time resolution of the difference images in this case becomes $2\,TR$.
- Each tag or control image is subtracted from the average of its neighbouring (in time) images. The first image is subtracted from image 2 and image N is subtracted from image $N-1$. The sign of each image is adjusted so that it corresponds to $M^{\text{con}} - M^{\text{tag}}$. This gives a total of N difference images with a time resolution of TR.

Although the images in the second method are not completely independent, this method is preferred due to the increased time resolution and since it automatically removes any linear drifts in the signal.

Reference Function

Once a series of magnetization difference images has been generated, the timeseries of each voxel can be correlated to a reference function. This reference function should be the expected signal response to the applied activation task. For a box-car paradigm, it is expected that perfusion increases in the activated region when the task is applied and drops back to the normal level during rest. A good starting point for the reference function would therefore be the box-car function itself. The amplitude of the function is not important, only the shape of it matters.

Since the signal reflects the response of a biological system, it cannot be expected that perfusion increases instantly at the onset of activation. A certain delay is therefore to be expected before perfusion increases at the onset of activation and before perfusion decreases again at the end of activation [163]. Furthermore the increase and decrease are not likely to be instantaneous, and the

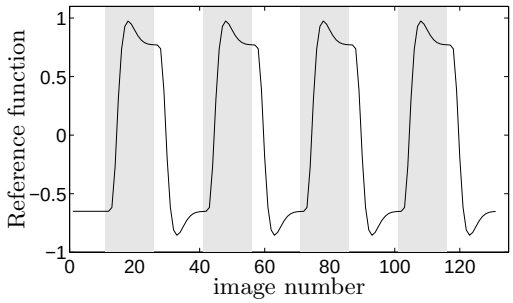

Figure 8.2: Reference function designed as the convolution of a box-car with the haemodynamic response function [159, 164]. The shaded areas are the actual activation periods.

reference function should therefore be somewhat smoothed. A more formalised way of introducing the delay and smoothing is by convolution of the box-car with the haemodynamic response function of the tissue. The haemodynamic response function can either be estimated from the data [164], or an average general shape found in previous studies can be used. The haemodynamic response function used here is that found by Friston *et al.* [159], which is also used in the fMRI analysis software package, SPM99[1]. The resulting reference function obtained by convolution of a box-car function with the haemodynamic response function is shown in figure 8.2, where there clearly is a delay between the onset of the task and the increase in the reference function.

Another approach to generating a reference function is from the measured timeseries directly. If the individual voxel timeseries are correlated to a box-car function, one could average the timeseries of a few of the most correlated voxels to generate a subject-specific reference function. The advantage of this method is that the reference function would have the correct value of response delays and shape. The disadvantage is that any artefactual signal due to for example noise or motion would be included in the reference function. Averaging the reference function over cycles would decrease the effect of noise, but wouldn't completely eliminate the effect of large artefacts.

Correlation Maps

The cross-correlation coefficient between the difference magnetization timeseries and the reference function is a measure of the similarity between the two functions. Typically, voxels having a cross-correlation coefficient above a certain threshold are said to be activated by the task used in the experiment. The threshold used may vary from experiment to experiment depending on SNR. However, assuming that the noise is Gaussian, the significance of activation, p, is uniquely related to the selected threshold, h, through [163]

$$p = 1 - \frac{2}{\sqrt{\pi}} \int_0^{h\sqrt{N/2}} \mathrm{e}^{-t^2} \mathrm{d}t, \tag{8.1}$$

[1]See the SPM website for more information. http://www.fil.ion.ucl.ac.uk/spm/

where N is the number of timepoints in the timeseries and p is the probability that the observed correlation could have occured by chance.

When SNR is low, as is usually the case with ASL, it is sometimes necessary to lower the activation threshold in order to find any activated voxels at all. However, this has the disadvantage that some voxels that were not activated may have correlation coefficients that exceed the threshold. In such cases, simply thresholding the cross-correlation maps may not be adequate for detecting or selecting an activated ROI. Cluster analysis can be used to alleviate this problem, where only voxels that are part of a cluster of voxels with high correlation coefficients are accepted as truly activated [165].

8.2.2 Simultaneous Perfusion and BOLD fMRI

Recall that the BOLD contrast is the modulation of the measured signals due to changes in T_2^*. ASL measurements will therefore contain of a mixture of perfusion and BOLD weighting unless TE is very short [29, 35, 166, 167]. While perfusion weighting is extracted from the ASL data by subtracting the tag signal from the control signal, the method of extraction of BOLD data from ASL measurements depends on the type of ASL sequence used and on the use of presaturation.

BOLD weighting is achieved when signals from tissue and incoming blood have the same sign. Table 8.1 lists how the BOLD weighted signal is extracted from the tag and control signals for PICORE and FAIR with or without presaturation. When presaturation is applied, averaging M^{con} and M^{tag} cancels the perfusion weighting and leaves the BOLD weighting. The cancelling of perfusion weighting is, however, only complete when blood and tissue have the same T_1. Wong *et al.* estimate that the remaining perfusion signal when M^{con} and M^{tag} are averaged for GM is approximately 18% of the perfusion signal in the magnetization difference. The flow signal will have the opposite sign of the BOLD signal and can therefore only underestimate the BOLD signal [29, 168]. The contamination of the perfusion signal with BOLD signal is expected to be even smaller and barely detectable.

As seen in table 8.1, the control signal in PICORE and the tag signal (ns) in FAIR [35, 66] are BOLD weighted when presaturation is not applied. Using these signals for BOLD weighting has the disadvantage that only every second image is used for extracting the BOLD signal. The time-resolution of the BOLD signal therefore becomes $2TR$. When presaturation is applied, and the BOLD signal is extracted by averaging M^{con} and M^{tag}, a time-resolution of TR can be achieved by averaging each value of M^{con} with the average of the preceding and succeeding M^{tag} and vice versa. It is therefore preferable to use presaturation in ASL sequences if the BOLD signal is going to be extracted.

Optimally, the best perfusion weighting is obtained with very short TE, while the best BOLD weighting is obtained with long TE. Using dual or multi-echo imaging can therefore improve the separation of the perfusion and BOLD effects [167–169].

Sequence		Tag		Control		BOLD
Type	Presat	Tissue	Blood	Tissue	Blood	weighting
PICORE	yes	0	–	0	+	$M^{\mathrm{con}} + M^{\mathrm{tag}}$
PICORE	no	+	–	+	+	M^{con}
FAIR	yes	0	–	0	+	$M^{\mathrm{con}} + M^{\mathrm{tag}}$
FAIR	no	–	–	–	+	M^{tag}

Table 8.1: Dependence of the method of extraction of BOLD data from ASL measurements on the type of ASL sequence used and on the use of presaturation. The signs indicate the sign of the in-slice (tissue) magnetization and that of the incoming blood. BOLD weighting is achieved when signals from tissue and incoming blood have the same sign.

8.2.3 Example

Perfusion weighted images were collected repeatedly in a functional study on one subject using both a PICORE and a PICORE QUIPSS II sequence at UCSD. Presaturation was applied in both cases. The activation paradigm consisted of 20 s rest followed by four cycles of 30 s bilateral finger tapping and 30 s rest giving a total imaging time of 260 s. Three 8 mm slices covering motor cortex were imaged. Imaging parameters were TR=2 s, 130 acquisitions, EPI readout with 64×64 matrix, TE=40 ms, FOV=240 mm, 10 cm inversion slab, 10 mm gap between the inversion slab and the imaging region. The PICORE sequence had TI=1050 ms, while the PICORE QUIPSS II sequence had $TI_1/TI_2 = 700/1400$ ms.

Perfusion and BOLD timeseries were generated from the measured images by subtracting/averaging each image from/with its neighbouring images. The timeseries were then inspected using cross-correlation analysis with the reference function shown in figure 8.2.

Perfusion Timeseries

Figure 8.3 shows the cross-correlation maps of the magnetization difference timeseries with the reference function. High correlation coefficients are observed in the motor cortex corresponding well with the expected activation area. Since the PICORE QUIPSS II sequence is quantitative while the PICORE sequence isn't, the first was used for ROI selection. A threshold of 0.304 corresponding to a p-value of 0.00064 (uncorrected) was set in the correlation map. An ROI was selected, based on the significantly activated voxels that were part of a cluster of at least five activated voxels. This gave an ROI consisting of 50 voxels.

The correlation coefficients in motor cortex are clearly higher in the PICORE sequence than in the PICORE QUIPSS II sequence. This is due to the higher activation signals in the PICORE sequence. Figure 8.4 shows the ROI mean magnetization difference timeseries for both sequences. The signal increase dur-

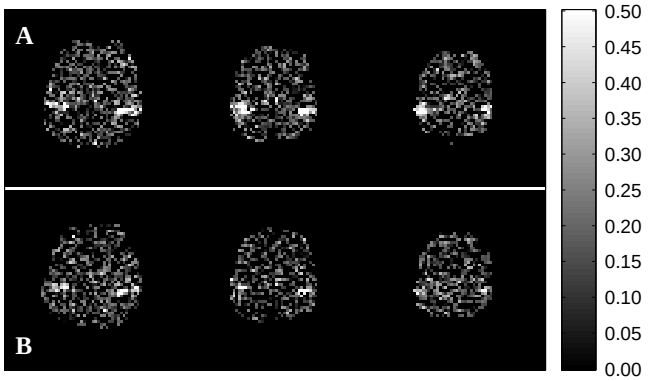

Figure 8.3: Cross-correlation maps of the magnetization difference timeseries with the reference function shown in figure 8.2. (A) PICORE sequence. (B) PICORE QUIPSS II sequence.

ing activation is larger in the PICORE sequence than in the PICORE QUIPSS II sequence and hence agrees well with the higher correlation maps.

The difference in activation signals is partly due to the difference in inversion time of the two sequences. Due to the shorter inversion time in the PICORE sequence less perfusion signal has relaxed, thus giving a higher magnetization difference. The long inversion time (TI_2) in the PICORE QUIPSS II sequence is, however, needed to satisfy equation (3.29).

The magnetization difference in the PICORE QUIPSS II experiment increases during activation from approximately 25 to around 50. Since perfusion is proportional to the magnetization difference, the increase in perfusion is around 100% during activation. For comparison, the signal increase in the PICORE experiment is around 130% which is higher than for the PICORE QUIPSS II sequence.

The PICORE sequence is therefore preferable if the aim of the experiment is merely to detect activation. However, if the aim also includes quantifying the perfusion increase, then PICORE QUIPSS II must be used at the cost of decreasing the SNR.

BOLD Timeseries

Figure 8.5 shows the correlation maps for the BOLD timeseries which were extracted from the ASL measurements by averaging the tag and control signals. The correlation coefficients are much higher than for the perfusion signal in figure 8.3. Due to the high SNR, an activation threshold of 0.65 was chosen, corresponding to a p-value $\ll 0.0005$. With the same cluster-size threshold described above, the activation ROI consisted of 100 voxels.

Figure 8.6 shows the normalized mean BOLD timeseries averaged over the ROI. The SNR of the curves is much higher than that of the magnetization

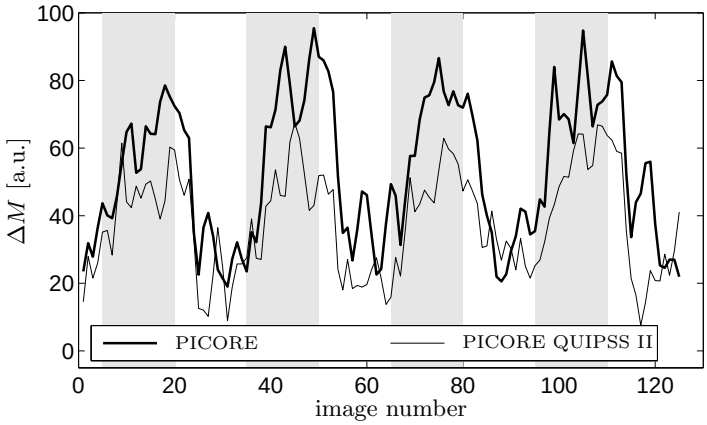

Figure 8.4: Magnetization difference timeseries averaged over the activated ROI for both the PICORE and PICORE QUIPSS II sequences. The shaded areas indicate the activation periods.

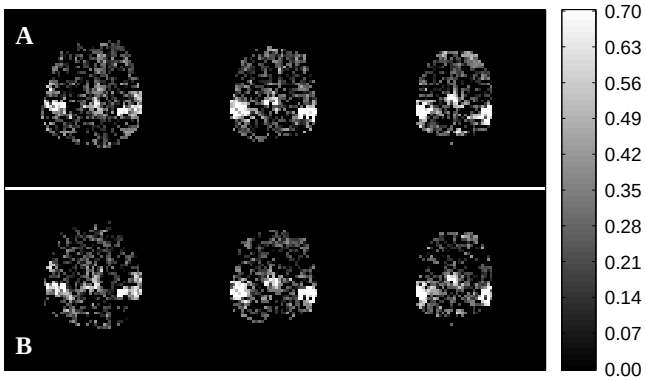

Figure 8.5: Cross-correlation maps of the BOLD timeseries with the reference function shown in figure 8.2. (A) PICORE sequence. (B) PICORE QUIPSS II sequence.

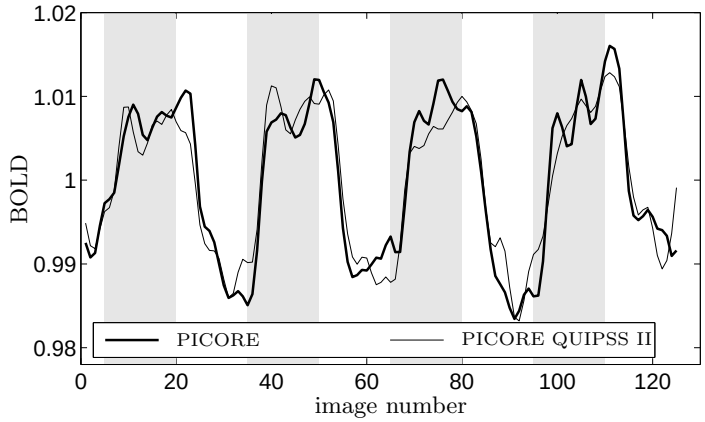

Figure 8.6: Normalized BOLD timeseries averaged over the activated ROI for both the PICORE and PICORE QUIPSS II sequences. The shaded areas indicate the activation periods.

difference timeseries in figure 8.4. Furthermore there is not any notable difference between the performance of the two sequences. Both the correlation maps and the timeseries of the PICORE and the PICORE QUIPSS II sequences are very similar. The BOLD signal in both sequences is around 2%. This illustrates that the BOLD signal is not affected by the inversion time or the QUIPSS saturation.

8.3 Offset Correction in ASL fMRI

It was seen in the previous example that quantitative perfusion fMRI using PICORE QUIPSS II suffers from low SNR at least partly due to the long inversion time, TI_2. Reducing TI_2 would decrease the signal loss due to relaxation and hence improve SNR. On the other hand, if TI_2 is decreased too much, equation (3.29) will be violated and the sequence won't be quantitative.

However, if TI_1 or δt are decreased, TI_2 can be decreased without violating equation (3.29). Reducing TI_1 is undesirable since it shortens the tagged bolus and thus decreases the amount of tagged blood that enters the imaging slice. Reducing δt can only be done by narrowing the gap between the inversion and imaging regions. As described in chapter 5, this may introduce an offset in the magnetization difference signal. However, in chapter 6, it was shown that such an offset can be estimated and corrected using an additional measurement, namely a T_1 measurement.

In this section, it will be shown how offset correction can be utilized in perfusion fMRI to increase the SNR and hence the activation detection power by lowering TI_2. This is done without sacrificing the correctness of perfusion quantification.

Imaging Protocol

Perfusion was measured in three subjects at UCSD using a PICORE QUIPSS II sequence with presaturation. The activation paradigm consisted of five periods of 30 s rest interleaved by four periods of 30 s bilateral finger tapping giving a total duration of 270 s. Three axial slices covering motor cortex were imaged. The imaging parameters were 10 cm inversion slab thickness, $TI_1 = 700$ ms, EPI readout with 64×64 matrix, FOV=240 mm, $TR = 2$ s, 135 acquisitions. The gap between the edges of the most proximal imaging slice and the inversion slab was either 5 or 10 mm. For the 10 mm gap experiment, TI_2 was 1400 ms, while for the 5 mm gap experiment, TI_2 was 1100/1200/1300/1400 ms. The difference in TI_2 between slices was $TR_{\text{slice}} = 93$ ms where the imaging order was proximal to distal. For each TI_2/gap combination, two runs were acquired.

With the RF pulses used, the 10 mm gap was sufficiently large to avoid an offset. The value of TI_2 used with the 10 mm gap (1400 ms) satisfies equation (3.29) and the TI_2/gap =1400 ms/10 mm experiments were therefore regarded as giving quantitatively correct perfusion values. These experiments will therefore in the remainder of this chapter be referred to as the *standard* experiments.

Three runs of T_1 measurements were done for the 5 mm gap experiments with 16 TI_1/TI_2 values. TI_1 values used were 50/150/350/700 ms and 4 values of TI_2 were used for each TI_1, logarithmically distributed between $TI_1 + 50$ ms and 5000 ms. $TR - TI_2$ was kept constant at 2900 ms (for the first slice). Two acquisitions were done per TI_1/TI_2 pair.

Due to motion, all images were 2D registered using the `imreg` routine from the AFNI package [170]. There was some through-plane motion, but this could not be corrected, since 3D registration partially destroyed the signal in the bottom and top slices. Since only three slices were acquired, and the technique of offset correction was only relevant for the most proximal slice, 3D registration was discarded.

Cross-Correlation Analysis

Both perfusion-weighted and BOLD-weighted timeseries were extracted from the measured data. The timeseries were cross-correlated to the reference function in figure 8.2. Figure 8.7 shows the cross-correlation maps of the magnetization difference timeseries for one subject for the five experiments. There is a clear increase in the cross-correlation coefficients in the TI_2/gap = 1100/5 experiment compared to the 1400/10 experiment which is regarded as the standard experiment. As TI_2 increases in the 5 mm gap experiments, the correlation coefficients decrease and end up very similar to the standard experiment.

Activated ROIs were defined for each experiment where the ROIs consisted of voxels having a correlation coefficient above 0.304 ($p = 0.0005$). Only activated voxels that were part of a cluster of at least 5 activated voxels were included in the ROIs. The mean number of significantly activated voxels averaged over

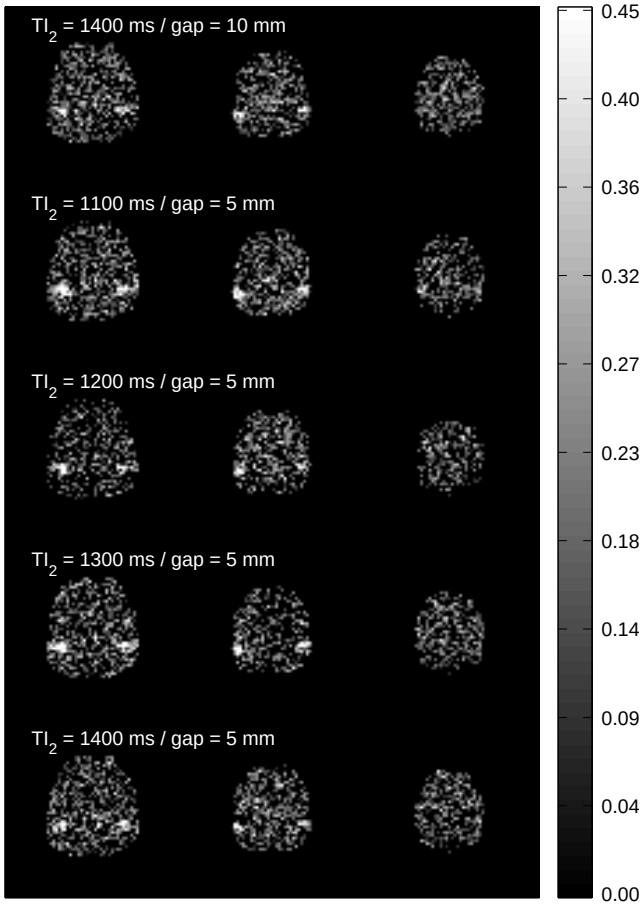

Figure 8.7: Cross-correlation maps of the magnetization difference timeseries with the reference function. The maps are for one subject and all five experiments.

Nr.	TI_2 [ms]	gap [mm]	ΔM	BOLD*
1	1400	10	49	80
2	1100	5	83	70
3	1200	5	61	71
4	1300	5	52	88
5	1400	5	34	67

Table 8.2: Number of activated voxels in the magnetization difference and the BOLD correlation maps, averaged over subjects and runs. The magnetization difference correlation maps were thresholded at 0.304 while the BOLD correlation maps were thresholded at 0.65. Only voxels that are part of a cluster of at least five significantly activated voxels are included.

*The number of activated voxels in the BOLD timeseries were only averaged over two subjects.

all subjects is listed in table 8.2. The number of activated voxels is almost 70% higher in the 1100/5 experiment than in the standard experiment.

For each subject, an ROI was defined for comparison across experiments. This ROI, which I will refer to as the *standard* ROI, was defined as the voxels that were significantly activated in both runs of the standard experiment (1400/10). This ROI did not contain any voxels in the most distal slice, and therefore it ranges over two slices only.

The correlation maps for the BOLD timeseries were very similar to those in figure 8.5 for two subjects. As found in section 8.2.3, the BOLD timeseries were not dependent on the inversion time. The BOLD timeseries in the third subject had very low cross-correlation coefficients, and only two out of the ten runs had any voxels at all with coefficients above the threshold of 0.65. Table 8.2 therefore shows the average number of activated pixels in the BOLD timeseries for the first two subjects only.

Offset Correction

Figure 8.8A shows the measured magnetization difference timeseries averaged over subjects and runs for the activated ROIs in the 1100/5 experiments. It is clear that the signal values in the timeseries of the most proximal slice have a much higher value than those in the other two slices. As in section 6.4.2, this is because the signal offset is largest in the most proximal slice.

Equations (6.30) and (6.31) were fit to the data from the T_1 measurements averaged over the same ROIs, and the fitted parameters were used to calculate the offset using equation (6.33). As expected, the most proximal slice had the largest offset. The calculated offset was subtracted from the measured magnetization difference timeseries according to equation (6.17). Figure 8.8B shows the timeseries after offset correction. The remaining difference in the signal values between slices is due to the difference in TI_2. The most proximal slice was imaged first with $TI_2 = 1100$ ms, slice 2 was imaged at $TI_2 + TR_{\text{slice}}$ and slice 3

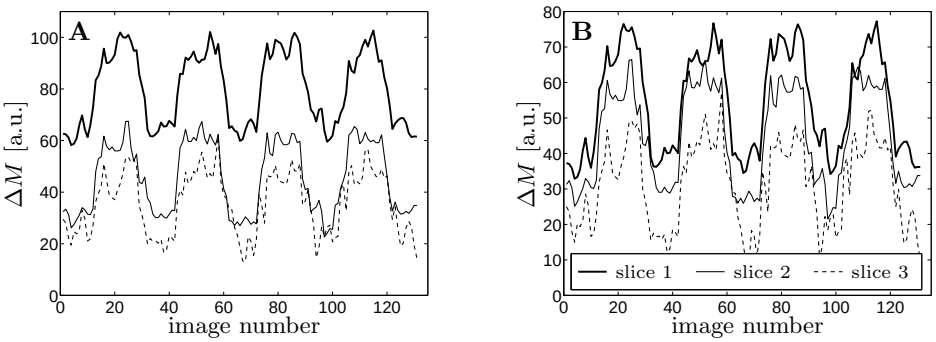

Figure 8.8: Magnetization difference timeseries averaged over subjects and runs for the activated ROIs in the 1100/5 experiments. Each slice is plotted separately, where slice 1 is the most proximal slice. (A) Before offset correction. (B) After offset correction.

was imaged at $TI_2 + 2\,TR_{\text{slice}}$.

The magnetization difference timeseries of the other 5 mm experiments were offset corrected in the same manner as above.

Effect of Inversion Time

Figure 8.9 shows the magnetization difference timeseries in the most proximal slice after offset correction, averaged over subjects. The timeseries from each of the 5 mm experiments are compared with that from the standard experiment. The standard ROI for each subject was used, so that the same ROI was used in all experiments.

The figure shows that the magnetization difference amplitude increases for decreasing TI_2 as would be expected. Both the baseline signal and increase in the signal during activation are affected by TI_2. The higher signal increase is responsible for the higher cross-correlation values found in the 1100/5 experiments compared to the standard experiment.

Figure 8.10 shows the magnetization difference timeseries after offset correction averaged both over subjects and slices. The same ROI is used for averaging the timeseries in all experiments within each subject. The results are qualitatively identical to those from figure 8.9.

General Linear Model

Since the magnetization difference timeseries depicted in figures 8.9 and 8.10 suffer from low SNR, it can be difficult to determine the magnitudes of the magnetization difference during rest and activation just by inspection. To overcome this difficulty a general linear model (GLM) [171] was used for analysing the timeseries. The covariates in the design matrix included a constant column and

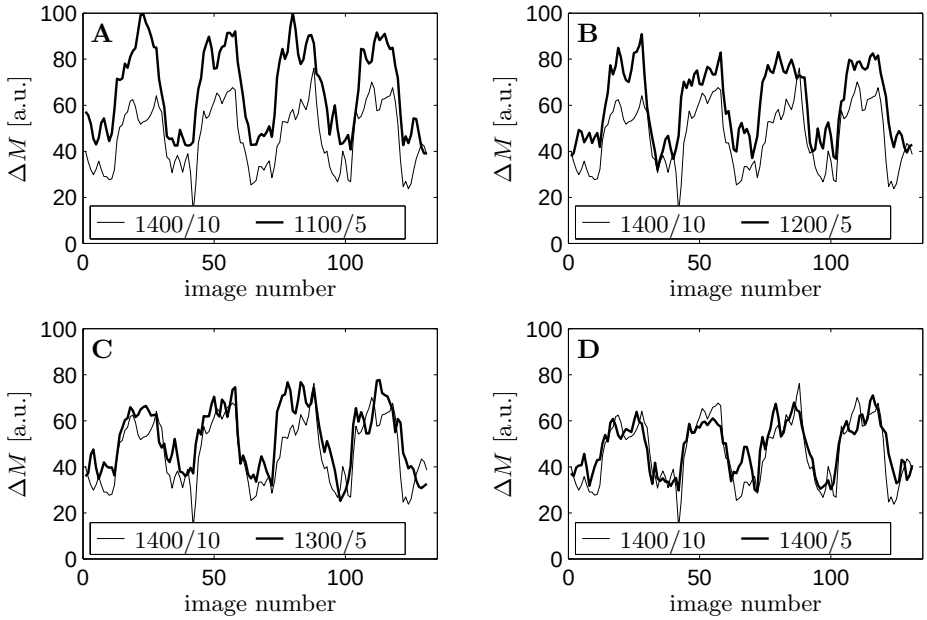

Figure 8.9: The magnetization difference timeseries in the most proximal slice after offset correction, averaged over the standard ROI in all subjects. The timeseries from the standard experiment (1400/10) is shown in each plot for comparison. TI_2 [ms] / gap [mm] = (A) 1100/5. (B) 1200/5. (C) 1300/5. (D) 1400/5.

the reference function. The reference function was rescaled to range from 0 to 1, so that the estimated parameters would be the magnetization difference baseline and magnetization difference increase during activation, respectively. The derivative of the reference function was also included in the design matrix to allow small differences in the activation lag between the measurements and the reference function.

The GLM was fit to the magnetization difference timeseries for each subject and slice separately, where the standard ROI was used for all experiments. The residuals were tested for normality and were found to be normally distributed. Perfusion values corresponding to the magnetization difference levels fit with the GLM were calculated with the same assumptions as in section 6.4.2 using equation (3.30). The calculated perfusion values were then averaged over subjects and slices.

The analyses were repeated using separate ROIs for each experiment. The ROIs used were those found with activation at a significance level of $p = 0.0005$ as described earlier. This is labelled the individual ROI analyses. The advantage

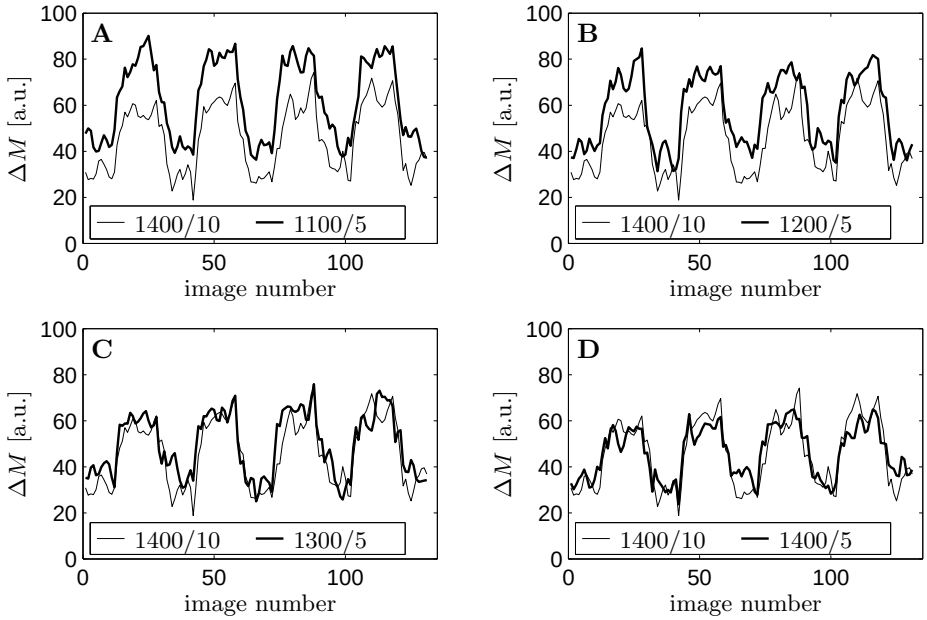

Figure 8.10: The magnetization difference timeseries after offset correction averaged over subjects and slices. The timeseries from the standard experiment (1400/10) is shown in each plot for comparison. TI_2 [ms] / gap [mm] = (A) 1100/5. (B) 1200/5. (C) 1300/5. (D) 1400/5.

of looking at each experiment separately is that the effects of motion between experiments are avoided.

Table 8.3 lists the averaged perfusion values, both for the standard ROI analyses and the individual ROI analyses. In both cases, the baseline or resting state perfusion values are listed before and after offset correction for the 5 mm experiments. As expected, perfusion is overestimated when the offset is not corrected in the narrow-gap experiments. However, baseline perfusion seems to be slightly overestimated even after offset correction in the standard ROI analyses. This is most likely due to uncorrected through-plane motion.

In the individual ROI analyses, perfusion estimates in the 5 mm experiments after offset correction are very close to those in the standard experiments. This confirms that by imaging with a narrower gap, and correcting the resulting offset, it is possible to measure perfusion increases at shorter inversion times without sacrificing the quantitative nature of the PICORE QUIPSS II sequence.

Table 8.4 lists the activation t-statistics estimated using the GLM, averaged over subjects. The t-statistics indicate the detectability of the activation given as the estimate of the signal increase divided by the standard deviation of that

	Standard ROI			Individual ROI		
Experiment	**Rest***	**Rest†**	**Increase‡**	**Rest***	**Rest†**	**Increase‡**
standard	82±3		65±4	68±2		58±3
1100/5	120±2	93±5	66±4	97±2	73±4	54±3
1200/5	118±3	94±4	61±4	93±2	72±4	54±3
1300/5	108±3	87±4	57±4	90±2	72±4	57±4
1400/5	108±3	89±4	49±4	90±2	73±3	54±4

Table 8.3: Perfusion values [ml/100g/min] averaged over all subjects and the two most proximal slices (mean±std). The baseline perfusion during rest is listed both before* and after† offset correction while the perfusion increase‡ does not depend on offset correction. Values are found by fitting a GLM to the data. Perfusion is compared for the two ROI-selection methods.

	Standard ROI		Individual ROI	
Experiment	**Slice 1**	**Slice 2**	**Slice 1**	**Slice 2**
standard	14.9	15.0	18.0	17.7
1100/5	18.5	16.7	20.0	22.5
1200/5	17.7	14.0	19.5	19.2
1300/5	13.3	13.6	15.1	17.4
1400/5	13.5	11.0	14.8	15.2

Table 8.4: Activation t-statistics of the magnetization difference found using the GLM, averaged over all subjects. The t-statistics are listed for each slice separately since the relative shortening of TI_2 is slice dependent.

estimate. The t-statistics can therefore be regarded as a contrast-to-noise ratio (CNR), where the contrast here is the activation signal. Table 8.4 therefore shows that reducing the inversion time from 1400 ms in the standard experiment to 1100 ms improves CNR by approximately 20%. In the few cases, where activation was detected in slice 3 (individual ROI analyses), CNR improved by up to 40%. This is not included in the table, though, since most runs didn't have any significantly activated voxels in slice 3.

The gain in CNR drops as TI_2 increases in the 5 mm experiments and especially in the 1400/5 experiments, CNR is somewhat lower than in the standard experiment. This is quite surprising since TI_2 is the same in the two cases. The drop in CNR is due to both a small drop in the signal increase during activation and to an increase in noise (see figure 8.10D). It is, however, not possible from the experiments at hand to determine the cause of this.

8.4 Discussion

It has in this chapter been demonstrated that ASL sequences can be used for functional imaging where it was possible to detect activation due to bilateral finger tapping. It was shown that both perfusion-weighted and BOLD-weighted images can be extracted from the measured tag and control images. While perfusion-weighted images are obtained by subtracting the tag magnetization from the control magnetization, the method of obtaining the BOLD-weighted images depends on the ASL sequence used.

The results presented here were all based on cross-correlation analyses with a reference function that was obtained by convolution of a box-car with an average haemodynamic response function [159]. Calculations were, however, also done using both a reference function which was simply a time-shifted box-car and one that was averaged from the timeseries of the ten most correlated voxels to a box-car (data not shown). The results were qualitatively very similar to the ones shown here.

Effect of QUIPSS II Saturation

The comparison of the PICORE sequence with and without QUIPSS II saturation revealed that correct quantification of perfusion changes comes at a price. During activation, perfusion not only increases, but the transit delays drop as well. Luh *et al.* found that the time-width of the tag, τ, drops from 900 ms to 700 ms during bilateral finger tapping [166]. This is caused by the increased flow velocity of incoming blood, which also induces a drop in the transit delays [65]. This drop alone can increase the magnetization difference when QUIPSS II saturation is not used, since more blood reaches the imaging slice within the inversion time.

For the PICORE QUIPSS II sequence, the drop in transit delays doesn't affect the signal increase since shorter transit delays don't affect the validity of equation (3.29). However, the drop in τ may become problematic, if it drops below 700 ms, in which case TI_1 would have to be lowered to satisfy equation (3.28). However for the experiments at hand, the PICORE QUIPSS II sequence is expected to give quantitatively correct perfusion values. This explains that the signal increase is higher in the PICORE sequence than in the PICORE QUIPSS II sequence.

The optimal choice of ASL sequence for functional imaging therefore depends on the aim of the measurement. If the aim is simply to detect activation, a non-quantitative sequence yields higher CNR, but if the aim to quantify perfusion increases, a quantitative sequence should be used.

Choice of ROI

Two methods were presented for selecting the ROI used to compare results across experiments. The first method, labelled the standard ROI method, is based on

using a reference scan for selecting an ROI which is then used in all subsequent studies. The second method, labelled the individual ROI method, is based on selecting a separate ROI for each experiment based on the activation pattern of the experiment itself. Each method has its advantages and disadvantages.

The standard ROI method is in a way more objective since no information from the experiments that are compared is used in the ROI selection. However, this requires firstly, that the area of true activation is the same in all experiments and secondly, that the images from all experiments are perfectly aligned. If the activation task is the same in all experiments, it is reasonable to expect that the associated perfusion changes are identical in all experiments. Using an ASL sequence with QUIPSS II saturation, it is therefore reasonable to expect that the area of activation is also identical in all experiments. This would not necessarily be the case, however, if QUIPSS II saturation is not used, since the changes in transit delays need not be completely coincident with the changes in perfusion.

All the experiments in section 8.3 use QUIPSS II saturation, and it can therefore be assumed that the true area of activation is identical in all experiments. However, perfect alignment was not possible due to through-plane motion. The individual ROI method overcomes the problem of motion between experiments.

The individual ROI method has another more principle advantage as well. A common aim of comparing different experiments in methodological development is to determine which set of experimental parameters has the best performance. Once one experiment is proven superior, it will often be used without the reference scan for ROI selection. It is therefore extremely relevant to consider the performance of each experiment individually.

The analyses in section 8.3 were therefore done with both types of ROI selection. Note, however, that the standard ROI method would ideally involve a third run of the standard experiment, which would be used for ROI selection and then discarded. This was, however, not possible since only two runs of each experiment were done.

Perfusion Quantification

As expected, it was found that the calculated baseline perfusion values in the narrow gap experiments without offset correction were much higher than the baseline perfusion in the standard experiment. After offset correction, perfusion was still slightly overestimated in the narrow gap experiments when the standard ROI method was used for ROI selection. An explanation for this could be that offset correction was incomplete. However, the same measurements were used for calculating global GM and WM perfusion in section 6.4.2, where perfusion values were correct, so this explanation is not very probable. The most likely reason for the difference in perfusion values is uncorrected motion. This is supported by the perfusion values found using the individual ROI method, which are very close to that found in the standard experiment.

Since the increase in magnetization difference during activation is indepen-

dent on the offset, the perfusion increase can be quantified correctly without offset correction regardless of the gap between the inversion slab and the imaging region. Therefore, if the aim of the experiment is to quantify the perfusion increase, but not the baseline, the T_1 measurements and offset estimation and correction can be omitted, saving both measurement and post-processing time.

It is worth noting that both perfusion baseline and increases are higher using the standard ROI method than using the individual ROI method. This may be due to arterial contamination of the standard ROI.

BOLD Contrast

Both perfusion-weighted and BOLD-weighted timeseries were analysed in the examples presented in this chapter, and it was found that unlike perfusion, the BOLD signal was largely independent of the inversion time. Furthermore the BOLD timeseries generally correlated better to the reference function and the activation was more widespread than that of perfusion.

If one looks at the peaks of the activation areas, it cannot generally be expected that the areas with highest perfusion changes coincide completely with the areas of highest BOLD signal changes. Figure 8.11 shows the location of the ten most-correlated voxels in each cerebral hemisphere from both the magnetization difference and the BOLD timeseries in the PICORE experiment in section 8.2.3. The peaks of activation only overlap by approximately 45%. This is in excellent agreement with the results of Luh *et al.*, who found that the activation peaks of perfusion and BOLD overlap by 40% [166]. Wong *et al.* found that the largest BOLD changes are located in the sulcus while the perfusion changes have a wider distribution and may appear to lie in two lines straddling the sulcus [29]. This agrees very well with BOLD changes having a large intravascular component [172] while perfusion changes being concentrated in GM. Activation areas found in perfusion fMRI are therefore believed to be better localized to the underlying neural activation than those found with BOLD fMRI.

Although it has been shown that functional imaging using ASL is feasible, conventional BOLD imaging, i.e. without the preparatory inversion pulses in ASL sequences, has some advantages. Firstly, the time-resolution is typically higher with BOLD imaging. In ASL sequences, time has to be allowed for the tagged blood to exchange with tissue before imaging. There is, however, an approach named Turbo ASL, that enables perfusion-weighted imaging at a time-resolution that is shorter than the inversion time [128]. The method can for example produce non-quantitative perfusion-weighted timeseries with $TR = 1$ s and $TI = 1.1$ s. Multislice BOLD imaging rarely has a time-resolution that is shorter than 1 s, but TR values less than 1 s are easily obtained for single-slice BOLD imaging.

Perfusion and BOLD imaging also differ in their brain coverage. Whole-brain coverage is typically possible in BOLD imaging at a TR of 4 s. Due to very long transit delays and longitudinal relaxation, whole-brain coverage in functional studies is rather problematic with ASL sequences. Usually, ASL sequences are

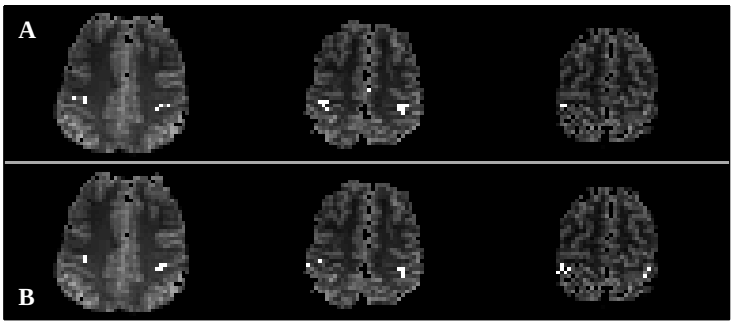

Figure 8.11: Differences in the activation areas in the magnetization difference and the BOLD timeseries in the PICORE experiment. The ten voxels with highest cross-correlation coefficients in each cerebral hemisphere are overlaid (in white) an M_0-map. (A) Magnetization difference timeseries. (B) BOLD timeseries.

not used for functional imaging in slabs thicker than 6–7 cm.

Perfusion and BOLD fMRI are used to complement each other in many studies. For example, perfusion fMRI has been used to explain the origin of negative BOLD responses found during activation in sleep studies [173]. Simultaneous perfusion and BOLD fMRI is also needed for measuring in oxygen consumption [52].

Activation Detectability

The gain found in CNR in the PICORE QUIPSS II measurements for decreasing TI_2 is due to reduced longitudinal relaxation of the tag. It was shown that an increase of 20% in CNR can be obtained by cutting TI_2 from 1400 ms in the standard experiment to 1100 ms in the narrow gap experiment. With such an increase, the activation detection power in the PICORE QUIPSS II sequence becomes almost the same as that in the PICORE sequence. Furthermore, using offset correction, the ability to quantify perfusion correctly is maintained. The increase in CNR increases in turn the number of significantly activated voxels by 70%.

This proves that through offset correction, functional imaging using quantitative ASL sequences can become as sensitive as non-quantitative ASL sequences in detecting perfusion changes during activation.

Chapter 9

Conclusions

9.1 Overall Conclusions

It has in this thesis been demonstrated how the slice profiles of the RF pulses used in ASL sequences greatly depend on the specific pulses used. However, even if optimized RF pulses are used, the slice profiles are not ideal and they will therefore affect the degree of static tissue subtraction in ASL measurements.

We introduced a new set of tools, named slice profile functions, to examine the effects of imperfect slice profiles on the measured magnetizations. Under certain commonly occurring conditions these functions can be used instead of full simulation of the Bloch equations. The slice profile functions are computationally faster and simpler to use than the full simulations.

Using both the slice profile functions and full simulations of the Bloch equations, it was found that complete static tissue subtraction in the ASL magnetization difference images can only be assured when there is a finite gap between the edges of the inversion slab and the imaging region. When this gap is too small, static tissue subtraction will be incomplete, leading to an offset or bias in the magnetization difference. The dependence of this offset on the gap was mapped for various ASL sequences and parameters using simulations.

It was found that the offset is very dependent on the specific RF pulses used in the sequence and that it can be positive, negative or oscillate as a function of the gap. Excellent agreement was found between the offset predicted by simulations and that measured in a phantom using a FAIR sequence.

Using simulations, it was also found that the use of presaturation in ASL sequences may have some surprising effects on the offset. Although the use

of one presaturation pulse before inversion generally decreases the offset, using two or more pulses actually increases the offset and causes it to oscillate as a function of the gap. This effect was found to be stronger in PICORE than in FAIR experiments and was confirmed experimentally. We also found that the order of presaturation and inversion had a large effect on this behaviour, where no oscillations were induced when the inversion preceded presaturation.

It was shown that if the inversion pulse is applied with insufficient RF power, the offset may assume very large values even at large gaps. This can be a problem when B_1 is low in some parts of the RF coil due to B_1 inhomogeneities. Adjusting the RF power in adiabatic inversion pulses should therefore balance the dangers of incomplete static tissue subtraction and RF power deposition.

Based on the notation of slice profile functions, we developed a set of equations that model the measured magnetizations in various ASL experiments. We introduced a set of scalar parameters that are theoretically related to the slice profiles, but can be estimated experimentally using T_1 measurements without any knowledge of the slice profiles. Once these parameters have been estimated, the offset can be calculated using the model equations.

Both conventional IR and fast T_1 measurements were considered for offset estimation, but it was found that only conventional IR T_1 measurements that use the same ASL sequence as that used for perfusion measurements, provide the correct information needed for offset estimation.

The model equations used to estimate the offset assume an effective relaxation rate for each of the tag and control experiments of an ASL sequence. The validity of this assumption was tested using simulations and offset estimation was found to be correct and independent of transit delays. The effective relaxation rates were, however, found to depend on the transit delays, and can therefore not be used to quantify perfusion using the T_1-method.

By subtracting the estimated offset from the measured magnetization difference, it was shown that perfusion can be quantified correctly even without complete static tissue subtraction. This method of offset correction was validated in phantom measurements with reduced gaps as well as *in vivo*.

It was found that decreasing the gap from 10 mm to 5 mm in PICORE QUIPSS II imaging induces a drop in the transit delays of 300 ms in grey matter and 100 ms in white matter. This can in turn be used to decrease the inversion time in the ASL measurements without violating the conditions needed for the sequence to be quantitative.

This was applied in functional imaging using a PICORE QUIPSS II sequence during bilateral finger tapping. Perfusion increases after offset correction in an experiment with reduced gap and inversion time were found to be identical within the error of the measurement to those in a standard experiment where there was no offset. However, an increase in CNR by 20% in the reduced gap experiment was observed along with an increase in the number of activated pixels by 70%. This shows that offset correction can be used in perfusion fMRI to increase

activation detectability without sacrificing perfusion quantification.

9.2 Outlook

A decade has now passed since Detre *et al.* [20] first measured perfusion using ASL in 1992. A lot of effort has since gone into the development of ASL into what it is today. ASL is beginning to mature as a technique and is starting to find more and more applications in numerous fields of medical imaging. This does not imply, however, that methodological development of ASL has stopped. There are still several aspects of ASL that have not been completely explored and new types of ASL labelling schemes are still being developed.

The following are a just a few of the trends in ASL that I expect will play a significant role in ASL development in the near future.

- It is generally assumed in ASL models that there is fast exchange between water in the capillaries and the tissue. This is only an approximation, and although there has been some research on this topic, I expect that we shall see the incorporation of more complex models for water exchange in the calculation of perfusion.

- A newly emerging labelling scheme is based on velocity-selective (VS) excitation. Instead of labelling spins that are in a certain position, spins flowing within a certain range of velocities are labelled in VS-ASL. This allows the labelling of spins down to arteriolar level throughout the brain for example. This method drastically reduces the transit delays especially for multislice and 3D perfusion imaging. This is certainly a labelling scheme that will be further developed in the future.

- Acquisition of both perfusion-weighted and BOLD-weighted images using double-echo spiral EPI is a powerful adversary of conventional BOLD imaging in fMRI, at least when whole-brain coverage is not needed. I expect that this application of ASL will be widely used in the future in functional imaging.

Appendix A

Scanner Implementation

This appendix contains some notes on the ASL sequences used for experimental measurements in this thesis. The measurements were conducted at two sites, namely the Danish Research Centre for Magnetic Resonance (DRCMR) and the University of California, San Diego (UCSD). The sequences will be commented for each site individually.

A.1 DRCMR

The measurements at DRCMR were conducted on a 1.5 T Siemens Magnetom Vision scanner. The sequence programming language on the Vision is `PARGEN` with a separate language for image reconstruction, namely `SPL`. Both FAIR and PICORE measurements conducted at DRCMR are included in this thesis.

FAIR Sequence

The FAIR sequence was based on modifications I made to a sequence originally provided by Henrik B.W. Larsson at DRCMR. It is a single-slice gradient-echo (GE) sequence with 64×64 matrix EPI readout.

The RF pulses used in this sequence were standard Siemens pulses. A 10.24 ms HS adiabatic inversion pulse was used with $\mu = 5$ and $\beta = 675$ Hz. A 2.56 ms Hamming filtered 3-lobe 90° sinc pulse was used for imaging.

Automated sequence running for T_1 measurements was implemented using a macro programming environment based on `Perl` scripts. This environment was provided by Lars G. Hanson.

PICORE Sequence

The PICORE sequence was based on modifications of a FAIR/EPISTAR sequence provided by Eric C. Wong at UCSD. It is a single-slice GE sequence with 128×128 matrix EPI readout.

The RF pulses used in this sequence are not Siemens standard pulses. A 15 ms HS adiabatic inversion pulse was used with $\mu = 10$ and $\beta = 800$ Hz. Imaging was done with a 5.12 ms 90° SLR pulse with 0.01% passband ripple and 0.4% rejectband ripple. Optional presaturation and QUIPSS II saturation were achieved with two 12.8 ms maximum phase 90° SLR pulses with 0.01% passband ripple and 0.4% rejectband ripple separated by a crusher gradient.

A.2 UCSD

The measurements at UCSD were conducted on a 1.5 T Siemens Magnetom Symphony scanner. The sequence programming language on the Symphony is `SDE` with the same language for image reconstruction as on the Vision, namely `SPL`. Only PICORE (with and without QUIPSS II saturation) measurements conducted at UCSD are included in this thesis.

PICORE Sequence

The PICORE sequence was provided by Thomas T. Liu and Eric C. Wong at UCSD. Although the sequence was capable of running with various labelling schemes and imaging schemes, the results included in this thesis only contain data from PICORE runs (with and without QUIPSS II saturation). The sequence was a multislice sequence with 64×64 matrix EPI readout (GE mode was used).

A 15 ms HS adiabatic inversion pulse was used with $\mu = 10$ and $\beta = 800$ Hz. Imaging was done with a 3.2 ms 90° Hamming filtered sinc pulse. Optional presaturation and QUIPSS II saturation were achieved with two 12.8 ms Hamming filtered sinc pulses separated by a crusher gradient.

I modified the sequence in order to automate running with multiple inversion times for the T_1 measurements.

Appendix B

Cayley-Klein Parameters

In the spin domain representation, rotation matrices are not given by 3×3 rotation matrices as in section 4.1, but by 2×2 complex unitary matrices containing the Cayley-Klein parameters.

In the classical three-dimensional space, the rotation matrix corresponding to a rotation by an angle Φ about an arbitrary vector, $\mathbf{n}$, as shown in figure B.1, is given by equation (4.24).

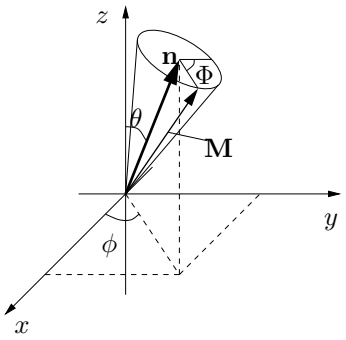

Figure B.1: Rotation of a vector $\mathbf{M}$ around an arbitrary vector, $\mathbf{n}$, by an angle Φ.

In the spin domain, a rotation matrix is given by the 2×2 complex unitary matrix

$$\mathbf{Q} = \begin{pmatrix} \alpha & -\beta^* \\ \beta & \alpha^* \end{pmatrix}, \tag{B.1}$$

where α and β are the complex Cayley-Klein parameters. Since α and β are complex, there are four quantities to be specfied in $\mathbf{Q}$. However, only three independent quantities are needed to specify a three-dimensional orientation, and an additional condition is therefore imposed. The condition is that $|\mathbf{Q}| = 1$, which gives

$$\alpha\alpha^* + \beta\beta^* = 1. \tag{B.2}$$

The Cayley-Klein parameters describing the rotation given in figure B.1 are given by

$$\alpha = \cos\frac{\Phi}{2} - in_z \sin\frac{\Phi}{2} \tag{B.3}$$

$$\beta = -i(n_x + in_y)\sin\frac{\Phi}{2}, \tag{B.4}$$

where n_x, n_y and n_z are the components of $\mathbf{n}$ [113].

The conventional 3×3 rotation can be calculated from the Cayley-Klein parameters as

$$\mathbf{R} = \begin{pmatrix} \frac{1}{2}(\alpha^2 + \alpha^{*2} - \beta^2 - \beta^{*2}) & \frac{i}{2}(-\alpha^2 + \alpha^{*2} + \beta^2 - \beta^{*2}) & \alpha\beta^* + \alpha^*\beta \\ \frac{i}{2}(\alpha^2 - \alpha^{*2} + \beta^2 - \beta^{*2}) & \frac{1}{2}(\alpha^2 + \alpha^{*2} + \beta^2 + \beta^{*2}) & i(\alpha\beta^* - \alpha^*\beta) \\ -\alpha\beta - \alpha^*\beta^* & i(\alpha\beta - \alpha^*\beta^*) & \alpha\alpha^* - \beta\beta^* \end{pmatrix}. \tag{B.5}$$

Comparing equations (B.3) and (B.4) with equation (4.26), it is easily derived that

$$\alpha = e_0 + ie_3\,, \qquad \beta = -e_2 + ie_1 \tag{B.6}$$

Equation (4.25) is then easily derived by inserting equation (B.6) into (B.5).

Coordinate Transformation

The rotation matrix, $\mathbf{R}$, is used for example to calculate the magnetization after a rotation by

$$\mathbf{M}^+ = \begin{pmatrix} M_x^+ \\ M_y^+ \\ M_z^+ \end{pmatrix} = \mathbf{R}\begin{pmatrix} M_x^- \\ M_y^- \\ M_z^- \end{pmatrix} = \mathbf{R}\mathbf{M}^-, \tag{B.7}$$

where $\mathbf{M}^-$ is the magnetization before the rotation, and $\mathbf{M}^+$ is the magnetization after the rotation.

Introducing the variable

$$M_{xy} = M_x + iM_y, \tag{B.8}$$

and $\mathbf{M}' = (M_{xy}, M_{xy}^*, M_z)^T = \mathbf{B}\mathbf{M}$, where

$$\mathbf{B} = \begin{pmatrix} 1 & i & 0 \\ 1 & -i & 0 \\ 0 & 0 & 1 \end{pmatrix}, \tag{B.9}$$

equation (B.7) transforms into

$$\mathbf{M'}^{+} = \mathbf{R'M'}^{-} = \mathbf{BRB}^{-1}\mathbf{M'}^{-} \tag{B.10}$$

or

$$\begin{pmatrix} M_{xy}^{+} \\ M_{xy}^{+*} \\ M_{z}^{+} \end{pmatrix} = \begin{pmatrix} (\alpha^*)^2 & -\beta^2 & 2\alpha^*\beta \\ -(\beta^*)^2 & \alpha^2 & 2\alpha\beta^* \\ -\alpha^*\beta^* & -\alpha\beta & \alpha\alpha^* - \beta\beta^* \end{pmatrix}, \begin{pmatrix} M_{xy}^{-} \\ M_{xy}^{-*} \\ M_{z}^{-} \end{pmatrix} \tag{B.11}$$

where the rotation matrix, $\mathbf{R'}$, is clearly more compact than $\mathbf{R}$ in equation (B.5). This notation gives rise to useful expressions for several special cases. If the initial magnetization is in equilibrium, i.e. $\mathbf{M}^{-} = (0, 0, M_0)^T$, the excitation slice profile is

$$M_{xy}^{+} = 2\alpha^*\beta M_0, \tag{B.12}$$

and the inversion slice profile is

$$M_{z}^{+} = (\alpha\alpha^* - \beta\beta^*)M_0. \tag{B.13}$$

Multiple Rotations

Mutiple rotations are achieved simply by multiplying the corresponding spin rotation matrices just as the case with conventional 3×3 rotation matices. If the j'th rotation matrix is given by

$$\mathbf{Q}_j = \begin{pmatrix} a_j & -b_j^* \\ b_j & a_j^* \end{pmatrix} \tag{B.14}$$

where a_j and b_j correspond to equations (B.3) and (B.4) with the j'th rotation angle, Φ_j. The total rotation is then given by $\mathbf{Q} = \mathbf{Q}_n\mathbf{Q}_{n-1}\ldots\mathbf{Q}_1$.

Appendix C

Publications

The following papers and conference proceedings contain some of the work on which this thesis is based.

- K. Sidaros, I. K. Andersen, H. Gesmar, E. Rostrup and H. B. W. Larsson, *Improved Perfusion Quantification in FAIR Imaging by Offset Correction*, Magn Reson Med 46(1), p.193-197, 2001.
- I. K. Andersen, K. Sidaros, H. B. W. Larsson, E. Rostrup and H. Gesmar, *A Model System for Perfusion Quantification using FAIR*, Magn Reson Imag, 18(5), p. 565-74, 2000.
- I. Andersen, K. Sidaros, H. Gesmar, H. Larsson, E. Rostrup, *The Influence of a Signal Offset on Perfusion Quantification using FAIR*, Proc. 5th Int. Conference on the Mapping of the Human Brain, NeuroImage 9(6), p. S150, 1999.
- K. Sidaros, I. Andersen, H. Larsson, H. Gesmar, E. Rostrup, *Zero Perfusion Calibration of FAIR Imaging with Arbitrary Inversion Slice Profiles*, Proc. 16th Annual Meeting of the European Society for Magnetic Resonance in Medicine and Biology, Magma, 8, suppl. 1, p. 165, 1999.
- K. Sidaros, I. Andersen, H. Larsson, H. Gesmar, E. Rostrup, *Offset Correction in FAIR Imaging*, Proc. 8th Annual Meeting of the International Society of Magnetic Resonance in Medicine, Denver, p. 712, 2000.
- K. Sidaros, I. Andersen, H. Larsson, H. Gesmar, E. Rostrup, *Effect of Slice Profiles on the Accuracy of Fast T_1 Measurements*, Proc. 8th Annual Meeting of the International Society of Magnetic Resonance in Medicine, Denver, p. 429, 2000.

- K. Sidaros, T. T. Liu, E. C. Wong and R. B. Buxton, *Offset Correction in PICORE QUIPSS II Imaging*, Proceedings of the 10th Annual Meeting of the International Society of Magnetic Resonance in Medicine, Honolulu, p. 1063, 2002.
- K. Sidaros, T. T. Liu, T. E. Lund, E. C. Wong and R. B. Buxton, *Improved SNR in Perfusion fMRI by Offset Correction*, Proceedings of the 10th Annual Meeting of the International Society of Magnetic Resonance in Medicine, Honolulu, p. 624, 2002.

These references are included on the following pages.

- Magn Reson Med 46(1), p.193-197, 2001.

Magnetic Resonance in Medicine 46:193–197 (2001)

Improved Perfusion Quantification in FAIR Imaging by Offset Correction

Karam Sidaros,[1,2*] Irene K. Andersen,[1,2] Henrik Gesmar,[2] Egill Rostrup,[2] and Henrik B.W. Larsson[2]

Perfusion quantification using pulsed arterial spin labeling has been shown to be sensitive to the RF pulse slice profiles. Therefore, in Flow-sensitive Alternating-Inversion Recovery (FAIR) imaging the slice selective (ss) inversion slab is usually three to four times thicker than the imaging slice. However, this reduces perfusion sensitivity due to the increased transit delay of the incoming blood with unperturbed spins. In the present article, the dependence of the magnetization on the RF pulse slice profiles is inspected both theoretically and experimentally. A perfusion quantification model is presented that allows the use of thinner ss inversion slabs by taking into account the offset of RF slice profiles between ss and nonselective inversion slabs. This model was tested in both phantom and human studies. Magn Reson Med 46:193–197, 2001. © 2001 Wiley-Liss, Inc.

Key words: pulse profiles; FAIR; perfusion quantification; spin labeling

It has been shown that pulsed arterial spin labeling can be used in quantifying perfusion (1–6) and in measuring perfusion changes (4,6–8). All pulsed arterial spin labeling techniques include an RF inversion pulse and it has been shown that perfusion measurements using these techniques are sensitive to the slice profile of this pulse (4). Much work has therefore been done to improve the slice profile of the inversion pulse (9–11).

In FAIR imaging (2,7), the perfusion-weighted images are acquired as the difference between an image acquired after slice-selective (ss) inversion and one acquired after nonselective (ns) inversion. However, the nonideal shape of the inversion and the imaging slice profiles results in an offset in the perfusion-weighted difference image at zero perfusion unless the ss inversion slab is several times thicker than the imaging slice (12–14). This reduces the sensitivity to perfusion since it increases the transit delays for the incoming blood (6), especially in multislice FAIR imaging. It is therefore desirable to overcome the errors due to the slice profiles without increasing the relative thickness of the inversion slab.

The aim of this study was to investigate the dependence of the offset in the difference image on the thickness of the ss inversion slab and to introduce a model that corrects for the effect of the offset on perfusion quantification.

THEORY

In previous work on perfusion quantification using FAIR (2,7,15), it has been assumed that the difference between the ss and the ns signals is zero in the absence of perfusion. In other words, the effective degree of inversion is the same in the ss and the ns cases and the slice profiles of the RF pulses are ignored. In the simple case where blood T_1 and transit delay effects are ignored, the relaxation equations for the longitudinal magnetization in the ss and the ns experiments are:

$$M^{ss}(TI) = (M(0) - M_0)e^{-R_1^{app}TI} + M_0 \quad [1]$$

$$M^{ns}(TI) = (M(0) - M_0)e^{-R_1 TI} + M_0, \quad [2]$$

where M_0 is the equilibrium magnetization, $M(0)$ is the longitudinal magnetization just after inversion, TI is the inversion time, R_1 is the longitudinal relaxation rate of tissue, $R_1^{app} = R_1 + f/\lambda$ is the apparent longitudinal relaxation rate of tissue in the ss experiment, f is perfusion and λ is the brain–blood partition coefficient of water (2). However, the assumption of $M(0)$ being the same in Eqs. [1] and [2] only holds if the ss inversion slab is several times thicker than the imaging slice. If this is not the case, the slice profiles of the inversion and the imaging pulses must be considered.

The imperfect slice profiles can be expressed as an imperfect degree of inversion that is different in the ss and the ns experiments (13,14,16). This is equivalent to allowing different values for the longitudinal magnetization immediately after the ss and the ns inversions, i.e., $M^{ss}(0)$ and $M^{ns}(0)$ may differ. Still assuming the simple case where blood T_1 and transit delay effects are ignored, the relaxation equations for the ss and the ns experiments become:

$$M^{ss}(TI) = (M^{ss}(0) - M_0)e^{-R_1^{app}TI} + M_0 \quad [3]$$

$$M^{ns}(TI) = (M^{ns}(0) - M_0)e^{-R_1 TI} + M_0. \quad [4]$$

Since $fTI/\lambda \ll 1$ for physiological perfusion ranges, the difference magnetization, $\Delta M \equiv M^{ss} - M^{ns}$, can be expressed as:

$$\Delta M(TI) \approx [M_0 - M^{ss}(0)]\frac{f}{\lambda} \cdot TI \cdot e^{-R_1 TI} + [M^{ss}(0) - M^{ns}(0)]e^{-R_1 TI}. \quad [5]$$

The second term in Eq. [5] is the offset at time TI. Perfusion can then be calculated from:

[1]Department of Mathematical Modelling, Technical University of Denmark, Lyngby, Denmark.
[2]Danish Research Center of Magnetic Resonance, Hvidovre Hospital, Hvidovre, Denmark.
*Correspondence to: Karam Sidaros, Hvidovre Hospital, DRCMR-340, Kettegaard Alle 30, 2650 Hvidovre, Denmark. E-mail: karams@magnet.drcmr.dk
Received 26 June 2000; revised 8 December 2000; accepted 8 January 2001.

$$\frac{f}{\lambda} = \frac{\Delta M(TI) - [M^{ss}(0) - M^{ns}(0)]e^{-R_1 TI}}{[M_0 - M^{ss}(0)]e^{-R_1 TI} \cdot TI}. \quad [6]$$

Predicting the Offset

Although the model given by Eqs. [3] and [4] takes the offset into account, it does not show how the offset depends on the slice profiles of the RF pulses. It has previously been shown (14) that the slice profiles can be incorporated directly in the model. In this case, the terms $M^{ss}(t)$ and $M^{ns}(t)$ in Eqs. [3] and [4] are calculated by integrating the spatially dependent magnetization over the direction, z, perpendicular to the slice. The observed signal offset at time zero is then given by:

$$M^{ss}(0) - M^{ns}(0) = M_0 \int_{-\infty}^{\infty} (g_z^{ss}(z) - g_z^{ns}(z)) \cdot g_y^{90}(z) dz. \quad [7]$$

Here M_0 is the equilibrium magnetization concentration per unit length, the functions $g_z^{ss}(z)$ and $g_z^{ns}(z)$ are the longitudinal magnetization (M_z) profiles of the ss inversion pulse and the ns inversion pulse, respectively, and the function $g_y^{90}(z)$ is the M_y profile of the $90°_x$ excitation pulse. The latter means that $M_y(z)$, the y-component of the transverse magnetization, just after the $90°_x$ excitation pulse is given by $g_y^{90}(z) \cdot M^-(z)$, assuming that the magnetization just before the pulse, $M^-(z)$, is purely longitudinal.

The functions $g_z^{ss}(z)$, $g_z^{ns}(z)$, and $g_y^{90}(z)$, which are dimensionless and normalized, can either be calculated theoretically using the Bloch equations (17) or measured experimentally (14).

METHODS

Phantom Studies

All measurements were performed on a Siemens Vision 1.5T scanner using a gradient echo blipped EPI sequence. FAIR measurements were made with interleaved ss and ns images of a homogeneous gel phantom doped with Gd-DTPA, giving it a T_1 of approximately 1.1 s. The measurements were repeated with different ss inversion slab thicknesses using an adiabatic hyperbolic secant (HS) inversion pulse. The range of the inversion slab thicknesses was 14–140 mm while the imaging slice had a constant thickness of 10 mm. The experimental parameters were TI/TR = 1/20 s, 64 × 64 matrix, 230 × 230 mm FOV and 32 repetitions. T_1 measurements were also carried out using the same sequence repeated with different inversion times (17 TI values in the range of 50–5000 ms, TR = 20 s and two repetitions).

The signals in each image were averaged over an ROI consisting of 37 pixels. Equations [3] and [4] were then simultaneously fitted to the measured T_1 relaxation curves using least squares fitting, giving estimates of the parameters M_0, $M^{ss}(0)$, $M^{ns}(0)$, R_1^{app}, and R_1.

The offset at time zero, $M^{ss}(0) - M^{ns}(0)$, was calculated as a function of ss inversion slab thickness. This was compared to the theoretical offset given by Eq. [7]. The functions $g_z^{ss}(z)$, $g_z^{ns}(z)$, and $g_y^{90}(z)$ used in Eq. [7] were calculated using the RF pulses and the Bloch equations (17). The RF pulses used in the experimental setup were an adiabatic HS inversion pulse (μ = 5, β = 675 Hz, T = 10,240 μs, BW = 1 kHz), and a standard 3-lobe sinc 90° excitation pulse (T = 2560 μs, BW = 1 kHz). The calculations were repeated for two other excitation pulses for comparison, namely, a 5-lobe sinc (T = 5120 μs, BW = 4 kHz) and an optimized pulse using the Shinnar-Le Roux algorithm (T = 5120 μs, BW = 2 kHz, 0.01% pass band ripple, 0.4% reject band ripple) (18,19).

Perfusion was calculated using Eq. [6] where the term $\Delta M(TI)$ was obtained from the FAIR measurement while the parameters $M^{ss}(0)$, $M^{ns}(0)$, R_1, and M_0 were obtained from the T_1 fit.

Equations [1] and [2], which do not correct for the signal offset, were also fitted to the data and perfusion was calculated on the basis of those equations for comparison.

Human Studies

FAIR measurements with different ss inversion slab thicknesses were also done on four healthy volunteers, ages 25–27 years. The range of the inversion slab thicknesses was 18–54 mm while the imaging slice had a constant thickness of 10 mm. The experimental parameters were TI/TR = 1/6 s, 30 repetitions. T_1 measurements were carried out using the same sequence repeated with 11 different inversion times within the range of 50–5000 ms using five repetitions.

The parameters M_0, $M^{ss}(0)$, $M^{ns}(0)$, R_1^{app}, and R_1 in Eqs. [3] and [4] were estimated as in the phantom studies. Perfusion images were then calculated using Eq. [6].

The acquired T_1 maps were used for segmentation where gray matter (GM) areas were defined using a threshold of $1.0 < T_1 < 1.1$ s. A number (from 6–10) of GM ROIs for each subject were drawn on the segmented T_1 images. Pixels including large blood vessels were not included in the ROIs. These pixels were characterized by their very high perfusion values and were located especially in the insula, the brain surface veins, and the central greater veins.

The calculated perfusion values in each ROI were analyzed using both parametric (regression) and nonparametric (Spearman's and Kendall's rank correlation coefficients) statistical methods (20).

For comparison, Eqs. [1] and [2], which do not correct for the signal offset, were also fitted to the data and perfusion was calculated on the basis of those equations.

RESULTS AND DISCUSSION

Phantom Studies

Figure 1 shows the slice profile functions, $g_z^{ss}(z)$ for the inversion pulse and $g_y^{90}(z)$ and $g_x^{90}(z)$ for the 3-lobe sinc excitation pulse. These functions are used to calculate the offset using Eq. [7]. Note that $g_x^{90}(z)$ is antisymmetric, and is therefore not included in Eq. [7]. It is assumed that $g_z^{ns}(z) = -1$ corresponding to perfect inversion over the entire range.

Figure 2 shows the theoretical offset as a function of the ss inversion-slab thickness (curves) given by Eq. [7] for the three sets of RF pulses. The excitation pulses were a 3-lobe

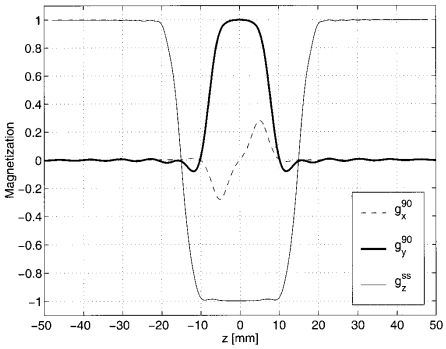

FIG. 1. The slice profile functions of the RF pulses used in the experimental setup. The function $g_z^{ss}(z)$ is the M_z profile of an ss adiabatic HS inversion pulse with a FWHM of 30 mm, and the functions $g_x^{90}(z)$ and $g_y^{90}(z)$ are the M_x and the M_y profiles of the 10 mm FWHM 90° 3-lobe sinc excitation pulse, respectively. Note that $g_x^{90}(z)$ is antisymmetric and is therefore not included in the integral in Eq. [7]. The side ripples in $g_y^{90}(z)$ have a very large effect on the shape of the offset curve.

sinc, a 5-lobe sinc, and an optimized pulse, while the inversion pulse was an adiabatic HS pulse in all cases. It is clear that the offset is strongly dependent on the RF pulse used.

We found that the ripples in the side lobes of the transverse magnetization profile, $g_y^{90}(z)$, completely defined the shape of the offset curve. Small variations in the shape of the ripples had a huge impact on the shape of the offset curve. Without these ripples the offset is always positive, as can be seen with the optimized pulse, which has very weak ripples. This result should be kept in mind when designing optimized excitation pulses for FAIR measurements, where ripples in the main lobe may be preferred over side lobe ripples.

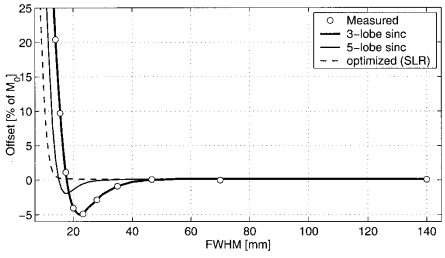

FIG. 2. The offset, $M^{ss}(0) - M^{ns}(0)$, found in the phantom studies (points), in percent of the equilibrium magnetization, M_0, as a function of the slice thickness of the inversion slab (FWHM). The imaging slice had a constant thickness of 10 mm. Also shown is the theoretical offset (curves) calculated using Eq. [7] for three excitation pulses: a 3-lobe sinc (used experimentally), a 5-lobe sinc, and an optimized pulse. An adiabatic HS pulse was used for inversion in all three cases.

The measured offset, $M^{ss}(0) - M^{ns}(0)$, found in the phantom studies is also depicted in Fig. 2 and it is found to be in excellent agreement with the theoretical curve.

Taking into consideration that the difference signal in gray matter due to perfusion is about 1% of M_0, Fig. 2 shows that when using the 3-lobe sinc excitation pulse the thickness of the inversion slab must be above approximately 45 mm for the offset to be negligible. Although the other pulses gave a smaller offset, the 3-lobe sinc was used for all the measurements to best illustrate the subject of this study. The relevance of this is also supported by the fact that customized RF pulses are not available on all MRI units.

Figure 3 shows the average perfusion values calculated in the phantom at different ss inversion slab thicknesses using Eq. [6]. The figure includes both the results obtained using the model with offset correction (Eqs. [3] and [4]) and those obtained using the model without offset correction (Eqs. [1] and [2]). It can be seen that the two models give the same results when the inversion slab thickness is large, corresponding to no offset. At low slab thicknesses, however, the model without offset correction (Eqs. [1] and [2]) gives erroneous perfusion estimates, while the offset correction in Eqs. [3] and [4] clearly compensates for the offset giving the correct perfusion value of zero. Linear regression analyses on the offset-corrected perfusion values show that neither slope ($p > 0.4$) nor intercept ($p > 0.18$) are significantly different from zero. Nonparametric analyses gave similar results. The standard deviation of the calculated perfusion values is 2.4 ml/100g/min.

Human Studies

Figure 4 shows the perfusion values found in GM ROIs in four subjects at different ss inversion slab thicknesses, normalized to the perfusion value found at the smallest slab thickness in the offset corrected case. Figure 4a shows the results obtained using the model with offset correction (Eqs. [3] and [4]), while Fig. 4b shows those obtained without offset correction (Eqs. [1] and [2]).

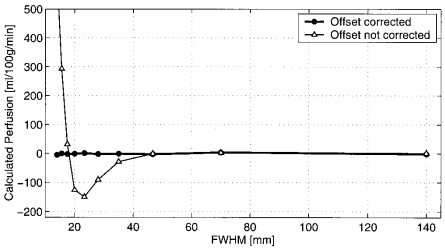

FIG. 3. Average perfusion values calculated in a homogeneous ROI in a phantom at different inversion slab thicknesses. The results from the simple model without offset correction as well as the results from the model with offset correction are shown.

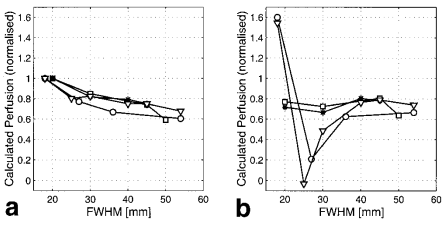

FIG. 4. Normalized perfusion values from GM ROIs in four subjects at different inversion slab thicknesses. **a:** Results from the model with offset correction. **b:** Results from the simple model without offset correction. Each marker type is for one subject.

As with the phantom results, it is seen that the two models give similar results when the offset is zero (large slab thickness). At low slab thicknesses, it is clear that the model without offset correction (Eqs. [1] and [2]) gives more varied and erroneous perfusion estimates in two of the subjects. The lack of variation in the perfusion estimates with varying inversion slab thickness in the remaining two subjects can be explained by differences in susceptibility between the subjects. The exact slice profiles of the RF pulses depend on the susceptibility, and since the offset is very sensitive to the slice profiles (Fig. 2), it will depend on the susceptibility as well. This agrees well with the fact that the perfusion estimates in all subjects were very sensitive to the specific ROI used when the offset was not corrected.

Analysis of the R_1 estimation using Eqs. [3] and [4] revealed a significant linear dependence of R_1^{app} on the slab thickness ($p < 0.005$) while R_1 was independent of the slab thickness ($p > 0.38$) as should be the case since $R_1^{app} = R_1 + f/\lambda$. This independence was not observed without the offset correction where the R_1 estimates were dependent on the offset.

Although the offset correction in Eqs. [3] and [4] markedly improves the perfusion estimation, it does not give a constant perfusion at all thicknesses. This is not due to inadequate offset compensation, but due to the transit delay of the incoming uninverted blood spins, which is not included in the model. When the inversion slab thickness increases the transit delay increases and perfusion is underestimated.

Intersubject Variation

The offset-corrected perfusion levels used for normalization of the data shown in Fig. 4 varied between 70–108 ml/100g/min, depending on the subject. The different values can be explained partly by different resting perfusion levels in the different subjects and partly by the difference in the blood vessel geometry proximal to the imaging slice. Note that the imaging slice was not positioned identically in all the subjects.

Regression analyses of the estimated perfusion values were done for each subject individually, which revealed that there were no significant differences in the decrease rate of the estimated perfusion values between the four subjects as a function of increasing ss inversion slab thickness ($p > 0.5$). This indicates that the transit delay has the same effect on the estimated perfusion regardless of the initial perfusion level.

Noise Considerations

Equation [6], which is used for perfusion estimation, can be schematically expressed as:

$$\text{Estimated perfusion} = \frac{[\text{True } \Delta M + \text{True offset}] - \text{Estimated offset}}{\text{Normalization factor}}, \quad [8]$$

where the term [True ΔM + True offset] is the measured ΔM. It is clear that errors in the offset estimation will propagate to the perfusion estimate. Assuming that the relative error of the estimated offset is constant, the absolute perfusion error will increase as the offset increases compared to the true ΔM. So, although using narrow inversion slabs gives higher sensitivity and accuracy of the perfusion estimate due to the reduced transit delay, the perfusion estimate becomes less precise.

We found evidence for this in two of the four subjects, where the standard error of the estimated perfusion increased with decreasing slab thickness. In the subject where this effect was strongest, this meant an increase in the ROI perfusion standard error of the mean from 3% of the perfusion value at 54 mm slab thickness to 5% at 18 mm slab thickness. Without ROI averaging, the errors were 47% at 54 mm and 77% at 18 mm. The corresponding estimated perfusion values were 48 ml/100g/min at 54 mm and 72 ml/100g/min at 18 mm.

Therefore, the optimal inversion slab thickness depends on the trade-off between the noise introduced by the offset and the error introduced by the transit delay, which is not uniform within the brain.

Application to Multislice and 3D Imaging

The application of the offset correction method presented here to interleaved multislice imaging is straightforward. Equation [7] is still valid, with $g_y^{90}(z)$ representing each imaging pulse. For true 3D imaging, Eq. [7] must be expanded to include the point spread function in the slice direction, and therefore the theoretical calculation of the offset becomes more difficult. However, the offset correction method using the experimental data remains valid.

CONCLUSION

Quantitative perfusion measurements consisting of FAIR and T_1 measurements were done at varying slab thicknesses of the slice selective inversion pulse. The offset between the slice-selective and the nonselective images at zero perfusion was measured in a phantom and found to perfectly match the theoretical values. It was shown that a simple correction for the offset in the signal equations considerably improves perfusion quantification when using narrow inversion slabs, both in phantom studies and in vivo. Although this correction does not compensate for

transit delay effects, it allows the use of narrow inversion slabs, thus reducing the transit delay effects and leading to considerably increased perfusion sensitivity.

It was also found that the shape of the offset as a function of the slab thickness was largely caused by ripples in the side lobes of the excitation pulse, whereas ripples in the main lobe had little effect on the offset. This should be kept in mind when designing optimized RF pulses for FAIR imaging.

REFERENCES

1. Detre JA, Leigh JS, Williams DS, Koretsky AP. Perfusion imaging. Magn Reson Med 1992;23:37–45.
2. Kwong KK, Chesler DA, Weisskoff RM, Donahue KM, Davis TL, Østergaard L, Campbell TA, Rosen BR. MR Perfusion studies with T_1-weighted echo planar imaging. Magn Reson Med 1995;34:878–887.
3. Kim S, Ugurbil K. Comparison of blood oxygenation and cerebral blood flow effects in fMRI: estimation of relative oxygen consumption change. Magn Reson Med 1997;38:59–65.
4. Wong EC, Buxton RB, Frank LR. Implementation of quantitative perfusion imaging techniques for functional brain mapping using pulsed arterial spin labeling. NMR Biomed 1997;10:237–249.
5. Wong EC, Buxton RB, Frank LR. Quantitative imaging of perfusion using a single subtraction (QUIPSS and QUIPSS II). Magn Reson Med 1998;39:702–708.
6. Buxton RB, Frank LR, Wong EC, Siewert B, Warach S, Edelman RR. A general kinetic model for quantitative perfusion imaging with arterial spin labeling. Magn Reson Med 1998;40:383–396.
7. Kim S. Quantification of relative cerebral blood flow change by flow-sensitive alternating inversion recovery (FAIR) technique: application to functional mapping. Magn Reson Med 1995;34:293–301.
8. Kim SG, Rostrup E, Larsson HB, Ogawa S, Paulson OB. Determination of relative CMRO2 from CBF and BOLD changes: significant increase of oxygen consumption rate during visual stimulation. Magn Reson Med 1999;41:1152–1161.
9. Frank LR, Wong EC, Buxton RB. Slice profile effects in adiabatic inversion: application to multislice perfusion imaging. Magn Reson Med 1997;38:558–564.
10. Payne GS, Leach MO. Implementation and evaluation of frequency offset corrected inversion (FOCI) pulses on a clinical MR system. Magn Reson Med 1997;38:828–833.
11. Yongbi MN, Branch CA, Helpern JA. Perfusion imaging using FOCI RF pulses. Magn Reson Med 1998;40:938–943.
12. Andersen IK, Sidaros K, Gesmar H, Larsson HBW, Rostrup E. The influence of a signal offset on perfusion quantification using FAIR. NeuroImage 1999;9:S150.
13. Sidaros K, Andersen IK, Gesmar H, Larsson HBW, Rostrup E, Bovee WMMJ. Zero perfusion calibration of FAIR imaging with arbitrary inversion slice profiles. MAGMA 1999;8(Suppl 1):165.
14. Andersen IK, Sidaros K, Gesmar H, Rostrup E, Larsson HBW. A model system for perfusion quantification using FAIR. Magn Reson Imaging 2000;18:565–574.
15. Zhou J, van Zijl PC. Perfusion imaging using FAIR with a short predelay. Magn Reson Med 1999;41:1099–1107.
16. Sidaros K, Andersen IK, Larsson HBW, Gesmar H, Rostrup E. Offset correction in FAIR Imaging. In: Proc ISMRM, 8th Annual Meeting, Denver, 2000. p 712.
17. Nishimura DG. Introduction to magnetic resonance imaging. Lecture notes, Department of Electrical Engineering, Stanford University; 1993.
18. Pauly J, Le Roux P, Nishimura D, Macovski A. Parameter relations for the Shinnar-Le Roux selective excitation pulse design algorithm. IEEE Trans Med Imaging 1991;10:53–65.
19. Matson GB. An integrated program for amplitude-modulated RF pulse generation and remapping with shaped gradients. Magn Reson Imaging 1994;12:1205–1225.
20. Altman DG. Practical statistics for medical research. London: Chapman & Hall; 1991.

- Magn Reson Imag 18(5), p. 565-74, 2000.

ELSEVIER

Magnetic Resonance Imaging 18 (2000) 565–574

MAGNETIC RESONANCE IMAGING

A model system for perfusion quantification using FAIR

Irene K. Andersen[a,b], Karam Sidaros[a,b], Henrik Gesmar[a,*], Egill Rostrup[a], Henrik B.W. Larsson[a],

[a]*Danish Research Center of Magnetic Resonance, Hvidovre Hospital, Kettegård Alle 30, Hvidovre, Denmark*
[b]*Department of Mathematical Modelling, Technical University of Denmark, Lyngby, Denmark*

Received 7 August 1999; accepted 3 February 2000

Abstract

Flow-sensitive experiments (FAIR) have been performed on a tube-flow phantom in order to validate quantitative perfusion measurements on humans. A straight-forward correspondence between perfusion and bulk-flow is found. It is shown that the flow phantom model only holds when the slice profiles of the involved RF pulses are taken into account. A small flow-independent off-set may be present in the data. The off-set is explained by the model. Based on the correspondence between the phantom and the in vivo models, it is shown that the lowest flow values that could be measured in the phantom correspond to perfusion values lower than the cortical perfusion in the brain. Thus, the experimental accuracy and the computational methods for quantitative perfusion measurements in vivo can be validated by a tube-flow phantom.

Keywords: Perfusion; Flow phantom; Slice profiles; Spin labelling

1. Introduction

Spin-labelled water has been used as an endogenous tracer to investigate perfusion noninvasively [1–5]. Qualitative information about perfusion can be obtained by subtracting a flow-insensitive image from a flow-sensitive image, the so called Flow-sensitive Alternating Inversion Recovery technique (FAIR) [5]. In this technique, the flow-sensitive image is usually generated by echo planar imaging (EPI) preceded by a slice-selective inversion RF pulse, whereas for the flow-insensitive image the inversion pulse is non-selective. Experiments with visual stimulation or hypercapnia indicate that the images are sensitive to relative perfusion changes [4,5]. To perform absolute quantitative measurements, a T_1-relaxation experiment with measurement of the magnetization at varying inversion times, T_I, is needed. The perfusion can be determined from a non-selective T_1-relaxation experiment together with FAIR experiments at one inversion time. This will be termed the FAIR method throughout the article. Alternatively, the perfusion can be determined from a non-selective and a slice-selective T_1 relaxation experiment. This method is termed the T_1 method. However, quantification of the perfusion level is demanding, since the perfusion level is low compared to the longitudinal relaxation rate, R_1, of the tissue, which results in very small signal differences in the experimental data. Further problems are the partial volume problem of cerebrospinal fluid (CSF) in grey matter and the fact that the longitudinal relaxation time of blood is different from that of tissue [4]. The transit time of blood from outside the inversion slab and into the tissue within the imaging slice is also of concern. The transit time induces a large error in the determination of the perfusion at short inversion times as shown by Tsekos et al. [6] in a validation study of the FAIR technique in rats.

Flow can be measured directly in flow phantoms so that the bulk-flow values obtained by the imaging technique can be validated. There is no partial volume problem in the phantom, since only one liquid is present. In addition, phantoms have no physiological noise due to motion and respiration. Thus, the spin-labelling technique can be explored and tested without additional confounding factors. Lee et al. [7] have also used inversion recovery for flow measurements. However, our approach is different in that we apply the FAIR method whereas flow relaxography, which is used by Lee et al., is based on measuring only the change in the

* Corresponding author. Tel.: +45-3632-3885; fax: +45-3657-302.
E-mail address: henrikg@magnet.drcmr.dk (H. Gesmar).

0730-725X/00/$ – see front matter
PII: S0730-725X(00)00136-3

T_1 components of the flowing spins. Furthermore, our model incorporates the imperfect slice profiles of the RF pulses.

This study had four main purposes: firstly to develop a model for the apparent spin relaxation in the bulk flow in a flow phantom; secondly to determine the accuracy and sensitivity of the spin-labelling technique by a comparison of the measured flow with a direct flow measurement and by a determination of the lowest flow values that can be measured; thirdly to compare the efficacy of the FAIR method and the T_1 method; and finally to relate the bulk-flow level to that of perfusion in order to evaluate if the FAIR technique can be used to measure perfusion in humans.

2. Theory

2.1. The simple perfusion model

As first suggested by Detre et al. [1], two terms must be added to the Bloch equation to take perfusion into account. The Bloch equation for the longitudinal magnetization becomes

$$\frac{dM_b(t)}{dt} = \frac{M_b(\infty) - M_b(t)}{T_1} + fM_a(t) - \frac{f}{\lambda}M_b(t), \quad (1)$$

where f is the perfusion in [(mL blood/g tissue · s)], λ is the brain–blood partition coefficient [(moles/g tissue)/(moles/mL blood)], T_1 is the relaxation time [s] of brain water in the absence of flow, M_b is the longitudinal magnetization of the brain tissue given in [arbitrary units/g brain], $M_b(\infty)$ is the equilibrium value of $M_b(t)$, and $M_a(t)$ is the longitudinal magnetization of arterial water in [arbitrary units/mL blood]. The quantities fM_a and $(f/\lambda)M_b$ represent the rates of spins entering and leaving the brain tissue, respectively, due to perfusion.

Assuming full relaxation between the slice-selective and non-selective part of the experiment, the solutions to the Bloch equation (1) at time $t = T_I$ after inversion become

$$M_b^{sel}(T_I) = [M_b^{sel}(0) - M_b(\infty)]e^{-R_1^{app}T_I} + M_b(\infty) \quad (2)$$

$$M_b^{non}(T_I) = [M_b^{non}(0) - M_b(\infty)]e^{-R_1T_I} + M_b(\infty), \quad (3)$$

where $R_1^{app} = R_1 + f/\lambda$ and $R_1 = 1/T_1$. Moreover $M_b^{sel}(0)$ and $M_b^{non}(0)$ describe the magnetization just after the inversion ($M_b^{sel}(0) \approx M_b^{non}(0) \approx -M_b(\infty)$). In the following, the difference between the slice-selective signal and the non-selective signal is termed the FAIR signal. A linear relation between perfusion and the FAIR signal is valid at the relevant magnitudes of perfusion and the time intervals, $fT_I/\lambda \ll 1$, and is given by

$$M_b^{sel}(T_I) - M_b^{non}(T_I) = [M_b(\infty) - M_b^{sel}(0)]e^{-R_1T_I}\frac{f}{\lambda}T_I + [M_b^{sel}(0) - M_b^{non}(0)]e^{-R_1T_I}. \quad (4)$$

In most studies where the FAIR technique has been applied, perfect inversion was assumed ($M_b^{sel}(0) = M_b^{non}(0) = -M_b(\infty)$), resulting in

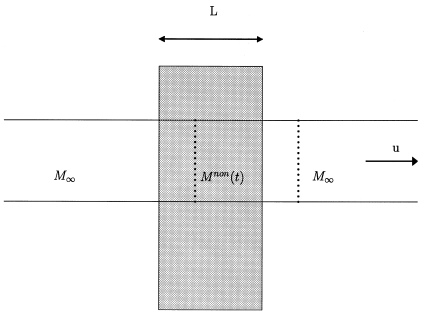

Fig. 1. A schematic outline of the flow with velocity u in a tube. The spins between the dotted lines were inverted by the selective inversion pulse. During the inversion time, fresh spins enter the imaging slice that is indicated by the shaded area.

$$M_b^{sel}(T_I) - M_b^{non}(T_I) = 2M_b(\infty)T_I\frac{f}{\lambda}e^{-R_1T_I}. \quad (5)$$

However, as discussed below, $M_b^{sel}(0)$ and $M_b^{non}(0)$ are not necessarily equal. One consequence hereof is, as seen from Eq. (4), that if $f = 0$ a perfusion independent off-set remains.

2.2. The simple bulk flow model

When water is led through the tubes of a phantom at a flow velocity sufficiently slow to assure laminar flow, the spins that first enter the detection slice are the first to leave. This is in contrast to the perfusion of the brain where a mixture of spins occurs in the volume of interest. Therefore Eq. (4) for perfusion is not valid for the flow through a phantom.

Because the flow in a tube is laminar, the profile is a paraboloid [8,9], but to simplify the calculations the profile is assumed to be plane. This assumption is true for a few pixels near the center of the tube. The flow is sketched in Fig. 1. The magnetization in the imaging slice may be written (still assuming full relaxation between acquisitions):

$$ALM^{sel}(T_I) = \begin{cases} AuT_I \cdot M(\infty) + A(L - uT_I) \\ \cdot[(M^{sel}(0) - M(\infty))e^{-R_1T_I} + M(\infty)], & T_I \le \frac{L}{u} \\ ALM(\infty), & T_I > \frac{L}{u} \end{cases}$$

where M is the magnetization per volume [arbitrary units/cm^3], A is the cross-sectional area of the tube [cm^2], u is the flow velocity [cm/s], and T_I is the time after inversion during which the non-inverted spins have been flowing into

the slice. The product AuT_I is the volume of the part of the imaging slice containing non-inverted spins, i.e. with magnetization $M(\infty)$. The rest of the volume, $A(L - uT_I)$, where L is the total thickness of the selected slice, is occupied by spins that were inverted at time $t = 0$, and which now relax as described by Eq. (3). The lower part of Eq. (6) is of no interest and is not considered in the following. In the non-selective case, all spins in the tube are inverted and their relaxation is similar to Eq. (3). When rearranging Eq. (6) the model is given by

$$M^{sel}(T_I) = [M^{sel}(0) - M(\infty)]e^{-R_1T_I}\left(1 - \frac{u}{L}T_I\right) + M(\infty) \tag{7}$$

$$M^{non}(T_I) = [M^{non}(0) - M(\infty)]e^{-R_1T_I} + M(\infty). \tag{8}$$

The FAIR signal can now be evaluated as

$$M^{sel}(T_I) - M^{non}(T_I) = [M(\infty) - M^{sel}(0)]e^{-R_1T_I}\frac{u}{L}T_I + [M^{sel}(0) - M^{non}(0)]e^{-R_1T_I}. \tag{9}$$

If Eq. (9) describing the FAIR signal in the case of bulk flow is compared with Eq. (4) describing the FAIR signal in the case of perfusion, it is seen that they are equivalent if

$$\frac{u\left[\frac{cm}{s}\right]}{L\ [cm]} = \frac{f\left[\frac{mL\ blood}{s\ g\ tissue}\right]}{\lambda\left[\frac{ml}{g}\right]}. \tag{10}$$

Moreover, if $u = 0$ in Eq. (9) a flow independent off-set remains just as is the case if $f = 0$ in Eq. (4). The left side of Eq. (10) depends on the thickness, L, of the selected slice, whereas the right-hand side depends on the partition coefficient, which is independent of the selected slice. Because Eq. (9) for the FAIR signal is equivalent to Eq. (4) that describes the case of perfusion, the flow phantom can be used to simulate perfusion. The experiments can be adjusted to the perfusion level in the brain by adjusting the flow velocity or the slice thickness.

The above considerations give the flow phantom an additional advantage to the ones mentioned in the introduction: no restrictions have been introduced on the rate of the flow as in the case of perfusion where it was assumed that $fT_I/\lambda \ll 1$ (Eqs. (4) and (5)). This means that Eq. (9) is valid even for large flow values within the limit $T_I < L/u$.

2.3. The effect of the non-ideal slice profiles

In the model described above, a sharp boundary between zones with inverted and noninverted spins was assumed, which corresponds to the application of RF pulses with ideal slice profiles. In reality, the boundary is less abrupt, which makes it necessary to solve the Bloch equations using arbitrary slice profiles. This means that the magnetization, M, is no longer a function of time only, but is also a function of z, where the z-axis is perpendicular to the imaging plane.

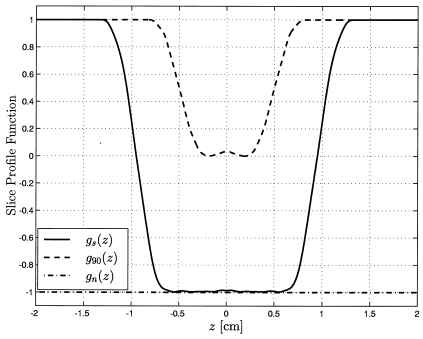

Fig. 2. The implemented slice profiles functions of the 180° RF pulse, $g_s(z)$, and the 90° RF pulse, $g_{90}(z)$, obtained from the measured magnetization along a direction perpendicular to the inverted slice and modified to unity at the edges. The non-selective 180° RF pulse, $g_n(z)$, is set to -1 in the entire range.

The functions $g_s(z)$, $g_n(z)$ and $g_{90}(z)$ are introduced in order to describe the slice profiles of the slice-selective 180°, the non-selective 180° and the 90° RF pulses respectively. Fig. 2 shows an example of such functions. Assuming that the duration of the RF pulse is negligible, the effect of the pulse at time t_0 is described by the function g(z) and given by $M(z, t_0^+) = g(z)M(z, t_0^-)$, where $M(z, t_0^+)$ is the longitudinal magnetization just after the pulse and $M(z, t_0^-)$ is the magnetization just before the pulse. The only condition that these functions must fulfill is $-1 \le g(z) \le 1$. The effect of the 90° RF pulse in the xy-plane is described by $g_{90,xy}(z) = \sqrt{1 - (g_{90}(z))^2}$.

Assuming the flow velocity to be constant (good approximation within a voxel), and its direction to be in the positive z-direction, the size of the observed magnetization in the xy-plane immediately after the 90° RF pulse is given by

$$M^{sel}_{obs}(T_I) = \int_{-\infty}^{\infty} [(M(\infty)g_s(z) - M(\infty))e^{-R_1T_I} + M(\infty)]g_{90,xy}(z + uT_I)\,dz. \tag{11}$$

The expression in the brackets represents the longitudinal relaxation, where $M(\infty)g_s(z) = M^{sel}(z, 0)$. A volume of length dz moves with the flow velocity u. After the inversion time, T_I, the 90° pulse is applied and the volume has reached the position $z + uT_I$. The total contribution to the signal is obtained by integration over z. The equation rearranges into

$$M^{sel}_{obs}(T_I) = M(\infty)e^{-R_1T_I}G^{sel}(uT_I) + M_{obs}(\infty), \tag{12}$$

where

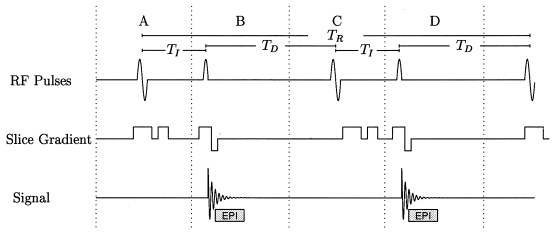

Fig. 3. The FAIR sequence, consisting of a slice-selective part (A and B) and a non-selective part (C and D). The FID is measured with an EPI module. The inversion time is termed T_I, whereas the time from the excitation RF pulse to the next inversion pulse is termed T_D.

$$G^{sel}(uT_I) = \int_{-\infty}^{\infty} (g_s(z) - 1)g_{90,xy}(z + uT_I)\,dz. \quad (13)$$

It is worthy of note that G^{sel} depends on the slice-profiles only. The last term in Eq. (12) is

$$M_{obs}(\infty) = M(\infty)\int_{-\infty}^{\infty} g_{90,xy}(z + uT_I)\,dz, \quad (14)$$

which is the observed equilibrium magnetization. Since $g_{90,xy}$ is used in both the selective and non-selective cases, $M_{obs}(\infty)$ remains the same in the two cases. Eq. (12) is reshaped into

$$M^{sel}_{obs}(T_I) = [M^{sel}_{obs}(0) - M_{obs}(\infty)]e^{-R_1T_I}\frac{G^{sel}(uT_I)}{G^{sel}(0)} + M_{obs}(\infty) \quad (15)$$

by applying the relation

$$M^{sel}_{obs}(0) - M_{obs}(\infty) = G^{sel}(0)M(\infty). \quad (16)$$

Eq. (15) is the same as Eq. (7), except that the contribution due to flow is incorporated in the function G^{sel} and not in $(1 - (u/L)T_I)$. When $u = 0$, there is no contribution from the profiles and the equations become identical. It is also seen that $G^{sel}(uT_I)$ is normalized with $G^{sel}(0)$. Thus, no problems with the choice of units of the profiles occur. The non-selective signal is obtained in a similar fashion and the resulting FAIR signal is given by

$$M^{sel}_{obs}(T_I) - M^{non}_{obs}(T_I) = \left[M^{sel}_{obs}(0)\frac{G^{sel}(uT_I)}{G^{sel}(0)} - M^{non}_{obs}(0)\frac{G^{non}(uT_I)}{G^{non}(0)}\right]e^{-R_1T_I} - \left[\frac{G^{sel}(uT_I)}{G^{sel}(0)} - \frac{G^{non}(uT_I)}{G^{non}(0)}\right]M_{obs}(\infty)e^{-R_1T_I}. \quad (17)$$

It is reasonable to assume that the non-selective pulse inverts the spins uniformly throughout the inspected area, hence $G^{non}(uT_I)/G^{non}(0) = 1$, and Eq. (17) rearranges into

$$M^{sel}_{obs}(T_I) - M^{non}_{obs}(T_I) = [M_{obs}(\infty) - M^{sel}_{obs}(0)] \cdot \left(1 - \frac{G^{sel}(uT_I)}{G^{sel}(0)}\right)e^{-R_1T_I} + [M^{sel}_{obs}(0) - M^{non}_{obs}(0)]e^{-R_1T_I}. \quad (18)$$

For ideal slice profiles the term $1 - G^{sel}(uT_I)/G^{sel}(0)$ turns out to be $(u/L)T_I$ in agreement with Eq. (9). However, for real slice profiles, Eq. (9) only equals Eq. (18) if $u = 0$. In this case, only the last term in the equations that describes the signal off-set remains.

In the present experiments, a reduced repetition time, T_R, was used, meaning that full relaxation between selective and non-selective acquisition was not obtained. Thus, equations including the effects of a reduced T_R must be developed. This is described in the appendix.

3. Materials and methods

3.1. Scanner and sequences

The flow experiments were carried out on a 1.5 T scanner (Siemens Vision, Erlangen, Germany). The inversion was performed by an adiabatic hyperbolic secant RF pulse [10]. After a period, T_I, the free induction decay (FID) was measured using blipped EPI (see Fig. 3). The non-selectivity of the inversion pulse was produced by shifting the gradient until immediately after the RF pulse in order to minimize differences in eddy currents. Matrix size = 96 × 128, echo time = 57 ms, field of view (FOV) = 230 × 230 mm^2, slice thickness L = 10 mm. The delays were T_I/T_D = 1.0 s / 2.15 s, $T_R = 2(T_I + T_D) = 6.30$ s, where T_D is the period from the 90° RF pulse to the next RF inversion pulse. Two experiments were performed for each of seven flow values. First, a steady state experiment in which the sequence was repeated 32 times for image averaging. This experiment is termed the FAIR experiment in the following. In the other experiment, the same sequence was used to measure T_1 relaxation. Five acquisitions were obtained at each of 16 values of T_I (first acquisition rejected before averaging). The inversion time, T_I, was varied in random order to reduce the effect of signal drifting. This experiment

Table 1
The average of *n* flow velocities calculated by the two methods and the observed 95% confidence interval

True Flow	T_1 method		FAIR method	
(cm/s)	(cm/s)	*n*	(cm/s)	*n*
0.57 ± 0.03	0.57 ± 0.05	15	0.58 ± 0.03	15
0.37 ± 0.01	0.37 ± 0.02	15	0.39 ± 0.02	15
0.194 ± 0.005	0.21 ± 0.03	15	0.22 ± 0.02	15
0.093 ± 0.001	0.09 ± 0.04	15	0.11 ± 0.02	15
0.047 ± 0.001	0.04 ± 0.03	8	0.05 ± 0.03	15
0.015 ± 0.002	0.05 —	1	0.03 ± 0.03	6

is termed the T_1 experiment in the following. In both experiments, the delay $T_D = 2.15$ s reduced the total acquisition time considerably.

3.2. Investigating slice profiles

The experiments to investigate the slice profiles were carried out in a slice perpendicular to the plane of the image slice by exciting spins with the RF pulse to be examined. The RF pulse being examined was positioned at the time of the slice-selective inversion pulse in section (A) in the implemented FAIR sequence of Fig. 3. The experiments were carried out on a cylindrical phantom. Plotting the magnetization along a line in the imaging plane perpendicular to the slice being examined reveals the slice profile of the 90° imaging RF pulse or the 180° RF pulse. Figure 2 illustrates the normalized magnetization modified to unity at the edges. The width of the slice is adjusted through the magnetic field gradients, which are turned on during the RF pulse.

If $M^{sel}(0) = M^{non}(0)$, the second term in Eq. (9) and in Eq. (18) vanishes, which makes the FAIR signal vanish when there is no flow. However, a signal off-set occurs if the equality is not true. The off-set consists of an initial magnetization difference and a factor $e^{-R_1 T_1}$. The magnetization difference is calculated from Eq. (11) and the corresponding non-selective equation. This leads to

$$M^{sel}_{obs}(0) - M^{non}_{obs}(0) = M(\infty) \int_{-\infty}^{\infty} (g_s(z) - g_n(z)) g_{90,xy}(z)\, dz. \quad (19)$$

In an earlier study [11], the off-set was measured at no flow with varying selective inversion pulse-widths while the 90° pulse-width was kept constant. With wide inversion pulses, the off-set vanished as expected from Eq. (19). At smaller width an off-set was present. The off-set originates from the tail of the 90° pulse profile when it is wider than the profile of the inversion pulse as seen from Eq. (19). The off-set can be either positive or negative [11] depending on the side bands of the sinc shaped 90° pulse.

In the present experiments, the width of the inversion pulse was twice the width of the 90° pulse. At this width an off-set is expected.

3.3. The flow phantom

The phantom was a cylinder that contained a liquid with $T_1 = 1.1$ s. The cylinder was penetrated by four tubes, which were serially connected. At one end of this long tube there was an elevated trough. It contained water added gadolinium(II) diethylenetriaminepentaacetic acid (Gd-DTPA) to decrease T_1 to a level comparable to that of grey matter. The solution flows from the trough, through the tubes and the direction of the flow in tubes 2 and 4 is opposite of that in tubes 1 and 3. It was possible to control the velocity, v, of the liquid using a tap at the other end of the tube. Since the flow was expected to be laminar, the average flow velocity was given by v_{av} [cm/s] = F/A [(cm^3/s)]/[cm^2], where the volume flow rate, F, was measured repeatedly by means of a stop-watch and a beaker. The inner diameter of the tubes was 21 mm. For laminar flow the maximum velocity, v_{max}, in the center of the tubes is twice the average velocity, v_{av}. The maximum velocities are shown as the true flow values in Table 1. One tube had a narrowing only about 10 cm away from the imaging plane and the laminar condition did not hold in this tube. Thus, only data obtained in the other three tubes were treated.

3.4. Calculations

In 5 pixels near the centers of three tubes, the models for the signals as a function of T_I were fitted to the data-set obtained in the T_1 experiment, in the following referred to as the T_1 data. The models for ideal and real slice profiles were used. The three parameters u, $M(\infty)$, and R_1 were fitted, while sequence delays and profile parameters such as inversion angle, width and slope were known from the experiment. All other quantities can be calculated from these. The Levenberg Marquardt method was applied to provide the least squares fit. In this way, u was determined by the T_1 method.

The slice-profile functions implemented in the model with real slice profiles were the profiles shown in Fig. 2. These functions were the normalizations of the measured slice profiles, set to unity at the edges.

For the FAIR experiment, where the data were obtained at a constant T_I at each flow value, the difference between the slice-selective and non-selective signals was calculated

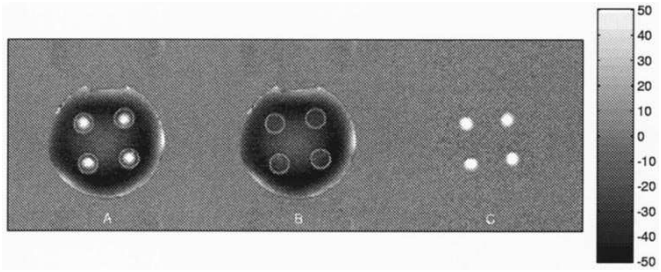

Fig. 4. (A) The mean of the acquired FAIR images (selective minus non-selective image) at a peak flow velocity of 0.19 cm/s. (B) The off-set found with zero flow. (C) The acquired FAIR image minus the off-set (A−B). It is clear that the off-set in (A) is indeed equal to the off-set in (B) since the difference only has significant signal in the tubes as should be the case, since there is no flow in the surrounding fluid.

as subtraction images. These FAIR signals were compared with the predicted FAIR signals calculated using values of $M(\infty)$ and R_1 obtained from the fitting procedure using T_1-data at each flow value. The predicted FAIR signals were calculated from the model with ideal slice profiles as well as the model with real slice profiles. The remaining parameters, T_I, T_D, and L, were known from the experiment.

Finally, the model with real slice profiles was fitted pixel-wise to the T_1-data, and the fitted flow velocities (T_1 method) were compared with the flow velocities calculated from the FAIR signal using $M(\infty)$ and R_1 from the fit (FAIR method).

4. Results and discussion

4.1. Initial observations

As expected from both models, a small signal difference was detected at zero flow due to the differences between $M_{obs}^{sel}(0)$ and $M_{obs}^{non}(0)$. This off-set is illustrated in Fig. 4(B). The magnitude of the signal off-set was about 5% of the slice-selective and the non-selective images. As described by Eq. (19), the reason for the off-set is the relative widths of the pulses and the non-ideal shape of the 90° pulse. From Fig. 4(B), is it seen that the off-set is not homogeneous throughout the phantom. This spatial inhomogeneity may be present for several reasons: Susceptibility effects arise due to the sharp borders between the different compartments of the phantom; Some differences in eddy currents may still remain even though a gradient was implemented in the non-selective part of the sequence to overcome this problem (section (C) in Fig. 3; Moreover B_1-inhomogeneity might introduce signal differences between the selective and non-selective signals. All of the above effects will influence the actual slice profiles that then may vary across the image. This means that the effects contribute to the signal off-set through Eq. (19). The off-set is therefore accounted for by the model regardless of the origin of inhomogeneity effects as long as the calculations are done on a pixel by pixel basis or in a small ROI.

The signal off-set was subtracted from the FAIR image at other flow values as shown in Fig. 4.

As expected, the signal to noise ratio in the FAIR image decreased drastically as the flow decreased. At the peak flow velocity of 0.015 cm/s, the tubes were not even visible. Based on Eq. (10) the flow velocity corresponding to physiological perfusion (approximately 60 ml/100 g/min) is 0.01 cm/s (when $L = 1$ cm), which is below the detectable level. However, Eq. (10) only holds for ideal slice profiles, and it will later be shown that by taking realistic slice profiles into account, the flow value corresponding to physiological perfusion is much higher than predicted by Eq. (10).

4.2. The model based on ideal slice profiles

To investigate the validity of the simple model based on ideal slice profiles given by Eq. (9), the quality of the T_1-fit was first inspected. The model fitted the data well, but in the slice-selective case the resulting relaxation rates, R_1, decreased significantly with increasing flow velocity. This result disqualified the model, as R_1 should be independent of the flow velocity.

Another validation of the model was carried out by comparing the signals measured in the FAIR experiment at the different flow velocities with the values predicted from the model. The predicted FAIR signal was calculated using R_1 and $M(\infty)$ fitted from the T_1-data obtained at a peak velocity of 0.37 cm/s.

The calculated FAIR signal as a function of u is plotted as the dashed line in Fig. 5. The measured FAIR signals are marked by asterisks. There is clearly a great difference between the simple model and the data. The model shows a linear relation between the FAIR signal and u, while the data-points do not. We therefore concluded that the model based on ideal slice profiles of the RF pulses was inadequate.

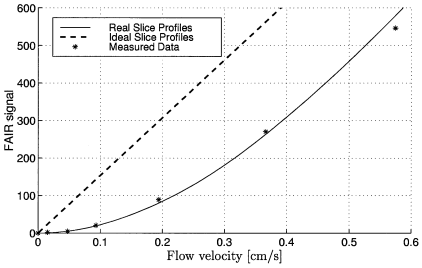

Fig. 5. The FAIR signals calculated using the model with ideal slices and the model with realistic slice profiles. The model with realistic slice profiles clearly matches the measured data much better than the model with the ideal slices.

4.3. The model based on non-ideal slice profiles

When the model based on real slice profiles was fitted to the measured T_1-data for all pixels, the results improved considerably as compared to the simple model. Fig. 6 shows the measured data together with the fitted curves. The data were taken from the center pixels at a peak flow velocity of 0.37 cm/s. The curves fit the data very well. The relaxation rates, R_1, were constant within the 95% confidence intervals, CI_{95}, and so were the values of $M(\infty)$.

The full-drawn curve in Fig. 5 was calculated using the realistic slice-profile functions together with R_1 and $M(\infty)$ fitted from the T_1 data obtained at a peak flow velocity of 0.37 cm/s. The shape of the curve is given by the factor $1 - G^{sel}(uT_I)/G^{sel}(0)$ in Eq. (18). The figure shows that the model with realistic slice profiles clearly matches the measured data much better than the linear model with the ideal slices. The mismatch between the experimental data

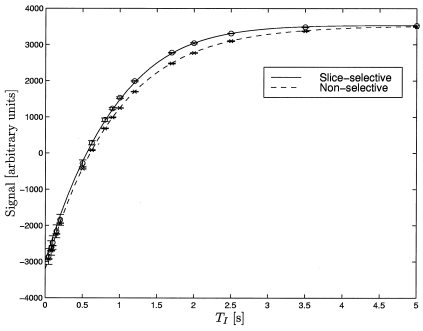

Fig. 6. The mean slice-selective and the non-selective data-points acquired at a peak flow velocity of 0.37 cm/s and the CI_{95} of the mean. The selected area consists of 5 pixels at the center of tube 2.

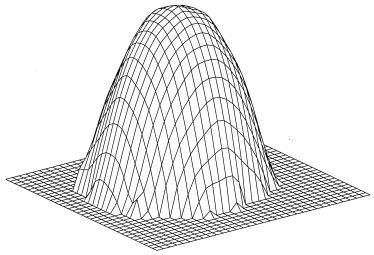

Fig. 7. A 3D visualization of the flow velocity when including the real slice profiles in the model.

and the model with ideal slice profiles is very similar to that found by Lee et al. [7]. Fig. 5 suggests that the mismatch is due to the slice profiles.

Fig. 7 shows the velocity profile of one of the tubes. The velocity corresponding to the measured FAIR signal was determined in each pixel from the curve of the realistic slice profiles in Fig. 5. It is clear that the velocity profile is parabolic as dictated by the laminar flow.

From the above observations it was concluded that the model with real slice profiles must be used, and that the model with ideal slices should be discarded.

4.4. Comparison of methods

The model that includes real slice profiles was used to fit the T_1 data in each of the 5 near-center pixels in the three tubes. The average of the fitted flow velocities of the 15 pixels is listed in Table 1 (T_1 method) at each flow value together with the observed CI_{95}, where CI_{95} is 1.96 times the standard deviation. The CI_{95}s correspond well to the confidence intervals determined from the least squares fit. Some of the smallest flow values could not be fitted. Only the pixels where the fit converged were averaged.

The parameters R_1 and $M(\infty)$ were used together with the FAIR signal to determine u pixel-wise. The average of the velocities is shown in Table 1 (FAIR method). Only pixels with positive FAIR signals were averaged. From Table 1, it is seen that the expected velocities lie within the CI_{95} determined by both types of experiments. It is seen that a flow velocity of 0.05 cm/s could be determined in every pixel by the FAIR method and in most pixels by the T_1 method.

The T_1 method is the most time consuming method of the two. The method is based on the subtraction of two T_1 values, which makes it extremely important to make two accurate measurements. The T_1 measurements for the FAIR method are less demanding. This means that more time can be spent on the measurement of the FAIR image.

For in vivo studies, one problem is the transit time of

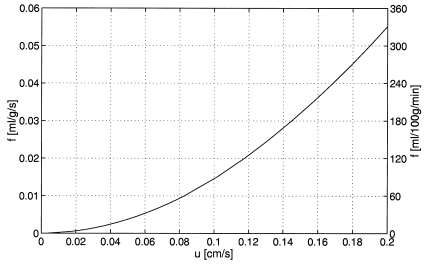

Fig. 8. The relationship between perfusion levels, f, and flow velocities, u, giving equal relative FAIR signals with the actual parameters and the implemented slice profiles. It is assumed here that the brain blood partition coefficient, $\lambda = 1$ mL/g.

blood into the imaged tissue. This delay induces errors in the determined perfusion at small inversion times [6]. By choosing the FAIR technique and a longer T_I, the influence from signals obtained at small inversion times is reduced. A longer inversion time also reduces the off-set, since the off-set is scaled with the factor $e^{-R_1 T_I}$.

Another advantage of the FAIR method to the T_1 method is the possibility of measuring at more inversion times to test the reproducibility of the calculated perfusion.

Therefore, the FAIR method is recommended for perfusion measurements in vivo.

4.5. The relation between flow and perfusion

The relationship describing the correspondence between the flow velocity in the phantom and the physiological perfusion given by Eq. (10) was based on the assumption of ideal slice profiles. It was shown above that this assumption did not hold. It is seen from Fig. 5, that the flow velocity corresponding to a given physiological perfusion level is higher than anticipated by Eq. (10).

Flow was compared with perfusion by considering the flow velocities and the perfusion levels that gave equal relative FAIR signals. With equal values of $M(\infty)$, R_1, T_D and T_I, the correspondence between flow and perfusion was calculated. Fig. 8 shows this relationship for $R_1 = 1.1\ s^{-1}$, $T_D = 2.15$ s and $T_I = 1$ s. The shape of this curve corresponds to the relation between $(f/\lambda)T_I$ and $1 - G^{sel}(uT_I)/G^{sel}(0)$. It is seen that the flow velocity corresponding to the nominal physiological grey matter perfusion was about 0.08 cm/s, i.e. in the range of the measurable flow velocities. Thus, the FAIR sequence was indeed capable of detecting flow values corresponding to grey-matter perfusion. Note that a velocity of 0.05 cm/s corresponded to a perfusion of 0.004 mL/g/s or 24 mL/100 g/min.

A prerequisite for the precise determination of the bulk flow was the possibility of subtracting the signal off-set at zero flow from the FAIR images at all other flow values. In measurements of brain perfusion, the zero perfusion image cannot be obtained. To overcome this problem, one possibility is to make the selective pulse substantially wider than the imaging slice. This reduces perfusion sensitivity due to increased transit time. Alternatively, the signal off-set should be included in the model [Eq. (4)] in which case a selective and a non-selective T_1 measurement must be acquired in order to determine the parameters of Eq. (4).

Another difference between measurements of bulk flow and perfusion is the need for slice-profile correction in bulk-flow measurements through the factor $G(uT_I)$ in Eq. (18). This is not necessary for perfusion due to the assumption of instantaneous mixing.

5. Conclusion

It was shown how a tube flow phantom can be used to validate quantitative perfusion measurements by MR. It was demonstrated that this can only be done, when the actual RF pulse profiles are taken into account. We found a relation between the flow velocity and a given perfusion giving the same relative FAIR signal. Thus, the flow velocity corresponding to physiological grey-matter perfusion was found to be in the detectable range for both the T_1 and the FAIR methods. Moreover, a flow velocity corresponding to the level of white-matter perfusion could be determined in several pixels by the T_1 method and in all pixels by the FAIR method, although with rather large standard deviations. It was argued that the FAIR method should be used for in vivo studies. It was also demonstrated that the estimated least squares standard deviations for the T_1 method were in good agreement with the observed. Thus, the lower limit of what can be measured with the described techniques seems to be around the level of white-matter perfusion.

Appendix: The model with reduced delay, T_D

In section 2, the bulk flow model taking non-ideal slice profiles into account was described. In this appendix, the solutions are developed to take into account the incomplete relaxation between acquisitions.

When the time between the 90° and the following 180° RF pulse in the sequence, T_D, is finite, the magnetization does not reach the equilibrium magnetization before the following 180° RF pulse and the time course eventually reaches a steady state. The functions $g_s(z)$, $g_n(z)$ and $g_{90}(z)$ are defined in section 2.3. If it is assumed that the flow velocity, u, is constant and points in the positive z direction, the longitudinal magnetization is given by the system of equations

$$M(z, 0^+) = g_s(z)M(z, 0^-)$$

$$M(z, T_I^-) = (M(z - uT_I, 0^+) - M(\infty))e^{-R_1T_I} + M(\infty)$$

$$M(z, T_I^+) = g_{90}(z)M(z, T_I^-)$$

$$M(z, T_I + T_D^-) = (M(z - uT_D, T_I^+) - M(\infty))e^{-R_1T_I} + M(\infty)$$

$$M(z, T_I + T_D^+) = g_n(z)M(z, T_I + T_D^-) \quad (A.1)$$

$$M(z, 2T_I^- + T_D) = (M(z - uT_I, T_I + T_D^+) - M(\infty))e^{-R_1T_I} + M(\infty)$$

$$M(z, 2T_I^+ + T_D) = g_{90}(z)M(z, 2T_I^- + T_D)$$

$$M(z, T_R^-) = (M(z - uT_D, 2T_I^+ + T_D) - M(\infty))e^{-R_1T_I} + M(\infty) = M(z, 0^-)$$

Before solving this system of equations, we will show the relation between the above magnetizations and the measured signals.

The longitudinal magnetization just before the 90° RF pulse in the slice-selective sequence is $M(z, T_I^-)$. The longitudinal magnetization just after the pulse, $M(z, T_I^+)$ is given by the system of Eqs. (A.1). The transverse magnetization at time $t = T_I^+$ is integrated over space to give the observed magnetization:

$$M_{obs}^{sel} = \int_{-\infty}^{\infty} \sqrt{1 - (g_{90}(z))^2}\, M(z, T_I^-)\, dz. \quad (A.2)$$

Eq. (A.2) is based on the assumption that the effect of the 90° RF pulse on the magnetization at any point, z, corresponds to some flip angle, $\theta(z)$. One might suspect that the relationship is not so simple and that the transverse magnetization on either side of the slice center may have opposite phases. It is demonstrated by Callaghan [12] that, starting with longitudinal magnetization only, a 90_x RF pulse produces an M_y which is symmetric about the slice center and an M_x which is asymmetric. Since both M_x and M_y are integrated, M_x will not contribute to the measured signal. Therefore the above assumption is reasonable.

Similarly, the observed non-selective signal is the integrated contribution from the transverse magnetization:

$$M_{obs}^{non} = \int_{-\infty}^{\infty} \sqrt{1-(g_{90}(z))^2}\, M(z, 2T_I^- + T_D)\, dz. \quad (A.3)$$

Before solving the system of Eqs. (A.1), two quantities are introduced:

$$e_I = e^{-R_1T_I} \quad \text{and} \quad e_D = e^{-R_1T_D} \quad (A.4)$$

Now solving the system of Eqs. (A.1) gives the following iterative solution for $M(z, T_I^-)$ and $M(z, 2T_I^- + T_D)$:

$$M(z, T_I^-) = A_{sel}(z)M(\infty) + B_{sel}(z) \cdot M(z - 2uT_R, T_I^-) \quad (A.5)$$

$$M(z, 2T_I^- + T_D) = A_{non}(z)M(\infty) + B_{non}(z) \cdot M(z - 2uT_R, 2T_I^- + T_D) \quad (A.6)$$

where

$$A_{sel}(z) = (1 - e_I)[1 + e_Ie_Dg_s(z - uT_I) \; g_{90}(z - u[T_I + T_D])] + e_Ig_s(z - uT_I)(1 - e_D)[1 + e_Ie_D \; g_n(z - u[2T_I + T_D])g_{90}(z - u[T_I + T_D])] \quad (A.7)$$

$$A_{non}(z) = (1 - e_I)[1 + e_Ie_Dg_n(z - uT_I) \; g_{90}(z - u[T_I + T_D])] + e_Ig_n(z - uT_I)(1 - e_D) \cdot [1 + e_Ie_Dg_s(z - u[2T_I + T_D])g_{90}(z - u[T_I + T_D])] \quad (A.8)$$

and

$$B_{sel}(z) = e_I^2e_D^2g_s(z - uT_I)g_n(z - u[2T_I + T_D]) \; g_{90} \cdot (z - u[T_I + T_D])g_{90}(z - 2uT_R) \quad (A.9)$$

$$B_{non}(z) = e_I^2e_D^2g_s(z - u[2T_I + T_D])g_n(z - uT_I) \; g_{90}(z - u[T_I + T_D])g_{90}(z - 2uT_R) \quad (A.10)$$

Far from the center of the slice, the magnetization is only affected by the non-selective RF inversion pulse, i.e. $g_s(z) = g_{90}(z) = 1$ and $g_n(z) = \cos\alpha(z)$, where $\alpha(z)$ is the true flip angle of the RF inversion pulse. Here it is possible to find a set of starting values for $M(z, T_I^-)$ and $M(z, 2T_I^- + T_D)$ needed for the iterations in Eqs. (A.5) and (A.6). These are given by:

$$M(z, T_I^-) = M(\infty)\left[1 - \frac{e_I^2e_D(1 - \cos\alpha(z))}{1 - e_I^2e_D^2\cos\alpha(z)}\right] \quad (A.11)$$

and

$$M(z, 2T_I^- + T_D) = M(\infty)\left[1 - \frac{e_I(1 - \cos\alpha(z))}{1 - e_I^2e_D^2\cos\alpha(z)}\right] \quad (A.12)$$

Eq. (A.11) is deduced by equating $M(z, T_I^-)$ and $M(z - uT_R, T_I^-)$ in Eq. (A.5). Similarly for Eq. (A.12).

References

[1] Detre J, Leigh J, Williams D, Koretsky A. Perfusion imaging. Magn Reson Med 1992;23:37–45.

[2] Kwong K, Belliveau J, Chesler D, Goldberg I, Weisskoff R, Poncelet B, Kennedy D, Hoppel B, Cohen M, Turner R, Cheng H-M, Brady T, Rosen B. Dynamic magnetic resonance imaging of human brain activity during primary sensory stimulation. Proc Natl Acad Sci USA 1992;89:5675–9.

[3] Kim S, Tsekos N. Perfusion imaging by a flow-sensitive alternating inversion recovery (FAIR) technique: application to functional brain imaging. Magn Reson Med 1997;37:425–35.

[4] Kwong KK, Chesler DA, Weisskoff RM, Donahue KM, Davis TL, Østergaard L, Campbell TA, Rosen BR. MR Perfusion Studies with

T_1-weighted echo planar imaging. Magn Reson Med 1995;34:878–87.
[5] Kim S. Quantification of relative cerebral blood flow change by flow-sensitive alternating inversion recovery (FAIR) technique: application to functional mapping. Magn Reson Med 1995;34: 293–301.
[6] Tsekos NV, Zhang F, Merkle H, Nagayama M, Iadecola C, Kim S-G. Quantitative measurements of cerebral blood flow in rats using the FAIR technique: correlation with previous iodoantipyrine autoradiographic studies. Magn Reson Imaging 1998;39:564–73.
[7] Lee J-H, Li X, Sammi MK, Springer CSJ. Using flow relaxography to elucidate flow relaxivity. J Magn Reson 1999;136:102–13.
[8] Fox RW, McDonald AT. Introduction to Fluid Mechanics, 3rd ed. New York: Wiley, 1985.
[9] Gullberg GT, Simons MA, Wehrli FW. A Mathematical model for signal from spins flowing during the application of spin echo pulse sequences. Magn Reson Imaging 1988;6:437–61.
[10] Silver MS, Joseph RI, Hoult DI. Highly selective $\pi/2$ and π pulse generation. J Magn Reson 1984;59:347–51.
[11] Sidaros K, Andersen I, Larsson H, Gesmar H, Rostrup E. Zero perfusion calibration of FAIR imaging with arbitrary inversion slice profiles. Magma 1999;8(suppl.):165.
[12] Callaghan PT. Principles of Nuclear Magnetic Resonance Microscopy. Oxford: Clarendon Press, 1991.

- Proc. 5th Int. Conference on the Mapping of the Human Brain, NeuroImage 9(6), p. S150, 1999.

The Influence of a Signal Offset on Perfusion Quantification using FAIR

I.K. Andersen, K. Sidaros, H. Gesmar, H.B.W. Larsson and E. Rostrup
Danish Research Center for MR, Hvidovre Hospital, Copenhagen, Denmark

Introduction: A number of spin labelling techniques have been used for non-invasive perfusion measurements [1-3]. In the so-called FAIR technique two inversion-recovery sequences are applied, using a slice-selective(SS) and a non slice-selective(NS) inversion pulse. Because only the SS sequence is perfusion sensitive, the resulting difference image (FAIR image) is perfusion weighted and has been used for fMRI studies with visual stimulation[4]. Under ideal experimental conditions the difference vanishes in areas of no perfusion. In reality, a small signal offset, due to disturbing effects such as eddy currents, B_0 inhomogeneities or non-ideal slice profiles, remains. In the present study measurements were carried out on a pipe flow phantom where the flow can be controlled and measured and the zero flow image determined. The effect of ignoring the signal offset is discussed by determining the lowest flow value measurable, using the FAIR technique, with and without taking the offset into consideration.

Theory: The basic principle is that perfusion can be linked to bulk flow in phantoms. The main difference is that the slice profiles must be included in the Bloch equations in the case of flow, resulting in a non-linear correspondance between perfusion and bulk flow. Apart from this the models are similar and contain an identical offset term given by $M_{\text{off}} = [M^{ss}(0) - M^{nn}(0)]\, exp(-\frac{T_I}{T_1})$. Thus flow measurements can be used to investigate perfusion quantification and offset influence.

Methods: The FID is measured by blipped EPI. T_R=6.3s, T_E=57ms, FOV=230 × 230mm^2, slice thickness=10mm and matrix size=96 × 128. In the FAIR measurement the sequence was repeated 32 times for averaging, with T_I=1s. For T_1 measurement 4 acquisitions were obtained at each of 16 values of T_I. Both measurements were repeated at 5 flow values and at zero flow. The flow FAIR model without the offset term was fitted by a least squares fit to the T_1-data with and without the zero flow image subtracted. This determined M^{∞} and T_1 which were used to calculate the flow velocity directly from the FAIR-data with and without the offset. The real flow velocities were calculated assuming a laminar flow profile. The SS 180° pulse slice profile was 1.8 times wider than the 90° pulse, which due to the non-ideal shape of the profiles made it cover the excitation area of the 90° pulse.

Results: In table 1 the flow velocities determined with and without subtraction of the offset are listed. The values are the averages of 15 near center pixels from 3 flow phantom tubes together with the observed 95% confidence intervals. Some of the smallest flow values could not be fitted. Only the number n of pixels which fitted were averaged. When the offset is not subtracted the lowest flow value determined correctly

Table 1: Flow velocities calculated with and without offset correction

Real Flow		**Offset Included**			**Offset Corrected**		
[cm/s]		[cm/s]		**n**	[cm/s]		**n**
0.37	±0.01	0.37	±0.02	15	0.39	±0.02	15
0.194	±0.005	0.18	±0.02	15	0.22	±0.02	15
0.093	±0.001	0.04	±0.01	8	0.11	±0.02	15
0.047	±0.001	-	± -	0	0.05	±0.03	15
0.015	±0.002	-	± -	0	0.03	±0.03	6

is 0.194 cm/s. With offset correction the flow velocities were determined to a level of 0.05 cm/s and even velocities of 0.015 cm/s were sometimes determined. All flow velocities were determined correctly. For comparison, the grey/white matter perfusion levels (≈ 60/24 ml/100g/min) correspond in our measurements to flow velocities of 0.08/0.05 cm/s.

Conclusion: It is shown that the signal offset has a large impact on the quantification of the flow. When the offset is subtracted a flow velocity corresponding to the perfusion level of white matter is determined. When the offset is not subtracted not even grey matter perfusion is measurable. The offset is therefore of great importance and must be taken into account in perfusion measurements.

REFERENCES

1. Kim et al. *Magn. Reson. Med.* **37**(3), 425:435, 1997.
2. Kwong K. et al. *Neurobiology*, **89**, 5675:5679, 1992.
3. Detre et al. *Magn. Reson. Med.* **23**, 37:45, 1992.
4. Kim et al. *Magn. Reson. Med.* **34**, 293:301, 1995.

- Proc. 16th Annual Meeting of the European Society for Magnetic Resonance in Medicine and Biology, Magma, 8, suppl. 1, p. 165, 1999.

Zero Perfusion Calibration of FAIR Imaging with Arbitrary Inversion Slice Profiles

K Sidaros[1,2], IK Andersen[2], HBW Larsson[2], H Gesmar[2], E Rostrup[2] and WMMJ Bovée[3]

[1] *The Technical University of Denmark.* [2] *Hvidovre University Hospital, Copenhagen, Denmark.* [3] *Delft University, The Netherlands.*

1. Introduction: Perfusion measurement studies using Arterial Spin Labelling (ASL) have been shown to be sensitive to the slice profiles of the RF inversion pulses [1]. The interaction between the inversion and imaging RF pulses in FAIR imaging [2], results in an offset in the FAIR image at zero perfusion unless the slice-selective inversion pulse profile is several times wider than that of the 90° imaging pulse. However, this reduces the sensitivity to perfusion and introduces larger transit delays for the incoming blood [3]. Therefore, it is desirable to overcome the errors due to the slice profile without increasing its thickness.

2. Methods: The imperfect slice profile of the RF inversion pulse can be expressed as an imperfect degree of inversion. This is expressed by having different values for the longitudinal magnetization immediately after inversion, i.e. the slice-selective (ss) and the non-selective (ns) magnetizations just after inversion, $M^{\mathrm{ss}}(0)$ and $M^{\mathrm{ns}}(0)$, are different.

We have performed FAIR measurements (32 repetitions) with interleaved ss and ns images and T_1 measurements (17 values of TI) in a homogeneous phantom with different ss inversion pulse thicknesses. The inversion pulse was a hyperbolic secant RF pulse. The parameters M_0, $M^{\mathrm{ss}}(0)$, $M^{\mathrm{ns}}(0)$, T_1^{ss} and T_1^{ns} were estimated using least squares fitting. Perfusion was calculated using the FAIR signals and the estimated parameters by the expression $M^{\mathrm{ss}} - M^{\mathrm{ns}} = \left[[M_0 - M^{\mathrm{ss}}(0)] \frac{f}{\lambda} \cdot TI + M^{\mathrm{ss}}(0) - M^{\mathrm{ns}}(0) \right] e^{-TI/T_1}$.

3. Results: Figure 1A shows the offset, $M^{\mathrm{ss}}(0) - M^{\mathrm{ns}}(0)$, in % of the equilibrium magnetization, M_0, as a function of the thickness of the inversion pulse (FWHM). The imaging slice had a constant thickness of 10 mm. Taking into consideration that the FAIR signal in grey matter is about 1% of M_0, it can be seen that the slice thickness of the inversion pulse must be above 45 mm for the offset to be negligible. Figure 1B shows the calculated perfusion as a function of the slice thickness. Compared to the perfusion level of grey matter ($\sim$ 0.01 ml/g s), the measured perfusion is negligible at all slice thicknesses. This shows that the effect of the slice thickness can be separated from perfusion. We are currently testing the perfusion measurements *in vivo* with different slice thicknesses.

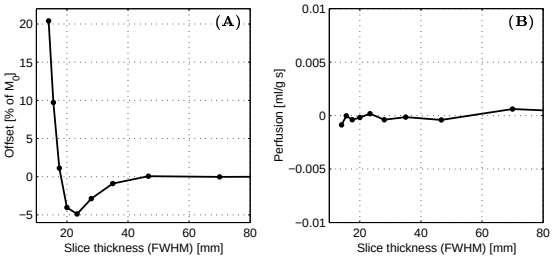

Figure 1: **(A)** The offset, $M^{\mathrm{ss}}(0) - M^{\mathrm{ns}}(0)$, in % of the equilibrium magnetization, M_0, as a function of the thickness of the inversion pulse. **(B)** The calculated perfusion as a function of the slice thickness. It is clear that the calculated values are well below the level of grey matter perfusion.

4. Conclusion: We have found that the effect of inversion slice thickness in FAIR imaging can be separated from perfusion. This allows us to decrease the thickness of the inversion slab thereby increasing the perfusion sensitivity of the FAIR measurements without introducing offset effects.

5. References:

[1] Frank LR, *et al.* [1997], *Magn.Reson.Med.* 38:558-564.
[2] Kwong KK, *et al.* [1995], *Magn.Reson.Med.* 34:878-887.
[3] Buxton RB, *et al.* [1998], *Magn.Reson.Med.* 40:383-396.

- Proc. 8th Annual Meeting of the International Society of Magnetic Resonance in Medicine, Denver, p. 712, 2000.

Offset Correction in FAIR Imaging

K. Sidaros[1,2], I.K. Andersen[1,2], H.B.W. Larsson[2], H. Gesmar[2], E. Rostrup[2]
[1]Dep. of Mathematical Modelling, Technical University of Denmark, [2]Danish Research Center of MR, Hvidovre Hospital, Denmark

Introduction: Perfusion measurements using Arterial Spin Labelling (ASL) have been shown to be sensitive to the slice profiles of the RF inversion pulses [1]. The interaction between the inversion and imaging RF pulses in FAIR imaging [2], results in an offset in the FAIR image at zero perfusion unless the slice-selective inversion pulse profile is several times wider than that of the 90° imaging pulse. However, this reduces the sensitivity to perfusion and introduces larger transit delays for the incoming blood [3], especially in multislice FAIR imaging. Therefore, it is desirable to overcome the errors due to the slice profile without increasing its relative thickness.

Methods: The imperfect slice profile of the RF inversion pulse can be expressed as an imperfect degree of inversion [4]. This is equivalent to allowing different values for the longitudinal magnetization of the slice-selective (ss) and the non-selective (ns) magnetizations immediately after inversion, i.e. $M^{ss}(0)$ and $M^{ns}(0)$, may differ.
We have performed FAIR measurements with interleaved ss and ns images and T_1 measurements in a homogeneous phantom and in 4 healthy volunteers with different slice thicknesses of the ss inversion pulse. The range of slice thicknesses was 14-140 mm in the phantom studies and 18-54 mm in the human studies. The imaging slice had a constant thickness of 10 mm. The inversion pulse was a hyperbolic secant RF pulse. All measurements were performed on a Siemens Vision 1.5T scanner. For the FAIR measurements, the experimental parameters were $TI/TR = 1/20$s (32 rep.) in the phantom studies and 1/3.15s (30 rep.) in the human studies.
The T_1 measurements were conventional IR experiments repeated with different inversion times (17 values in the phantom studies and 11 in the human studies). The parameters M_0, $M^{ss}(0)$, $M^{ns}(0)$, T_1^{ss} and T_1^{ns} were estimated using least squares fitting. Perfusion was calculated using either the difference signals (FAIR method) by the expression:

$$M^{ss} - M^{ns} = \left[[M_0 - M^{ss}(0)] \frac{f}{\lambda} \cdot TI + M^{ss}(0) - M^{ns}(0) \right] e^{-\frac{TI}{T_1^{ns}}},$$

or using the relation $f/\lambda = 1/T_1^{ss} - 1/T_1^{ns}$ (T_1 method).

Results: Figure 1 shows the offset, $M^{ss}(0) - M^{ns}(0)$, found in the phantom studies, in % of the equilibrium magnetization, M_0, as a function of the thickness of the inversion pulse (FWHM). Taking into consideration that the FAIR signal in grey matter is about 1% of M_0, it can be seen that the slice thickness of the inversion pulse must be above 45 mm for the offset to be negligible.
Figure 2 shows perfusion maps (FAIR method) for one of the volunteers at two slice thicknesses, 30 and 50 mm. It is noticed that the two maps are similar. However, the perfusion values are slightly higher in the first case.

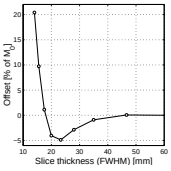

Figure 1: The offset, $M^{ss}(0) - M^{ns}(0)$, found in the phantom studies, in % of the equilibrium magnetization, M_0, as a function of the slice thickness of the inversion pulse (FWHM). The imaging slice had a constant thickness of 10 mm.

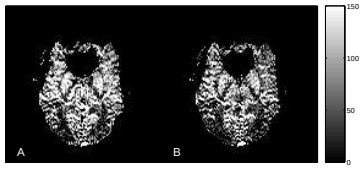

Figure 2: Perfusion maps [ml/100g/min] for one of the volunteers at two slice thicknesses of the inversion pulse: (A) 30 and (B) 50 mm. The maps were calculated using the FAIR method.

Figure 3 shows the average perfusion values found in the four subjects in a global grey matter ROI along with the perfusion values calculated in the phantom at different slice thicknesses of the inversion pulse. Both the values obtained with the FAIR method and those obtained with the T_1 method are shown. The figures also show the values obtained if the offset is ignored, i.e. it is assumed that $M^{ss}(0) \equiv M^{ns}(0)$. It is clear that the offset correction improves the results greatly. However, it is also seen that the correction described here is not adequate to give a constant perfusion at all thicknesses. This illustrates that transit delays depend on the slice thickness. When the slice thickness increases, the transit delays increase and perfusion is underestimated. When the slice thickness of the inversion pulse is large, the sensitivity to perfusion therefore decreases due to the large transit delay. This is seen from figure 3 as an underestimation of perfusion at large slice thicknesses.

Conclusion: The offset acquired between the ss and ns images has been measured as a function of the slice thickness of the ss pulse. It has been shown that a simple correction for the offset in the signal equations can improve perfusion quantification greatly. Although this correction does not compensate for tansit delay effects, it illustrates the decreased sensitivity to perfusion at large slice thicknesses of the inversion pulse.

References:

[1] Frank L.R., Wong E.C. and Buxton R.B. *Magn Reson Med* **38**(4), 558–64, 1997.

[2] Kwong K., Chesler D., Weisskoff R., Donahue K., Davis T., Østergaard L., Campbell T. and Rosen B. *Magn. Reson. Med.* **34**, 878–87, 1995.

[3] Buxton R.B., Frank L.R., Wong E.C., Siewert B., Warach S. and Edelman R.R. *Magn Reson Med* **40**(3), 383–96, 1998.

[4] Sidaros K., Andersen I.K., Gesmar H., Larsson H.B.W., Rostrup E. and Bovée W.M.M.J. *MAGMA* **8 suppl. 1**, 165, 1999.

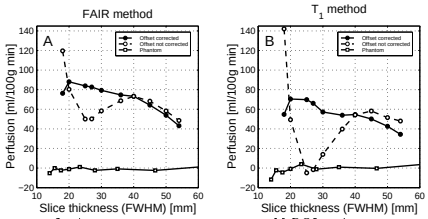

Figure 3: Average perfusion values in a GM ROI in 4 subjects and in a phantom at different slice thicknesses. (A) FAIR method, (B) T_1 method. The results of ignoring the offset are also shown.

- Proc. 8th Annual Meeting of the International Society of Magnetic Resonance in Medicine, Denver, p. 429, 2000.

Effect of Slice Profiles on the Accuracy of Fast T_1 Measurements

K. Sidaros[1,2], I.K. Andersen[1,2] and H.B.W. Larsson[2]
[1]Dep. of Mathematical Modelling, Technical University of Denmark, [2]Danish Research Center of MR, Hvidovre Hospital, Denmark

Introduction: Accurate and rapid T_1 measurements are required to study rapidly changing systems such as dynamic measurements of the rate of contrast agent uptake in quantitative perfusion measurements [1]. Rapid measurements are also desirable to reduce acquisition time and hence motion artifacts.
A number of techniques have been proposed for fast T_1 measurements [2, 3, 4]. The aim of this study is to investigate the effect of slice profiles on the accuracy of the measured T_1 values.

Theory: The sequence used consists of a non-selective hyperbolic secant inversion pulse followed by a series of α pulses each followed by an EPI module to measure the transverse magnetization. Since the α pulse has an imperfect slice profile, the magnetization will vary along the slice encoding direction, z. The magnetization just before the i'th α pulse is

$$M_i^-(z) = M_0 \frac{b}{1-a(z)} \left(1 - a(z)^{i-1}\right) + a(z)^{i-1} M_1^- \qquad (1)$$

where

$$M_1^- = [M(0) - M_0]\, e^{-R_1 TI} + M_0 \qquad (2)$$
$$a(z) = e^{-R_1 \Delta TI} \cdot \cos\alpha(z) \qquad (3)$$
$$b = 1 - e^{-R_1 \Delta TI}, \qquad (4)$$

and $M(0)$ is the magnetization just after the inversion pulse, M_0 is the equilibrium magnetization, $R_1 = 1/T_1$, TI is the time from the inversion pulse to the first α pulse and ΔTI is the time between the α pulses. The measured signal after each α pulse is

$$M_i^{\text{meas}} = \int_{-\infty}^{\infty} M_i^-(z) \sin\alpha(z) \cdot e^{-T_E/T_2^*}\, \mathrm{d}z. \qquad (5)$$

The T_2^* factor can be ignored since it can be included in M_0.
The numerical computations to estimate T_1 from equations (1-5) are quite demanding due to the required integration. It is therefore desirable to investigate whether the slice profile, $\alpha(z)$ can be substituted in the calculations by a mean angle, $\overline{\alpha}$, without loss in T_1 accuracy.

Methods: The true slice profile of a 25° pulse was measured and found to have the profile shown in figure 1A. The mean flip angle, $\overline{\alpha}$, corresponding to a given slice profile was calculated in the following way. A data-set was generated using equations (1-5) and a fixed T_1. A model incorporating a mean flip angle was then fitted to this data-set, giving an estimate of this angle.
Both simulations and *in vivo* measurements were done.
In the simulations, data-sets were generated using equations (1-5) with the approximate trapezoidal slice profile and a range of T_1 values. A model incorporating a mean flip angle was then fitted to the data, added noise.

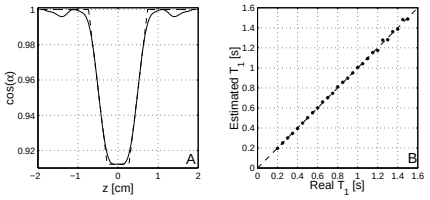

Figure 1: (A) The measured slice profile of the 25° pulse (solid curve) and a trapezoidal approximation (dashed curve). (B) Results of simulations of mean angle, $\overline{\alpha} = 21.0°$.

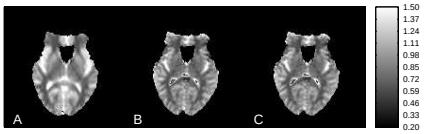

Figure 2: T_1 maps measured with (A) conventional IR, (B) fast T_1 measurement fitted with the slice profile and (C) fast T_1 measurement fitted with a mean flip angle.

The *in vivo* T_1 measurements were done both using the above mentioned sequence with $TR/TI/\Delta TI = \infty/42/106$ ms, $n = 27$, and with a conventional IR experiment with 11 TI values ranging from 50 to 5000 ms. All measurements were done on a Siemens Vision 1.5T scanner on a healthy volunteer.

Results: Figure 1B shows the results of the simulations. It is clear that the estimated T_1 values using the mean angle model perfectly match the true values
Figure 2 shows the resulting T_1 maps from the in vivo measurements: (A) shows T_1 acquired by the conventional IR experiment, while (B) and (C) show T_1 acquired by the fast method. (B) was fitted using $\alpha = \alpha(z)$, while (C) was fitted using $\alpha = \overline{\alpha}$. The T_1 maps are very similar in magnitude. However, the tissue contrast is clearer in the fast measurement. This is due to unavoidable motion of the subject during the conventional T_1 measurement (approx. 10 minutes).
Table 1 shows the mean estimated T_1 values in two GM and two WM ROIs. All three methods give the same results within the standard deviation. The equivalence between the slice profile calculations and the mean angle approximation is apparent.

Conclusion: It was found that the fast T_1 measurement using a series of α pulses during longitudinal relaxation gives as accurate results and better contrast compared to a conventional IR. It was also found that the slice profile of the α pulse can be approximated to a mean flip angle without any loss in accuracy.

References:

[1] Larsson H., Stubgaard M., Søndergaard L. and Henriksen O. *J Magn Reson Imaging* **4**(3), 433–40, 1994.

[2] Gowland P. and Mansfield P. *Magn. Reson. Med.* **30**, 351–354, 1993.

[3] Deichmann R. and Haase A. *J. Magn. Reson.* **96**, 608–612, 1992.

[4] Larsson H.B.W., Rosenbaum S., Andersen I.K. and Rostrup E. In Proc. Intl. Soc. Magn. Reson. Med., p. 1187. 7th Annual Meeting, Philadelphia, 1999.

	Conv. IR		Slice Profile		Mean Angle	
GM1	0.99	± 0.05	0.98	± 0.05	0.98	± 0.05
GM2	1.07	± 0.06	1.07	± 0.06	1.07	± 0.06
WM1	0.65	± 0.03	0.63	± 0.02	0.63	± 0.02
WM2	0.66	± 0.03	0.63	± 0.03	0.63	± 0.03

Table 1: Estimated T_1 values [s] (mean±SD) in four ROIs. The first column is the conventional IR experiment, and is regarded as the "true value". It is clear that including the slice profile in the fast measurement or using a mean flip angle ($\overline{\alpha} = 21.0°$) gives equally accurate results.

- Submitted to the 10th Annual Meeting of the International Society of Magnetic Resonance in Medicine, Honolulu, 2002.

Offset Correction in PICORE QUIPSS II Imaging

K. Sidaros[1,2], T.T. Liu[3], E.C. Wong[3,4], R.B. Buxton[3]

[1]Danish Research Center of MR, Hvidovre Hospital, Copenhagen, Denmark. [2]Informatics and Mathematical Modelling, Technical University of Denmark, Copenhagen, Denmark. Depts. of [3]Radiology and [4]Psychiatry, University of California San Diego, CA, USA.

Abstract: The gap between the inversion and imaging slabs in PICORE QUIPSS II arterial spin labeling is reduced thus decreasing the transit delay of incoming blood. This allows the reduction of the inversion time from 1400ms to 1100ms giving a higher perfusion signal at the cost of having to correct for an offset in the signal of stationary spins. It is shown that offset correction gives consistent perfusion values at different gaps and inversion times.

Introduction: Perfusion measurements using Arterial Spin Labeling (ASL) are sensitive to transit delays. Perfusion quantification therefore requires either the measurement of the transit delays or the utilization of a sequence that is insensitive to transit delays, such as PICORE QUIPSS II [1].

Transit delays can only be avoided by eliminating the gap between the tagging and imaging regions. However, due to imperfect slice profiles, a finite gap is necessary to ensure the complete canceling of static tissue signal in the ASL difference images. It has previously been shown that reducing the gap causes an offset in FAIR images [2]. Although this offset could be corrected, the dependence on transit delays was still evident [3]. In this study we demonstrate how the offset correction technique can be modified for QUIPSS II imaging, thus giving consistent perfusion values for different gaps.

Theory: It has previously been shown [2, 3], that the effect of an RF pulse on the magnetization can be expressed as a multiplicative factor. For a PICORE QUIPSS II sequence, three such factors are needed: p^{tag}, p^{con} and p^{q}, where p^{tag} gives the effect of the tag pulse on the longitudinal magnetization, p^{con} gives the effect of the control pulse, and p^{q} gives the effect of the QUIPSS saturation pulse. If presaturation is applied immediately before or after the tag and control pulses, the effect of the presaturation pulses can be included in p^{tag} and p^{con}. Equations for the evolution of the magnetization can then be written using these factors along with the longitudinal relaxation rates during the tag and control experiments, R_1^{tag} and R_1^{con} respectively, the inversion time for the QUIPSS saturation pulse TI_1 , the inversion time for the imaging pulse TI_2, and the repetition time TR.

The unknown parameters p^{tag}, p^{con}, p^{q}, R_1^{tag}, R_1^{con} and M_0 can be estimated by repeating the measurements at a series of different TI_1 and TI_2 values and fitting magnetization equations to the measured data.

When the gap between the tag and the imaging slab is small, the offset can be calculated directly from the magnetization equations and is strongly dependent on the difference between p^{tag} and p^{con}. The decrease in the gap will inherently cause a decrease in the transit delay, δt. TI_2 can therefore be reduced correspondingly without violating the condition for quantitation [1],

$$TI_2 > TI_1 + \delta t \ . \qquad (1)$$

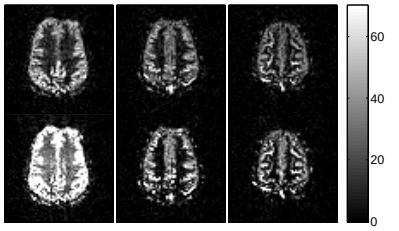

Figure 1: Magnetization difference images [a.u.] in one subject at TI_2/gap = 1400/10 (top row) and 1100/5 (bottom row) before offset correction. Left to right is proximal to distal.

	TI_2 [ms] / gap [mm]				
Slice	**1400/10**	**1100/5**	**1200/5**	**1300/5**	**1400/5**
1	65±6	104±6	100±6	97±6	93±6
		64±6	64±6	65±6	65±6
2	62±6	59±6	59±6	58±6	57±6
3	54±7	51±6	52±6	54±7	52±7

Table 1: GM perfusion values [ml/100g/min] averaged over all subjects (mean±std). Top/bottom row under slice 1 are values before/after offset correction.

Methods: Measurements were carried out on a Siemens Symphony 1.5T scanner using a PICORE QUIPSS II sequence with two presaturation pulses and two QUIPSS pulses. A phantom and three subjects were imaged for validation of the offset correction method. The phantom studies had the following parameters TI_2/TR = 1.4/6 s, FOV=200 mm, five 8 mm slices, 20 acqs., gap=1–15 mm. The human studies had $TI2$ = 1100–1400 ms, TR = 2 s, FOV=240 mm, three 8 mm slices, 135 acqs., gap=5/10 mm. Common parameters were TE/TI_1 = 40/700 ms and 64×64 matrix using EPI readout. T_1 measurements were performed with 16 TI_1/TI_2 pairs. The unknown parameters in the magnetization equations were fit to the T_1 curves giving estimates of the offset. M_0 of blood was estimated from the sagittal sinus in the high-TI_2 measurements while T_1 of blood was assumed to be 1.5 s and perfusion was calculated according to [1].

Results: A significant offset was detected in the phantom in the most proximal slice when the gap was less than 10 mm. After offset correction, the magnetization difference was not significantly different from zero ($p > 0.39$).

Figure 1 shows the mean magnetization difference images in the standard experiment, TI_2/gap = 1400/10, compared to the reduced gap and TI_2 experiment before offset correction. All slices in the TI_2/gap = 1100/5 experiment have slightly increased signal due to the reduced TI_2, while only the most proximal slice has very high intensity mainly due to the large offset.

Table 1 lists the mean perfusion values found in a grey matter (GM) ROI for each slice separately. Slice 1 is the most proximal slice and the only slice with a significant offset. It is evident that before offset correction, the perfusion values are highly overestimated, but that offset correction compensates fully for the existing offset. Since the perfusion estimates are consistent for all values of TI_2, the decrease in the gap from 10 to 5 mm allows the decrease of TI_2 from 1400 to 1100 ms without violating Eq. (1). The same analysis for a white matter (WM) ROI showed that the same decrease in the gap only allowed a decrease in TI_2 to 1300 ms. This agrees with WM having a longer transit delay than GM.

The decreased inversion time could potentially be used for imaging more slices before the signal relaxes or for increasing SNR in functional perfusion imaging.

Conclusion: Offset correction is feasible in quantitative perfusion imaging using QUIPSS II. Perfusion values calculated after offset correction in a reduced gap experiment are identical to those found with the standard parameter settings. The reduced transit delay resulting from the reduced gap allowed reduction of the inversion time from 1400 ms to 1100 ms for GM and 1300 ms for WM without affecting the accuracy of perfusion quantitation.

References:

[1] Wong EC *et al. Magn Reson Med*, **39**(5), 702–8, 1998.

[2] Andersen IK *et al. Magn Reson Imag*, **18**(5), 565–74, 2000.

[3] Sidaros K *et al. Magn Reson Med*, **46**(1), 193–7, 2001.

- Submitted to the 10th Annual Meeting of the International Society of Magnetic Resonance in Medicine, Honolulu, 2002.

Improved SNR in Perfusion fMRI by Offset Correction

K. Sidaros[1,2], T.T. Liu[3], T.E. Lund[1], E.C. Wong[3,4], R.B. Buxton[3]

[1]Danish Research Center of MR, Hvidovre Hospital, Copenhagen, Denmark. [2]Informatics and Mathematical Modelling, Technical University of Denmark, Copenhagen, Denmark. Depts. of [3]Radiology and [4]Psychiatry, University of California San Diego, CA, USA.

Abstract: Perfusion based fMRI using arterial spin labeling generally has lower SNR than conventional BOLD fMRI. One method of increasing the SNR of perfusion fMRI is decreasing the inversion time. This necessitates a reduction of the gap between the inversion and imaging slabs, which in turn gives incomplete subtraction of the static tissue signal. However, the resulting offset can be corrected. This is applied to fMRI with bilateral finger-tapping using a PICORE QUIPSS II sequence. The number of significantly activated pixels increased by 138% and the activation t-scores increased by 32% while the quantitative accuracy of the perfusion estimates was maintained.

Introduction: Compared to conventional BOLD-fMRI, measurement of perfusion [1] using arterial spin labeling (ASL) during functional activation suffers from low SNR and hence low detectability. SNR is further decreased when a quantitative measure of perfusion is desired. The advantage of using an ASL sequence is to be able to measure the perfusion changes associated with functional activation directly. Activation sites found with perfusion measurements are believed to correlate better with neural activation sites than sites found with BOLD [2].

For quantitative ASL sequences, such as PICORE QUIPSS II [3], a long inversion time is required to account for transit delays. Decreasing the inversion time increases SNR in the ASL measurements, but violates the condition needed for quantitative imaging unless the gap between the tagging and imaging regions also is decreased. This gives an offset in the difference images due to incomplete static tissue subtraction. This offset can be corrected if a separate T_1 measurement is acquired [4]. In this study we show that the SNR can be increased in perfusion fMRI while maintaining a quantitative measure of perfusion.

Methods: Measurements on two subjects were carried out on a Siemens Symphony 1.5T scanner using a PICORE QUIPSS II sequence with presaturation. The imaging parameters were TR = 2 s, TI_1 = 700 ms, TE = 40 ms, FOV=240 mm, 64×64 matrix, 135 acquisitions, 10 cm inversion slab. Three 8 mm slices were imaged. Two runs of each of two TI_2/gap settings were acquired. The standard experiment had the parameters TI_2 = 1400 ms and gap=10 mm. The reduced gap experiment had TI_2 = 1100 ms and gap=5 mm. The activation paradigm for each experiment was alternating periods of 30 s rest and 30 s bilateral finger-tapping with a total duration of 4.5 min per run.

The offset was measured, estimated and corrected using separate T_1-measurements in a manner similar to that in [4], except that both TI_1 and TI_2 were varied during the measurements. The added scanning time was approximately 5 min.

All images were 2D-registered and the running subtraction of the tag and control images was used to generate a series of perfusion weighted images. The individual voxel timeseries of the difference images were correlated to a reference function that was a box-car convolved with the hemodynamic response [5] (see figure 2) and an activation threshold corresponding to p=0.0005 was selected. The number of activated voxels was registered for each subject.

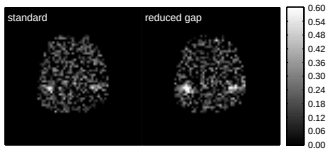

Figure 1: Cross-correlation coefficient maps of the perfusion signal with the reference function in the standard experiment and the experiment with the reduced gap.

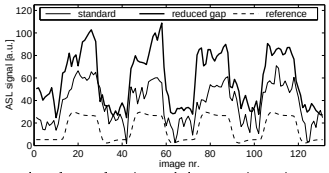

Figure 2: The reference function and the mean timeseries averaged over the same ROI for one subject in the most proximal slice in the standard experiment and the experiment with the reduced gap.

An ROI for comparison of the two parameter sets was selected. The ROI contained only the voxels activated in both runs of the standard experiment. The timeseries were averaged over this ROI and both runs for each slice separately. A general linear model (GLM) with a design matrix containing a constant term, the reference function and the derivative of the reference function, was fit to the timeseries giving a measure of activation. Relative perfusion increases during activation and t-scores of the activation signal were calculated.

Results: Figure 1 shows the cross-correlation coefficient maps of the magnetization difference signal with the reference function for one run. The number of significantly activated pixels ($p < 0.0005$) common to both runs of each experiment increased from 21 in the standard experiment to 50 in the reduced gap experiment. This is due to the lower inversion time that may be utilized due to a reduction in the transit delay.

Figure 2 shows the mean timeseries of the signal in the most proximal slice (which has largest offset) for both the standard experiment and the reduced gap experiment after offset correction. The SNR in the latter is clearly higher. The activation t-scores and hence detectability increased on average by 32%.

Table 1 shows the relative perfusion increases during activation in the two experiments. Note that the perfusion increase in slice 1 (proximal slice) is underestimated with the narrow gap before offset correction. However, after offset correction, the value is correct. The offset is negligible in slice 2 and there is therefore no significant difference between the corrected and uncorrected values. There were no significantly activated voxels in slice 3 in the standard experiment.

Experiment	Slice 1	Slice 2
standard	41±4	43±5
reduced gap (uncorrected)	31±2	38±4
reduced gap (corrected)	41±3	40±4

Table 1: Relative perfusion increase during activation in percent. Values are mean±2SEM.

Conclusion: Offset correction in perfusion imaging is applicable to functional imaging and gives improved SNR. The number of significantly activated pixels increased by 138% and the t-scores increased by 32% by decreasing the gap between the tagging and imaging regions in a PICORE QUIPSS II sequence. This was achieved while maintaining the quantitative accuracy of the perfusion increase estimate.

References:

[1] Kwong K *et al. Magn Reson Med*, **34**, 878–87, 1995.
[2] Luh W *et al. Magn Reson Med*, **44**(1), 137–43, 2000.
[3] Wong EC *et al. Magn Reson Med*, **39**(5), 702–8, 1998.
[4] Sidaros K *et al. Magn Reson Med*, **46**(1), 193–7, 2001.
[5] Friston K *et al. Magn Reson Med*, **39**(1), 41–52, 1998.

References

[1] Edelman R, Hesselink J, Zlatkin M, editors. Clinical Magnetic Resonance Imaging. Philadelphia: W.B. Saunders Company, 2nd edition 1996.

[2] Mansfield P, Morris PG. NMR Imaging in Biomedicine. London: Academic Press 1982.

[3] Callaghan PT. Principles of Nuclear Magnetic Resonance Microscopy. Oxford: Clarendon Press 1991.

[4] Ernst RR, Badenhausen G, Wokaun A. Principles of Nuclear Magnetic Resonance in One and Two Dimensions. Oxford: Clarendon Press 1987.

[5] Le Bihan D. Theoretical principles of perfusion imaging. Application to magnetic resonance imaging. Invest Radiol 1992;27:6–11.

[6] Le Bihan D, Turner R. The capillary network: a link between IVIM and classical perfusion. Magn Reson Med 1992;27:171–8.

[7] Buxton R, Frank L, Prasad P. Principles of Diffusion and Perfusion MRI, Philadelphia: W.B. Saunders Company. In: Editors, R. R. Edelman and J. R. Hesselink and M. B. Zlatkin, Clinical Magnetic Resonance Imaging. 2nd edition 1996; pp. 233–270.

[8] Barbier EL, Lamalle L, Decorps M. Methodology of brain perfusion imaging. J Magn Reson Imaging 2001;13:496–520.

[9] Lassen NA, Henriksen O, Sejrsen P. Indicator methods for measurements of organ and tissue blood flow. In: Editors, Shephard J T and Abboud F M, Handbook of Physiology – The Cardiovascular System III 1983; pp. 21–63.

[10] Schmitt F, Stehling M, Turner R. Echo-Planar Imaging – Theory, Technique and Application. Heidelberg: Springer-Verlag 1998.

[11] Østergaard L, Weisskoff R, Chesler D, Gyldensted C, Rosen B. High resolution measurement of cerebral blood flow using intravascular tracer bolus passages. part I: mathematical approach and statistical analysis. Magn Reson Med 1996;36:715–25.

[12] Østergaard L, Sørensen A, Kwong K, Weisskoff R, Gyldensted C, Rosen B. High resolution measurement of cerebral blood flow using intravascular tracer bolus passages. part II: experimental comparison and preliminary results. Magn Reson Med 1996;36:726–36.

[13] Le Bihan D, Breton E, Lallemand D, Aubin M, Vignaud J, Laval-Jeantet M. Separation of diffusion and perfusion in intravoxel incoherent motion MR imaging. Radiology 1988;168:497–505.

[14] Le Bihan D, Turner R. Intravoxel incoherent motion imaging using spin echoes. Magn Reson Med 1991;19:221–7.

[15] Müller M, Prasad P, Edelman R. Can the IVIM model be used for renal perfusion imaging? Eur J Radiol 1998;26:297–303.

[16] Neil J, Bosch C, Ackerman J. An evaluation of the sensitivity of the intravoxel incoherent motion (IVIM) method of blood flow measurement to changes in cerebral blood flow. Magn Reson Med 1994;32:60–5.

[17] Wirestam R, Borg M, Brockstedt S, Lindgren A, Holtås S, Ståhlberg F. Perfusion-related parameters in intravoxel incoherent motion MR imaging compared with CBV and CBF measured by dynamic susceptibility-contrast MR technique. Acta Radiol 2001;42:123–8.

[18] Henkelman RM. Does IVIM Measure Classical Perfusion? Magn Reson Med 1990;16:470–475.

[19] Wong EC, Buxton RB, Frank LR. Quantitative perfusion imaging using arterial spin labeling. Neuroimaging Clin N Am 1999;9:333–42.

[20] Detre JA, Leigh JS, Williams DS, Koretsky AP. Perfusion Imaging. Magn Reson Med 1992;23:37–45.

[21] Williams DS, Detre JA, Leigh JS, Koretsky AP. Magnetic resonance imaging of perfusion using spin inversion of arterial water. Proc Natl Acad Sci USA 1992;89:212–216.

[22] Calamante F, Thomas D, Pell G, Wiersma J, Turner R. Measuring cerebral blood flow using magnetic resonance imaging techniques. J Cereb Blood Flow Metab 1999;19:701–35.

[23] Zhang W, Williams DS, Detre JA, Koretsky AP. Measurement of Brain Perfusion by Volume-Localized NMR Spectroscopy Using Inversion of Arterial Water Spins: Accounting for Transit Time and Cross-Relaxation. Magn Reson Med 1992;25:362–371.

[24] Zhang W, Silva A, Williams D, Koretsky A. NMR measurement of perfusion using arterial spin labeling without saturation of macromolecular spins. Magn Reson Med 1995;33:370–6.

[25] Silva A, Zhang W, Williams D, Koretsky A. Multi-slice MRI of rat brain perfusion during amphetamine stimulation using arterial spin labeling. Magn Reson Med 1995;33:209–14.

[26] Alsop D, Detre J. Multisection cerebral blood flow MR imaging with continuous arterial spin labeling. Radiology 1998;208:410–6.

[27] Ye FQ, Mattay VS, Jezzard P, Frank JA, Weinberger DR, McLaughlin AC. Correction for vascular artifacts in cerebral blood flow values measured by using arterial spin tagging techniques. Magn Reson Med 1997;37:226–35.

[28] Alsop DC, Detre JA. Reduced transit-time sensitivity in noninvasive magnetic resonance imaging of human cerebral blood flow. J Cereb Blood Flow Metab 1996;16:1236–49.

[29] Wong E, Buxton R, Frank L. Implementation of quantitative perfusion imaging techniques for functional brain mapping using pulsed arterial spin labeling. NMR Biomed 1997;10:237–49.

[30] Wong EC, Buxton RB, Frank LR. A theoretical and experimental comparison of continuous and pulsed arterial spin labeling techniques for quantitative perfusion imaging. Magn Reson Med 1998;40:348–55.

[31] Barbier E, Silva A, Kim H, Williams D, Koretsky A. Perfusion analysis using dynamic arterial spin labeling (DASL). Magn Reson Med 1999; 41:299–308.

[32] Barbier E, Silva A, Kim S, Koretsky A. Perfusion imaging using dynamic arterial spin labeling (DASL). Magn Reson Med 2001;45:1021–9.

[33] Edelman RR, Siewert B, Garby D, Thangaraj V, Nobre AC, Mesulam MM, Warach S. Qualitative Mapping of Cerebral Blood Flow and Functional Localization with Echo-planar MR Imagaing and Signal Targeting with Alternating Radio Frequency. Radiology 1994;192:513–520.

[34] Kwong K, Chesler D, Weisskoff R, Donahue K, Davis T, Østergaard L, Campbell T, Rosen B. MR Perfusion Studies with T_1-Weighted Echo Planar Imaging. Magn Reson Med 1995;34:878–87.

[35] Kim S. Quantification of relative cerebral blood flow change by flow-sensitive alternating inversion recovery (FAIR) technique: application to functional mapping. Magn Reson Med 1995;34:293–301.

[36] Schwarzbauer C, Morrissey S, Haase A. Quantitative magnetic resonance imaging of perfusion using magnetic labeling of water proton spins within the detection slice. Magn Reson Med 1996;35:540–6.

[37] Helpern JA, Branch CA, Yongbi MN, Huang NC. Perfusion Imaging by Un-inverted Flow-sensitive Alternating Inversion Recovery (UNFAIR). Magn Reson Imag 1997;15:135–139.

[38] Schwarzbauer C, Heinke W. BASE imaging: a new spin labeling technique for measuring absolute perfusion changes. Magn Reson Med 1998;39:717–22.

[39] Chen Q, Siewert B, Bly B, Warach S, Edelman R. STAR-HASTE: perfusion imaging without magnetic susceptibility artifact. Magn Reson Med 1997;38:404–8.

[40] Golay X, Stuber M, Pruessmann K, Meier D, Boesiger P. Transfer Insensitive Labeling Technique (TILT): Application to Multislice Functional Perfusion Imaging. J Magn Reson Imaging 1999;9:454–61.

[41] Kao Y, Wan X, MacFall J. Simultaneous multislice acquisition with arterial-flow tagging (SMART) using echo planar imaging (EPI). Magn Reson Med 1998;39:662–5.

[42] Zhou J, Mori S, van Zijl PCM. FAIR Excluding Radiation Damping (FAIRER). Magn Reson Med 1998;40:712–719. 50.

[43] Mai V, Knight-Scott J, Kallmes D, Marx W, Cail W, Christopher J, Berr S. Quantification of Steady-State Perfusion Rates Using Flow-Sensitive Alternating Inversion Recovery with an Extra Radiofrequency Pulse (FAIRER). In: Proc. Intl Soc Magn Reson Med. 6th Annual Meeting, Sydney 1996; p. 1215.

[44] Berr S, Mai V. Extraslice spin tagging (EST) magnetic resonance imaging for the determination of perfusion. J Magn Reson Imaging 1999;9:146–50.

[45] Silver MS, Joseph RI. Selective spin inversion in nuclear magnetic resonance and coherent optics through an exact solution of the Bloch-Riccati equation. Phys Rev A 1985;31:2753–2755.

[46] Frank LR, Wong EC, Buxton RB. Slice profile effects in adiabatic inversion: application to multislice perfusion imaging. Magn Reson Med 1997; 38:558–64.

[47] Yongbi MN, Branch CA, Helpern JA. Perfusion Imaging Using FOCI RF Pulses. Magn Reson Med 1998;40:938–43.

[48] Wong EC, Buxton RB, Frank LR. Quantitative imaging of perfusion using a single subtraction (QUIPSS and QUIPSS II). Magn Reson Med 1998; 39:702–8.

[49] Ogawa S, Lee T, Kay A, Tank D. Brain Magnetic Resonance Imaging with Contrast Dependent on Blood Oxygenation. Proc Natl Acad Sci U S A 1990;87:9868–72.

[50] Kwong K, Belliveau J, Chesler D, Goldberg I, Weisskoff R, Poncelet B, Kennedy D, Hoppel B, Cohen M, Turner R. Dynamic Magnetic Resonance Imaging of Human Brain Activity During Primary Sensory Stimulation. Proc Natl Acad Sci U S A 1992;89:5675–9.

[51] Buxton RB, Wong EC, Frank LR. Dynamics of blood flow and oxygenation changes during brain activation: the balloon model. Magn Reson Med 1998;39:855–64.

[52] Hoge RD, Atkinson J, Gill B, Crelier GR, Marrett S, Pike GB. Investigation of BOLD signal dependence on cerebral blood flow and oxygen consumption: the deoxyhemoglobin dilution model. Magn Reson Med 1999;42:849–63.

[53] Edelman RR, Chen Q. EPISTAR MRI: Multislice Mapping of Cerebral Blood Flow. Magn Reson Med 1998;40:800–805.

[54] Tanabe J, Yongbi M, Branch C, Hrabe J, Johnson G, Helpern J. MR perfusion imaging in human brain using the UNFAIR technique. Un-inverted flow-sensitive alternating inversion recovery. J Magn Reson Imaging 1999; 9:761–7.

[55] Wu D, Johnson Jr. CS. Radiation-Damping Effects on Relaxation-Time Measurements by the Inversion-Recovery Method. J Magn Reson A 1994; 110:113–117.

[56] Chen JH, Mao XA, Ye CH. Intensity Jumping and Beating in Inversion-Recovery Experiments of Water Due to Radiation Damping. J Magn Reson 1997;124:490–494.

[57] Mai V, Berr S. MR perfusion imaging of pulmonary parenchyma using pulsed arterial spin labeling techniques: FAIRER and FAIR. J Magn Reson Imaging 1999;9:483–7.

[58] Thomas DL, Lythgoe MF, Calamante F, Gadian DG, Ordidge RJ. Simultaneous noninvasive measurement of CBF and CBV using double-echo FAIR (DEFAIR). Magn Reson Med 2001;45:853–63.

[59] Ye FQ, Frank JA, Weinberger DR, McLaughlin AC. Noise reduction in 3D perfusion imaging by attenuating the static signal in arterial spin tagging (ASSIST). Magn Reson Med 2000;44:92–100.

[60] Blamire A, Styles P. Spin Echo Entrapped Perfusion Image (SEEPAGE). a Nonsubtraction Method for Direct Imaging of Perfusion. Magn Reson Med 2000;43:701–4.

[61] Duyn J, Tan C, van Gelderen P, Yongbi M. High-sensitivity single-shot perfusion-weighted fMRI. Magn Reson Med 2001;46:88–94.

[62] Buxton RB, Frank LR, Wong EC, Siewert B, Warach S, Edelman RR. A general kinetic model for quantitative perfusion imaging with arterial spin labeling. Magn Reson Med 1998;40:383–96.

[63] Calamante F, Williams SR, van Bruggen N, Kwong KK, Turner R. A Model for Quantification of Perfusion in Pulsed Labelling Techniques. NMR Biomed 1996;9:79–83.

[64] Tsekos N, Zhang F, Merkle H, Nagayama M, Iadecola C, Kim S. Quantitative measurements of cerebral blood flow in rats using the FAIR technique: correlation with previous iodoantipyrine autoradiographic studies. Magn Reson Med 1998;39:564–73.

[65] Yang Y, Engelien W, Xu S, Gu H, Silbersweig DA, Stern E. Transit time, trailing time, and cerebral blood flow during brain activation: Measurement using multislice, pulsed spin-labeling perfusion imaging. Magn Reson Med 2000;44:680–685.

[66] Kim S, Tsekos N, Ashe J. Multi-slice Perfusion-based Functional MRI using the FAIR Technique: Comparison of CBF and BOLD Effects. NMR Biomed 1997;10:191–6.

[67] Zhou J, van Zijl PC. Effect of Transit Times on Quantification of Cerebral Blood Flow by the FAIR T_1-Difference Approach. Magn Reson Med 1999; 42:890–4.

[68] Wong E, Buxton R, Frank L. Quanititative Imaging of Perfusion Using a Single Subtraction (QUIPSS). NeuroImage 1996;3:S5.

[69] Wong E, Frank L, Buxton R. QUIPSS II: A Method for Improving Quantitation of Perfusion Using Pulsed Arterial Spin Labeling. In: Proc. Intl Soc Magn Reson Med. 5th Annual Meeting, Vancouver 1997; p. 1761.

[70] Lipton M, Branch C, Hrabe J, Lewis D, Helpern J. RF Excitation Profiles with FAIR: Impact of Truncation of the Arterial Input Function on Quantitative Perfusion. J Magn Reson Imaging 2001;13:207–14.

[71] Silva A, Zhang W, Williams D, Koretsky A. Estimation of water extraction fractions in rat brain using magnetic resonance measurement of perfusion with arterial spin labeling. Magn Reson Med 1997;37:58–68.

[72] St Lawrence KS, Frank JA, McLaughlin AC. Effect of restricted water exchange on cerebral blood flow values calculated with arterial spin tagging: A theoretical investigation. Magn Reson Med 2000;44:440–9.

[73] Andersen IK, Sidaros K. MR Perfusion Imaging by Spin Labelling. Master's thesis, The Technical University of Denmark, Dept. of Mathematical Modelling 1998.

[74] Zhou J, van Zijl PC. Perfusion imaging using FAIR with a short predelay. Magn Reson Med 1999;41:1099–107.

[75] Meyer CH, Hu BS, Nishimura DG, Macovski A. Fast spiral coronary artery imaging. Magn Reson Med 1992;28:202–13.

[76] Mai V, Hagspiel K, Christopher J, Do H, Altes T, Knight-Scott J, Stith A, Maier T, Berr S. Perfusion Imaging of the Human Lung using Flow-sensitive Alternating Inversion Recovery with an Extra Radiofrequency Pulse (FAIRER). Magn Reson Imaging 1999;17:355–61.

[77] Hatabu H, Tadamura E, Prasad PV, Chen Q, Buxton R, Edelman RR. Noninvasive pulmonary perfusion imaging by STAR-HASTE sequence. Magn Reson Med 2000;44:808–812.

[78] Roberts D, Detre J, Bolinger L, Insko E, Lenkinski R, Pentecost M, Leigh Jr. JS. Renal perfusion in humans: MR imaging with spin tagging of arterial water. Radiology 1995;196:281–6.

[79] Karger N, Biederer J, Lusse S, Grimm J, Steffens J, Heller M, Gluer C. Quantitation of renal perfusion using arterial spin labeling with FAIR-UFLARE. Magn Reson Imaging 2000;18:641–7.

[80] Frank LR, Wong EC, Haseler LJ, Buxton RB. Dynamic imaging of perfusion in human skeletal muscle during exercise with arterial spin labeling. Magn Reson Med 1999;42:258–67.

[81] Gonzalez-At J, Alsop D, Detre J. Cerebral perfusion and arterial transit time changes during task activation determined with continuous arterial spin labeling. Magn Reson Med 2000;43:739–46.

[82] Kim SG, Rostrup E, Larsson HB, Ogawa S, Paulson OB. Determination of relative $CMRO_2$ from CBF and BOLD changes: significant increase of oxygen consumption rate during visual stimulation. Magn Reson Med 1999;41:1152–61.

[83] Hendrich K, Kochanek P, Melick J, Schiding J, Statler K, Williams D, Marion D, Ho C. Cerebral perfusion during anesthesia with fentanyl, isoflurane, or pentobarbital in normal rats studied by arterial spin-labeled MRI. Magn Reson Med 2001;46:202–6.

[84] Liu H, Kochunov P, Hou J, Pu Y, Mahankali S, Feng C, Yee S, Wan Y, Fox P, Gao J. Perfusion-weighted imaging of interictal hypoperfusion in temporal lobe epilepsy using FAIR-HASTE: comparison with $H_2{}^{15}O$ PET measurements. Magn Reson Med 2001;45:431–5.

[85] Hendrich K, Kochanek P, Williams D, Schiding J, Marion D, Ho C. Early perfusion after controlled cortical impact in rats: quantification by arterial spin-labeled MRI and the influence of spin-lattice relaxation time heterogeneity. Magn Reson Med 1999;42:673–81.

[86] Siewert B, Schlaug G, Edelman R, Warach S. Comparison of EPISTAR and T_2^*-weighted gadolinium-enhanced perfusion imaging in patients with acute cerebral ischemia. Neurology 1997;48:673–9.

[87] Chalela JA, Alsop DC, Gonzalez-Atavales JB, Maldjian JA, Kasner SE, Detre JA. Magnetic resonance perfusion imaging in acute ischemic stroke using continuous arterial spin labeling. Stroke 2000;31:680–7.

[88] Silva A, Kim S, Garwood M. Imaging blood flow in brain tumors using arterial spin labeling. Magn Reson Med 2000;44:169–73.

[89] Hoult D. The Solution of the Bloch Equations in the Presence of a Varying B_1 Field – An Approach to Selective Pulse Analysis. J Magn Reson 1979; 35:69–86.

[90] Goldstein H. Classical Mechanics. Reading: Addison-Wesley, 2nd edition 1980.

[91] Nishimura DG. Introduction to Magnetic Resonance Imaging. Lecture notes, Department of Electrical Engineering, Stanford University 1993.

[92] Matson GB. An integrated program for amplitude-modulated RF pulse generation and re-mapping with shaped gradients. Magn Reson Imaging 1994;12:1205–25.

[93] Center for Devices and Radiological Health. Guidance for the Submission Of Premarket Notifications for Magnetic Resonance Diagnostic Devices. Technical report, Food and Drug Administration, http://www.fda.gov/cdrh/ode/mri340.pdf,1998.

[94] Tannus A, Garwood M. Adiabatic pulses. NMR Biomed 1997;10:423–34.

[95] Bendall MR, Garwood M, Ugurbil K, Pegg DT. Adiabatic refocusing pulse which compensates for variable RF power and off-resonance effects. Magn Reson Med 1987;4:493–9.

[96] Ugurbil K, Garwood M, Bendall MR. Amplitude- and Frequency-Modulated Pulses to Achieve 90° Plane Rotations with Inhomogeneous B_1 Fields. J Magn Reson 1987;72:177–85.

[97] Conolly S, Nishimura D, Macovski A. A Selective Adiabatic Spin-Echo Pulse. J Magn Reson 1989;83:324–34.

[98] Norris DG, Haase A. Variable excitation angle AFP pulses. Magn Reson Med 1989;9:435–40.

[99] Garwood M, Ke Y. Symmetric Pulses to Induce Arbitrary Flip Angles with Compensation for RF Inhomogeneity and Resonance Offsets. J Magn Reson 1991;94:511–25.

[100] Garwood M, Ugurbil K. B_1 Insensitive Adiabatic RF Pulses, Berlin: Springer-Verlag, volume 26 of *NMR Basic Principles and Progress* 1992; pp. 110–147.

[101] de Graaf RA, Luo Y, Terpstra M, Merkle H, Garwood M. A new localization method using an adiabatic pulse, BIR-4. J Magn Reson B 1995; 106:245–52.

[102] de Graaf RA, Nicolay K, Garwood M. Single-shot, B_1-insensitive slice selection with a gradient-modulated adiabatic pulse, BISS-8. Magn Reson Med 1996;35:652–7.

[103] Tannus A, Garwood M. Improved Performance of Frequency-Swept Pulses Using Offset-Independent Adiabacity. J Magn Reson A 1996;120:133–37.

[104] Silver MS, Joseph RI, Hoult DI. Highly Selective $\pi/2$ and π Pulse Generation. J Magn Reson 1984;59:347–351.

[105] Payne GS, Leach MO. Implementation and Evaluation of Frequency Offset Corrected Inversion (FOCI) Pulses on a Clinical MR System. Magn Reson Med 1997;38:828–33.

[106] Shinnar M; Bolinger L. Synthesis of Soft Pulses with Specified Frequency Response. In: Proc Soc Magn Reson Med. 7th Annual Meeting 1988; p. 1040.

[107] Shinnar M, Eleff S, Subramanian H, Leigh J. The synthesis of pulse sequences yielding arbitrary magnetization vectors. Magn Reson Med 1989; 12:74–80.

[108] Shinnar M, Bolinger L, Leigh J. The use of finite impulse response filters in pulse design. Magn Reson Med 1989;12:81–7.

[109] Shinnar M, Bolinger L, Leigh J. The synthesis of soft pulses with a specified frequency response. Magn Reson Med 1989;12:88–92.

[110] Shinnar M, Leigh J. The application of spinors to pulse synthesis and analysis. Magn Reson Med 1989;12:93–8.

[111] Le Roux P. Exact Synthesis of Radiofrequency Waveforms. In: Proc Soc Magn Reson Med. 7th Annual Meeting 1988; p. 1049.

[112] Le Roux P. Simplified RF Synthesis. In: Proc Soc Magn Reson Med. 8th Annual Meeting 1989; p. 1168.

[113] Pauly J, Le Roux P, Nishimura D, Macovski A. Parameter relations for the Shinnar-Le Roux selective excitation pulse design algorithm. IEEE Trans Med Imaging 1991;10:53–65.

[114] Sidaros K, Andersen IK, Larsson HBW. Effect of Slice Profiles on the Accuracy of Fast T_1 Measurements. In: Proc. ISMRM, 8th Annual Meeting, Denver 2000; p. 429.

[115] Andersen IK, Sidaros K, Gesmar H, Rostrup E, Larsson HBW. A Model System for Perfusion Quantification using FAIR. Magn Reson Imag 2000; 18:565–74.

[116] Sidaros K, Andersen I, Gesmar H, Rostrup E, Larsson H. Improved Perfusion Quantification in FAIR Imaging by Offset Correction. Magn Reson Med 2001;46:193–7.

[117] Yongbi MN, Yang Y, Frank JA, Duyn JH. Multislice perfusion imaging in human brain using the C-FOCI inversion pulse: comparison with hyperbolic secant. Magn Reson Med 1999;42:1098–105.

[118] Yongbi M, Tan C, Frank J, Duyn J. A protocol for assessing subtraction errors of arterial spin-tagging perfusion techniques in human brain. Magn Reson Med 2000;43:896–900.

[119] Wong E, Luh WM. Similarities and Differences Between FOCI Pulses and VERSE Transformed Hyperbolic Secant Pulses. In: Proc. Intl Soc Magn Reson Med. 8th Annual Meeting, Denver 2000; p. 1427.

[120] Schepers J, Garwood M, van Der Sanden B, Nicolay K. Improved subtraction by adiabatic FAIR perfusion imaging. Magn Reson Med 2002; 47:330–6.

[121] Sidaros K, Andersen IK, Larsson HBW, Gesmar H, Rostrup E. Offset Correction in FAIR Imaging. In: Proc. ISMRM, 8th Annual Meeting, Denver 2000; p. 712.

[122] Keilholz-George S, Knight-Scott J, Berr S. Theoretical analysis of the effect of imperfect slice profiles on tagging schemes for pulsed arterial spin labeling MRI. Magn Reson Med 2001;46:141–8.

[123] Sidaros K, Liu T, Wong E, Buxton R. Offset Correction in PICORE QUIPSS II Imaging. In: Proc. ISMRM, 10th annual meeting, Honolulu 2002; p. 1063.

[124] Sidaros K, Liu T, Lund T, Wong E, Buxton R. Improved SNR in Perfusion fMRI by Offset Correction. In: Proc. ISMRM, 10th annual meeting, Honolulu 2002; p. 624.

[125] Kim S, Tsekos N. Perfusion imaging by a flow-sensitive alternating inversion recovery (FAIR) technique: application to functional brain imaging. Magn Reson Med 1997;37:425–35.

[126] Yang Y, Frank JA, Hou L, Ye FQ, McLaughlin AC, Duyn JH. Multi-slice imaging of quantitative cerebral perfusion with pulsed arterial spin labeling. Magn Reson Med 1998;39:825–32.

[127] Pell GS, Thomas DL, Lythgoe MF, Calamante F, Howseman AM, Gadian DG, Ordidge RJ. Implementation of quantitative FAIR perfusion imaging with a short repetition time in time-course studies. Magn Reson Med 1999; 41:829–40.

[128] Wong EC, Luh WM, Liu TT. Turbo ASL: arterial spin labeling with higher SNR and temporal resolution. Magn Reson Med 2000;44:511–5.

[129] Luh WM, Wong EC, Bandettini PA, Hyde JS. QUIPSS II with thin-slice TI1 periodic saturation: a method for improving accuracy of quantitative perfusion imaging using pulsed arterial spin labeling. Magn Reson Med 1999;41:1246–54.

[130] Kaldoudi E, Williams S. Relaxation Time Measurements in NMR Imaging. Part I: Longitudinal Relaxation Time. Concepts in Magnetic Resonance 1993;5:217–242.

[131] Ordidge R, Gibbs P, Chapman B, Stehling M, Mansfield P. High-speed multislice T_1 mapping using inversion-recovery echo-planar imaging. Magn Reson Med 1990;16:238–45.

[132] Press WH, Flannery BP, Teukolsky SA, Vetterling WT. Numerical Recipies in C - The Art of Scientific Computing. Cambridge: Cambridge University Press 1988.

[133] Kingsley P, Monahan W. Effect of increased repetition time TR on precision of inversion-recovery T_1 measurements. Magn Reson Imaging 2001; 19:279–82.

[134] Gowland P, Leach M. A simple method for the restoration of signal polarity in multi-image inversion recovery sequences for measuring T_1. Magn Reson Med 1991;18:224–31.

[135] Kim S, Hu X, Ugurbil K. Accurate T_1 Determination from Inversion Recovery Images: Application to Human Brain at 4 Tesla. Magn Reson Med 1994;31:445–9.

[136] Clare S, Jezzard P. Rapid T_1 mapping using multislice echo planar imaging. Magn Reson Med 2001;45:630–4.

[137] Look DC, Locker DR. Time Saving in Measurement of NMR and EPR Relaxation Times. Rev Sci Instrum 1970;41:250–1.

[138] Kay I, Henkelman RM. Practical implementation and optimization of one-shot T_1 imaging. Magn Reson Med 1991;22:414–24.

[139] Gowland PA, Leach MO. Fast and Accurate Measurements of T_1 Using a Multi-readout Single Inversion-Recovery Sequence. Magn Reson Med 1992;26:79–88.

[140] Deichmann R, Haase A. Quantification of T_1 Values by SNAPSHOT-FLASH NMR Imaging. J Magn Reson 1992;96:608–612.

[141] Gowland P, Mansfield P. Accurate Measurement of T_1 in Vivo in Less Than 3 Seconds Using Echo-Planar Imaging. Magn Reson Med 1993;30:351–354.

[142] Freeman AJ, Gowland PA, Mansfield P. Optimization of the ultrafast Look-Locker echo-planar imaging T_1 mapping sequence. Magn Reson Imaging 1998;16:765–72.

[143] Karlsen O. Quantitative MR Perfusion Imaging Using Arterial Blood Water as a Natural Marker. Ph.D. thesis, Technical University of Delft 1999.

[144] Ogawa S, Tank D, Menon R, Ellermann J, Kim S, Merkle H, Ugurbil K. Intrinsic Signal Changes Accompanying Sensory Stimulation: Functional Brain Mapping with Magnetic Resonance Imaging. Proc Natl Acad Sci U S A 1992;89:5951–5.

[145] Bandettini P, Wong E, Hinks R, Tikofsky R, Hyde J. Time Course EPI of Human Brain Function During Task Activation. Magn Reson Med 1992; 25:390–7.

[146] Meyer M, Yu O, Eclancher B, Grucker D, Chambron J. NMR Relaxation Rates and Blood Oxygenation Level. Magn Reson Med 1995;34:234–41.

[147] Spees W, Yablonskiy D, Oswood M, Ackerman J. Water Proton MR Properties of Human Blood at 1.5 Tesla: Magnetic Susceptibility, T_1, T_2, T_2^*, and Non-Lorentzian Signal Behavior. Magn Reson Med 2001;45:533–42.

[148] Buxton RB, Frank LR. A model for the coupling between cerebral blood flow and oxygen metabolism during neural stimulation. J Cereb Blood Flow Metab 1997;17:64–72.

[149] Janz C, Speck O, Hennig J. Time-resolved measurements of brain activation after a short visual stimulus: new results on the physiological mechanisms of the cortical response. NMR Biomed 1997;10:222–9.

[150] Kim S, Ugurbil K. Comparison of Blood Oxygenation and Cerebral Blood Flow Effects in fMRI: Estimation of Relative Oxygen Consumption Change. Magn Reson Med 1997;38:59–65.

[151] Zhu X, Kim S, Andersen P, Ogawa S, Ugurbil K, Chen W. Simultaneous oxygenation and perfusion imaging study of functional activity in

primary visual cortex at different visual stimulation frequency: quantitative correlation between BOLD and CBF changes. Magn Reson Med 1998; 40:703–11.

[152] Hoge RD, Atkinson J, Gill B, Crelier GR, Marrett S, Pike GB. Linear coupling between cerebral blood flow and oxygen consumption in activated human cortex. Proc Natl Acad Sci U S A 1999;96:9403–8.

[153] Hoge RD, Atkinson J, Gill B, Crelier GR, Marrett S, Pike GB. Stimulus-dependent BOLD and perfusion dynamics in human V1. Neuroimage 1999; 9:573–85.

[154] Hoogenraad F, Pouwels P, Hofman M, Reichenbach J, Sprenger M, Haacke E. Quantitative Differentiation Between BOLD Models in fMRI. Magn Reson Med 2001;45:233–46.

[155] Lee S, Duong T, Yang G, Iadecola C, Kim S. Relative changes of cerebral arterial and venous blood volumes during increased cerebral blood flow: implications for BOLD fMRI. Magn Reson Med 2001;45:791–800.

[156] Buxton R. The elusive initial dip. Neuroimage 2001;13:953–8.

[157] Mildner T, Norris D, Schwarzbauer C, Wiggins C. A Qualitative Test of the Balloon Model for BOLD-based MR Signal Changes at 3T. Magn Reson Med 2001;46:891–9.

[158] Bandettini P, Ungerleider L. From neuron to bold: new connections. Nat Neurosci 2001;4:864–6.

[159] Friston K, Josephs O, Rees G, Turner R. Nonlinear event-related responses in fMRI. Magn Reson Med 1998;39:41–52.

[160] Friston K, Zarahn E, Josephs O, Henson R, Dale A. Stochastic designs in event-related fMRI. Neuroimage 1999;10:607–19.

[161] Glover G. Deconvolution of impulse response in event-related BOLD fMRI. Neuroimage 1999;9:416–29.

[162] Liu T, Frank L, Wong E, Buxton R. Detection power, estimation efficiency, and predictability in event-related fMRI. Neuroimage 2001;13:759–73.

[163] Bandettini P, Jesmanowicz A, Wong E, Hyde J. Processing strategies for time-course data sets in functional MRI of the human brain. Magn Reson Med 1993;30:161–73.

[164] Friston K, Jezzard P, Turner R. Analysis of Functional MRI Time-Series. Human Brain Mapping 1994;1:153–171.

[165] Forman S, Cohen J, Fitzgerald M, Eddy W, Mintun M, Noll D. Improved assessment of significant activation in functional magnetic resonance imaging (fMRI): use of a cluster-size threshold. Magn Reson Med 1995;33:636–47.

[166] Luh W, Wong E, Bandettini P, Ward B, Hyde J. Comparison of simultaneously measured perfusion and BOLD signal increases during brain activation with T_1-based tissue identification. Magn Reson Med 2000; 44:137–43.

[167] Schwarzbauer C. Simultaneous detection of changes in perfusion and BOLD contrast. NMR Biomed 2000;13:37–42.

[168] Schulte AC, Speck O, Oesterle C, Hennig J. Separation and quantification of perfusion and BOLD effects by simultaneous acquisition of functional I_0- and T_2^*-parameter maps. Magn Reson Med 2001;45:811–6.

[169] Glover G, Lemieux S, Drangova M, Pauly J. Decomposition of inflow and blood oxygen level-dependent (BOLD) effects with dual-echo spiral gradient-recalled echo (GRE) fMRI. Magn Reson Med 1996;35:299–308.

[170] Cox R. AFNI: software for analysis and visualization of functional magnetic resonance neuroimages. Comput Biomed Res 1996;29:162–73.

[171] Conradsen K. En Introduktion Til Statistik 2. The Technical University of Denmark: Institute of Mathematical Statistics and Operations Research, 4th edition 1984.

[172] Boxerman J, Bandettini P, Kwong K, Baker J, Davis T, Rosen B, Weisskoff R. The intravascular contribution to fMRI signal change: Monte Carlo modeling and diffusion-weighted studies in vivo. Magn Reson Med 1995; 34:4–10.

[173] Born P, Leth H, Miranda M, Rostrup E, Stensgaard A, Peitersen B, Larsson H, Lou H. Visual activation in infants and young children studied by functional magnetic resonance imaging. Pediatr Res 1998;44:578–83.